JOURNAL OF CONDENSED MATTER NUCLEAR SCIENCE

Experiments and Methods in Cold Fusion

Proceedings of the 26th International Conference on Condensed Matter Nuclear Science, ICCF26, May 26–30, 2025, Morioka, Japan

VOLUME 41, March 2026

JOURNAL OF CONDENSED MATTER NUCLEAR SCIENCE

Experiments and Methods in Cold Fusion

JOURNAL OF CONDENSED MATTER NUCLEAR SCIENCE

Volume 41, March 2026

Orders, claims, author inquiries and journal inquiries

Please contact the Editor in Chief, CMNSEditor@iscmns.org or webmaster@iscmns.org

J. Condensed Matter Nucl. Sci. 41 (2026) 1–201

ISSN 2227-3123

JOURNAL OF CONDENSED MATTER NUCLEAR SCIENCE

Volume 41 2026

CONTENTS

RESEARCH ARTICLES

Preface

The 26th International Conference on Condensed Matter Nuclear Science (ICCF26) was held on May 26–30, 2025, in Morioka, Japan. The conference brought together researchers and engineers from around the world to present recent advances and exchange ideas in the field of condensed matter nuclear science (CMNS), also known as low-energy nuclear reactions (LENR). A total of 169 participants attended, including 132 in-person and 37 remote attendees.

Continuing the long-standing tradition of the ICCF series, ICCF26 provided a platform for interdisciplinary discussions among participants from academia, industry, and research institutions, covering a wide range of topics, including heat generation, transmutation phenomena, electrochemical and gas-loading experiments, plasma and beam studies, materials science, diagnostics, and theoretical modeling. The contributions presented at the conference reflect both the steady progress in experimental capabilities and the ongoing efforts to address key challenges such as reproducibility and theoretical understanding.

The technical program consisted of plenary, invited, and contributed oral presentations, as well as poster sessions, with 44 oral presentations and 35 poster presentations. These presentations demonstrated the diversity of approaches in the field and highlighted emerging directions, including advanced materials design, improved measurement techniques, and increasing engagement with broader scientific and industrial communities.

ICCF26 was co-organized with Iwate University, whose support was essential in the successful organization of the conference. We gratefully acknowledge the generous support of our sponsors, including the Anthropocene Institute, Solid State Fusion, New Energy Foundation / Infinite Energy Magazine, The Thermal & Electric Energy Technology Inc. Foundation (TEET), Morioka Tourism and Convention Association, Japan CF-Research Society (JCF), Iwate Prefecture International Linear Collider Promotion Council, Clean Planet Inc., New Hydrogen Fusion Energy Inc., Industrial Heat LLC, as well as individual donors. Their contributions were indispensable to the success of the conference.

All papers included in this volume were submitted to the conference and accepted through a peer-review process following the standard review procedures of the Journal of Condensed Matter Nuclear Science. We hope that this collection will serve as a useful reference for researchers and will encourage further developments in the field.

On behalf of the Local Organizing Committee, I would like to express my sincere appreciation to all authors, speakers, session chairs, and participants for their valuable contributions. I am also grateful to the International Advisory Committee and all supporting organizations for their guidance and support.

The International Advisory Committee has selected Niagara Falls, Canada as the venue for ICCF27, which will be held from August 31 to September 4, 2026. We look forward to continued progress in the field and to meeting again at the next conference.

April 2026
Shinya Narita, Chair, Local Organizing Committee, ICCF26

J. Condensed Matter Nucl. Sci. 41 (2026) 1–18

Research Article

A New and Improved Understanding of Cold Fusion Based on the Observed Behavior

Edmund Storms

Santa Fe, NM

Abstract

Cold fusion requires two essential conditions for it to occur. First, a location in which the Coulomb barrier can be reduced must be created. This unique condition is called the nuclear active environment (NAE). Second, the nuclear fuel, which is any isotope of hydrogen, must diffuse from its usual location in the crystal structure and enter the NAE. Upon arrival in the NAE, the fuel is converted to a nuclear product by a very unusual nuclear process, which involves the electrons within the NAE reducing the Coulomb barrier and carrying away part of the nuclear energy as they are emitted with kinetic energy. Helium is the final nuclear product when deuterium is used. This paper describes how these requirements can be met without violating the rules governing a chemical environment while being consistent with the nuclear requirements. A model describing the process is provided using only the observed behaviors and their implications.

Keywords: LENR, cold fusion, energy source, nuclear mechanism, hot fusion

1. Introduction

In 1989, Professors Fleischmann and Pons (F-P) [1] published a discovery that would eventually be identified as the fusion of deuterons within the palladium deuterium compound. After thousands of studies conducted in laboratories worldwide (LENR.org), the mechanism can now be described in simple terms. To fully understand this description, it is essential to first understand the more familiar **hot fusion** process to avoid mistaking this kind of fusion for the new kind, referred to as **cold fusion**.

Hot fusion was initially proposed as an explanation for the energy produced by stars when hydrogen is fused to form heavier elements. The nuclear reaction is relatively easy to induce; for example, striking a crystal of lithium deuteride (LiD) with a hammer will generate a burst of neutrons as the D nuclei fuse and the result fragments. However, to make the reaction frequent enough to generate useful power, temperatures in excess of millions of degrees are required. These high temperatures increase the chance of random encounters between two fuel nuclei, thereby increasing the probability that these encounters will result in fusion. This process has been applied on a large scale for the production of useful energy at a facility in France called ITER [2]. Many other large and small efforts are also underway in other countries.

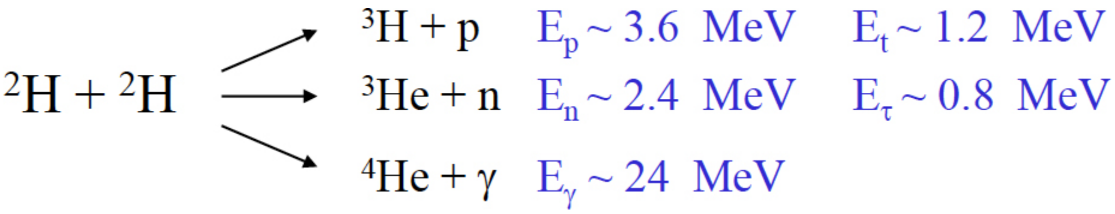

Figure 1. The energy of the emissions resulting from hot fusion between deuterons as provided by Czerski [3], [4]. The emission of ^{4}He with a very energetic gamma ray has a very low probability. These reactions are never observed when cold fusion occurs.

When deuterium (D) is used as the fuel, the hot fusion process results in the fragments of a helium nucleus, as shown in Fig. 1. The two fragmentation paths have nearly equal probability across all applied energies to produce a total of about 3.9 MeV/(D+D). This value is in contrast to 23.85 MeV/(D+D) produced by the cold fusion mechanism. The emission of neutrons is frequently used to measure the reaction rate of the hot fusion process. Neutrons are not emitted by the cold fusion mechanism.

The same reaction can also be initiated by bombarding a material containing D with D+ ions having energy sufficient to initiate the hot fusion mechanism. In this scenario, the reaction rate is enhanced by the surrounding electrons in the physical structure when the kinetic energy of the bombarding D+ ions is at the low end of the required energy [4], [5]. This effect is significant as it demonstrates that electrons within a structure can interact with a nuclear process. However, in spite of help from the electrons, the observed reaction rate becomes too small to detect when the applied energy is less than about 1000 eV. In contrast, cold fusion is easy to detect when no kinetic energy is applied. Although the increased reaction rate caused by the electrons in the lattice structure is small, it can be understood, fostering collaboration within the scientific community to study the process in more detail.

In contrast, cold fusion behaves entirely differently. In this case, the fusion reaction occurs spontaneously in various materials after they have undergone specific treatments, without the application of enough energy to cause hot fusion. Moreover, the nuclear product when D is used is the intact nucleus of helium-4 (He^4) that is measured as the gas. In other words, the conditions needed to trigger the fusion process, the resulting reaction rates, and nuclear product are entirely different between hot and cold fusion. These facts strongly support the conclusion that these two fusion reactions result from two entirely different and unrelated mechanisms with the electrons playing entirely different roles.

The understanding of cold fusion has been further complicated by the inability to agree on an effective explanation. This paper will attempt to clarify this confusion by describing a combination of simple and well-understood chemical processes that precede the spontaneous nuclear process. Nature is not creating this chemical environment in order to produce a nuclear reaction; instead, the nuclear reaction occurs simply because certain conditions just happen to enable a nuclear interaction at rare locations within the structure. The process cannot be initiated by a local concentration of energy because this would violate the Laws of Thermodynamics and cause chemical changes in the structure before nuclear interaction would result. The challenge is to identify and then create these conventional but rare conditions in large numbers.

The only mystery involves the nuclear process itself and the means by which it dissipates the resulting nuclear energy into the surrounding structure. Because the nuclear reaction is spontaneous after certain chemical conditions are created, knowledge about how the nuclear process works is not required to create a source of useful energy. Nevertheless, this knowledge is important because it reveals a new kind of nuclear-electron interaction with the advantage of producing useful energy without creating harmful nuclear products. A proposed description of the nuclear process is described in order to encourage a better replication and study of the mechanism.

2. Discussion

The cold fusion process can be described as the operation of three events. The first two are related to behaviors typical of a chemical process. The final event is related to the nuclear behavior. Each event is logically justified based on only the observed behavior. Neither part violates any rule of chemistry or physics although new rules may operate.

The three events consist of:

1. *Creation of a special location in a solid material, in which cold fusion can occur, called the nuclear active environment (NAE).* Cold fusion cannot happen at any other location. The total number of NAE creates an upper limit to the total amount of fusion power produced by the material being studied. Large local concentrations can even cause local melting [6]. A large concentration throughout a structure can cause self-heating and eventual melting of the entire material [7].
2. *Transport of hydrogen fuel to these unique sites by diffusion from its normal location in the surrounding crystal structure.* The mechanism of transport involves common and well-understood processes. The rate of fuel transport controls the amount of power produced by a material containing a fixed number of NAE [8].
3. *Operation of a nuclear fusion reaction that occurs spontaneously and nearly instantaneously by a universal mechanism operating in the NAE regardless of the material, treatment, or hydrogen isotope.* Triggering is not required although other processes can increase the rate. If very high energy is applied, such as in the form of gamma rays, the cold fusion mechanism would not be the result. The lasers presently used do not have enough energy to initiate the hot fusion mechanism [9]–[11].

2.1. Event 1

The NAE consists of physical gaps or voids in the arrangement of atoms in a solid. These flaws are independent of the crystallographic structure and are very common in all materials. The only requirement is a critically small size, which is rarely formed. These gaps are not caused by or related to atom vacancies in the crystal structure. They can be created many different ways including by nano machining or nano etching, as described in the next section.

To state the obvious, this kind of flaw is a common and accepted part of all materials without the need to demonstrate its existence. Because they are created by random chance with a variable size, the number of suitable flaws is variable and rarely formed in significant numbers, thus accounting for the difficulty to cause the cold fusion process. The only mystery is how the gap can change the rules that govern electron interactions so as to reduce the Coulomb barrier between the fuel nuclei without affecting or conflicting with the chemical behavior. Remember, the fusion process takes place in a chemical environment to which the Laws of Thermodynamics apply. The amount of local energy available to any process operating on the atomic scale is limited to a fraction of an eV because a greater energy would interact with and destroy the chemical bonds holding the structure together before it reached a level required to cause nuclear interaction.

Figure 2 shows a cartoon describing the crystal arrangement and the proposed irregular conditions surrounding the NAE. The normal arrangement of the palladium (Pd) and hydrogen atoms is illustrated by the first cartoon. In this arrangement, large spheres represent the electrons surrounding the Pd nucleus, while smaller spheres indicate the possible positions of the hydrogen atoms. The electrons in this configuration are fully committed to forming a fcc structure and hence are not available to offset the Coulomb barrier between hydrogen atoms. In addition, the hydrogen nuclei are too far apart for their nuclear energy states to interact by a process that would not also affect the chemical properties. Therefore, a different electron and atom arrangement is necessary to achieve this goal. Nevertheless, this structure is the source of the fuel to the sites where fusion occurs. This means that for fusion to occur, the hydrogen nuclei must move from their normal locations to find and enter the NAE located some distance away, thus the role of the diffusion process.

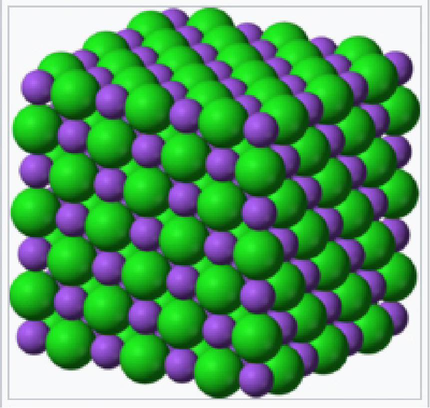

fcc Lattice Structure

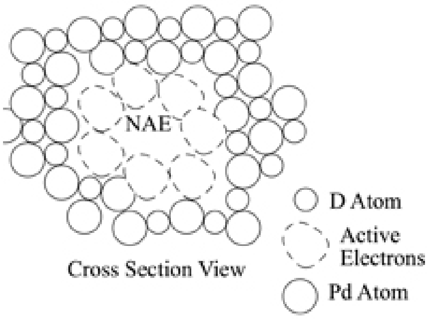

Figure 2. Cartoons showing the normal atom arrangement in a face centered cubic (fcc) structure (from Wikipedia) and the chaotic atom arrangement forming an idealized NAE. The NAE is a three-dimensional structure surrounded on all sides by electrons, some of which can support nuclear fusion when hydrogen nuclei (D, H, or T) enter the NAE [12].

The NAE can be described as an arrangement of the atom positions that create a gap surrounded by electrons so disorganized and chaotic that some of them are available to interact in unexpected ways with any hydrogen nuclei present in the NAE. The active electrons have energy states that do not involve the energy states of electrons normally associated with the Pd nucleus. These disorganized electrons are represented as the dashed circles in Fig. 2. When the region identified as the NAE is occupied by two hydrogen nuclei (D, H, or T), the uncommitted electrons can reduce the Coulomb barrier and facilitate fusion, which is described in a later section identified as EVENT 3.

The NAE structure can form in any solid material. The challenge is to find the most efficient method for its creation.

How can the NAE be formed within a material?

Examples of a few materials found to cause cold fusion are listed in Table 1. Although each material has been treated in different ways, the same active structure can be identified as being present as the NAE.

The challenge is to identify the common feature present in all these materials needed to support a fusion process. This goal is important because the ability to support fusion is frequently explained in several conflicting ways. Here the assumption is made that Nature would have only a single environment in which such an unusual and rare mechanism

Table 1. Processes that can increase the formation of the NAE The proposed location of the NAE in the material is identified.

1. Codeposit (CoD) of a metal (surface)
   - Szpak [13]: Slow electrolytic deposit of Pd from $\mathrm{PdCl_2}$ + LiCl or HCl in D_2O or H_2O.
2. Sintering of small particles (bulk)
   - Arata [14]: Palladium black
3. Imbedded inert particles in Pd (bulk)
   - Storms [15]: Particles of CaO or $\mathrm{SiO_2}$ < 36 micron
4. Creation of porous material (bulk)
   - Takahashi [16]: Oxidized Pd+Zr and other alloys
   - Case [17], [18]: Charcoal + Pd particles
   - Mizuno [19]: Stress induced gaps in Ni or Pd
   - Imam et al. [20], [21]: Stress induced gaps in Pd-B alloy
   - Iwamura et al. [22], [23] Stress induced gaps between layers of CaO and Pd
   - Biberian et al. [24] Hydrotalcites precursors
5. Accidental formation (surface)

   Damage caused by low-voltage gas discharge [25], [26]

   Damage caused by super wave [27]

   Damage caused by extended electrolysis

   Damage caused by ultra sound [28], [29]

   Damage caused by mechanically created cavitations [30]
6. Nano-machining (surface)

could occur. To this end, each item in Table 1 is discussed below in sequence to identify the location of the NAE and how this condition can be created on purpose.

1. The so-called CoD method uses a very small electrolytic current to deposit a very porous and poorly bonded collection of particles on the surface of the cathode. Although the method is a reliable source of fusion power, the resulting small amount of power is suitable only for research. The nanosized pores in the particles are proposed to be the NAE.
2. When small particles of Pd sinter into a solid mass, small gaps form throughout the bulk material where the particles did not have the correct crystal alignment required to form a uniform structure. These gaps can have a size required to support fusion when the initial particles are sufficiently small. Any method that involves very small particles will form such gaps, which eliminates the surface of the particles as the unique nuclear active location.
3. When small particles of an inert material, such as CaO or $\mathrm{SiO_2}$, are present in Pd, gaps will form around the particles when the metal expands as it reacts with hydrogen. The gap can have the required size when the particle is sufficiently small. This process is proposed to explain the success Fleischmann and Pons had when using Pd supplied by Johnson Matthey plc. In this case, the small particles of CaO are proposed to result from the method used to reduce the dissolved oxygen content in the Pd melt.
4. Porous material having a random collection of flaws with a suitable small size can be created many different ways. One method of special note is the use of coconut charcoal to which small particles of Pd have been added. Being made from a natural product, the charcoal contains many different structures with flaws of many different sizes. Ordinary charcoal containing the same type of Pd particles was not found to be nuclear active,

Table 2. Processes that can increase the rate at which the fuel can reach the NAE.

1. Increased temperature [8], [24]
2. Electromigration and the Gorsky Effect (Gorsky Effect) [33]– [35] + magnetic field
3. Laser radiation [9], [36]
4. Gross diffusion caused by a concentration or pressure gradient [37], [38]
5. Concentration of fuel in the lattice (D(H)/Pd ratio) when the concentration of NAE is large at low temperatures [39], [40].

thereby eliminating the Pd as the site of the NAE. Apparently in this case, the Pd is needed only to split the surrounding D_2 gas molecule to make D ions available to the NAE in the charcoal. The unique impurities in the natural charcoal probably created the required small gaps.

Stress between two materials that expand by different amounts can create the required NAE structure. In this case, the differential expansion results when the material reacts with hydrogen [31].

5. Various treatments can produce surface damage containing some NAE [30], [32]. These methods tend to be unreliable because they are very sensitive to the controlling variables and experience repeated destruction and creation at uncontrolled rates. Nevertheless, the various processes have supported many useful studies.
6. Gaps of suitable size can be created in a surface region by methods available to the integrated circuit industry. This approach could be used to make the NAE in large numbers with reproducibility.

These examples support the conclusion that the universal NAE can be produced many different ways in many different materials. The only challenge is to create it in high concentration with reliability. The material and methods need to be considered only with this goal in mind. The most effective method would be their creation by nanomachining. This method would allow a high concentration of NAE to be manufactured in any material, with very little material being required, thereby removing the justification of using a cheaper metal less effective than palladium.

2.2. Event 2

After some NAE has formed, the fuel located in the lattice structure or in the surrounding gas must move to the NAE by a conventional process, with a successful encounter being controlled by random chance. Processes known to increase the ability of hydrogen to move in a structure are summarized in Table 2.

The expected ability of increased temperature to enhance the fusion rate was recognized by Fleischmann and Pons [41] and others [42]–[44], but this effect was not properly exploited at the time. Consequently, most studies that were intended to demonstrate the fusion process were conducted at room temperature, which rarely allowed for a detectable fusion rate, given the low sensitivity of the calorimeters being used at the time. For example, notice in Figure 3 that no excess power is detected at room temperature during this study, yet power is clearly produced when the temperature is increased. This behavior has been frequently observed. Ironically, the many failures that were used to reject the claim for cold fusion might have been reduced if the temperature had been increased. Storms [8] demonstrated that the effect of temperature on fusion power is related to the normal diffusion process, as both processes share similar activation energy.

Applying a voltage, along with the resulting current, can increase the diffusion rate of ions through a lattice structure. This phenomenon was termed the “Coehn effect” by Fleischmann [35] when deuterium (D) was caused to move to the negative region when a voltage was applied to PdD. When observed in other materials, it is known as electromigration. The integrated circuit industry has studied this mechanism because it impacts on the longevity of computer circuits.

The effects of temperature and electromigration were explored using a sample of palladium (Pd) that was activated by a deposit of CoD palladium. This sample was placed in deuterium (D_2) gas, which could be heated while a direct

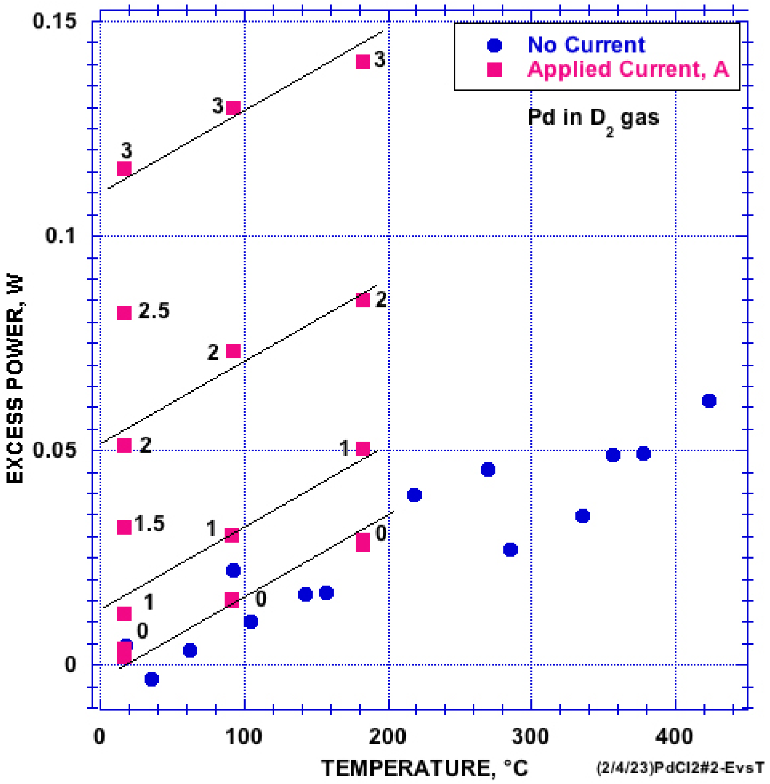

Figure 3. Effect of applied current is shown in units of ampere(A). The values for “no current” were obtained first followed by the values designated as “applied current”. The current at a constant temperature was measured and then the temperature was increased and held for 100 min until the temperature became constant.

current (DC) was passed through its length. The D_2 pressure created a D/Pd ratio of approximately 0.7 at room temperature, with a reduction in the D/Pd ratio as the temperature is increased. Measurements were taken while both the applied current and temperature were varied. Each data point, shown in Fig. 3, was obtained after maintaining constant conditions for 100 minutes, allowing the Seebeck calorimeter [45], [46] to reach a steady state.

The temperature effect was studied first, after which a current was applied while measuring the resulting excess energy. The power added to the calorimeter by the current was measured and subtracted from the measured power. However, the added power was trivial due to the PdD having a very small resistance of 0.026 ohm.

It is notable that the applied current produced a significantly greater increase in the fusion rate compared to the increase caused by temperature alone, as expected. When the amount of excess power is plotted as a function of current at room temperature, the results shown in Fig. 4 exhibit consistent behavior that can be fit by a quadratic equation. This behavior was independent of time and remained unchanged even when the current direction was reversed, indicating that the effect was not caused by the increased concentration of deuterium at the cathode, which involves a very slow change in D concentration. The good fit to a quadratic equation suggests the amount of power applied by the current might be measured incorrectly. This possibility needs to be explored by future studies.

The ability of D+ ions to locate and occupy a NAE site also can be enhanced by a flux of D resulting from a concentration gradient or a pressure difference across the thickness of a material because the resulting flux would cause the fuel to encounter the NAE with greater probability.

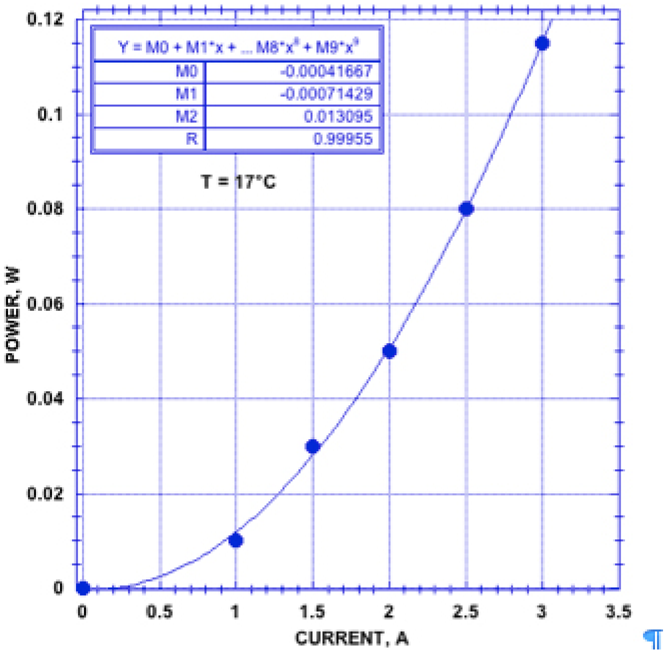

Figure 4. Excess power as a function of applied current at 17°C. Notice that no power is detected in the absence of applied current at 17° C.

The application of laser radiation will also increase the reaction rate, possibly due to a local increase in temperature or enhanced diffusion caused by phonon activity. Other, unknown processes might operate.

Additionally, the application of a magnetic field is expected to improve the efficiency of ion diffusion, as the ions are guided along a more complex path created by the lines of magnetic force, thereby increasing the probability of encountering the NAE.

Many researchers believe a large concentration of the fuel in the lattice structure is required to achieve a useful rate of fusion. Apparently, a high concentration is only effective when the concentration of NAE is large at low temperatures. When the concentration is small, the fuel concentration has very little effect. A previous paper shows the effect of the D/Pd ratio with greater clarity [47].

In summary, the amount of power generated by a material can be increased and controlled using demonstrated methods that align with established chemical behavior. These methods are all consistent with an increased ability for the fuel to move from its normal location to find and then enter the special site that supports the fusion process. The most effective method is electromigration, which causes an immediate change in the amount of fusion power. This rapid response would allow for effective fast control to match the load change on an industrial energy generator.

2.3. Event 3

The true mystery of cold fusion involves the nature of the fusion process itself. Nevertheless, nothing about this mechanism needs to be known to design an effective source of energy because the nuclear process happens spontaneously after the fuel has assembled in the NAE. Therefore, a useful generator of power only requires the NAE to be created with a high concentration in a suitable material.

For the sake of a complete discussion, the proposed nuclear mechanism is summarized in Table 3.

Table 3. Summary of the proposed events occurring during the fusion process.

1. The Coulomb barrier is overcome by a concentrated assembly of electrons in the NAE without kinetic energy being applied.
2. When deuterons fuse, the mass energy is emitted as energetic ^{4}H ion radiation and energetic electrons. Helium is the final nuclear product when ^{4}H decays by beta emission. Neutrons are not emitted. Deuterium results as the nuclear product when H+H fuse. Tritium results as the nuclear product when H+D fuse. Neutrons and helium result when D+T fuse. These products result because an electron is captured in the nuclear product before the mass-energy is released as kinetic energy. The energy required to add the extra electron is supplied by the energy released by the fusion reaction.
3. The momentum is conserved during each nuclear product emission by the emission of many electrons in suitable directions.
4. The process is spontaneous in the required environment identified as the NAE.
5. Secondary nuclear reactions with energetic emission, including neutrons, are produced by local hot fusion and transmutation reactions. These result when the energetic emission created by cold fusion encounters a stationary nucleus within the lattice.

These events are described in more detail by Storms [48] and in a future paper.

These events cause ^{4}He gas and heat energy to be detected when deuterium is used. The measurements are summarized in Figure 5 as a histogram showing values of He/energy from seventeen measurements by four separate studies using electrolysis at 20° C. Notice that these values combine to show a variation typically produced by random errors as shown by the good fit by the Gaussian equation. It's important to realize that this ratio involves two independent measurements that could have resulted in a very large spread in the values as the consequence of random errors, yet it does not.

When the average is compared to the amount of He/energy calculated using $E=mc^2$, with m being the mass change, about 50% of the expected helium seems to be missing. This missing helium appears be trapped within the Pd metal because when efforts are made to remove this gas, the total amount of helium collected is very close to the expected value. The measured heat-energy could be too large as the result of any transmutation reactions that would result from the fusion reaction. Some energy might also be missing as an antineutrino is emitted by the proposed beta decay of ^{4}H. The ratio plotted in Fig. 5 needs to be studied with greater precision for the process to be fully understood.

One additional value was obtained from a sample of coconut charcoal containing small particles of Pd that was heated in D_2 at about 250° C [49]. This value agrees very well with the values (Fig. 5) obtained using electrolysis, demonstrating that electrolysis is not required to cause the fusion reaction.

Notice that when two D's combine to form helium, no nucleons are left over. Therefore, the observed neutron radiation cannot result from this reaction.

A Serious Problem

Now we come to the true mystery of the process. Apparently, only one nuclear product is emitted. Consequently, momentum cannot be conserved when nuclear energy is released into the environment as kinetic energy of the nuclear product. This problem can be better understood by considering that all nuclear reactions require the emission of two different masses in opposite directions with equal momentum along with the energy resulting from the nuclear process. This requirement is as important to nuclear processes as the Law of Thermodynamics is to chemistry.

The apparent failure of cold fusion to comply with the conservation of momentum has led people to propose new mechanisms never before observed in Nature [51]. Some people suggest that cold fusion is actually a variation of hot fusion that occurs at low energy. In this scenario, momentum is conserved by the fragmentation of the helium nucleus, as illustrated in Figure 1. The apparent detection of helium gas, summarized in Figure 5, is even seen by some as an artifact resulting from poor measurements. Others propose that the detected helium gas is real, and that energy is communicated to the surrounding material through phonon interactions, resonance processes, or other unique mechanisms. At one time, I proposed the slow serial emission of photons [48] as a mechanism to avoid

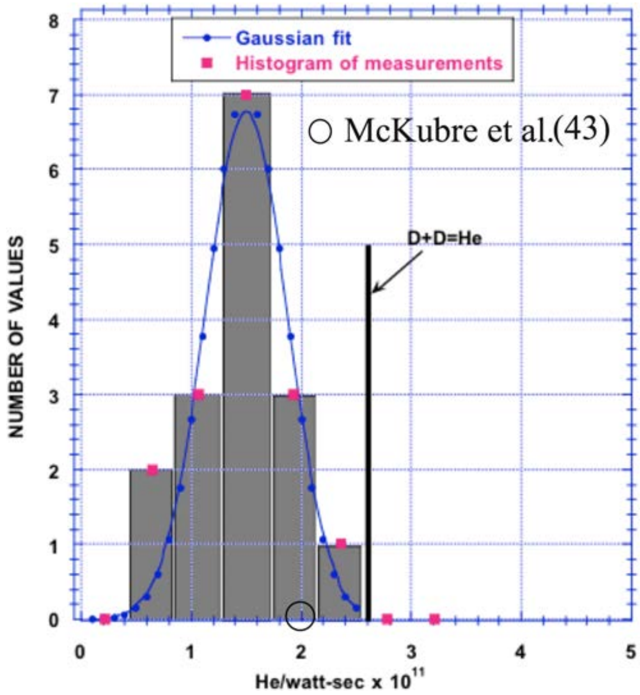

Figure 5. Histogram of measured He/energy values compared to the ratio obtained using the mass change when the fusion reaction D+D=He occurs [50] [48]. The vertical line represents 23.85 MeV/He.

the conundrum. These conflicting explanations have created confusion and uncertainty within the field, delaying the practical application of this mechanism as a source of useful energy.

This model proposes that momentum is conserved and energy is communicated to the surrounding material by the emission of electrons along with the nuclear product. This process is illustrated using the cartoon shown in Figure 6. The logic begins with the fact that the Coulomb barrier between two nuclei must be reduced to allow their nuclear energy states to interact, which is a basic requirement of any fusion process. This reduction is proposed to occur in the NAE, where electrons are available to facilitate this interaction. These electrons are represented by the green structure at the top of the figure. They are not associated in a conventional way with the nuclei of the Pd atoms. Their presence causes the two nuclei, represented as red circles, to move closer together. Eventually, they come close enough for their nuclear energy states to interact by means of the strong force. Since electrons are involved in this process, they are available to become part of the newly combined nuclear energy state, as shown by the purple structure. This structure embodies the true mystery of the process.

However, this combined structure contains a large amount of excess energy that must be released for the stable nuclear product to form. Because the structure contains many electrons, these electrons are emitted in opposite directions, thereby conserving momentum and releasing kinetic energy equal to the mass change into the surrounding material as heat energy. One electron is proposed to remain in the emitted nuclear product. The electron emission can take different paths as summarized by the last three reactions. These paths are discussed in the following section.

What evidence supports this description? The first evidence for energetic electron emission was provided by Gordon and Whitehouse [52], [53]. They called this process a Lattice Energy Converter (LEC) and proposed it as a source of useful electrical energy. Several replications followed [54].

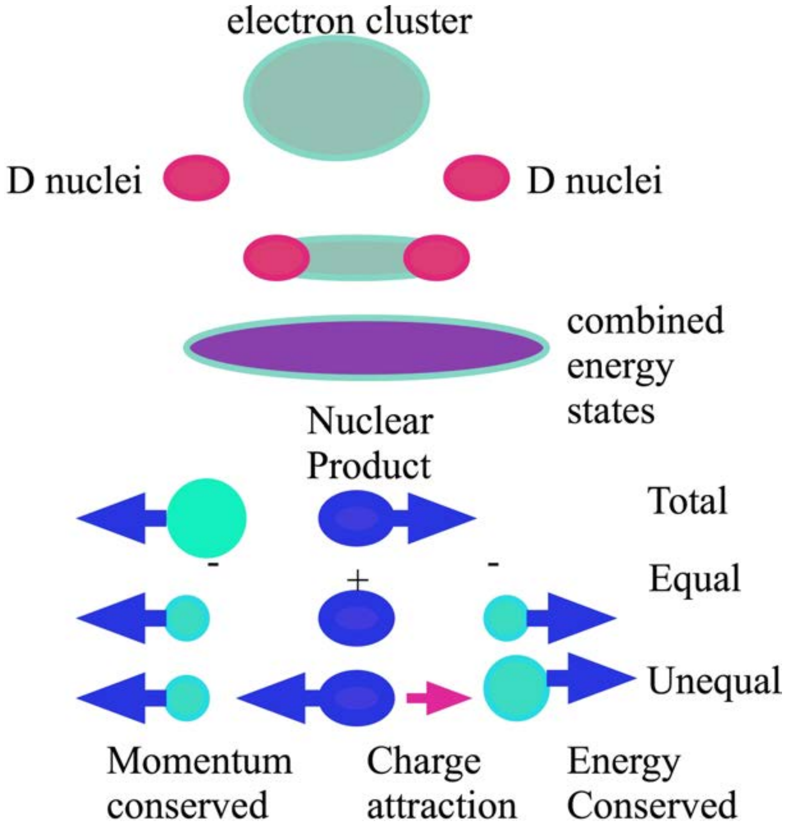

Figure 6. Cartoons showing the sequence of events occurring during the cold fusion process. The final cartoons show three possible ways the energy can be dissipated into the surrounding structure by the emission of the nuclear product and electrons.

A measurement of electron emission done by the author is described next. The sample is palladium (Pd) coated with palladium using the CoD method (see Table 1). This was exposed to deuterium gas (D_2) at a pressure that would place the PdD in the two-phase region (α+β) at room temperature. The current was measured without an external voltage applied between the Pd emitter and the platinum (Pt) collector. Figure 7 shows the effect of temperature on both the excess power, measured using a Seebeck calorimeter, and the emitted current, which was measured as a voltage across a resistor connected between the emitter and collector. Both the fusion power and the emitted current increase as the temperature is increased, suggesting a common source. However, the reason for the rapid increase in current at temperatures above 350° C is unknown.

The number of electrons emitted by each fusion reaction was calculated. This value is obtained using the measured amount of power to calculate the fusion rate at 298° C. The collected current is obtained from Fig. 8 without voltage being applied. The resulting value of electron/fusion is doubled because at least ½ of the electrons would to be emitted away from the collector. The resulting value of 30 electrons/fusion would be a lower limit for the actual value, as some electrons would be stopped before reaching the collection electrode. This value supports the proposed emission of electrons as the carriers of momentum and nuclear energy.

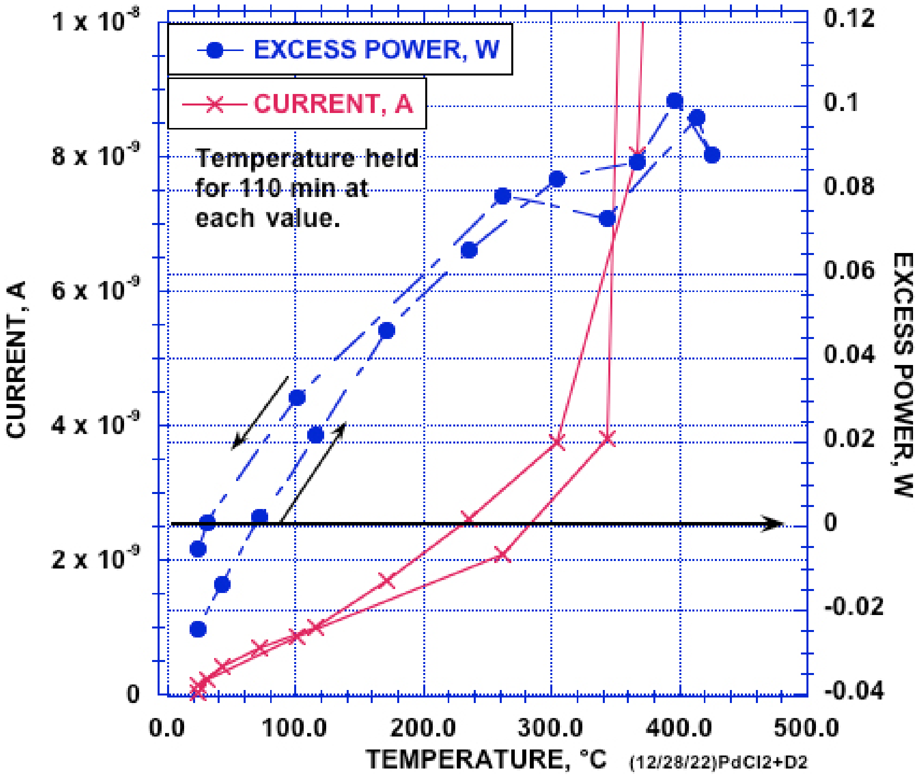

Figure 7. Comparison between excess power and electron emission current from α-PdD + β-PdD in D_2 as a function of temperature.

Next, a voltage was applied between the collector and emitter. When this voltage was positive (Fig. 8), all electrons with energy less than the applied voltage would be returned to the emitter, resulting in a reduction of the measured current. The figure shows that the emitted electrons had a range of energies exceeding 100 eV. This energy level is too high to have resulted from a chemical process or from differences in work function. It is proposed that this energy reflects what remains after the electrons emitted from the fusion reaction have passed through the palladium on their way to the surface of the sample. Notice that the excess power increased as electrons were returned to the surface by the applied voltage.

Even more interesting, the amount of emitted current was sensitive to how long the voltage was applied (Fig. 9). This effect is especially obvious after a steady value of 100 eV was applied. This enhancement of the emitted current and, presumably, the fusion rate is proposed to result from electromigration, which was increased in the surface due to an additional returned electron current in that region. Clearly, these behaviors warrant further exploration, as they reveal important information about the process.

In addition to the emission of electrons, the emitted nuclear product exhibits very unusual behavior. Figure 10 shows the energy distribution of the detected emissions produced by gas discharge in D_2 gas using Pd as the cathode, as reported in extensive studies conducted by Karabut et al. in Russia [55]. A replication of this experiment was performed by Storms and Scanlan (SS) [56] using a modern silicon barrier detector (SBD), which resulted in the spectrum shown in Figure 11. These two studies produce similar behavior when compared in Figure 12, demonstrating

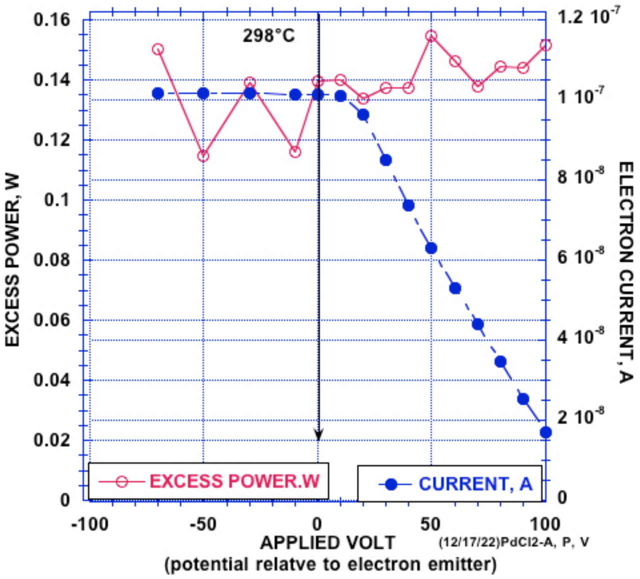

Figure 8. Effect of a voltage applied between the emitter and collector on the electron current at 298° C emitted from $\alpha+\beta$ PdD in D_2 gas. The excess power is also shown.

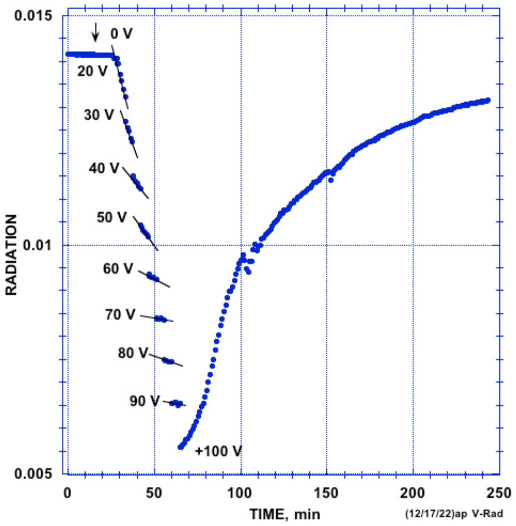

Figure 9. Effect of time on the measured current shown in Fig. 8, plotted as arbitrary units identified as Radiation. The voltages applied between the emitter and the collector for each measurement shown in Fig. 8 are identified.

agreement not only in values but also in the slope as a function of the sequence number. In addition, both data sets extrapolate to near zero energy at point #0. The small difference between the two results can be attributed to the emitted ions having to travel through different amounts of material before reaching the respective SBD.

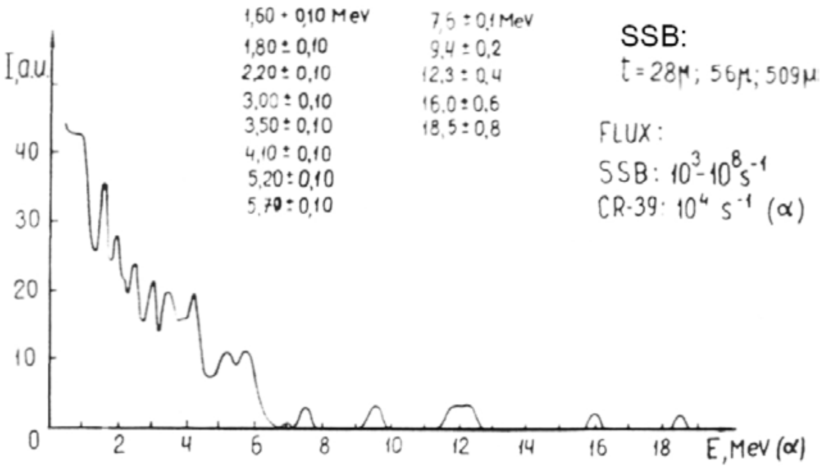

Figure 10. Energy measured using a silicon barrier detector for ions emitted from Pd by gas discharge in D_2 [55] KK.

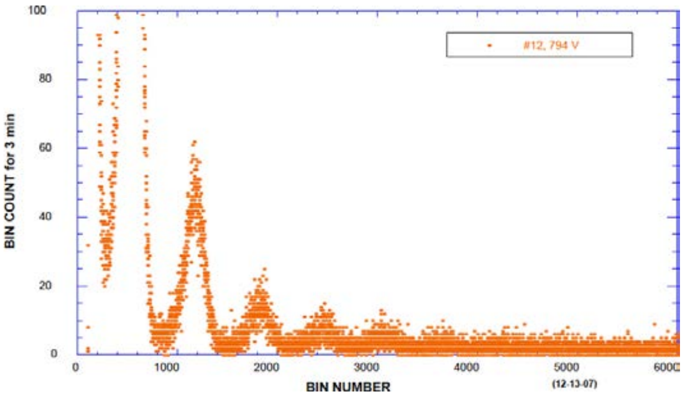

Figure 11. Energy measured using a silicon barrier detector for ions emitted from Pd by gas discharge in D_2 + H_2 [56] SS.

The proposed explanation predicts that the same kind of emission with the same energy characteristics would result from cold fusion occurring in any material containing deuterium, not just Pd. In addition, because fusion between H+H+e is proposed to produce deuterium, this nuclear product is predicted to fuse with another D to produce this emission behavior even in the absence of D_2 in the gas, although at a lower rate. These predictions need to be tested.

The study by SS also revealed that the emission had characteristics of an isotope of hydrogen rather than helium when it passed through absorbers of various thicknesses. This observation provides further support for ^{4}H being emitted. The energy of 0.76 MeV required to form the extra neutron in the ^{4}H nucleus is subtracted from the fusion energy. This subtracted energy is eventually added to the measured heat energy when the ^{4}H decays to form ^{4}He by beta decay. Of course, some of this energy would be lost as the result of antineutrino emission, which would shift the measured He/energy plotted in Fig. 5 to slightly larger values. This possibility adds importance to measuring the He in both the gas and the PdD.

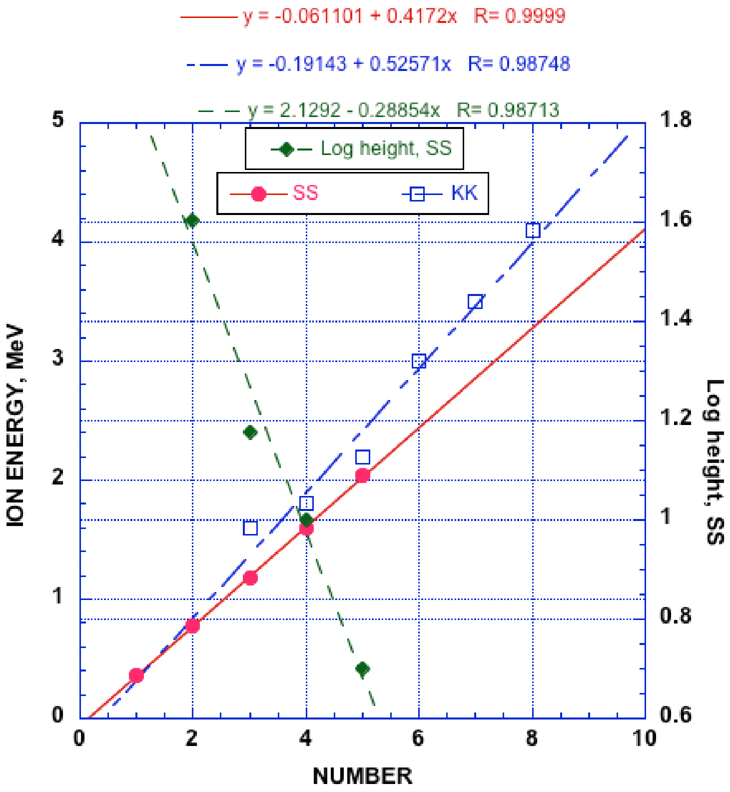

Figure 12. Comparison between the data sets in Figures 10 and 11. The log ion intensity is obtained from the data in Fig. 11. The first value in Fig. 10 is assumed to be point #3 in the sequence with the previous values being hidden in the noise.

It's important to note that the only way for the energy of an emitted particle to change is for its velocity to change. The regular change in the emitted energy of ^{4}H indicates that the square of its velocity changes in equal steps, with an increased velocity leading to a decreased probability of emission. The challenge is to understand the mechanism that causes this behavior. Perhaps it's more than coincidence that the energy difference between each adjacent peak is nearly equal to the mass-energy of an electron.

This information allows for a logical explanation that combines the observed behavior of the emitted electrons with the measured energy of the nuclear product. The lower part of Figure 6 describes this process as a cartoon. Several possible behaviors can be suggested. The nuclear product and electrons can each be emitted in opposite directions, ensuring that the momentum of the many electrons equals the momentum of the nuclear product when the total combined energy of both emissions equals the required 23.85 MeV/He. The consequence of this behavior was examined in a previous paper [57]. While the behavior of the electrons can be calculated using this description, the series of emitted energies exhibited by the nuclear product remains unexplained.

Instead, an equal number of electrons can be emitted in opposite directions so that the electrons alone conserve momentum and carry all of the kinetic energy. Under these conditions, the nuclear product would remain stationary, increasing the likelihood of it being trapped in the material. Extrapolation of the log intensity to point #0 (Fig. 12) shows that about 50% of the fusion products would be expected to have no kinetic energy.

Table 4. Summary of the storms model.

1. A special condition called the nuclear active environment (NAE), consisting of a void having a special small size, must be formed in large numbers by suitable treatments. (Table 1)
2. The material must be exposed to an isotope of hydrogen, preferably deuterium as the fuel.
3. The fuel must be caused to move more rapidly from its normal locations in the material and assemble in the NAE. (Table 2)
4. The Coulomb barrier is reduced by a large local assembly of electrons in the NAE. (Table 3)
5. The fusion of D results in the formation of ^{4}H that decays to ^{4}He by beta emission.
6. The nuclear energy is dissipated into the surrounding material by the emission of energetic electrons among with the ^{4}H, which rapidly decays by beta emission to form ^{4}He.
7. Neutron emission and transmutation occur as secondary reactions as a result of the energetic fusion products encountering a stationary nucleus in the surrounding structure.
WARNING:
1. The NAE is expected to have a limited lifetime as the NAE becomes saturated with the nuclear products.
2. The use of H_2 is not recommended because it is expected to produce tritium while making much less energy/fusion reaction compared to D, which does not make tritium.

These several possibilities are too complex to explain here. Consequently, further understanding will have to await future studies. For the present, the process can be seen as complex with several process operating to satisfy the conditions required to dissipate the nuclear energy.

3. Future Plans

Future plans should focus on creating the NAE with increased reliability. The methods identified in Table 1 provide examples of how this might be accomplished. As the method to make NAE is mastered, the treatments listed in Table 2 can be used to control the amount of power generated as heat energy. Proper design then can be used to harvest enough electrical energy from the emitted electrons to make useful electrical power directly, as envisioned by Gordon and Whitehouse. This model provides a clear path to accomplish these goals.

4. Summary

Table 4 provides a summary of the events that lead to fusion.

Acknowledgments

The author is grateful for the editorial efforts of Dr. Thomas Grimshaw and Carol Storms. Jacques Ruer was especially helpful in making the ideas easier to understand.

References

[1] M. Fleischmann, S. Pons, M. Hawkins, Electrochemically induced nuclear fusion of deuterium, J. Electroanal. Chem. 261 (1989) 301-8 and errata in Vol. 263, 187–8.

[2] J.-P. Petit, ITER Chronicle of a probable failure, http://www.jp-petit.org/NUCLEAIRE/ITER/ITER_fusion_non_controlee/ITER_en.pdf, 2012.

[3] K. Czerski, Enhanced electron screening and nuclear mechanism of cold fusion, in: V. Violante, F. Sarto (Eds), 15th International Conference on Condensed Matter Nuclear Science, ENEA, Italy, Rome, Italy, 2009, pp. 197–202.

[4] K. Czerski, New evidence of the cold nuclear fusion – accelerator experiments at very low energies, New Advances on the Fleischmann-Pons Effect, European Parliament, Brussels, 2013.

[5] A. Krauss, H.W. Becker, H.P. Trautvetter, C. Rolfs, Low-energy fusion cross sections of D + D and D + 3He reactions, Nucl. Phys. A 465 (1987) 150.

[6] D. Nagel, A.E. Moser, High Energy Density and Power Density Events in Lattice-enabled Nuclear Reaction Experiments and Generators, J. Cond. Mater. Nucl. Sci. 19 (2016) 219–29.

[7] S. Pons, M. Fleischmann, Heat after death, in: T.O. Passell (Ed) Fourth International Conference on Cold Fusion, Electric Power Research Institute 3412 Hillview Ave., Palo Alto, CA 94304, Lahaina, Maui, 1993, pp. 8.

[8] E. Storms, The Nature of the D+D Fusion Reaction in Palladium and Nickel, JCMNS 36 (2022) 377–94.

[9] J.P. Biberian, L.P. Forsley, P.A. Mosier-Boss, Transmutation of Palladium Induced by Laser Irradiation, JCMNS 37 (2023) 9–22.

[10] D. Letts, Highly reproducible LENR experiments using dual laser stimulation, Current Science 108 (2015) 559–61.

[11] J. Tian, L.H. Jin, B.J. Shen, Z.K. Weng, X. Lu, Excess heat triggering by 532 nm laser in a D/Pd gas loading system, in: D.L. Nagel, M.E. Melich (Eds), ICCF-14 International Conference on Condensed Matter Nuclear Science, www.LENR.org, Washington, DC, 2008, pp. 328–32.

[12] E.K. Storms, The nature of the energy-active state in Pd-D, Infinite Energy #5-6 (1995) 77–81.

[13] S. Szpak, The Pd + D Co-Deposition: Process, Product, Performance, J. Cond. Matter Nucl. Sci. 14 (2014) 68–75.

[14] Y. Arata, Y.-C. Zhang, A new energy generated in DS-cathode with ‘Pd-black’, Koon Gakkaishi 20 (1994) 148 (in Japanese).

[15] E. Storms, The Nature of Cold Fusion (Cold Fusion Made Simple), JCMNS 38 (2024) 130–46.

[16] A. Takahashi, H. Ido, A. Hattori, R. Seto, A. Kamei, J. Hachisuka, T. Yokose, Y. Mori, A. Taniike, Y. Furuyama, Latest Progress in Research on AHE and Circumstantial Nuclear Evidence by Interaction of Nano-Metal and H(D)-Gas, J. Cond. Mater. Nucl. Sci. 33 (2020) 14–32.

[17] L.C. Case, Catalytic fusion of deuterium into helium-4, in: F. Jaeger (Ed) The Seventh International Conference on Cold Fusion, ENECO, Inc., Salt Lake City, UT, Vancouver, Canada, 1998, pp. 48.

[18] L. Case, There is a Fleischmann-Pons effect. The process is electrolytic, but the effect is catalytic., in: X.Z. Li (Ed) The 9th International Conference on Cold Fusion, Condensed Matter Nuclear Science, Tsinghua Univ. Press, Tsinghua Univ., Beijing, China, 2002, pp. 22.

[19] T. Mizuno, T. Ohmori, K. Azumi, T. Akimoto, A. Takahashi, Confirmation of heat generation and anomalous element caused by plasma electrolysis in the liquid, in: F. Scaramuzzi (Ed) 8th International Conference on Cold Fusion, Italian Physical Society, Bologna, Italy, Lerici (La Spezia), Italy, 2000, pp. 75–80.

[20] M.H. Miles, M. Fleischmann, M.A. Imam, Calorimetric analysis of a heavy water electrolysis experiment using a Pd-B alloy cathode, Naval Research Laboratory, NRL/MR/6320--01-8526, Washington, 2001, pp. 154.

[21] A. Imam, D.J. Nagel, M.H. Miles, Fabrication and Characterization of Palladium–Boron Alloys Used in LENR Experiments, J. Cond. Matter. Nucl. Sci. 29 (2019) 1–11.

[22] Y. Iwamura, T. Itoh, J. Kasagi, S. Murakami, M. Saito, Excess Energy Generation using a Nano-sized Multilayer Metal Composite and Hydrogen Gas, J. Cond. Mater. Nucl. Sci. 33 (2020) 1–13.

[23] Y. Iwamura, T. Itoh, J. Kasagi, A. Kitamura, A. Takahashi, K. Takahashi, R. Seto, T. Hatano, T. Hioki, T. Motohiro, M. Nakamura, M. Uchimura, H. Takahashi, S. Sumitomo, Y. Furuyama, M. Kishida, H. Matsune, Anomalous Heat Effects Induced by Metal Nano-composites and Hydrogen Gas, J. Cond. Matter. Nucl. Sci. 29 (2019) 119–28.

[24] J.P. Biberian, R. Michel, C. Le Roux, M. Valat, S. Bucher, A. Kodeck, J.R. Sjöberg, J. Ruer, D. Chaudanson, Excess Heat in Nanoparticles of Nickel Alloys in Hydrogen, JCMNS 38 (2024) 186–95.

[25] I. Savvatimova, Y. Kucherov, A. Karabut, Cathode material change after deuterium glow discharge experiments, Trans. Fusion Technol. 26 (1994) 389–94.

[26] B. Wu, S. Jin, F. Shang, D. Yao, Y. Ding, J. Yao, P. Yao, The SEM observation of palladium-deuterium system after the gas discharge process, Gaojishu Tongxun 1 (1991) 1 (in Chinese).

[27] I. Dardik, SuperWaves™ as the Natural Origin of Excess Heat, in: V. Violante, F. Sarto (Eds), 15th International Conference on Condensed Matter Nuclear Science, ENEA, Italy, Rome, Italy, 2009, pp. 307–11.

[28] R. Stringham, When bubble cavitation becomes sonofusion, J. Cond. Matter Nucl. Sci. 6 (2012) 1–12.

[29] R.S. Stringham, Deuteron Plasmas Driven to Neutrality and 4He, J. Cond. Mater. Nucl. Sci. 30 (2020) 44–65.

[30] T. Ohta, On the molecular kinetics of acoustic cavitation and the nuclear emission, Int. J. Hydrogen Energy 28 (2003) 437.

[31] Y. Iwamura, M. Sakano, T. Itoh, Elemental analysis of Pd complexes: effects of D_2 gas permeation, Jpn. J. Appl. Phys. A 41 (2002) 4642-50.

[32] I. Dardik, Superwave reality, in: J.-P. Biberian (Ed) 11th International Conference on Cold Fusion, World Scientific Co., Marseilles, France, 2004, pp. 81.

[33] A.H. Verbruggen, C.W. Hagen, R. Griessen, Gorsky effect in concentrated α'-PdHx, J. Phys: Metal Physics 14 (1984) 1431.

[34] H. Wipf, The gorsky effect, electrotransport and thermotransport of hydrogen in metals, J. Less-Common Metals 49 (1976) 291–307.

[35] A. Coehn, Nachweis Von Protonen in Metallen, Z. Elektrochem. 35 (1929) 676.

[36] D. Letts, D. Cravens, Laser stimulation of deuterated palladium: past and present, in: P.L. Hagelstein, S.R. Chubb (Eds), Tenth International Conference on Cold Fusion, World Scientific Publishing Co., Cambridge, MA, 2003, pp. 159–70.

[37] A. Caravella, G. Barbieri, E. Drioli, Concentration polarization in Pd-based membranes for hydrogen separation: modeling and simulation, in: V. Violante, F. Sarto (Eds), 15th International Conference on Condensed Matter Nuclear Science, ENEA, Italy, Rome, Italy, 2009, pp. 154–7.

[38] Y. Arata, Y.C. Zhang, Achievement of intense ‘cold’ fusion reaction, Proc. Jpn. Acad., Ser. B 66 (1990) 1.

[39] M.C.H. McKubre, S. Crouch-Baker, A.M. Riley, S.I. Smedley, F.L. Tanzella, Excess power observations in electrochemical studies of the D/Pd system; the influence of loading, in: H. Ikegami (Ed) Third International Conference on Cold Fusion, "Frontiers of Cold Fusion", Published by: Universal Academy Press, Inc., Tokyo, Japan, Held at: Nagoya Japan, 1992, pp. 5.

[40] P.L. Hagelstein, M.C. McKubre, D.J. Nagel, T. Chubb, R. Hekman, New physical effects in metal deuterides. Report of the review on low energy nuclear reactions, in "Review of Low Energy Nuclear Reactions", DoE, Office of Sci., Washington, DC, 2004, in: J.-P. Biberian (Ed) 11th International Conference on Cold Fusion, World Scientific Co., Marseilles, France, 2004, pp. 23.

[41] M. Fleischmann, S. Pons, Calorimetry of the Pd-D_2O system: from simplicity via complications to simplicity, Phys. Lett. A 176 (1993) 118.

[42] G. Lonchampt, J.-P. Biberian, L. Bonnetain, J. Delepine, Excess heat measurement with Pons and Fleischmann Type cells, in: F. Jaeger (Ed) The Seventh International Conference on Cold Fusion, ENECO, Inc., Salt Lake City, UT, Vancouver, Canada, 1998, pp. 202.

[43] G. Lonchampt, L. Bonnetain, P. Hieter, Reproduction of Fleischmann and Pons experiments, in: M. Okamoto (Ed) Sixth International Conference on Cold Fusion, Progress in New Hydrogen Energy, Published by: New Energy and Industrial Technology Development Organization, Tokyo Institute of Technology, Tokyo, Japan, Held at: Lake Toya, Hokkaido, Japan, 1996, pp. 113–20.

[44] G. Mengoli, M. Bernardini, C. Manduchi, G. Zannoni, Calorimetry close to the boiling temperature of the D_2O/Pd electrolytic system, J. Electroanal. Chem. 444 (1998) 155.

[45] E.K. Storms, The method and results using Seebeck calorimetry, in: D.L. Nagel, M.E. Melich (Eds), ICCF-14 International Conference on Condensed Matter Nuclear Science, www.lenr.org, Washington, DC, 2008, pp. 11–25.

[46] E. Storms, The Enthalpy of Formation of PdH as a Function of H/Pd Atom Ratio, J. Cond. Matter. Nucl. Sci. 29 (2019) 275–85.

[47] E. Storms, Anomalous Energy Produced by PdD, J. Cond. Matter. Nucl. Sci. 20 (2016) 81–99.

[48] E.K. Storms, The explanation of low energy nuclear reaction, Infinite Energy Press, Concord, NH, 2014.

[49] M.C.H. McKubre, F.L. Tanzella, Results of initial experiment conducted with Pd on C hydrogenation catalyst materials, 1999.

[50] E.K. Storms, The status of cold fusion (2010), Naturwissenschaften 97 (2010) 861.

[51] P. Hagelstein, Relativistic Phonon-Nuclear Coupling Matrix Element for the D2/4He Transition, JCMNS 39 (2025) 140–64.

[52] F.E. Gordon, H.J. Whitehouse, Progress in Understanding and Scaling Up the Lattice Energy Converter (LEC), JCMNS 39 (2025) 14–35.

[53] F.E. Gordon, H.J. Whitehouse, Lattice Energy Converter, JCMNS 35 (2022) 30–48.

[54] S.C. Hang Zhang, Experimental Results of Lattice Energy Converter LEC, JCMNS 39 (2025) 241–8.

[55] A.B. Karabut, Y.R. Kucherov, I.B. Savvatimova, Nuclear product ratio for glow discharge in deuterium, Phys. Lett. A 170 (1992) 265–72.

[56] E.K. Storms, B. Scanlan, Detection of radiation from LENR, in: D.L. Nagel, M.E. Melich (Eds), 14th International Conference on Condensed Matter Nuclear Science, www.LENR.org, Washington, DC, 2008, pp. 263–87.

[57] E. Storms, Cold Fusion Explained, JCMNS 39 (2025) 249–85.

J. Condensed Matter Nucl. Sci. 41 (2026) 19–24

Research Article

High Temperature LEC Experiments

Jean-Paul Biberian*
Aix-Marseille University, France

Robert Michel
VEGATEC, France

Christophe Le Roux
CNRS, France

Abstract

The Lattice Energy Converter (LEC), discovered by Gordon and Whitehouse, has opened the way to a new form of energy production with the important characteristic of directly generating electricity. Experiments conducted so far, performed near room temperature, have shown that a voltage is generated between an activated electrode—obtained by palladium deposition—and a reference electrode in hydrogen or deuterium atmospheres. These studies have also demonstrated that the generated voltage varies with temperature. Since both palladium and hydrogen are used in Cold Fusion as well as in LEC experiments, this similarity suggests that the two effects may share a common origin.

The authors of the present paper have previously reported excess heat production using nickel alloy nano powders (Ni/Cu) embedded in an amorphous alumina matrix after activation and reduction of a hydrotalcite precursor. However, the excess heat was observed only above approximately 700 °C.

To investigate whether excess heat and the LEC effect arise from the same underlying mechanism, we designed a device capable of performing LEC experiments with powders at temperatures up to 950 °C. The results show that the LEC effect occurs within the same temperature range as the observed excess heat. These findings support the hypothesis that the LEC effect and Cold Fusion phenomena may originate from a common mechanism.

Keywords: LEC; Cold Fusion; Mechanism; Hydrogen

---

1. Introduction

The Lattice Energy Converter (LEC) was discovered by Gordon and Whitehouse [1], who demonstrated that a voltage is generated between an activated electrode—typically palladium—and a reference electrode made of various materials

---

[*] Corresponding author: jpbiberian@yahoo.fr

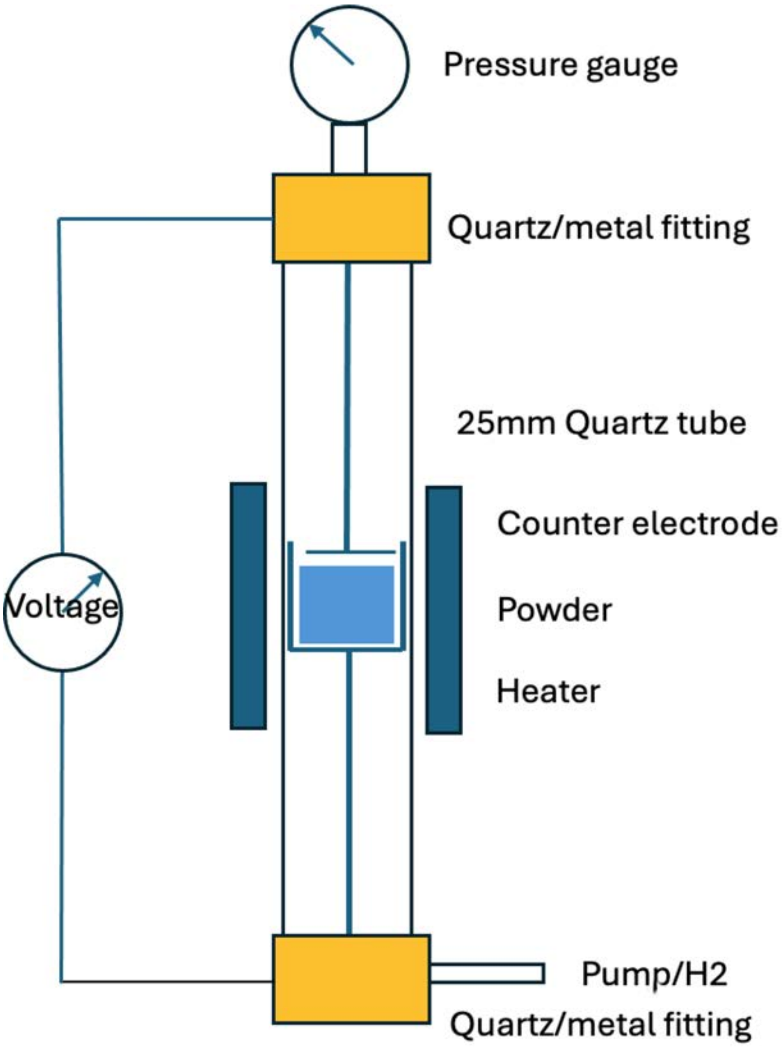

Figure 1. Sketch of the design of the high temperature LEC device.

in a hydrogen or deuterium atmosphere. They also reported that the generated voltage varies with temperature, up to approximately 200 °C [2].

In LENR-type experiments, we have previously shown [3] that excess heat can be observed using nickel alloy nano powders (Ni/Cu) embedded in an amorphous alumina matrix, obtained after activation and reduction of a hydrotalcite precursor. However, this excess heat appears only above about 700 °C.

Since LEC effects have primarily been reported using palladium—the first material employed in Cold Fusion studies—it is of interest to investigate whether similar materials and conditions could produce both excess heat and an LEC effect. To explore this possibility, we designed an experimental setup capable of performing LEC measurements at temperatures up to 900 °C.

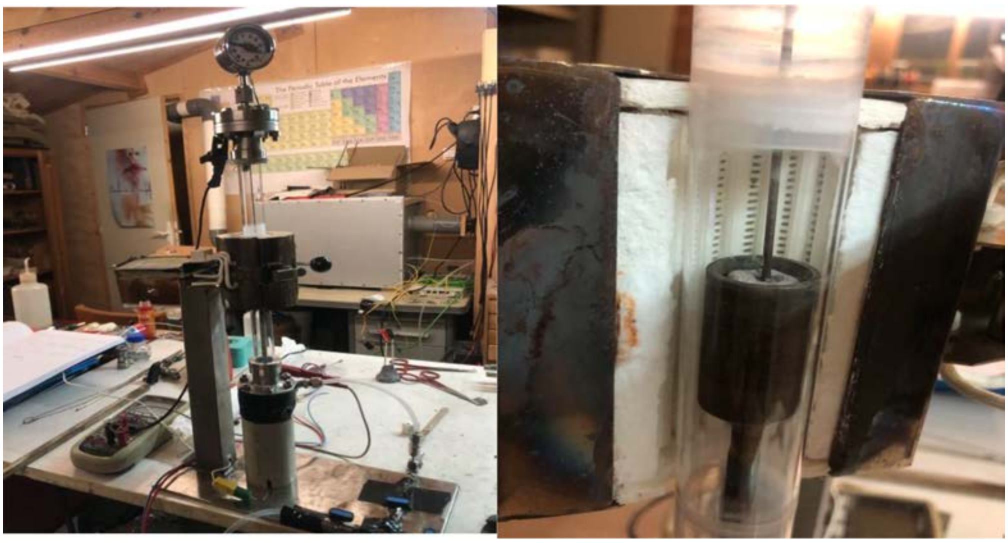

Figure 2. Two pictures of the experimental set-up.

2. Experimental Set-up

The setup is composed of a quartz tube 33 cm long and 25 mm in diameter, with a crucible inside. The powder to be analyzed is placed in the crucible. A small heater is placed outside the tube to heat the crucible. (See Fig. 1) The bottom of the quartz tube is equipped with a quartz/metal fitting, through which passes a 6 mm stainless steel tube for pumping out gas, and for the introduction of hydrogen. The lead wire for a K-type thermocouple also passes through this fitting. The thermocouple is positioned near the crucible. The top of the quartz tube is equipped with another quartz/metal fitting containing a pressure gauge and a metal rod with a stainless-steel counter electrode positioned one or two millimeters above the crucible. The voltage is measured between the two fittings.

3. Experimental Results

3.1. Excess Heat

Experiments with nanoparticles of nickel–bismuth alloys embedded in an amorphous alumina matrix have shown the production of excess heat [3]. Figure 3 shows a curve of excess heat vs. temperature. There is no excess heat below 700 °C; above this temperature excess heat begins, and then increases exponentially with temperature.

3.2. LEC voltage

The same material used to produce excess heat (described in section 3.1) has been employed in the high temperature LEC. The solid blue line in Fig. 4 shows the voltage as a function of temperature, obtained after several cycles of heating in hydrogen and cooling in a vacuum using the same method described previously by Biberian et al. [3].

We have also analyzed the voltage with an oscilloscope. Figure 5 shows that the voltage is composed of a constant voltage superimposed with short pulses. The frequency of the pulses is not constant and varies between 2 and 4 kHz.

Figure 6 is a zoom of the voltage showing the shape of the voltage pulses composed of a negative pulse of about 30 mV followed by a positive peak of 80 mV.

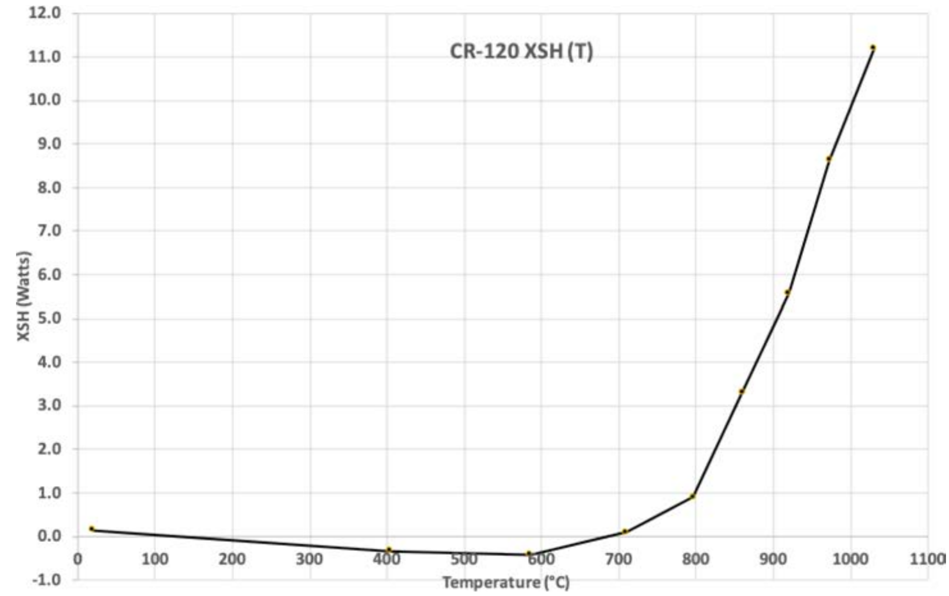

Figure 3. Excess heat vs. temperature, showing an exponential increase with temperature above about 700 °C.

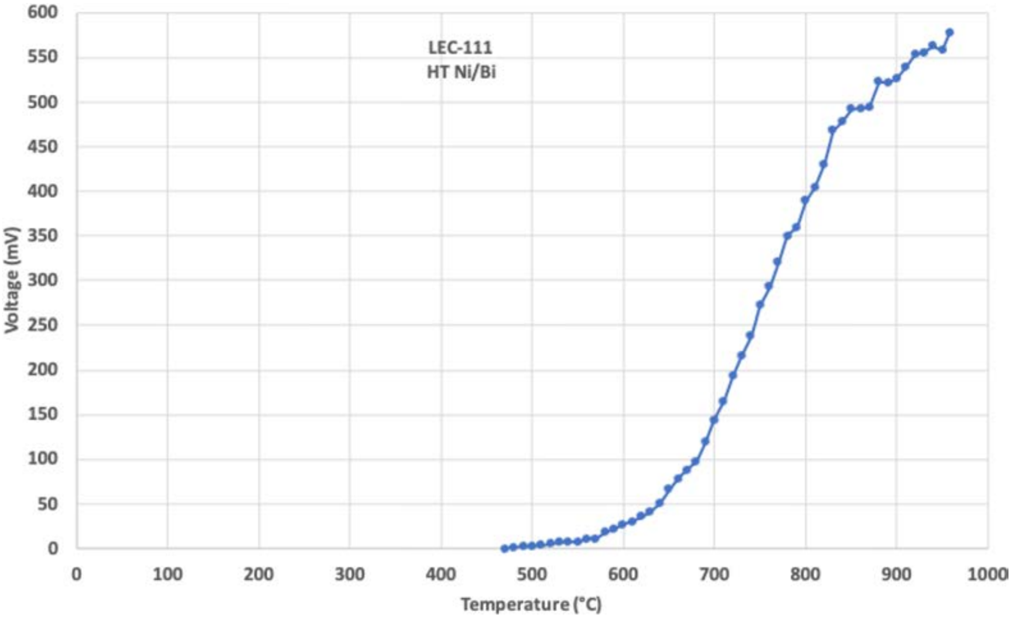

Figure 4. LEC experiment showing the voltage between a Ni/Bi nano powder vs. temperature.

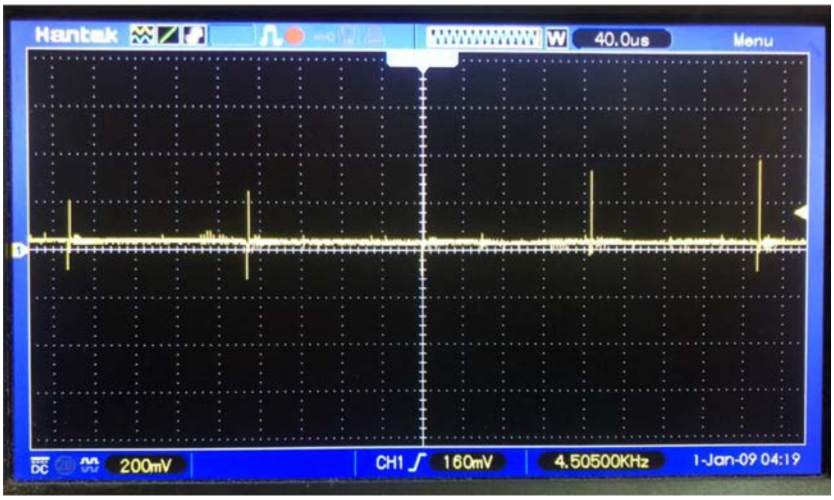

Figure 5. Screenshot of the voltage showing both a DC component and short pulses.

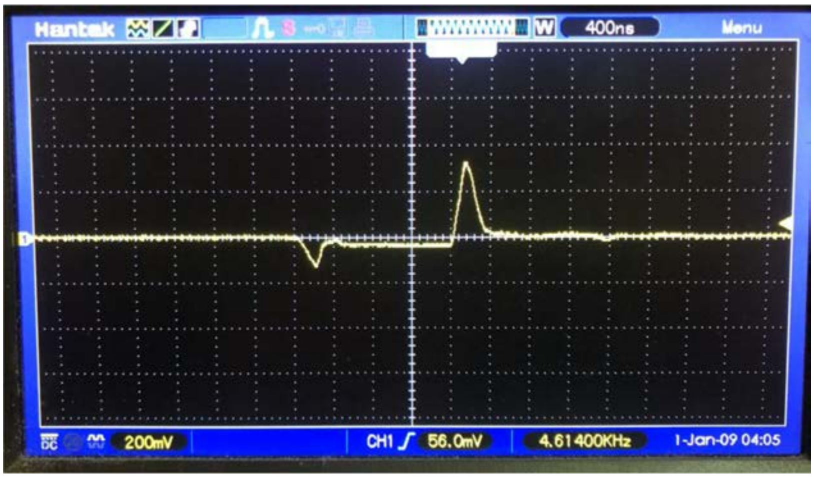

Figure 6. Details of the voltage pulses.

4. Conclusion

The voltage obtained at high temperature cannot be coming from thermionic emission, because it only occurs under a hydrogen atmosphere, and there is no emission in a vacuum. We have shown that the same powder used for heat production was also capable of producing a LEC voltage at high temperatures. The variation of excess heat vs. temperature is very similar to the increase in voltage produced by the LEC. This strongly suggests that the same mechanism is at work in both experiments. This conclusion is in agreement with the one obtained by Storms [4] showing that the LEC effect is of the same origin as Cold Fusion.

References

[1] Gordon F. E., Whitehouse H. J., *“Lattice Energy Converter”,* J. Condensed Matter Nucl. Sci. 35 (2022) 30–48.

[2] Gordon F. E., Whitehouse H. J., *“Lattice Energy Converter II: Iron Hydrogen Host Metal”,* J. Condensed Matter Nucl. Sci. 36 (2022) 1–24.

[3] Biberian J.-P., Michel R., Le Roux C., Valat M., Bucher S., Kodeck A., Sjöberg P.J.R., Ruer J., Chaudanson D., “*Excess Heat in Nanoparticles of Nickel Alloys in Hydrogen*”, J. Condensed Matter Nucl. Sci. 38 (2024) 186–195.

[4] Storms E. “*A New and Improved Understanding of Cold Fusion Based on the Observed Behavior*”, J. Condensed Matter Nucl. Sci. 41 (2026) 1–18.

J. Condensed Matter Nucl. Sci. 41 (2026) 25–37

Research Article

Anomalous Heat Effects via Longitudinal and Transversal Excitations in Constantan Wires: Advances in Electromigration and Plasma Generation

F. Celani, C. Lorenzetti, E. Purchi, S. Cupellini, M. Nakamura, and P. Cerreoni
ISCMNS_L1

G. Vassallo
DIDI, Univ. Palermo

Abstract

We present an integrated set of experiments that advance the long-standing search for Anomalous Heat Effects (AHE) in metal–hydrogen systems, with a decisive shift toward inexpensive materials and dynamic drive conditions. Our working medium is commercial Constantan wire ($Cu_{55}Ni_{44}Mn_1$), selected in 2011 to replace palladium due to its lower cost and higher defect density. The wire is operated in a compact INFN-LNF reactor that reaches internal temperatures of 900 °C, while the external jacket remains below 350 °C. The wire is simultaneously excited in two orthogonal modes: (i) high-density axial current pulses that drive thermionic emission, electromigration, and the characteristic "wire-breathing" pressure wave; and (ii) a transverse plasma, generated either as a Paschen spark or, more desirably, as a self-quenching dielectric-barrier discharge (DBD) stabilized by a Ca/Sr/Ba low-work-function coating, analogous to those employed in thermionic valve cathodes. Custom dimmer-based power electronics (50 Hz mains frequency, 90–95% efficiency) allow real-time adjustment of fall time (with rise time <1 μs), duty cycle, and polarity. Embedded K-type thermocouples provide in-situ calorimetry accurate to ± 1 W. In a 50% H_2–50% Ar atmosphere at 200 mbar, direct-current operation serves as the "null" line. Pulsed driving lifts the thermal baseline, and adding a pulsed counter-electrode (CE) increases net excess heat to 20–21 W for an 80 W input (peak COP ≈ 1.27 at 60 W). Reducing the pressure to 140 mbar and enlarging the CE coupling capacitor maintains Paschen/DBD activity and yields comparable—or slightly enhanced—AHE, despite incurring an additional 4–5 W of circuit losses. After two weeks of dormancy, the effect diminishes but can be partially recovered through in-situ redox cycling and extended pulsing, consistent with the involvement of metastable vacancy clusters anticipated by the Fukai–Staker super-loading model. Thermionic emission and electromigration show a strong correlation with excess heat generation, in agreement with Preparata's coherence framework. Future work will investigate tungsten–NiCu multilayer electrodes driven by SiC pulse electronics, complemented by fast optical and X-ray diagnostics to resolve sub-millisecond dynamics. The reproducibility achieved here—using only commodity components—underscores the potential of Constantan-based AHE modules for high-temperature process heat, lightweight aerospace power systems, and distributed micro-grid applications.

© 2026 ICCF. All rights reserved. ISSN 2227-3123

Keywords: Dielectric Barrier Discharge (DBD), Paschen Breakdown, Solid-State Fusion, Lattice-Enhanced Nuclear Fusion (LENF), Pulsed Electric Excitation

---

1. Experimental Motivation and Rationale

Our research programme was initiated in the wake of the 1989 announcements by Fleischmann and Pons, as well as Jones, which sparked renewed interest in the possibility of anomalous heat effects (AHE) in metal–hydrogen systems. Early experimental results from our group and others clearly indicated that AHE manifest only under far-from-equilibrium conditions. This insight steered our focus toward the use of high-frequency electromagnetic stimulation as a means to sustain non-equilibrium states in the system. Advances in pulse electronics have since enabled the generation of controlled, microsecond-scale excitations with high precision, which form the backbone of our current experimental approach. Over time, we identified a key principle: AHE is highly sensitive to the material's defect structure. Ultra-pure palladium showed little to no effect, while defect-rich alloys—such as Constantan—proved far more responsive. Imperfections such as vacancies, grain boundaries, and impurities appear essential to enabling excess heat generation. We also found that dynamic hydrogen movement through the lattice—not just static loading—plays a critical role. By managing the pressure–temperature–composition (P–T–C) matrix, we can achieve transient H/M ratios necessary for triggering AHE. Supporting evidence dates back to Gustav Fralick's 1989 NASA experiment [1], which showed reproducible excess heat from deuterium flowing through heated porous palladium. This benchmark continues to shape the field. In 2011 [2], we adopted Constantan ($Cu_{55}Ni_{44}Mn_1$) as our main material. Its robustness, defect-rich structure, and compatibility with ordinary hydrogen—not just deuterium—offered practical and strategic advantages. This lowered barriers to experimentation and enabled broader parameter testing. Similar approaches have emerged globally. Takahashi's group in Japan studied Ni–Cu powders [3]; Iwamura and Mitsubishi developed nanostructured multilayers [4]; and Alexandrov's team in Canada demonstrated near-instant AHE onset at $960\,^\circ C$ in vacuum-based setups shortly after deuterium immission at 100 mbar [5], [6]. These developments point toward high-power-density applications, including aerospace propulsion. The idea of Cu–Ni alloys for AHE was first proposed by Brian Ahern in 1994 [7], [8], though largely overlooked at the time. Our strategic pivot came in 2020, upon joining the EU-funded CleanHME Project (H2020, Grant No. 951974). Our mission: to develop simple, scalable methods for loading Constantan with H/D and to replace bulky lab equipment with compact, low-cost pulse systems. Dimmer-based electronics emerged as a cost-effective yet powerful tool, achieving high P_out/P_in ratios under stable conditions. These principles—defect-driven reactivity, dynamic hydrogen handling, and efficient pulse control—remain central to our approach. As the demand for clean, decentralised energy grows, these methods offer a promising foundation for turning AHE into practical energy technology.

2. Key Experimental Findings and Future Directions

Our Constantan reactor operates in two orthogonal excitation modes, each compensating for the limitations of the other. Longitudinal stimulation applies high-density current pulses ($100–500\ A\ mm^{-2}$) along the wire, transiently elevating the surface temperature by several tens of degrees above the core. The resulting thermal gradient, coupled with Lorentz pinch forces, compresses the lattice while the accompanying electric field drives hydrogen atoms toward vacancies. As the surface cools a few milliseconds later, it effectively "re-inhales" gas from the surrounding chamber. Repeating this cycle at 50 Hz sustains the supersaturated defect clusters envisioned by the Fukai–Staker model [9], [10] and, at temperatures above $\sim 700\,^\circ C$, may even enable the emergence of coherent charge domains, as proposed by Preparata [11]. In practice, pre-loading the wire with hydrogen followed by the application of sharp pulses consistently yields the strongest and most reproducible AHE signatures.

Transversal stimulation provides a complementary layer of control. A wire counter-electrode (CE), positioned 2–3 mm from the Constantan filament, is driven either into Paschen breakdown or into a gentler dielectric-barrier discharge (DBD) regime. Classical Paschen theory predicts a breakdown voltage of 900–1000 V at 200 mbar for the gas used, yet ignition is routinely observed at $\sim$700 V when pulses with sub-microsecond rise times are applied—highlighting that waveform dynamics can be as critical as the textbook $p{\cdot}d$ product. The reduced breakdown threshold may also reflect the strong local electric field around the small-diameter wire. When the wire is coated with a porous Ca–Sr–Ba oxide (with minor additions of K, Mn, and Fe), the discharge frequently self-organizes into a stable filamentary DBD. In this regime, the current becomes intrinsically self-limiting—not because of the ohmic resistance of the coating, but due to the alternating buildup and collapse of surface charge across the dielectric layer, which quenches the discharge each half-cycle. As a result, electrode erosion is effectively suppressed. The bombarding electrons typically carry energies in the 5–30 eV range, as estimated from the applied voltage, sheath thickness, and characteristic micro-discharge dynamics reported for low-pressure DBD systems. These moderately energetic electrons strike the already-hot surface, promoting secondary emission and enhanced surface reactions. This energy range is particularly well suited for splitting molecular hydrogen (H_2), while remaining low enough to prevent sputtering or damage to the active surface. Under these combined conditions—longitudinal current flow and transversal discharge—the system is capable of delivering up to 20 W of net excess heat with an input of 80 W. Maintaining surface reactivity while avoiding hot-spot failure remains a central engineering challenge. Figure 2 illustrates the simplified behaviour of electrons under negative unipolar pulses applied to Constantan wires operating in the DBD regime. The combination of low-conductivity mixed-oxide coatings and porous dielectric sheaths sustains stable filamentary discharges while suppressing destructive sparking. By precisely managing voltage amplitude, pulse duration, and duty cycle, the system achieves stable electron flow and enhances Anomalous Heat Effects (AHE), all while avoiding arcing and local overheating. This mild filamentary discharge regime—intentionally maintained below the Paschen breakdown threshold—creates a non-equilibrium state that strongly favours both electron emission and AHE generation. Although such regimes often require complex and costly electronics, we have implemented more economical alternatives. The key parameters currently under active control include: (a) the maximum applied voltage, and (b) the maximum and variable current, with ultra-fast response ($\approx$50 ns) and rise times in the 500–800 ns range. Very recently, we began fabricating a hybrid main electrode whose tungsten core ($T_m > 3400\,^\circ$C) carries a Cu–Ni shell laced with low-work-function (LWF) oxides. Preliminary tests show earlier discharge onset and no necking after 10 hours at 900 °C. Polarity studies reveal that a negative main electrode and a positive CE produce the most stable plasma—possibly by favouring transient H^- formation, as suggested by Piantelli [12]. Reversed and bipolar configurations will be explored next. Other near-term trials include H_2–He blends to sharpen the Paschen window, SiC-switch pulse packs for faster rise times, and in-situ optical spectroscopy to capture sub-millisecond events. The precise arrangement of the spectroscopy system is still under study, but the reactor will likely incorporate quartz optical fibers for light collection together with a high-voltage pulse generator based on SiC MOSFETs. **All of this fits within the compact coaxial reactor sketched in Fig. 1**, developed at INFN-LNF since 2019 [2], [13]. Its modular design allows rapid swapping of electrodes, pulse boards, and gas feeds—typically in under an hour—accelerating the iterate–test–refine cycle that drives the project toward a robust, scalable AHE module.

This platform supports systematic studies of AHE under finely controlled excitation and offers a scalable foundation for the development of decentralized, high-efficiency energy systems.

3. Core Physical–Chemical Mechanisms

Since the 1990s, our methodology has prioritized empirical observation over reliance on unverified theoretical models. In response to recent inquiries, we now present a provisional mechanistic framework—anchored in established physical and chemical principles, while deliberately avoiding speculative overreach. Anomalous heat generation in Constantan

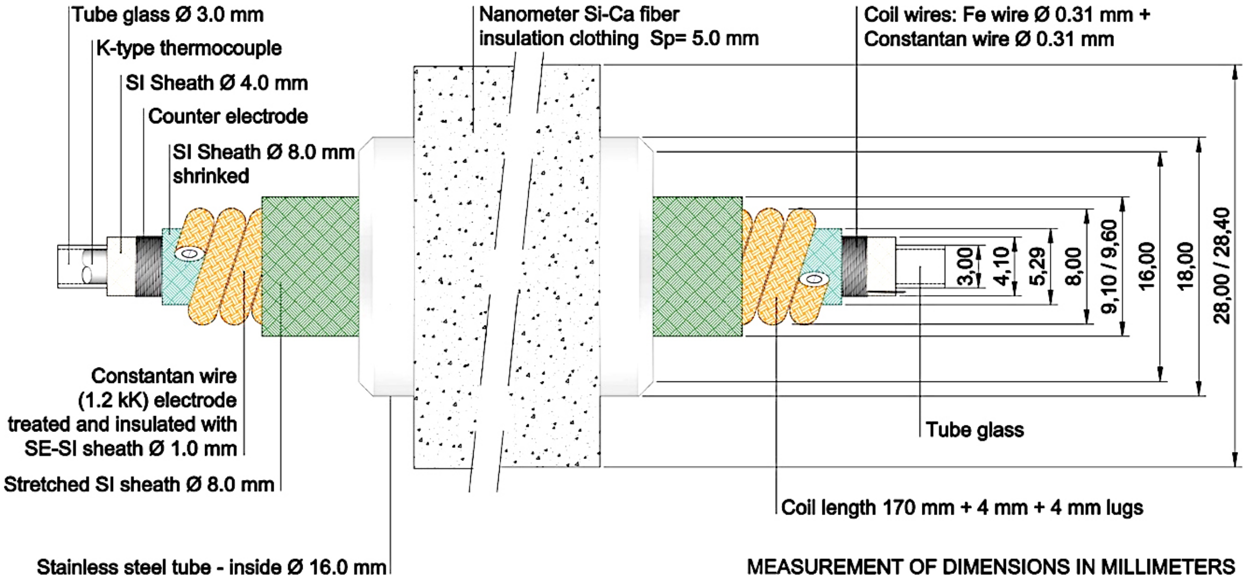

Figure 1. The updated coil-based CE design using Constantan and Fe wires.

appears to result from a tightly coupled sequence of plasma-driven processes. Once the wire exceeds approximately 700 °C, its porous Ca–Sr–Ba oxide coating—characterized by a low work function (< 2 eV)—dramatically increases the effective thermionic-emitting surface area by up to three orders of magnitude. This intense thermionic emission, described as an *"electron geyser,"* injects a dense current that conditions the interelectrode gap for Paschen breakdown. Experimentally, the breakdown voltage is consistently lower than predicted by the canonical Paschen curve. This deviation arises from the steep rise of the excitation pulses and the small diameter electrode geometry, both of which accelerate the avalanche process. Instead of triggering a destructive arc, the oxide coating acts as a dielectric barrier, steering the discharge into a filamentary dielectric-barrier discharge (DBD) glow. Each micro-plasma filament delivers electrons in the 5–30 eV range—sufficient to dissociate molecular hydrogen (H_2) without causing significant sputtering. Concurrently, the wire surface cycles rapidly through oxide → metal → hydride → oxide states, with transitions unfolding on millisecond timescales. We designate this rapid, self-sustaining renewal process as "catalytic breathing": a dynamic mechanism that perpetually regenerates reactive defect sites, maintains hydrogen supersaturation, and facilitates continuous heat release. All stages of this non-equilibrium process are maintained by a simple, dimmer-based pulser, modestly upgraded with commercial high-current silicon-controlled rectifiers (SCRs) and ultrafast high-voltage diodes. This setup demonstrates that low-cost, off-the-shelf electronics are fully capable of sustaining the plasma sheath conditions necessary for the observed anomalous heat effects.

4. Contemporary Models and Electrodynamic Phenomena

Explaining Anomalous Heat Effects (AHE) requires moving beyond classical thermodynamics into electrodynamic frameworks suited to non-equilibrium, high-current-density systems. Our thin Constantan wires, pulsed under controlled gas-phase conditions, offer an ideal platform to test such models. One central mechanism is electromigration—the movement of atoms driven by high current densities. While often associated with metal degradation, in our system it refers specifically to hydrogen or deuterium drift within the metal lattice. Pulsed electric fields exceed-

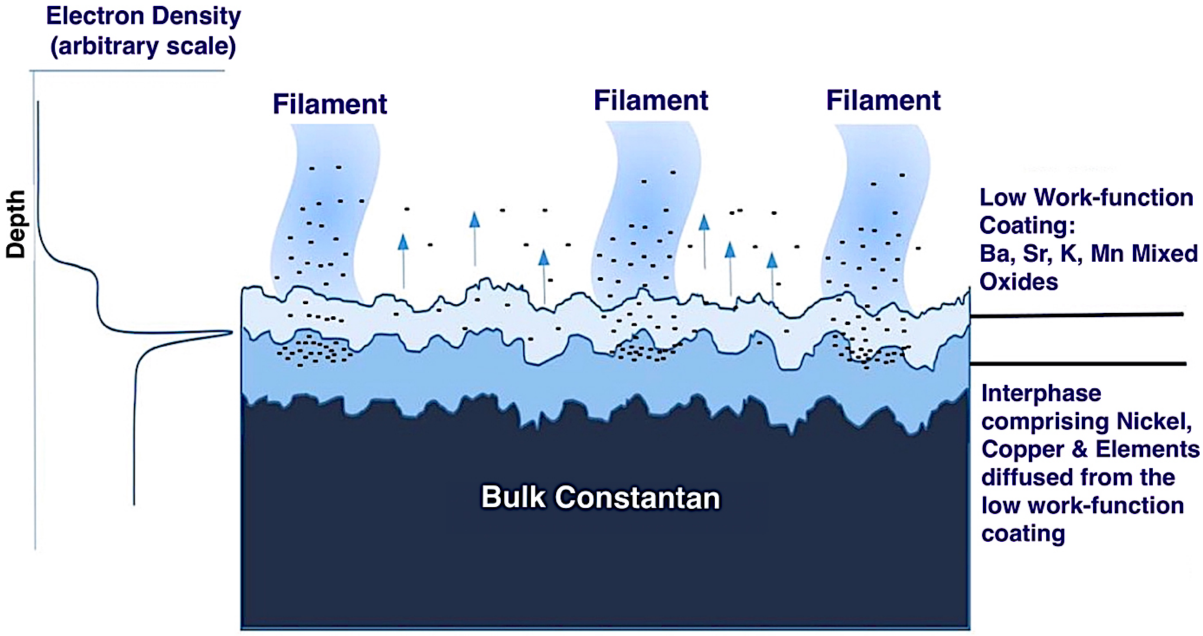

Figure 2. Electron Behaviour During Negative Unipolar Pulsing in Dielectric Barrier Discharge (DBD).

ing 0.5–1.2 V/cm can drive H/D atoms into defect-rich regions, promoting clustering, lattice rearrangement, and increased local reactivity [14], [15]. These effects are consistent with the Fukai–Staker super-loading model, which predicts metastable hydrogen-rich states forming under dynamic, non-equilibrium conditions [16], [9], [10]. A complementary perspective comes from Preparata's deuterium coherence theory [11], which suggests that under sufficient voltage and spatial confinement, deuterons may form coherent quantum domains. These domains could, in theory, release energy through collective, non-classical mechanisms. While direct experimental validation remains elusive, our sharp-pulse systems—with their steep thermal and electric gradients—may come close to enabling such conditions. Among these models, the super-loading framework remains the most experimentally grounded. It postulates that defects such as vacancies or grain boundaries can trap hydrogen at concentrations far exceeding equilibrium solubility. These supersaturated zones, being energetically unstable, may release energy when subjected to suitable pulse-driven perturbations. Our empirical observations—particularly the progressive buildup of AHE with repeated pulsing—align closely with this interpretation. Together, these models—electromigration, quantum coherence, and super-loading—describe a plausible path for how electrical excitation, lattice defects, and hydrogen mobility may converge to trigger AHE. Rather than being mutually exclusive, these mechanisms likely operate synergistically under real-world conditions. Ongoing experiments aim to clarify their respective domains and guide the optimization of reactor designs to exploit their combined effects.

5. AI-Aided Analysis of Current Density and Stress in Thin Wires

To better understand the stress conditions experienced by Constantan wires during operation, we used AI-assisted tools to model the relationship between current density, thermal load, and mechanical failure modes. These simulations allow for predictive insights into the thresholds beyond which structural degradation, runaway heating, or outright failure may occur. As a reference case, we considered a wire with a diameter of 200 μm, giving a cross-sectional area of approximately 0.0314 mm^2. Under pulsed excitation with peak currents reaching 10 A, the resulting current density approaches 318 A/mm^2. While such a value is tolerable for short-duration pulses, it becomes unsustainable under continuous DC operation. For example, even a 2-meter-long Constantan wire, with a typical resistivity yielding $\sim$16 Ω/m at 600 °C, will experience substantial Joule heating under much lower steady-state currents. At just 3 A, surface heat dissipation can exceed 23 W/cm^2, driving internal wire temperatures past 1100 °C—perilously close to the alloy's melting point of 1200 °C. Beyond thermal limits, prolonged operation introduces secondary degradation mechanisms. Evaporation of surface atoms, particularly copper, may thin the wire locally, altering its resistance and destabilising thermal balance. Mechanical deformation, often in the form of folding or buckling, further modifies the geometry and internal stress distribution. Oxidation or subtle compositional shifts from the original alloy can also lead to resistivity drift, creating feedback loops where local overheating becomes more likely. These combined phenomena point to the importance of precise duty cycling, fast-reacting circuit protections, and high-fidelity diagnostics to avoid catastrophic failure and maintain AHE-favourable conditions.

5.1. Electromagnetic and Electron Dynamics

High-current pulses in Constantan wires trigger a cascade of coupled electromagnetic and structural processes that help establish the conditions for Anomalous Heat Effects (AHE). Axial currents generate Lorentz forces that produce a radial magnetic pinch, transiently compressing the wire and potentially destabilizing pre-existing defect structures. At high frequencies, the skin effect confines current and heat to the outer surface. In nickel-containing alloys this effect is particularly relevant—not because of magnetostriction, which is negligible since Ni is paramagnetic at the operating temperatures—but because of their higher resistivity compared to copper and the strong chemical affinity of Ni sites for hydrogen and oxygen. Although simple estimates suggest only a modest skin effect at the nominal drive frequencies, the sharp rise times of the excitation pulses introduce high-frequency components that significantly enhance surface current crowding. These factors are hypothesized to intensify localized thermal gradients, mechanical stress, and chemical reactivity, thereby rendering the skin layer the dominant region for electromigration and surface reactions. The pulses also increase electron drift velocity, promoting enhanced scattering with phonons and defects. Sharp surface asperities, combined with low-work-function (LWF) oxide coatings, amplify field emission and can trigger micro-plasma events, adding further complexity to the near-surface electron dynamics critical for AHE.

Lattice Responses to Pulsing: Joule heating dominates the wire's energy budget. Constantan exhibits nearly linear ohmic behavior up to $\sim$700 °C in inert atmospheres, but beyond this point its resistivity increases non-linearly, necessitating active cooling. Each current pulse raises the surface temperature by several tens of degrees. With a linear expansion coefficient of $\alpha \approx 1.8 \times 10^{-5}\ \mathrm{K}^{-1}$, this thermal swing imposes a cyclic hoop stress of $\sim$85 MPa—remarkably close to the $\sim$90 MPa threshold at which the Fukai–Staker model predicts vacancy-loop punching. Thus, each burst may generate fresh dislocations that serve as hydrogen trapping sites. The high electron flux also drives electromigration, redistributing Cu and Ni atoms, reshaping defect networks, and alternately degrading the wire or generating new AHE-active pathways. The interplay of thermal expansion, magnetic compression, mechanical deformation, and electromigration creates a narrow yet reproducible window in which hydrogen supersaturation is renewed, coherent domains may nucleate, and excess heat becomes detectable.

5.2. Effects in Hydrogen/Deuterium-Loaded Constantan Wires

Hydrogen or deuterium absorption into Constantan wires initiates a cascade of transformations that fundamentally alter system behavior, fostering the non-equilibrium conditions associated with Anomalous Heat Effects (AHE). At the **electronic level**, interstitial H/D atoms perturb local charge density and electric field distributions, particularly

Table 1. Key effects activated in H/D-loaded Constantan wires as a function of current density. At ~318 A/mm^2, multiple AHE-relevant mechanisms are simultaneously active.

Rank	Effect	J (A/mm^2)	Status at 318 A/mm^2
1	Joule heating	10–100	Dominant
2	Thermal strain	50–200	Significant
3	Phonon–electron scattering	100–300	Strongly active
4	H/D electromigration	300–500	Likely active
5	Lorentz forces	300–500	Emerging
6	Field emission	500–1000	Possible onset
7	Magnetostriction	500–1000	Magnetostriction is only plausible in Ni domains below the Curie point.
8	Surface plasma	>1000	Unlikely without DBD
9	Field-assisted nuclear effects	>300 (spec.)	Under study

under pulsed excitation. These distortions may induce transient charge separation and the formation of polarized domains, especially under unipolar waveforms—an effect that could contribute to AHE. At the **lattice level**, H/D atoms enhance phonon activity and soften the lattice, thereby increasing hydrogen mobility and strengthening electron–phonon coupling. This dynamic may enable transient, high-reactivity states favorable for excess heat generation. Electromigration further drives H/D transport under applied fields, producing non-equilibrium concentration gradients. Such supersaturated regions may exceed thermodynamic solubility limits, potentially triggering AHE-relevant conditions. At the **magnetic level**, H/D loading modifies electronic states near the Fermi level, altering magnetic susceptibility and domain structures. These effects are most relevant within the nickel-rich matrix, though they become negligible above the Curie temperature. At the **frontier**, high current densities in deuterium-loaded wires may facilitate field-assisted nuclear-scale processes—still speculative, but actively investigated due to persistent anomalous experimental signatures. Table 1 summarizes how the various effects scale with current density. At our operational level (~318 A/mm^2), multiple mechanisms act in concert, placing the system in a highly reactive, non-equilibrium regime.

In summary, hydrogen-loaded Constantan under pulsed excitation enters a regime where multiple, intersecting processes—thermal, electronic, magnetic, and possibly nuclear—combine to create the right environment for AHE.

6. Circuit Architecture and Pulse Generation

A core innovation in our AHE research is the development of a low-cost, flexible pulsed power system centered around a modified commercial **TECNEL 8034 dimmer**. Unlike traditional lab-grade equipment, this setup enables precise control over pulse shape, voltage, and current, while maintaining **90–95% energy efficiency**—a critical feature for sustaining AHE under non-equilibrium conditions. The dimmer generates sharp, variable-amplitude pulses that significantly enhance electromigration quality, particularly in hydrogen-rich environments where the wire's resistance drops markedly ($R/R_o < 1$) [17], indicating active hydrogen–metal interactions. Figure 3 compares different excitation modes, highlighting the improved performance of the dimmer-based configuration.

Peak current monitoring is carried out with precision 1 Ω, 25 W resistors, selected for their stability and accuracy across a broad frequency range (up to 20 MHz) while limiting power dissipation to ~2 W. For transversal discharges—Paschen and Dielectric Barrier Discharges (DBD)—a custom high-voltage transformer with an integrated protection network drives the counter-electrode (CE). This configuration supports safe operation up to +1000 V and 200 mA, with adjustable current limits in 50 mA increments and a 50 ns delay line for fine pulse-timing control. The positive high voltage required for Paschen/DBD excitation is derived from the main negative pulse applied in parallel to the Constantan wire input. The negative pulse passes through a fast, high-voltage ceramic capacitor (100–400 nF) into an inverting toroidal transformer (1:4 ratio, 10 kHz–2 MHz bandwidth). The capacitor value represents a trade-off: larger

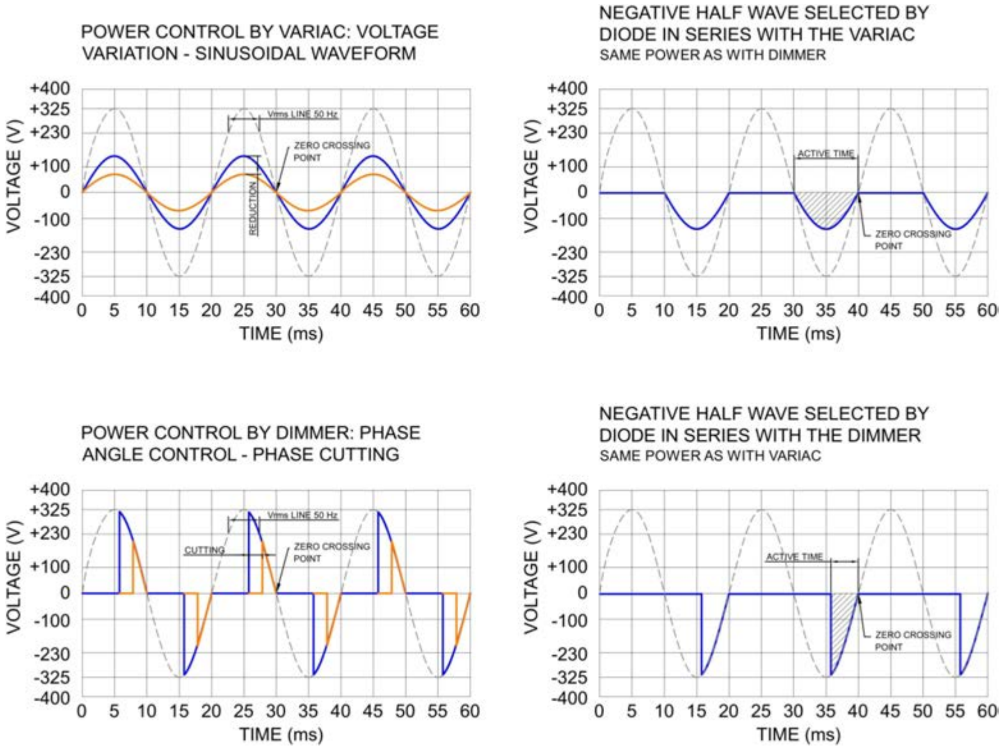

Figure 3. Peak voltage profiles for different excitation waveforms. Dimmer-based pulses provide fine control over AHE stimulation. A reduction in normalized resistance (R/R_o) under hydrogen indicates absorption. Overall system efficiency is approximately 95%.

capacitance improves energy transfer from the main pulse but increases low-frequency losses in the transformer. A 400 nF capacitor was ultimately chosen, as it enhances plasma ignition stability, although it introduces ∼4–5 W of additional dissipation within the transformer and limiting circuitry. Waveform measurements highlight the dynamics: under standard conditions, a full-power pulse delivers 69 W to the reactor, with the voltage pulse driving longitudinal current through the Constantan wire (see Fig. 4). Importantly, the input briefly peaks above 1150 W (green trace, value divided by four), illustrating the sharp, non-equilibrium excitations required to trigger Anomalous Heat Effects (AHE).

Figure 5 documents a successful Paschen-like breakdown at 1150 V peak-to-peak, accompanied by a –150 V main electrode (ME) response—clear evidence of full gap ionisation and plasma formation. This compact yet robust platform enables flexible exploration of both longitudinal and transversal excitation modes without requiring bulky infrastructure. Its combination of geometric simplicity, waveform adaptability, and controlled discharge behavior makes it well suited for scalable AHE experimentation across varying operating conditions and reactor geometries. At the lower end of the stimulation frequency range investigated (50 Hz), the nominal DBD regime frequently collapses into a pulsed, **low-pressure spark or arc across the 1 mm hydrogen gap.** While generally undesirable—due to electrode erosion and unstable discharge localization—this transient arc paradoxically produces the strongest AHE enhancements. The effect may stem from the arc's pinpoint current channel, which generates exceptionally high current densities and introduces arc-specific phenomena such as bursts of highly ionized hydrogen, impulsive UV/soft X-ray emissions, and electromagnetic shock fronts. This behavior is reminiscent of Mills-style spark experiments [18], though the current lack of spatial control limits the ability to draw firm conclusions.

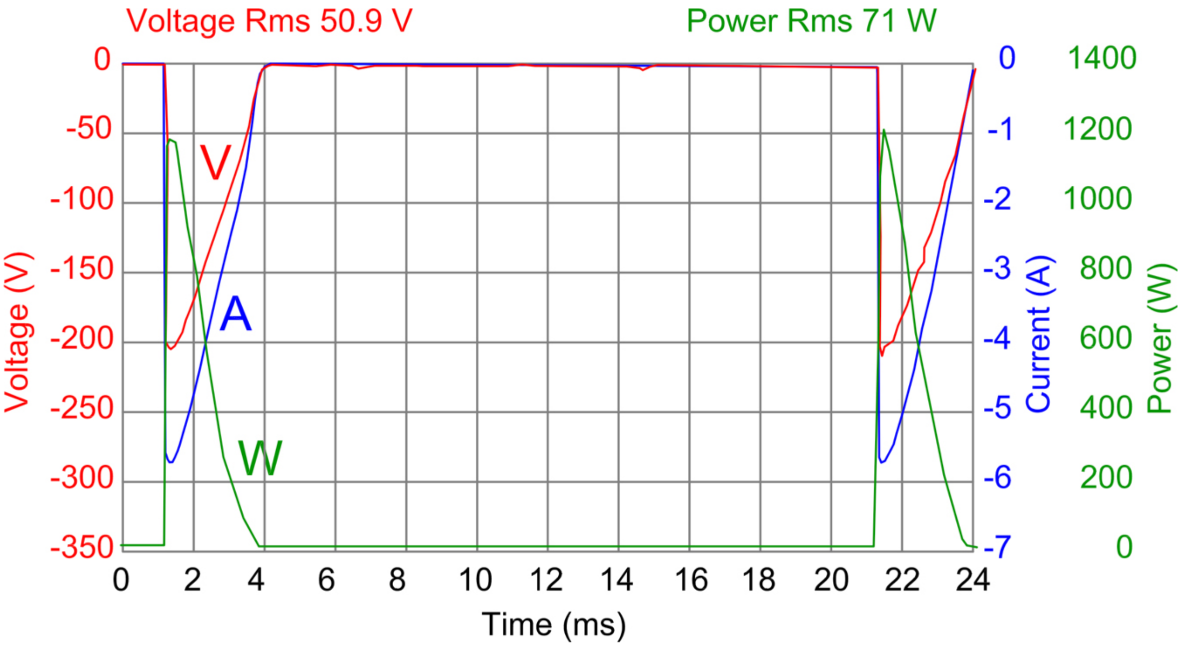

Figure 4. Pre-discharge waveform at 69 W RMS. With no plasma yet ignited, the voltage–current trace is smooth and free of spikes. Net electrical input is 69 W; 2 W of that is lost in the 1 Ω sensing resistor. Momentary peaks reach ≈ 1150 W—about 16 × the RMS level—providing the sharp, high-power bursts needed to trigger also Paschen or DBD breakdown once the threshold conditions are met.

7. Some Results

A series of side-by-side runs compared two 50 mol % gas mixtures at 200 mbar: inert He/Ar (control) and reactive H_2/Ar. Under direct current (DC) operation, the control showed no excess heat, while the H_2/Ar trace defined the zero reference line. Pulsed operation increased the H_2/Ar signal, with a further rise observed when the counter-electrode (CE) was also pulsed. After subtracting the 2–3 W consumed by the pulser, the net power output rose to approximately 20 W for an 80 W input, yielding a coefficient of performance (COP) of about 1.27 at only 60 W input—double the best result from earlier 170 W trials (Fig. 6). The reactor core exceeded 900 °C, while the jacket remained at approximately 280 °C. Excess power was determined from the slope of the ΔT curve, where $\Delta T = Tc - Ta$, with Tc representing the reactor wall temperature and Ta the ambient temperature. This slope was referenced against a calibration curve obtained under inert-gas conditions. Full experimental details are provided in earlier publications [19]. Subsequently, the pressure was reduced to 140 mbar while maintaining the same H_2/Ar blend. To restore Paschen/DBD activity, the CE coupling capacitor was increased from 100 nF to 400 nF, adding an estimated 4–5 W of power loss but sustaining a stable plasma. Despite this added dissipation, the excess heat matched—or slightly exceeded—the 200 mbar result (Fig. 6 and 7), indicating that careful discharge tuning can offset lower gas density and may even enhance performance.

8. Speculative Model, Ongoing Adjustments, and Outlook

Our current working hypothesis—better described as a structured thought experiment than established physics—is that a “breathing” Constantan filament, pulsed in sync with a surface DBD micro-plasma, functions as a persistent hydrogen pump. Each microsecond current burst heats the outer tens of microns, compresses the skin layer via Lorentz forces,

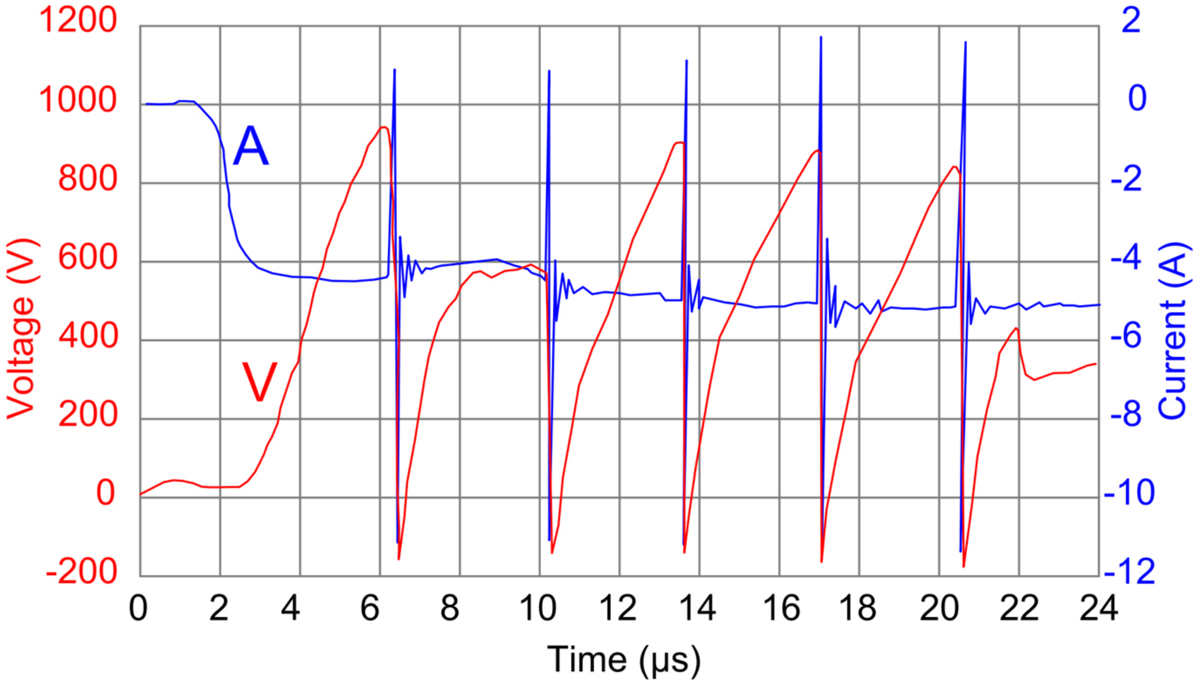

Figure 5. Counter-electrode (CE) voltage under positive-bias operation. The red trace, representing the voltage between the Constantan wire and the counter-electrode (CE), demonstrates a stable cyclic Paschen-type discharge (low-pressure spark). The clean, quasi-sawtooth waveform exhibits a consistent peak-to-peak amplitude of approximately 1150 V, confirming that the reactor pressure and electrode gap are well within the breakdown window and thus support sustained discharge.

and then releases it. This cyclic action may cause the filament to inhale hydrogen into vacancies during compression and exhale it as the lattice rebounds. The sequence unfolds as follows: Joule heating initiates the thermal pulse; magnetic and structural forces drive hydrogen inward; thermal expansion cracks surface oxides; and slower electromigration redistributes hydrogen longitudinally. Together, these effects generate defect clusters faster than they anneal, maintaining the supersaturated, vacancy-rich state highlighted in the Fukai–Staker model as conducive to anomalous heat effects (AHE). The oxide layer plays a dual role: enabling thermionic emission while also serving, together with the quartz glass fiber sheath, as the dielectric for localized filamentary DBDs. When the hot skin expands, both the local temperature and electric field increase, igniting a plasma filament. As cooling sets in, charge accumulation in the oxide quenches the discharge before it evolves into an arc. Each “breath” therefore resets the surface charge, while the transient filament bombards the wire with electrons in the **5–30 eV range**—energies inferred from typical DBD electron energy distributions under similar conditions [20]. These are sufficient for H_2 dissociation but generally too low to cause significant sputtering. This pulse–plasma feedback loop keeps the wire chemically reactive and structurally dynamic. We view it as a centimeter-scale *pulse–plasma engine*: compact, cyclic, and currently the most consistent source of excess heat in our work. Its fragility, however, is evident. After a two-week interruption during relocation from INFN-LNF to Frosinone, the excess power output dropped from 15–20 W to just 2–6 W, despite identical gas composition and pulsing parameters. This suggests that once the lattice cools and vacancy clusters relax, the feedback

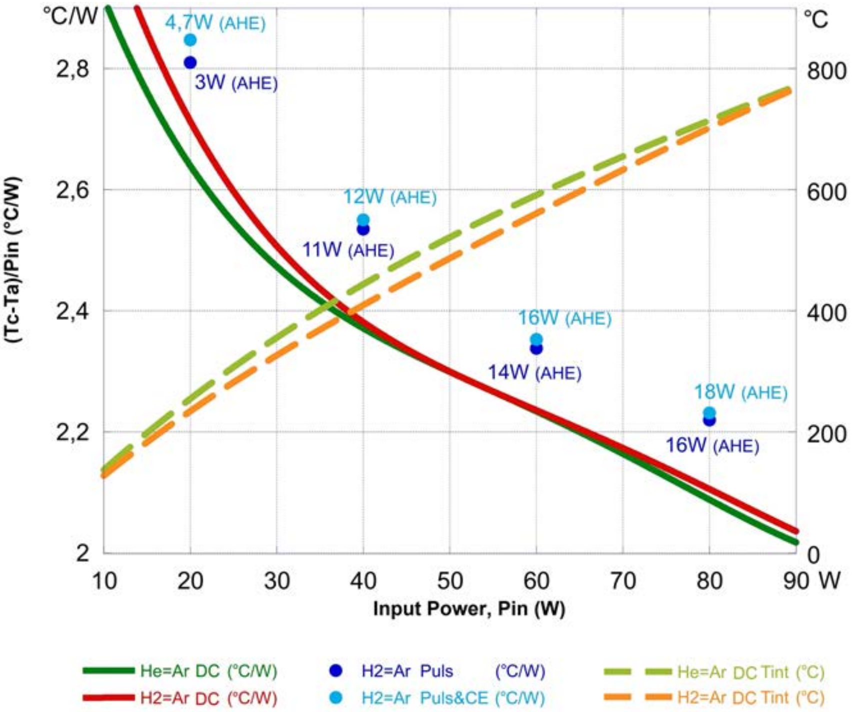

Figure 6. **AHE at 200 mbar.** Net excess heat vs. input power for DC, pulsed, and pulsed + CE modes in 50 % H_2/Ar (control He/Ar shown for reference).

loop stalls. Recovery is being pursued through oxidation–reduction cycling and extended pulse sequences, particularly with the counter-electrode (CE) energized.

Temperature remains a decisive gatekeeper. Paschen-type discharges rarely ignite below ∼650 °C unless local hotspots facilitate field breakdown. In one unusual case, a discharge initiated at only 250 °C, hinting that surface geometry or field-enhanced emission can bypass the conventional Paschen $p{\cdot}d$ rule. Mild gamma irradiation from thorium-doped TIG rods (enclosed in stainless steel tubing) also appears beneficial above 650 °C—possibly by liberating electrons from low-work-function oxides or directly ionizing the gas. Although CE pulsing can enhance AHE, it incurs a 2–5 W power penalty. To address this, we are developing hybrid main electrodes: tungsten cores clad with Ni–Cu–Fe alloys doped with Ca/Sr/Ba oxides. The goal is to suppress hotspots without suppressing surface reactivity, enabling stronger "breathing" at higher duty cycles and with larger wire diameters. Future comparisons will focus on DBD excitation versus spark discharges. While sparks applied via the CE may eventually exceed the filament's tolerance, a spark gap integrated along the main Constantan wire could combine strong longitudinal impulses with the mechanisms described above. Scaling remains the critical challenge. AHE appears to arise from a delicate interplay of nonlinear, temperature- and geometry-sensitive processes—where even slight variations in pulse rise time or oxide morphology can switch the system between dormant and active states. Yet the guiding principles first outlined in our 1990s framework remain valid. By tuning current density, waveform, gas pressure, and defect chemistry, we are narrowing in on a repeatable activation window. Should this window be broadened, Constantan-based modules may evolve into off-grid heaters, micro-generators, or—if the pulse–plasma engine proves scalable—even novel propulsion elements.

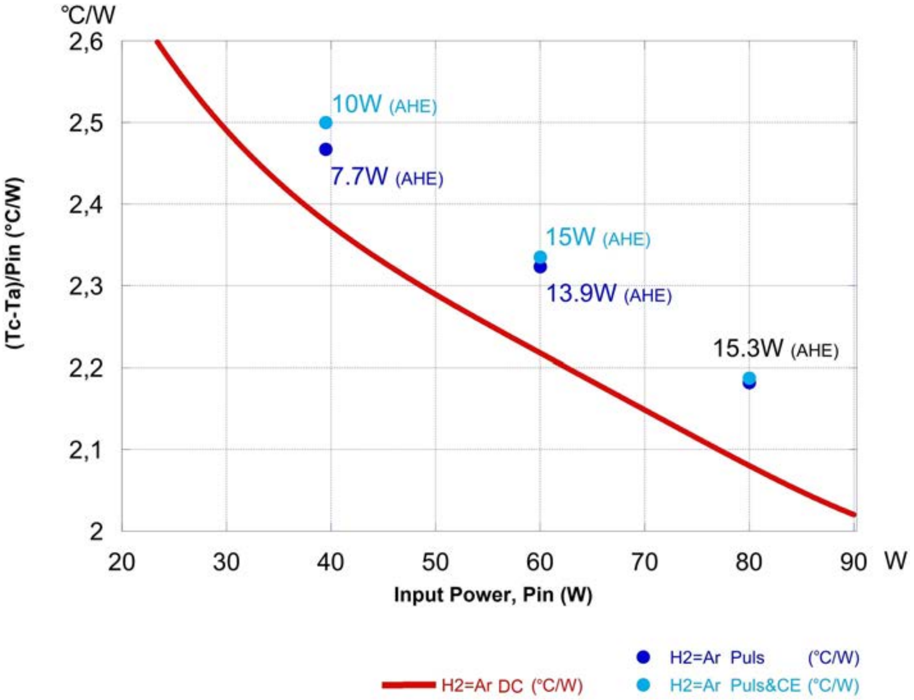

Figure 7. **AHE at 140 mbar.** Same H_2/Ar mix at reduced pressure; larger coupling capacitor restores strong discharge and sustains AHE with only minor efficiency loss.

Acknowledgments

This work was funded by the EU CleanHME project (Grant 951974, coordinator K. Czersky) and further supported by NEMC (Italy), the Anthropocene Institute (USA), and IFA (Italy). Their continuing help keeps our little engine breathing.

References

[1] G. C. Fralick, A. J. Decker and J. W. Blue, “Results of an attempt to measure increased rates of the reaction D-2 + D-2 yields He-3 + n in a nonelectrochemical cold fusion experiment,” NASA-TM-102430, E-5198, NAS 1.15:102430 , Cleveland, 1989.

[2] F. Celani, C. Lorenzetti, E. Purchi, S. Fiorilla, C. Stefano, M. Nakamura, P. Cerreoni, E. Marano and A. Spallone, “Electromagnetic Excitation of Coaxially-Coiled Constantan Wires by High-Power, High-Voltage, Microsecond Pulses,” *Journal of Condensed Matter Nuclear Science,* vol. 36, p. 408–435, 2022.

[3] A. Takahashi, “Anomalous Excess Heat by D2O/Pd Cell under L-H Mode Electrolysis,” in *Proceedings of the Third International Conference on Cold Fusion* , Nagoya, Japan, 1992.

[4] Y. Iwamura, T. Itoh, M. Sakano, S. Sakai and S. Kuribayashi, “Low Energy Nuclear Transmutation in Condensed Matter induced by D2 Gas Permeation through Pd Complexes: Correlation between Deuterium Flux and Nuclear Products,” in *Proc. of ICCF10, Condensed Matter Nuclear Science*, Cambridge, MA, 2006.

[5] D. Alexandrov, “Entering the Hot Case of Cold Nuclear Fusion,” Elsevier, 5 June 2023. [Online]. Available: Available at http://dx.doi.org/10.2139/ssrn.4469848. [Accessed 10 January 2024].

[6] D. Alexandrov, “Low-energy nuclear fusion reactions in solids: Experiments,” *International Journal of Energy Research,* vol. 45, no. Issue8 - Special Issue: Progress in Emerging Nuclear Energy Systems, pp. 12234-12246, 8 June 2021.

[7] B. S. Ahern, K. H. Johnson and H. R. Clark, “Method of maximizing anharmonic oscillations in deuterated alloys”. United States Patent US5674632A, 28 10 1994.

[8] B. S. Ahern, “Amplification of Energetic Reactions”. USA Patent US 2011/0233061, 29 9 2011.

[9] M. R. Staker, “Estimating volume fractions of superabundant vacancy phases and their potential roles in low energy nuclear reactions and high conductivity in the palladium – isotopic hydrogen system,” *Materials Science and Engineering: B,* vol. 259, 2020.

[10] M. R. Staker, “How to achieve the Fleischmann-Pons heat effect,” *International Journal of Hydrogen Energy,* vol. 48, no. 5, pp. 1988-2000, 2023.

[11] G. Preparata, “QED Coherence in Matter,” 1995.

[12] F. Piantelli, “Method for producing energy and apparatus therefor”. Europe Patent EP2368252B1, 24 11 2009.

[13] F. Celani and C. Lorenzetti, “Chapter 7 - Electrically induced anomalous thermal phenomena in nanostructured wires,” in *Cold Fusion*, Amsterdam, Elsevier, 2020, pp. 101-113.

[14] A. Remhof, J. L. M. van Mechelen, N. J. Koeman, J. H. Rector, R. J. Wijngaarden and R. P. Griessen, “Generation and detection of H electrodiffusion waves,” *Review of Scientific Instruments,* vol. 74, no. 1, pp. 445-447, 2003.

[15] J. Hou , X.-S. Kong , C. S. Liu and J. Song, “Hydrogen clustering in bcc metals: Atomic origin and strong stress anisotropy,” *Acta Materialia,* vol. 201, pp. 23-35, 2020.

[16] Y. Fukai and N. Ōkuma, “Formation of Superabundant Vacancies in Pd Hydride under High Hydrogen Pressures,” *Physical Review Letters,* vol. 73, no. 1640, 1994.

[17] W. Brückner, S. Baunack, G. Reiss, G. Leitner and T. Knuth, “Oxidation behavior of Cu-Ni(Mn) (constantan) films,” *Thin Solid Films,* vol. 258, no. 1-2, p. 252, 1995.

[18] R. L. Mills, “Power generation systems and methods regarding same”. United States of America Patent US10753275B2, 1 10 2014.

[19] F. Celani, C. Lorenzetti, G. Vassallo, E. Purchi, M. Nakamura, P. Cerreoni and U. Mastromatteo, “Effects of Electric Pulse Shape on AHE Generation in High-Temperature Surface-Modified Constantan under Hydrogen and Deuterium Gases,” *Journal of Condensed Matter Nuclear Science,* vol. 39, pp. 1-25, 2025.

[20] K. Tomita, Y. Inada and A. K. Xiang , “Measurement of electron velocity distribution function in a pulsed positive streamer discharge in atmospheric-pressure air,” *Journal of Physics D: Applied Physics,* vol. 53, no. 8, 2019.

J. Condensed Matter Nucl. Sci. 41 (2026) 38–43

Research Article

Introducing Hyper-Cold Fusion

Ryoji Furui

Nano Fusion Design, Hyogo, Japan

Abstract

Hyper-cold fusion is an innovative nuclear fusion approach that exploits the unique electronic properties of 2D materials. Unlike conventional cold fusion using hydrogen-occluded metals, our method operates on graphene surfaces under elevated gas pressures while maintaining low-energy states. The mechanism relies on graphene's ability to emit terahertz radiation, creating an excited electron-rich environment where plasmons with Fermi velocities of 6000 km/s interact with hydrogen nuclei. High-pressure hydrogen gas on graphene surfaces shows enhanced mobility compared with hydrogen in conventional systems, increasing the probability of fusion interactions. The proposed electron capture mechanism involves ground-state hydrogen atoms interacting with graphene plasmons, potentially enabling fusion reactions on the material surface. This approach addresses fundamental limitations of traditional cold fusion by providing a more controlled and potentially scalable fusion pathway through the strategic utilization of 2D material properties.

Keywords: Low-energy nuclear reaction, Cold fusion, Graphene, Borophane, Hyper-cold fusion.

---

1. Introduction

In 1989, two electrochemists, Fleischmann and Pons, reported that electrolysis with palladium and deuterium generated nuclear energy in the form of heat [1]. Since then, cold fusion research has been conducted by numerous experts worldwide. Although cold fusion has not gained widespread attention and acceptance in the mainstream scientific community, significant developments have highlighted the potential of cold fusion in recent years. In 2022, the US Department of Energy began funding cold fusion projects as part of its Exploratory Topics program, and several academic institutions have received funding to conduct cold fusion research [2].

My research lab, Nano Fusion Design, was established with a clear mission: to harness the potential of graphene materials for nuclear fusion. While reviewing past experiments, I discovered that excess heat has not been observed for graphite powder and hydrogen under pressures below 1 MPa [3], but excess heat has been confirmed for the hydrogenation of carbon at 5.4 MPa [4]. The pressure threshold of 5.4 MPa appears to be critical for achieving sufficient hydrogen density on carbon surfaces to enable electron capture mechanisms [5] and support efficient fusion reactions. At lower pressures, the hydrogen coverage is insufficient to obtain fusion reactions with enough energy to power a generator. Another experiment confirmed nuclear reactions with carbon nanotubes in heavy water by detecting helium production [6]. Additionally, excess heat has been achieved using terahertz pulses [7]. Building

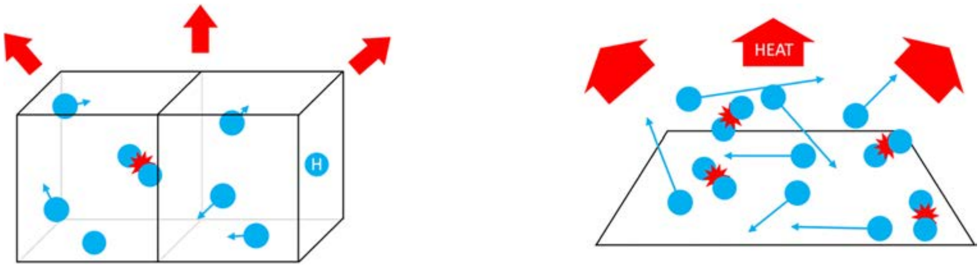

Figure 1. Conceptual comparison of the energy density and efficiency in cold fusion vs. hyper-cold fusion.

on these observations, I am planning further experiments using terahertz-emitting graphene [8] and borophane—a material with a high hydrogen density [9]. These materials may facilitate the development of practical cold fusion systems.

2. Design of Hyper-Cold Fusion

Hyper-cold fusion represents a significant enhancement in traditional cold fusion. Whereas traditional cold fusion relies on 3D metals to absorb hydrogen in near-vacuum conditions, hyper-cold fusion operates on 2D material surfaces under high-pressure gas environments, giving rise to the term ‘hyper.’ This innovative approach leverages the unique properties of 2D materials such as graphene and borophane to achieve fusion reactions more efficiently. Fig. 1 illustrates how 2D materials are revolutionizing the cold fusion landscape, contrasting traditional methods with this groundbreaking new approach.

In addition to graphene, the proposed system relies on borophane, a 2D borohydride sheet composed of boron and hydrogen atoms with an H:B ratio of 1:1 [8]. When heated above 200 °C, borophane releases hydrogen atoms from its surface. This temperature-dependent desorption process enables proton-boron fusion reactions through electron capture mediated by graphene. By irradiating the graphene-borophane mixture with electromagnetic waves, excess heat or electrical power may be generated under rigorously controlled conditions. Instead of using only high-pressure hydrogen gas as a fuel, this approach makes it easier to perform experiments, improves fuel mobility, and enhances the shelf life.

A three-step reaction pathway is hypothesized:

1. Hydrogen desorbs from borophane heated above 200 °C.
2. Hydrogen collides with fast electrons on graphene and converts to neutrons.

$$\mathrm{p} + \mathrm{e}^- \rightarrow \mathrm{n} + \nu_e$$

3. Neutrons fuse with boron and convert to lithium and helium, releasing nuclear energy.

$$\mathrm{n} + {}^{10}\mathrm{B} \rightarrow {}^{7}\mathrm{Li} + {}^{4}\mathrm{He}\ (Q \approx 2.79\ \mathrm{MeV})$$

Theoretically, 1 g of borophane can yield thermal energy equivalent to burning 100 kg of oil—enough to power a small home for a month without producing problematic nuclear waste or radiation. This energy estimation is based on the electron capture theory. Therefore, when estimating energy for the initial experiment(s), it is more accurate to use the value of 8.7 MeV, which is the energy released during general proton-boron fusion. While scientific rigor demands the term ‘hyper-low-energy nuclear cold fusion’ to reflect the spectrum of possible nuclear processes, as opposed to the narrower term ‘hyper-cold fusion,’ I am inclined to include these reactions within the broad definition of cold fusion when the core phenomenon involves the transmutation of hydrogen into heavier elements.

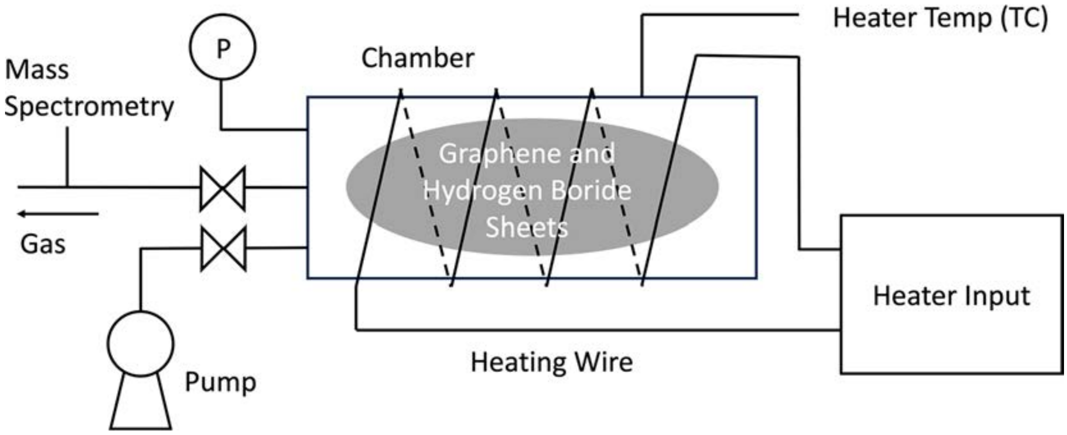

Figure 2. Schematic of the experimental setup.

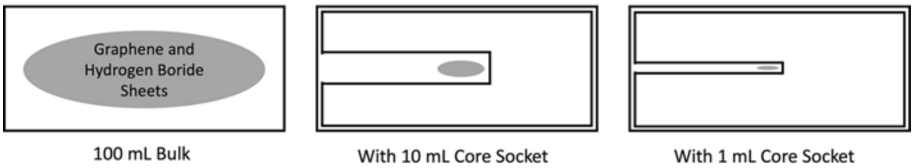

Figure 3. The chamber with core sockets.

3. Experimental Setup

A schematic of the experimental setup is shown in Fig. 2. A mixed powder of graphene and borophane is enclosed in a 100 mL pressure-resistant chamber. The chamber is evacuated to a vacuum level ranging from 1 Pa to 150 MPa. The outer wall is heated to several hundred °C using an electric heating wire, causing borophane to release hydrogen gas. Under these conditions, hydrogen exists as a supercritical fluid, a state in which the distinction between liquid and gas phases disappears. This hydrogen is expected to interact with graphene and boron, initiating fusion reactions through electron capture. The detection of excess heat or fusion byproducts (e.g., alpha particles) is necessary to validate the proposed mechanism.

The prototype chamber is made of a high-performance alloy, namely Hastelloy X, which is designed to withstand pressures up to 150 MPa and temperatures up to 1,000 °C. The operating conditions are 100 MPa and 600 °C. The 100 mL chamber accommodates 50 mL of fuel—graphene and borophane—using core sockets for precise loading control, as shown in Fig. 3. These specifications strike a balance between safety and performance, providing a foundation for future iterations.

4. Experimental Procedures

Disclaimer: The experiments described in this paper involve high pressures (up to 150 MPa) and high temperatures (up to 1,000 °C), as well as the handling of potentially hazardous materials. These experiments should only be conducted in a fully equipped laboratory environment with appropriate safety infrastructure and by highly experienced personnel trained in high-pressure and high-temperature systems, including nuclear safety protocols. Strict adherence

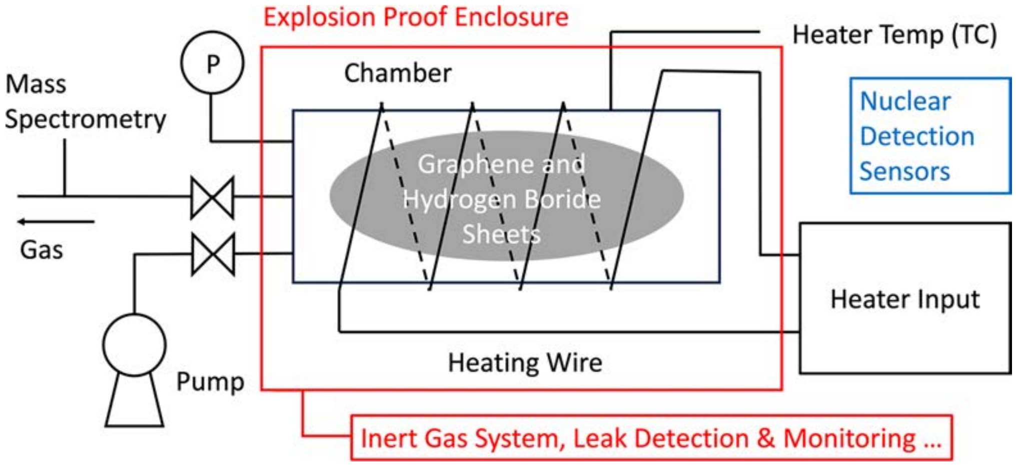

Figure 4. The experimental setup with essential safeguards (shown in red and blue).

to all relevant safety regulations, laws, and institutional guidelines is mandatory to prevent accidents, explosions, and exposure to radioactive materials. The author and publisher are not liable for damages or injuries resulting from the misuse or improper execution of the experimental procedures described herein.

In the experiment, high-pressure hydrogen gas is generated at temperatures of several hundred °C from the solid graphene-borophane fuel. If hydrogen leaks from the chamber, there is a risk of explosion. The appropriate equipment and safety measures are required to eliminate such risks, following the relevant laws and standards. The possibility of excess heat generation due to nuclear reactions should also be considered. The quantity of this heat has not been theoretically determined yet.

High-pressure gas and residual powder generated during the experiment may contain trace amounts of tritium and the radioactive carbon isotope ^{14}C. In the initial stages of the experiment, the residual amount is expected to be below regulatory limits, but the experiment should be conducted following proper management protocols, including analysis of the waste by mass spectrometry.

Essential safeguards must be incorporated for high-pressure and -temperature hydrogen systems, primarily comprising a pressurized explosion-proof enclosure with an inert gas system, a cooling system, and leak detection and monitoring systems, as well as various nuclear detection sensors, as illustrated in Fig. 4.

The initial experimental procedure involves five fundamental steps; however, the safety precautions must also be addressed, as described above.

1. Mix 0.1 g of powdered graphene with 0.02 g of borophane, place the mixture in the 100 mL pressure-resistant chamber (without core sockets), and perform vacuum evacuation.
   - During the initial stages of the experiment, the container performance can be low-spec, gradually increasing in stages.
   - Estimates show that 0.02 g of borophane produces approximately 5 MPa of hydrogen gas in a 100 mL chamber.
2. Heat the chamber's outer wall to 250 °C for 3 h using an electric heating wire wrapped around it.
   - These conditions (250 °C and 3 h) are considered sufficient for hydrogen to desorb from borophane and reach equilibrium.

3. Confirm excess heat on the outer wall.
    - Monitor the temperature using calibrated thermocouples with ±0.1 °C precision, recording data every 10 s to detect excess heat above the baseline electrical input.
    - The Joule–Thomson effect must be accounted for, which describes how the temperature of the gas decreases as its pressure increases.
    - Three control experiments are considered: Control 1, graphene only (0.1 g) under identical conditions; Control 2, borophane only (0.02 g) under identical conditions; and Control 3, empty container baseline measurement.
4. Stop heating the chamber and let it cool to room temperature.
5. Collect and conduct mass spectrometry analysis on the gas inside the chamber.
    - Mass spectrometry analysis enables the detection of (1) helium isotopes (^{3}He, ^{4}He) and lithium (^{7}Li) as fusion products, (2) tritium (^{3}H) as a potential byproduct, and (3) carbon isotopes (^{12}C, ^{13}C, ^{14}C) for contamination assessment.

5. Future Work & Optimization

Once the proof-of-concept is demonstrated, the next steps involve optimizing the fusion reaction. This includes determining the optimal mixing ratio of graphene and borophane, as well as refining the powder particle shape and the furnace temperature through experiments and computer simulations. It would also be beneficial to develop fuel rods that can withstand high loads and long-term operation. Ultimately, the fuel rods can be utilized as heat sources in reactors optimized for their output, and complete systems, such as boilers and small module reactors aimed at power generation, can be developed.

6. Concluding Remarks

Despite longstanding skepticism about the viability of cold fusion, recent experimental research has shown significant progress, leading many experts and enthusiasts to question whether this technology can ultimately sustain our modern lifestyle and provide hope for future generations. Hyper-cold fusion, leveraging the unique properties of 2D materials under high pressure, represents a promising pathway to overcome the historical limitations of cold fusion and potentially unlock a new clean energy source.

Acknowledgments

The author thanks Prof. Shinya Narita at Iwate University for his moderation of the ICCF26 meeting. The author thanks Robert Ireland, PhD, from Edanz (https://jp.edanz.com/ac) for editing a draft of this manuscript. Sincere thanks also go to the LENR-forum.com community members for their useful discussions.

Appendix A: How Electron Capture Can Occur in Cold Fusion

In this Appendix, one of the controversial topics [10] in cold fusion—electron capture—is explained based on the interaction between a plasmon on graphene and hydrogen. A plasmon is a quasi-particle or coherent state of electrons that can move on graphene at a velocity of around 1,000 km/s. A hydrogen atom is easily ionized when it encounters a plasmon, becoming a ground-state proton. Electrons in a plasmon are tightly packed and oscillate collectively, but they still repel each other because of their similar negative charge.

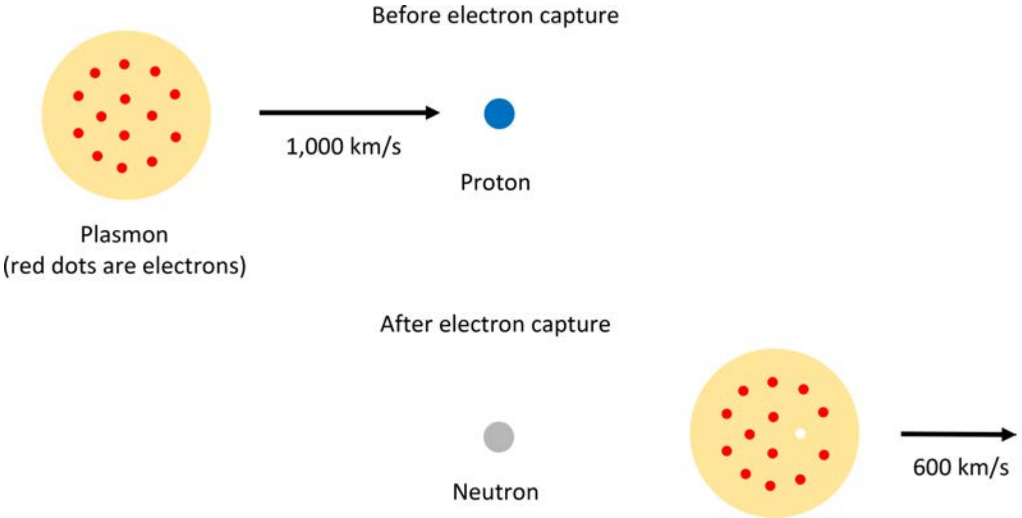

Figure 5. Illustration of the electron capture process between a hydrogen atom and a plasmon on graphene.

Figure 5 illustrates the situation before and after electron capture. Initially, a plasmon moves toward a proton at 1,000 km/s. When the plasmon collides with the proton, one electron is captured by the proton, forming a neutron. At the moment of capture, the electron's velocity alone is insufficient to form a neutron; without additional factors, the electron would scatter without being captured. However, because electrons in the plasmon are tightly bound, the scattering energy is rebounded by the plasmon, forcing an electron into the proton during collision.

Notably, the plasmon loses velocity because its kinetic energy is partially consumed by the electron capture process. This mechanism may enable electron capture at low energies, as in cold fusion.

References

[1] M. Fleischmann and S. Pons, Electrochemically induced nuclear fusion of deuterium, J. Electroanol. Chem. Int. Electrochem. 261 (2), 301–308, 1989.

[2] H. Kozima, The cold fusion phenomenon and the ARPA-E project 2022 of DOE: a facet of the sociology of modern science, Proc. JCF23 6–36, 2023.

[3] W. Ishida, H. Miyaoka, T. Ichikawa, et al., Hydrogenation properties of lithium intercalated graphite, TANSO, 2008 (233), 136–139, 2008.

[4] T. Mizuno and S. Sawada, Anomalous heat generation during hydrogenation of carbon (Phenanthrene), Proc. ICCF14, 2008.

[5] A. Widom and L. Larsen, Ultra low momentum neutron catalyzed nuclear reactions on metallic hydride surfaces, Eur. Phys. J. C 46, 107–111, 2006.

[6] C.H. Cooper, J.F. Loan, W.K. Cooper, et al., Methods of generating energetic particles using nanotubes and articles thereof, US Patent Application Publication, US 2009/0147906 A1.

[7] D. Letts, Highly reproducible LENR experiments using dual laser stimulation, Current Science 108 (4), 559–561, 2015.

[8] S. Boubanga-Tombet, W. Knap, D. Yadav, et al., Room temperature amplification of terahertz radiation by grating-gate graphene structures, Phys. Rev. X 10 (3), 031004, 2020.

[9] H. Nishino, T. Fujita, N.T. Cuong, et al., Formation and characterization of hydrogen boride sheets derived from $\mathrm{MgB_2}$ by cation exchange, J. Am. Chem. Soc. 139 (39), 13761–13769, 2017.

[10] V. Vysotskii, On problems of Widom–Larsen theory applicability to analysis and explanation of Rossi experiments, J. Condensed Matter Nucl. Sci. 13, 615–623, 2014.

J. Condensed Matter Nucl. Sci. 41 (2026) 44–61

Research Article

Current Status of Research and Development of Condensed Matter Nuclear Science in Japan

Yasuhiro Iwamura

School of Science, Yokohama City University, Yokohama, Japan

Abstract

This paper reviews the progress of CMNS (Condensed Matter Nuclear Science) research in Japan and outline the main findings. An overview of past state-sponsored and private foundation-sponsored research projects in Japan will be presented. We also report on current university-based research trends and private companies entering this field. We will discuss the challenges and directions of future research and development of CMNS in Japan.

Keywords: Condensed matter nuclear science, Low energy nuclear reaction, Cold fusion, Heat generation, Transmutation

---

1. Past Research (1989-2015) in Japan

This section introduces key research, research projects, and research organizations in this field in Japan from the announcement of Cold Fusion in 1989 until around 2015.

1.1. Electrolysis Experiments in the Early Days

Following the announcement of Cold Fusion, numerous experiments replicating Fleischman and Pons' experiment—electrolysis of heavy water using Pd as the cathode—were reported. However, it is well known that many laboratories could not reproduce the excess heat. Others did succeed. Among these, Professor Takahashi's group at Osaka University successfully detected excess heat and low-level neutrons with good reproducibility using an electrolysis method that switched the current applied to the Pd between high and low states. They presented their findings at ICCF-3. Figure 1 shows an overview of their experimental setup [1]. They used a Pd sheet cathode centered within a Pt-wired anode in D_2O/LiOD electrolyte with the L-H mode pulse operation. They detected anomalously large excess heat (32 W on average for 2 months, 100 - 130 W at peak and averaged output/input power ratio of 1.7) was associated with very low neutron emission ($\sim$1 n/s) [1].

Reports of nuclear transmutation occurring as a result of electrolysis have existed since relatively early in the history of cold fusion. Figure 2 shows the experimental results of Mizuno, Omori, and Enyo from Hokkaido University [2].

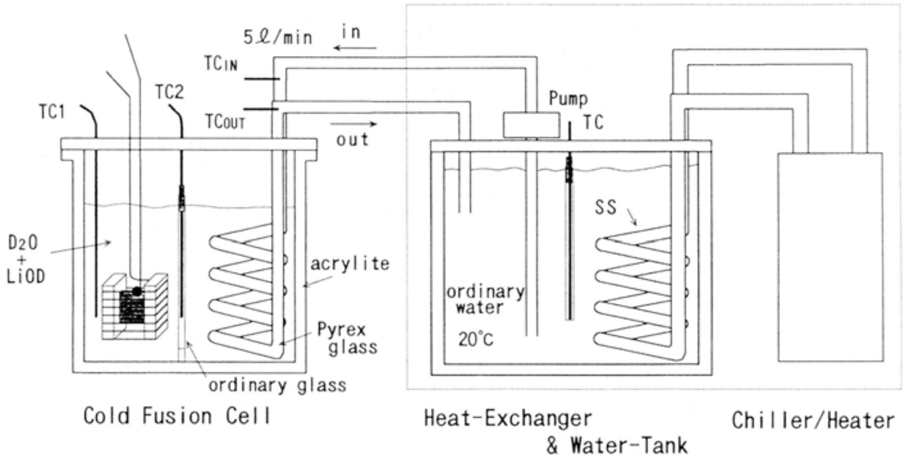

Figure 1. Schematic view of electrolysis cell and cooling system of Takahashi's group [1].

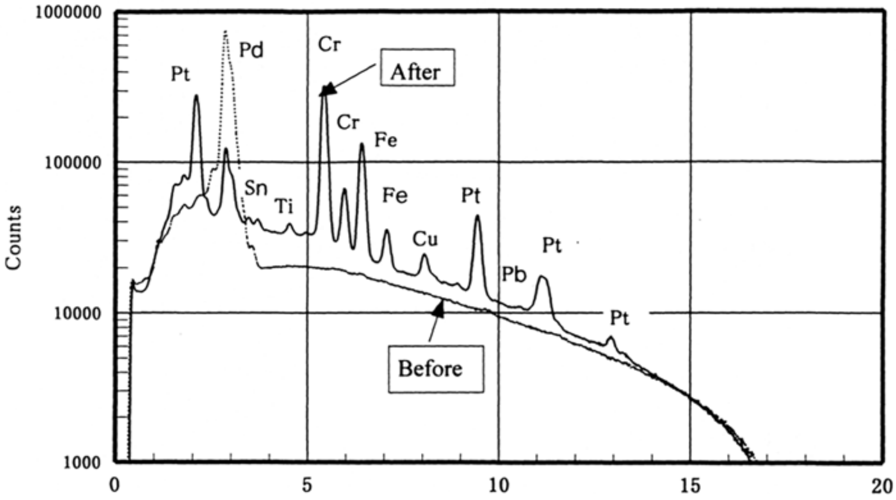

Figure 2. EDX Changes in surface elements of Pd before and after electrolysis (nuclear transmutation) by Mizuno, Omori, and Enyo [2].

They measured Pd before and after the experiment using techniques such as EDX and SIMS, reporting the detection of transmutation products and differences from the natural isotope ratio.

Excess heat was detected not only with heavy water and Pd but also with light water and metals such as Ni or Au, indicating simultaneous nuclear transmutation. This finding was mainly reported by researchers from Hokkaido University [3]–[5].

Table 1 shows part of the results from Reference 5. In this experiment, electrolysis of a dilute Na_2SO_4 solution was performed using gold electrodes, varying the current density and duration. Table 1 presents the measured isotope ratios of iron detected in large quantities after the experiment, revealing a significant change in the ^{57}Fe isotope ratio.

Table 1. Isotopic contents of Fe produced in various electrolysis systems [5]

Sample	Total Ion Intensity (count)	Isotopic Content (%)		
		^{54}Fe	^{56}Fe	^{57}Fe
1	17 205	3.2	74.7	22.0
2	619 950	5.6	84.7	9.6
3	192 134	3.7	67.4	28.9
4	1 254 164	7.0	67.6	25.3
5	141 211	6.6	84.1	9.2
Natural value		5.82	91.66	2.19

1.2. NHE (New Hydrogen Energy) Project (1993-1998)

In response to the above results emerging domestically, a national research project (NHE: New Hydrogen Energy) led by the Ministry of International Trade and Industry (MITI) was conducted from 1993 to 1998. The budget scale was 3 billion yen (approximately 25 million dollars at the exchange rate at the time). This project consisted of two teams: the NHE Demonstration Team and the Fundamental Research Team.

The NHE Demonstration Team performed experiments at IMRA Japan (Toyota Group) with seconded staff from Hitachi, Toshiba, Mitsubishi Heavy Industries, Aisin Seiki, etc. However, they were unable to achieve any noteworthy results. The fundamental research team was divided into the following four teams, primarily conducting research at universities.

1) Excess Heat: Ota (Yokohama National University)
2) Correlation: Takahashi (Osaka University)
3) Nuclear Physics: Kasagi (Tohoku University)
4) Materials: Sakamoto (Nagasaki University)

Although the Fundamental Research Team yielded several interesting results, the final conclusion of the NHE project was negative.

1.3. Hybrid Experiments of Electrolysis and Gas Loading With Sub-Nano or Nano Scale Pd

Shortly after 1989, an experimental method called “gas loading” was also reported, which involved adsorbing deuterium gas into Pd to observe phenomena, rather than using electrolysis. In Japan, experimental methods combining electrolysis and gas loading with sub-nano or nano scale Pd were reported.

Arata and Zhang at Osaka University invented an experimental method to adsorb deuterium gas onto Pd-black by packing subnano-meter-scale Pd powder (Pd-black) into a Pd cylinder called a DS cathode by performing D_2O electrolysis [6]–[8]. Figure 3 shows schematic view of electrolysis apparatus and structure of DS-cathode (right). This enabled the high-density filling of high-purity deuterium gas onto Pd-black. They demonstrated that excess heat was generated only when deuterium gas was adsorbed into Pd, as shown in Figure 4 [7]. They succeeded in detecting 4He from Pd-black after the experiment [8].

Iwamura, Itoh and their colleagues of Mitsubishi Heavy Industries, Ltd. presented a new experimental method: By supplying deuterium gas via heavy water electrolysis from the nanoscale Pd/CaO multilayer film side while maintaining the opposite side under vacuum conditions, they induced deuterium permeation. In this experiment, they detected excess heat and transmutation products (Ti) [9]–[10].

1.4. Gas Loading Experiments

Experiments with the gas loading type were actively conducted in Japan from a relatively early stage. NTT’s Yamaguchi reported the adsorption of deuterium into a sample where gold was deposited on one side of Pd and MnOx

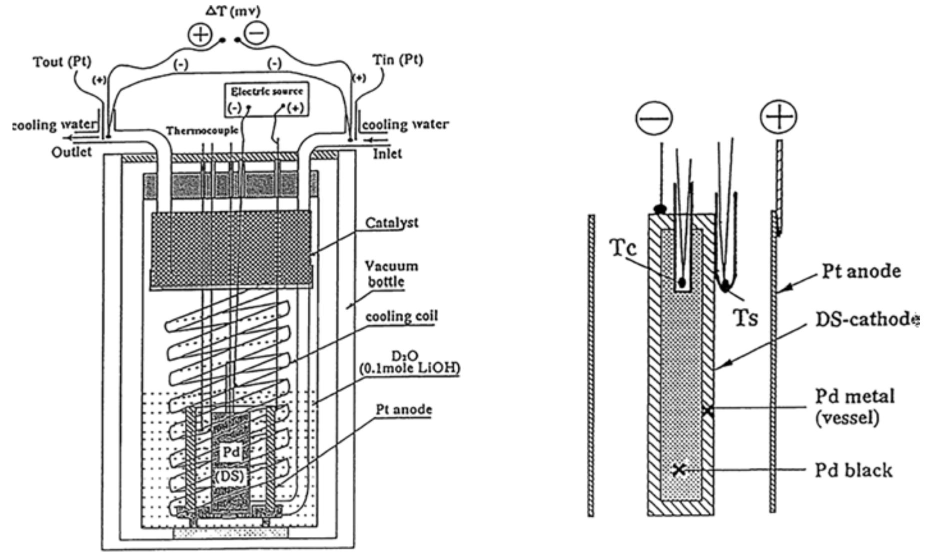

Figure 3. Schematic view of electrolysis apparatus (left) and structure of DS-cathode (right) by Arata and Zhang [8].

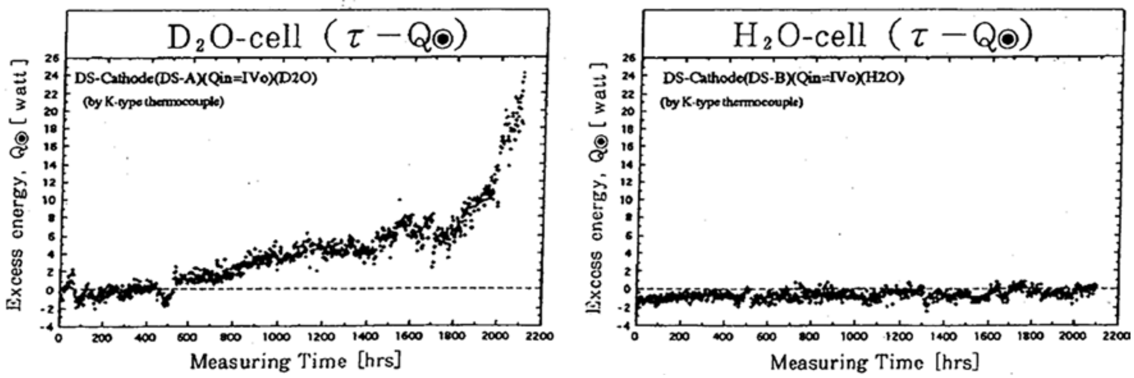

Figure 4. Excess heat generation during the adsorption of deuterium into Pd-black via electrolysis of a DS cathode [7].

on the opposite side, along with the detection of heat release and neutrons or ^{4}He [11], [12]. His presentation drew significant attention at ICCF-3, which was held in Japan.

Iwamura and Itoh of Mitsubishi Heavy Industries conducted experiments to induce transmutation reactions by making deuterium gas permeation through nano-structured Pd and CaO samples [13]–[15], building upon the hybrid experimental method shown in Figure 5. Figure 7 shows their experimental apparatus, the structure of the samples, and representative experimental results. Figure 7 illustrates an example of transmutation from Cs into Pr. They also observed nuclear transmutation reactions from Sr into Mo, Ba into Sm, and W into Pt. Notably, in the Ba transmutation, placing ^{138}Ba on the nanostructured Pd/CaO sample yielded ^{150}Sm, whereas placing ^{137}Ba on the sample yielded ^{149}Sm by deuterium gas permeation. This demonstrates that the isotope ratio of the transmuted material changes depending

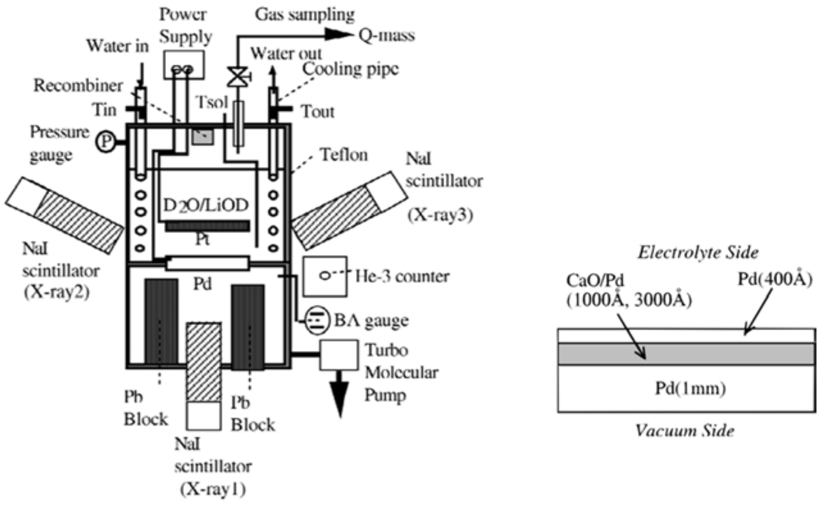

(a) (b)

Figure 5. Schematic of Iwamura and Itoh’s experimental method; (a) An experimental apparatus employing a nanoscale Pd/CaO multilayer film, where one side undergoes heavy water electrolysis while the other side is evacuated, enabling deuterium gas permeation through the Pd multilayer film. (b) Structure of the Pd/CaO multilayer film [10].

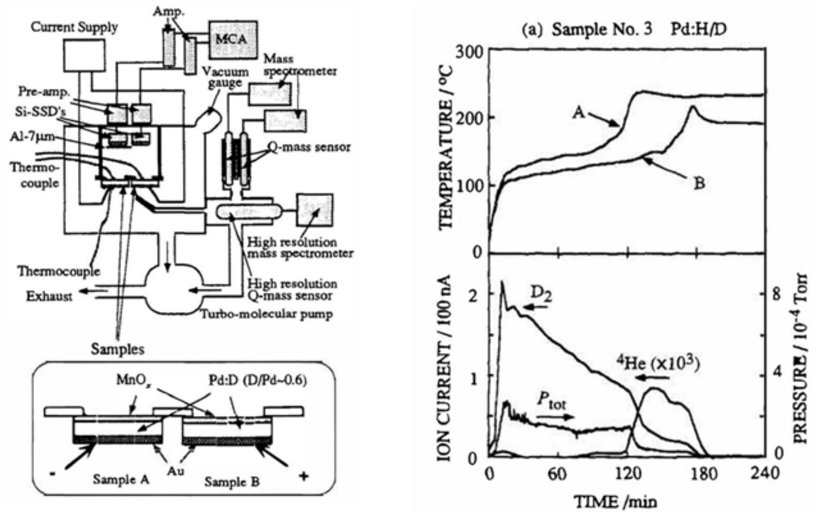

(a) (b)

Figure 6. Yamaguchi’s Experimental Method and an example of ^{4}He; (a) An experimental apparatus with a heterostructure of deuterated Pd (Pd:D), (b) An example of detection of 4He and temperature rise [12].

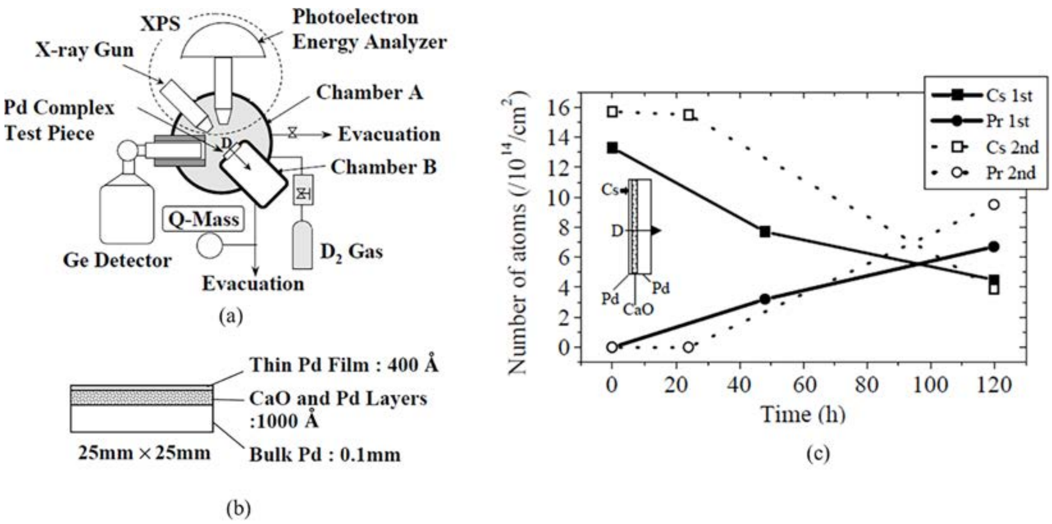

Figure 7. Experimental method inducing nuclear transmutation by permeating deuterium gas through Pd/CaO multilayer thin films developed by Iwamura, Itoh et al.; (a) Overview of the experimental apparatus, (b) Pd complex with Pd/CaO multilayer thin film, (c) Example of transmutation experiment results from Cs into Pr [13].

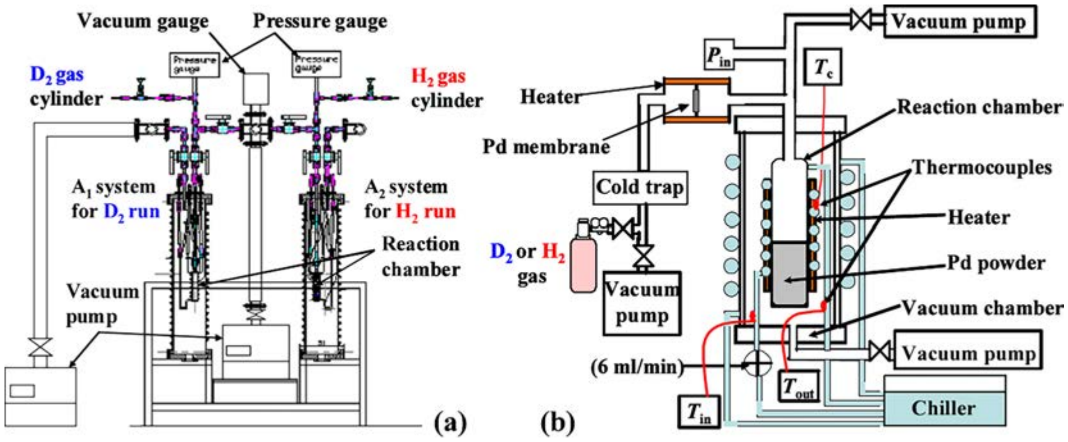

Figure 8. A twin system for hydrogen absorption experiments by Kitamura and Takahashi et.al; (a) Reduced view of the A1·A2 twin system, and (b) functional view of A1. [17].

on the isotope ratio of the given material, providing strong evidence for nuclear reactions. Replication experiments have been successfully performed by some researchers and T. Hioki at Toyota R&D Center published almost complete replication experiments [16] on the transmutation of Cs into Pr.

In order to replicate the phenomenon of heat and ^{4}He generation by D_2 gas absorption in nano-sized Pd powders reported by Arata and Zhang [6]–[8], Kitamura and Takahashi et al. at Kobe University performed gas-loading type experiments with a twin system for hydrogen absorption experiments as shown in Figure 8.

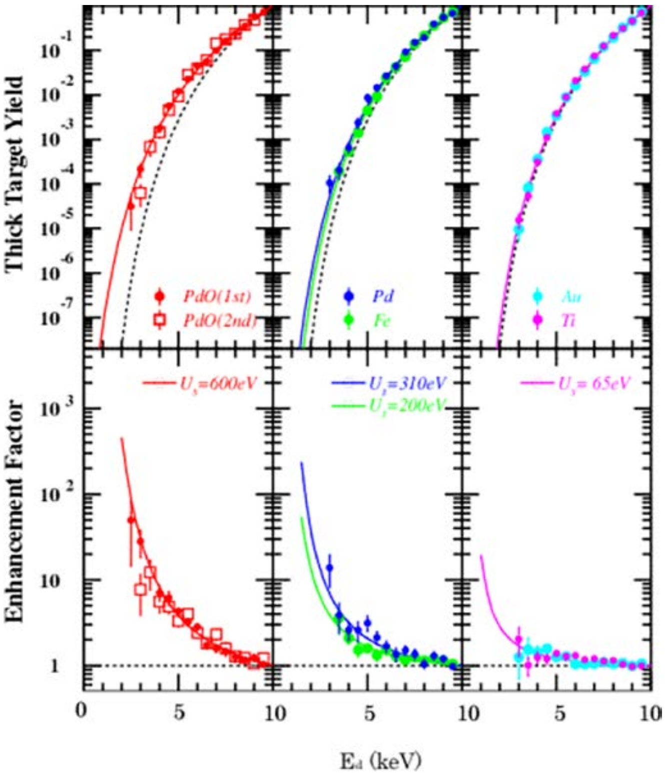

Figure 9. Anomalously Large Enhancement of DD Fusion rate at Low Energy by Kasagi et.al. Relative yields of the D(d,p)T reaction in metals against the bombarding energy are plotted. In the lower part, the ratios of the experimental yield to the standard calculation are shown [19].

They observed anomalously large energies of hydrogen isotope absorption, 2.4±0.2 eV/D-atom and 1.8±0.4 eV/H-atom for Pd ·Zr oxide nano-powders, in the phase of deuteride/hydride formation. The sample charged with D2 also showed significantly positive output energy in the second phase after the deuteride formation.

1.5. Beam Experiments

Researchers including Kasagi at Tohoku University conducted experiments irradiating materials such as Pd and Ti with low-energy D beams to clarify the physics of nuclear reactions within solids [18]–[21]. Figure 9 shows the anomalous increase in the DD fusion rate below 10 keV observed by Kasagi et al., revealing that the rate of enhancement varies depending on the type of metal.

1.6. Japan CF-Research Society (1999-)

Japan CF-Research Society (JCF) was established in 1999 by Professor Emeritus Takahashi of Osaka University. The current president is Professor Shinya Narita (Iwate University), with approximately 70 members. The purpose of this organization is to contribute to the advancement of science and technology through research on the condensed matter nuclear phenomena, to facilitate information exchange among JCF members, and to hold conferences for condensed

Table 2. Summary of NEDO project results [22]

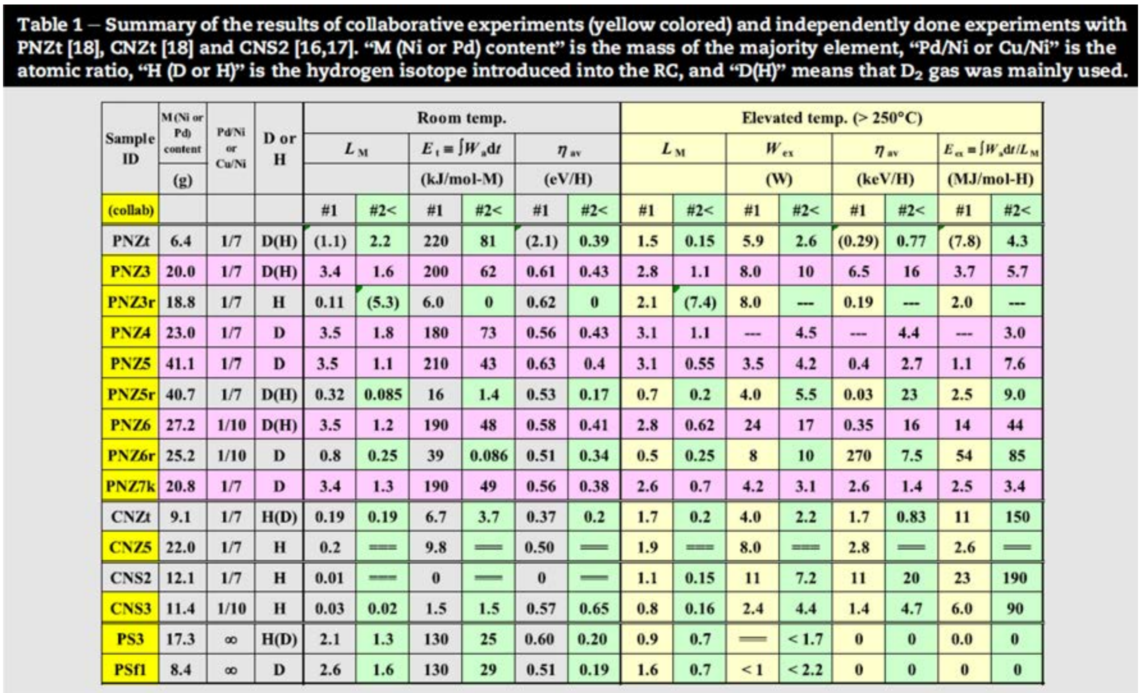

Table 1 – Summary of the results of collaborative experiments (yellow colored) and independently done experiments with PNZt [18], CNZt [18] and CNS2 [16,17]. "M (Ni or Pd) content" is the mass of the majority element, "Pd/Ni or Cu/Ni" is the atomic ratio, "H (D or H)" is the hydrogen isotope introduced into the RC, and "D(H)" means that D_2 gas was mainly used.

Sample ID	M (Ni or Pd) content	Pd/Ni or Cu/Ni	D or H	Room temp.						Elevated temp. (> 250°C)							
				L_M		$E_t \equiv \int W_a dt$		η_{av}		L_M		W_{ex}		η_{av}		$E_{ex} \equiv \int W_a dt/L_M$	
	(g)					(kJ/mol-M)		(eV/H)				(W)		(keV/H)		(MJ/mol-H)	
(collab)				#1	#2<	#1	#2<	#1	#2<	#1	#2<	#1	#2<	#1	#2<	#1	#2<
PNZt	6.4	1/7	D(H)	(1.1)	2.2	220	81	(2.1)	0.39	1.5	0.15	5.9	2.6	(0.29)	0.77	(7.8)	4.3
PNZ3	20.0	1/7	D(H)	3.4	1.6	200	62	0.61	0.43	2.8	1.1	8.0	10	6.5	16	3.7	5.7
PNZ3r	18.8	1/7	H	0.11	(5.3)	6.0	0	0.62	0	2.1	(7.4)	8.0	---	0.19	---	2.0	---
PNZ4	23.0	1/7	D	3.5	1.8	180	73	0.56	0.43	3.1	1.1	---	4.5	---	4.4	---	3.0
PNZ5	41.1	1/7	D	3.5	1.1	210	43	0.63	0.4	3.1	0.55	3.5	4.2	0.4	2.7	1.1	7.6
PNZ5r	40.7	1/7	D(H)	0.32	0.085	16	1.4	0.53	0.17	0.7	0.2	4.0	5.5	0.03	23	2.5	9.0
PNZ6	27.2	1/10	D(H)	3.5	1.2	190	48	0.58	0.41	2.8	0.62	24	17	0.35	16	14	44
PNZ6r	25.2	1/10	D	0.8	0.25	39	0.086	0.51	0.34	0.5	0.25	8	10	270	7.5	54	85
PNZ7k	20.8	1/7	D	3.4	1.3	190	49	0.56	0.38	2.6	0.7	4.2	3.1	2.6	1.4	2.5	3.4
CNZt	9.1	1/7	H(D)	0.19	0.19	6.7	3.7	0.37	0.2	1.7	0.2	4.0	2.2	1.7	0.83	11	150
CNZ5	22.0	1/7	H	0.2	===	9.8	===	0.50	===	1.9	===	8.0	===	2.8	===	2.6	===
CNS2	12.1	1/7	H	0.01	—	0	—	0	—	1.1	0.15	11	7.2	11	20	23	190
CNS3	11.4	1/10	H	0.03	0.02	1.5	1.5	0.57	0.65	0.8	0.16	2.4	4.4	1.4	4.7	6.0	90
PS3	17.3	∞	H(D)	2.1	1.3	130	25	0.60	0.20	0.9	0.7	—	< 1.7	0	0	0.0	0
PSf1	8.4	∞	D	2.6	1.6	130	29	0.51	0.19	1.6	0.7	< 1	< 2.2	0	0	0	0

matter nuclear phenomena research. An annual meeting is held each year for information exchange, with 24 conferences held to date (JCF1–JCF24). Proceedings from all conferences are published at Proceedings of JCF meeting. Recently, the JCF entered into a partnership with the ISCMNS.

2. Current Research (2015-) in Japan

Next, the research projects and the current state of research in Japan over the past decade are described.

2.1. NEDO Project (2015-2017)

A research project funded by NEDO (New Energy and industrial technology Development Organization) was conducted over a two-year period from October 2015 to October 2017. Participating organizations included Technova Inc., Nissan Motor Co., Kyushu University, Kobe University, Nagoya University, and Tohoku University, with a budget of 0.12 billion yen. In this project, heating nanoparticles composed of Pd, Ni, Cu, and ZrO_2 that had adsorbed H_2 or D_2 gas to approximately 300°C resulted in the observation of anomalous heat generation that could not be explained by known chemical reactions. The nanoparticle samples were divided between Kobe University and Tohoku University, and experiments conducted under identical conditions confirmed similar levels of excess heat generation.

Table 2 shows a summary of NEDO project collaborative experiments. Hydrogen isotope absorption and heat evolution both at room and elevated temperatures have been examined for ZrO2-supported Pd/Ni nanocomposites (shown as PNZ), ZrO2-supported Cu/Ni nanocomposites (shown as CNZ), SiO2-supported CuNi nanocomposites (shown as CNS) and Pd nanoparticles (shown as PS). As can be seen from the Table 2, heat generation that cannot be

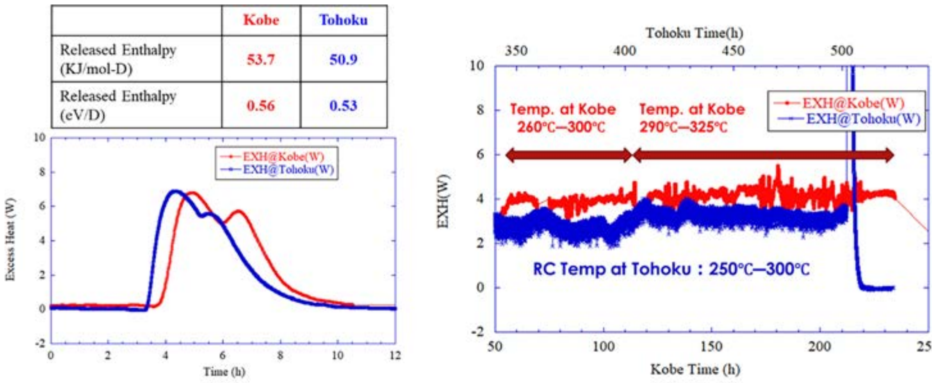

	Kobe	Tohoku
Released Enthalpy (KJ/mol-D)	53.7	50.9
Released Enthalpy (eV/D)	0.56	0.53

(a) (b)

Figure 10. Comparison of released heat power between Kobe University and Tohoku University; (a) at room temperature, (b) elevated temperature [23].

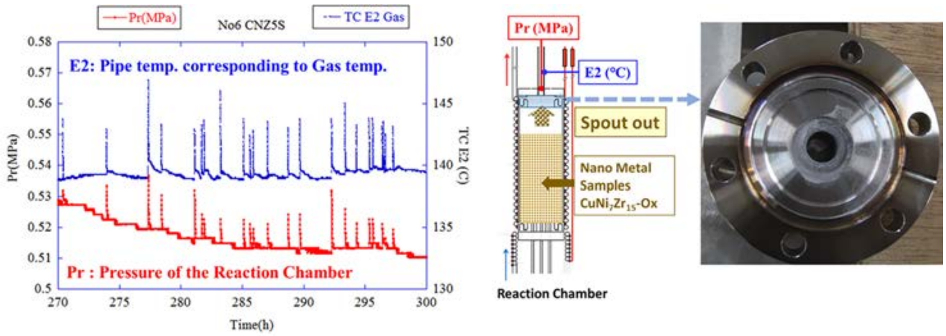

(a) (b) (c)

Figure 11. Heat and pressure burst phenomena; (a) burst-like coincident increase events of chamber pressure (Pr) and upper side temperature (E2), (b) heat generation chamber and the measurement points for temperature and pressure, (c) photo of the upper flange on which CNZ nanoparticles adhered [23].

explained by chemical reactions, likely originating from adiation-free nuclear process, was observed with PNZ, CNZ and CNS.

In the NEDO project, a heat generation experimental apparatus with specifications nearly identical to that at Kobe University was installed at Tohoku University to confirm the reproducibility of the phenomenon. PNZ samples prepared at Kobe University were divided into two, and heat generation experiments using the PNZ samples were conducted under nearly identical experimental conditions at both Kobe University and Tohoku University. The results are shown in Figure 10. Figure 10 (a) shows the comparison of heat generation at room temperature, and Figure10 (b) shows the comparison of excess heat during heating. As these results indicate, nearly identical excess heat was observed in both experiments. This demonstrates that reproducibility can be ensured by maintaining identical samples for heat generation and temperature conditions.

In the NEDO project, phenomena indicating the presence of heat generation were observed in addition to excess heat and reproducibility. Figure 11 shows experimental results [23] from Tohoku University, where heat generation

Table 3. Current research conducting organizations in Japan

Universities	Companies
Kyushu University	Nissan motor corporation
Kobe University	Toyota Central Research Lab.
Kyoto University	DENSO corporation
Waseda University	Mitsubishi Heavy Industries, Co., Ltd.
Tohoku University	Clean Planet, Inc.
Iwate University	New Hydrogen Fusion Energy, Inc.
Yokohama City University	Hydrogen Engineering Application
Nagoya University	& Development Company
Tokyo University of Science	Z Mechanism technology Co., Ltd.
	Cool Fusion, Co., Ltd.

experiments were conducted using CNZ samples and light hydrogen. Figure 11 (b) shows the heat generation chamber and the measurement points for temperature and pressure. As shown, the sample, consisting of Cu and Ni nanoparticles supported on ZrO_2, was placed inside a cylindrical stainless-steel chamber. After hydrogen was introduced, the entire chamber was heated by a heater to induce the heat generation reaction. During this process, as shown in Figure 11 (a), a phenomenon was observed where the hydrogen pressure (Pr) inside the chamber and the hydrogen gas temperature (E2) at the top of the chamber rose simultaneously in bursts. This suggests that during the heat generation reaction, heat bursts occurred, causing high-temperature hydrogen to be ejected. Indeed, photographs of the chamber top after the experiment as shown in Figure 11(c) revealed CNZ nanoparticles adhering to the surface. This can be interpreted as follows: the sudden heat generation reaction caused the lower CNZ nanoparticles to be ejected, triggering a pressure increase, the high-temperature hydrogen gas moved upward and the nanoparticles collided with the flange. This phenomenon provides evidence that very large burst-like heat generation events occurred.

2.2. Current Research Participating Organizations (Universities and Companies) in Japan

Table 3 summarizes Japanese universities and companies currently conducting research in this field. These institutions are based on information such as their participation and presentations at previous JCF and ICCF conferences, or announcements to the media.

While numerous researchers from universities and companies are engaged in research and development in this field, given the breadth of the research and the size of the market, we hope to see more researchers and engineers join this field.

2.3. Overview of Main University Research

This section introduces research overviews from Kobe University, Waseda University, Iwate University, and Tohoku University, highlighting current university research being conducted in Japan.

Kobe University has continued its research while developing the methodology [24]–[26] from the previously mentioned NEDO project, and recently succeeded in detecting significant amounts of He-3 from nanoparticle samples that exhibited heat generation [27]. This provides strong evidence that nuclear reactions are occurring.

Figure 12 shows the He-3 detection results obtained by the NRA. The He-3 produced by irradiation of the nanoparticle sample exhibiting excess heat generation with a deuterium beam was detected using the following reaction.

$$\mathrm{d} + {}^{3}\mathrm{He} \rightarrow {}^{4}\mathrm{He} + \mathrm{p} + 18.354\ \mathrm{MeV} \tag{1}$$

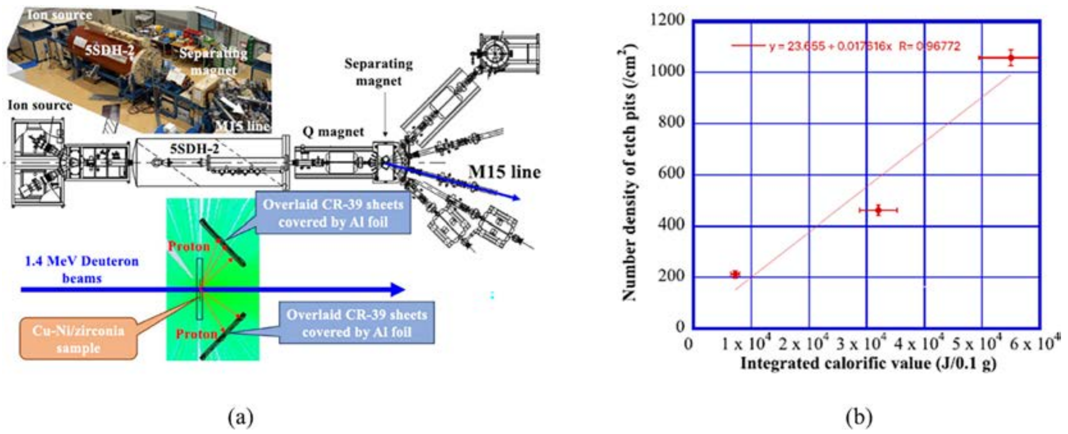

Figure 12. Detection of He-3 in nickel-based metal nano-composites supported on ZrO2, which exhibited anomalous excess heat generation, by NRA (Nuclear Reaction Analysis); (a) NRA system using deuteron beams from the tandem accelerator at Kobe University, (b) Total heat generated and number of etch pits detected by NRA [27].

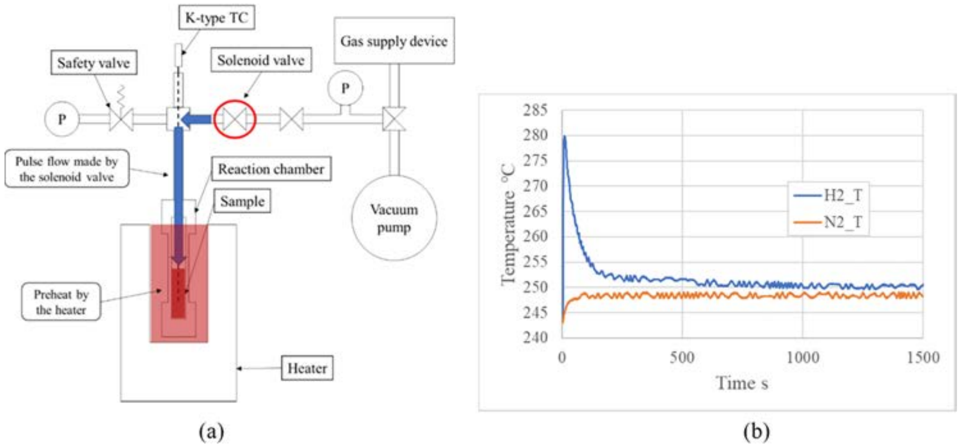

Figure 13. Excess heat generation by high-speed, high-pressure pulsed hydrogen gas impinging on a nanoparticle sample performed at Waseda University; (a) schematic of experimental apparatus, (b) an example of temperature rise difference between H_2 and N_2 pulse flow [28].

Produced protons reach energies above 14 MeV and can be easily ejected from the sample, making it possible to measure them with some conventional radiation detectors such as CR-39 plates. The vertical axis in Fig. 12(b) represents the number of CR-39 etch pits, proportional to the number of protons detected by the NRA, i.e., the number of He-3. Horizontal axis represents the total excess heat. This demonstrates a proportional relationship between the total excess heat and the number of He-3. This result strongly suggests that He-3 was generated during the anomalous excess heat generation. It should be added that this paper also detects He-3 using Thermal Desorption Spectrometry (TDS) [27].

Waseda University first reported that colliding a hydrogen gas jet with nanoparticles such as PNZ, similar to those used at NEDO, generates excess heat. Figure 13(a) shows a schematic of the experimental apparatus. Three grams of

Table 4. Experimental results of the experiments without H2 gas pulse flow

No.	Sample	Gas pressure	Initial temp.	Temp. rise	Heat generation	
1	Pd-Ni-Zr 3.0 g	0.12 MPa	95 °C	1.2 K	5.47 J	0.01 W
2	Pd-Ni-Zr 3.0 g	0.9 MPa	240 °C	12.4 K	56.5 J	0.72 W

Table 5. Experimental results of the experiments with H2 gas pulse flow

No.	Sample	Gas pressure	Initial temp.	Temp. rise	Heat generation	
3	Pd-Ni-Zr 3.0 g	0.12 MPa	95 °C	9.1 K	41.5 J	1.06 W
4	Pd-Ni-Zr 3.0 g	0.9 MPa	240 °C	35.0 K	159 J	17.7 W
5	Pd-Ni-Zr 3.0 g	5 MPa	295 °C	115 K	524 J	105 W

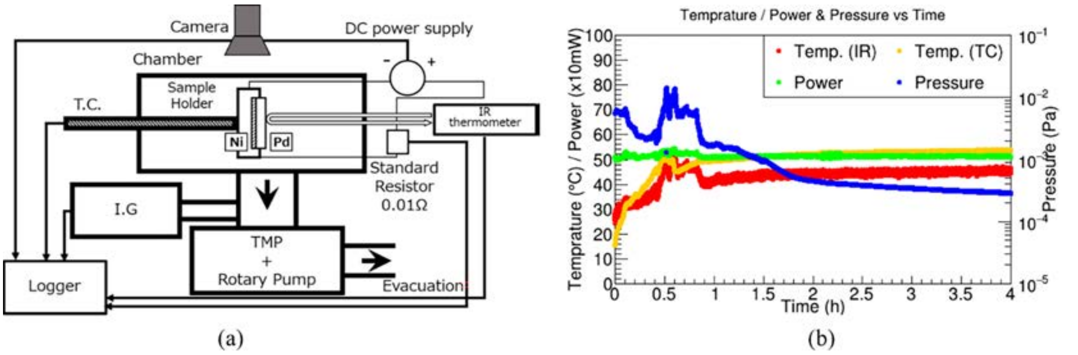

Figure 14. Hydrogen absorption and desorption experiment performed using Ni-Pd sample at Iwate University; (a) schematic of experimental apparatus, (b) an example of temperature rise with gas release from the sample [32].

Pd and Ni nanoparticles supported on ZrO_2 were placed at the center of the chamber made of SUS316L. A temperature increase of the sample is measured by the K-type thermocouple. The control experiment using nitrogen gas is done before using hydrogen gas. Figure 13(b) shows an example plot comparing the temperature rise when using hydrogen gas versus nitrogen gas. As shown, a clearly significant difference is observed between hydrogen and nitrogen.

Table 4-5 shows the excess heat evaluated based on these temperature increases. Table 4 shows the case without hydrogen pulse flow, while Table 5 shows the case with hydrogen pulse flow applied. Comparing these results reveals that heat generation is low in the absence of hydrogen gas flow, but significant heat generation occurs when a hydrogen gas pulse flow is applied under high pressure conditions. Obtained excess heat is substantially greater than values derived from chemical reactions or enthalpy changes.

At Iwate University, adsorption and desorption experiments of deuterium or hydrogen have been conducted using Pd-based metal complex samples. Especially, in deuterium/hydrogen desorption experiments using Pd samples coated with a Ni film, highly reproducible intermittent temperature rises were observed. Figure 14(a) shows the experimental apparatus, and Figure 14(b) shows an example of the experimental results. As shown in Figure 14(b), a significant increase in sample temperature was observed simultaneously with gas release from the sample, as measured by both the thermocouple and the infrared thermometer. This temperature-pressure behaviour was observed with high reproducibility in both the deuterium and hydrogen experiments. Deformation of the sample was observed during each experiment, which may be related to the generation of excess heat.

Following the NEDO research, a new experimental method was developed [34]–[37] based on insights gained from past transmutation experiments [13]–[15] and the NEDO research [22], [23] at Tohoku University. Figure 15 (a), (b)

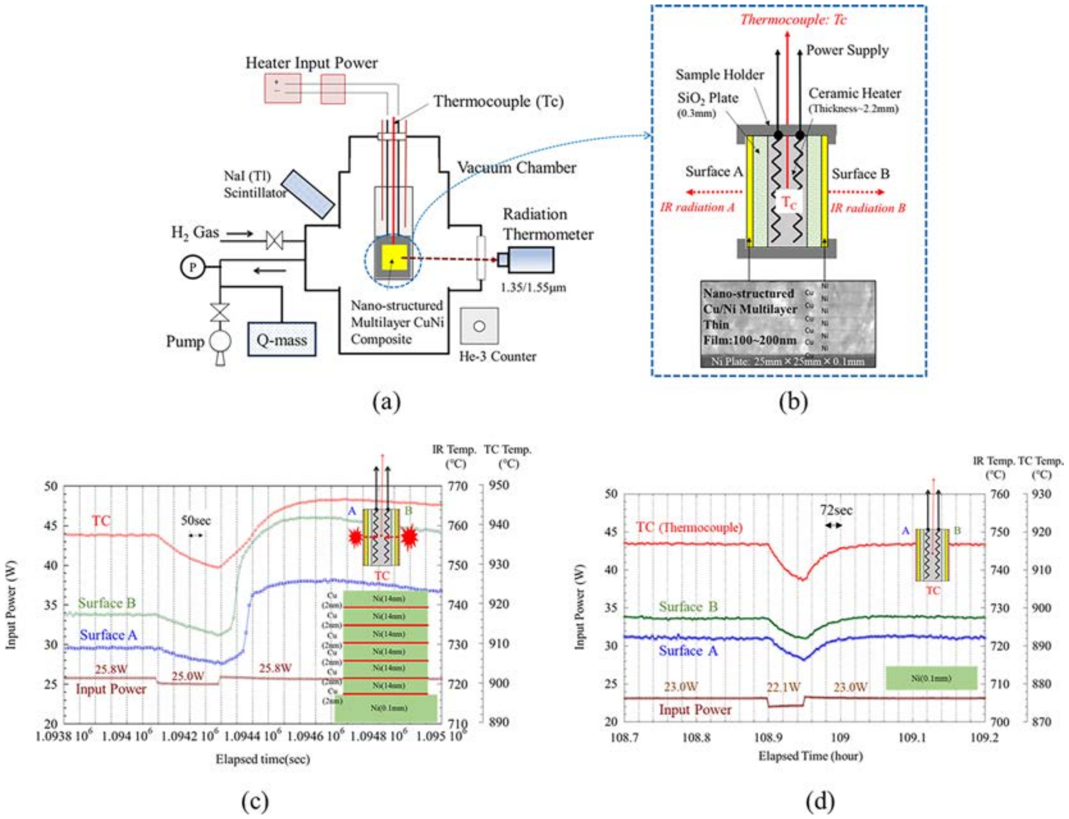

(a) (b)

(c) (d)

Figure 15. Experimental set-up for anomalous heat generation and an example of heat burst phenomenon induced by input power perturbation; (a) schematic of experimental apparatus and (b) detailed drawing around nano-structured multilayer metal composite, (c) an example of heat burst phenomenon was induced by input power perturbation, (d) an example where heat burst phenomenon did not occur [34].

shows experimental set-up for anomalous heat generation. In this experiment, Ni-based nanoscale multilayer film was preloaded with hydrogen gas and heated rapidly to move hydrogen and induced anomalously large heat generation that cannot be explained by any known chemical processes.

Figure 15 (c) and (d) show cases where heat burst phenomena occur and do not occur due to perturbations in input power, depending on the materials used. Figure 15 (d) shows the case with only the Ni plate. When the input power is temporarily reduced and then restored, the thermocouple temperature (TC) and the surface temperatures of the two samples A and B return to their original values. This is entirely reasonable, with no particular heat burst occurring. However, for the sample with a nanostructured Cu-Ni multilayer film, as shown in Figure 15 (c), after the input power was temporarily reduced and then restored, the surface temperature suddenly increased up several tens of seconds later, followed by an increase in the temperature of the thermocouple (TC) inside the heater. This can be assumed to be caused by hydrogen diffusion disturbances induced by the input perturbation triggered the heat burst. Note that no additional energy was introduced into the system during this period. Furthermore, following such a heat burst induced by the input perturbation, the elevated temperature persists for an extended period, resulting in heat generation that cannot be explained by chemical reactions. This experiment is currently being continued at Yokohama City University.

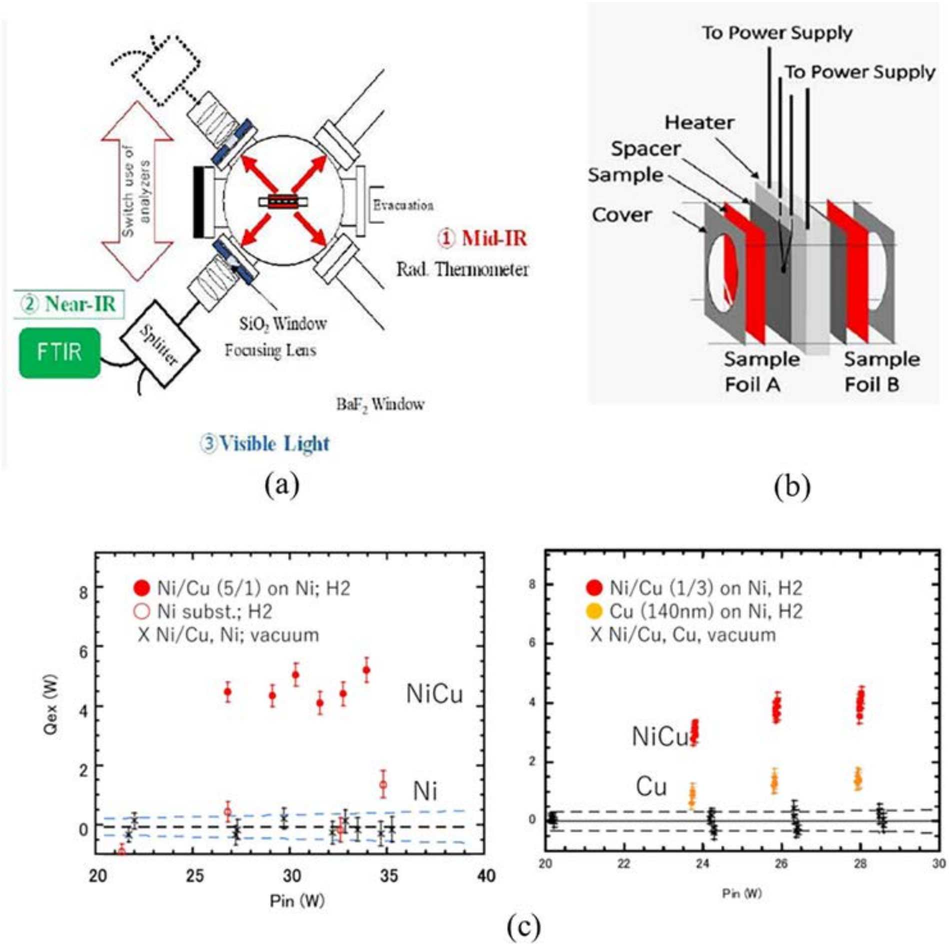

(a) (b)

(c)

Figure 16. Photon radiation calorimetry for anomalous heat generation; (a) Top view of experimental apparatus which has two sets of radiation thermometer in mid-infrared region (Md-IR), an FTIR spectrometer in near-infrared region (Nr-IR) and a multi-channel spectrometer in visible to UV light region (Light). (b) Structure of sample holder, (c) Excess heat power Qex (W) plotted against heater input Pin (W): Red solid circles are data for NiCu composite samples (Ni5Cu1 in left graph and Ni_1Cu_3 in right graph), red open circles are for Ni pure sample, orange solid circles for Cu pure sample, and x-marks for the data without H_2 gas [38].

In the experimental method shown in Fig. 15, excess heat was initially evaluated based on the temperature rise of the thermocouple (TC) embedded in the heater. To improve the reliability and accuracy of this heat evaluation, experiments were conducted to evaluate excess heat by measuring the radiation emitted from the sample surface at Tohoku University. The procedures inducing anomalous heat, samples for heat generation and a sample holder are identical to those in Figure 15, but measurement systems for emitted radiation were installed.

Figure 16(a) shows the experimental setup, Fig. 16 (b) shows the structure of the sample holder, and (c) plots the relationship between excess heat Q_{ex} evaluated from radiation and input power P_{in}. As seen in Fig. 16 (c), when experiments were conducted using a nanostructured film fabricated from Cu and Ni multilayers, the case with a Ni/Cu ratio of 5 exhibited excess heat of approximately 5 W, which is nearly equivalent to the value evaluated using only the

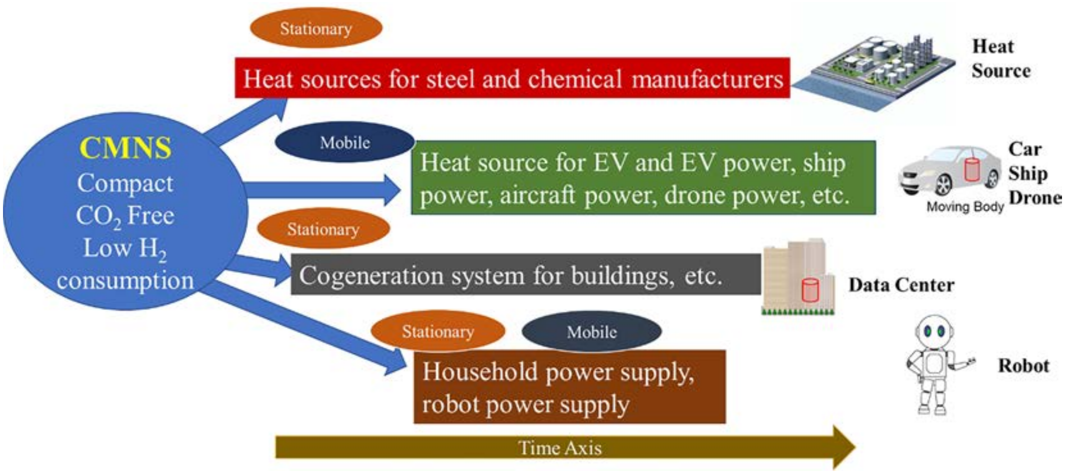

Figure 17. Possible CMNS business opportunities.

thermocouple (TC) [34]–[37]. Thus, even when excess heat was evaluated using radiation from the sample surface, the anomalous excess heat phenomenon observed with the CuNi nanostructured film was confirmed.

2.4. TEET Project (2023-2027)

Currently, no national research projects are being conducted in Japan, however, a research project by the TEET Foundation is underway from April 2023 to March 2027. TEET stands for Thermal & Electric Energy Technology. This project, themed "New Hydrogen Energy Innovation," has a budget of 200 million yen. Participating universities are Kyushu University (until March 2025), Kobe University, Waseda University, Tohoku University, Iwate University, and Yokohama City University (from April 2025). Most of the research constitutes an extension or development of the research described in the previous section.

3. Challenges and Directions of Future Research

The following outlines the societal impact of CMNS-based technologies moving forward. The socioeconomic impact of CMNS is undoubtedly significant. Among its applications, new energy sources represent the largest market, and nuclear transmutation of radioactive elements into stable ones also carries substantial societal implications. However, this discussion will focus on its application as a new energy source.

CMNS-based technologies, as shown in Figure 17, feature "compactness", "CO_2-free operation", and "extremely low hydrogen fuel consumption". Figure 17 illustrates my personal view on the future products these technologies could be applied to, with the horizontal axis representing the time axis. Roughly speaking, applications can be divided into stationary energy sources and mobile energy sources. Technologically simpler stationary energy sources are expected to be commercialized first. Primary uses include heat sources for steel and chemical manufacturers and cogeneration systems for buildings. These applications are quite diverse. And many do not require rapid output control.

However, mobile energy sources are the most effective way to leverage the compact size and high-power density that characterize CMNS-based technologies. Potential mobile applications include power sources for EVs and EV power, ship power, aircraft power, drone power, and others. Applications such as robot power supplies are also expected to grow increasingly important. Needless to say, applying these technologies to mobile systems requires overcoming technical challenges such as steep power control and vibration resistance.

CMNS-based technologies hold immense potential for significant social and economic impact when implemented. There is no doubt that understanding phenomena in this field is crucial for harnessing this technology for the benefit of society. However, I also believe that demonstrating how CMNS technology can be applied to provide significant benefits to society is crucial for stimulating research investment. My current understanding of our field is as follows:

- Many experimental results have been obtained and theoretical clarification is in progress.
- Experimental results up to now are still weak to declare the effect “nuclear”.
- Acceptance by the academic community and the general public is critical.

Based on these, I believe the following approach is important. First,

1) Develop the most practical and feasible method based on previous conducted studies,
2) Demonstrate that the method can be put to practical use,

while simultaneously elucidating phenomena in the CMNS field.

This will enable people worldwide to recognize the research utility of this field, securing funding to expand the number of researchers.

Subsequently,

3) Clarification of the reaction mechanism.

is expected to advance further.

4. Concluding remarks

Research in CMNS has been continuously and actively conducted in Japan.

The primary focus has been on experimental studies concerning the adsorption and desorption of deuterium and hydrogen using nanoscale metal composite particles and multilayer metal complexes.

- Heat generation is observed not only with deuterium but also with hydrogen. Reproducibility is fairly good.
- Heat generation that cannot be explained by chemical reactions, and observed excess power implies that the heat is likely to be of nuclear origin.

In my opinion, researchers in the fields of condensed matter physics and condensed matter chemistry, which have seldom participated so far, should be brought into our community and systematic research should be conducted to clarify what is happening. At the same time, it is important to demonstrate that this phenomenon can be put to practical use as a new energy source.

References

[1] A. Takahashi et al., Anomalous Excess Heat by D2O/Pd Cell Under L-H Mode Electrolysis. in Third International Conference on Cold Fusion, “Frontiers of Cold Fusion”. 1992. Nagoya Japan: Universal Academy Press, Inc.,Tokyo, Japan.

[2] T. Mizuno et al., Anomalous Isotopic Distribution in Palladium Cathode After Electrolysis. *J. New Energy*, 1996. **1**(2): p. 37.

[3] T. Ohmori and M. Enyo, Excess Heat Production during Electrolysis of H2O on Ni, Au, Ag and Sn Electrodes in Alkaline Media, in Third International Conference on Cold Fusion, “Frontiers of Cold Fusion”. 1992. Nagoya Japan: Universal Academy Press, Inc., Tokyo, Japan.

[4] R. Notoya et al., Cold fusion by electrolysis in a light water-potassium carbonate solution with a nickel electrode, *Fusion Technology*., **24** (1993) 202.

[5] T. Ohmori, M. Enyo, T. Mizuno et al., Transmutation in a gold-light water electrolysis system, Fusion Technology, **33:3** (1998) 367.

[6] Arata and Zhang, Excess Heat and Mechanism in Cold Fusion Reaction, in 5th International Conference on Cold Fusion. 1995. Monte-Carlo, Monaco: IMRA Europe, Sophia Antipolis Cedex, France.

[7] Arata and Zhang, Anomalous difference between reaction energies generated within D2O-cell and H2O-cell, Jpn. J. Appl. Phys. **37** (1998)1274.

[8] Arata and Zhang, Observation of Anomalous Heat Release and Helium-4 Production from Highly Deuterated Fine Particles, Jpn. J. Appl. Phys. **38** (1999) 774.

[9] Y. Iwamura et al., Correlation between behavior of deuterium in palladium and occurrence of nuclear reactions observed by simultaneous measurement of excess heat and nuclear products, in Sixth International Conference on Cold Fusion, Progress in New Hydrogen Energy. 1996. Lake Toya, Hokkaido, Japan: Lake Toya, Hokkaido, Japan.

[10] Y. Iwamura et al., Detection of anomalous elements, x-ray, and excess heat in a D2-Pd system and its interpretation by the electron-induced nuclear reaction model, Fusion Technology, 33 (1998) 476.

[11] Yamaguchi, E. and T. Nishioka, Cold fusion induced by controlled out-diffusion of deuterons in palladium. Jpn. J. Appl. Phys. Part 2, **29**(4) (1990) 666.

[12] Yamaguchi, E. and T. Nishioka. Direct Evidence for Nuclear Fusion Reactions in Deuterated Palladium. in Third International Conference on Cold Fusion, “Frontiers of Cold Fusion”. 1992. Nagoya Japan: Universal Academy Press, Inc., Tokyo, Japan.

[13] Y. Iwamura et al., Elemental Analysis of Pd Complexes: Effects of D2 Gas Permeation, Jpn. J. App. Phys., **41** (2002) 4642.

[14] Y. Iwamura and T. Itoh et al., Observation of Low Energy Nuclear Transmutation Reactions Induced by Deuterium Permeation through Multilayer Pd and CaO thin Film, J. Condensed Matter Nucl. Sci. 4 (2011) 132–144.

[15] Y. Iwamura and T. Itoh et al., Transmutation reactions induced by deuterium permeation through nano-structured palladium multilayer thin film, Current Science, **108** (2015) 628.

[16] T. Hioki *et al.*, Inductively Coupled Plasma Mass Spectrometry Study on the Increase in the Amount of Pr Atoms for Cs-Ion-Implanted Pd/CaO Multilayer Complex with Deuterium Permeation, *Jpn. J. Appl. Phys.*, **52**, (2013)107301.

[17] A. Kitamura and A. Takahashi et al., Anomalous Effects in Charging of Pd Powders with High Density Hydrogen Isotopes, Physics Letters A 373 (2009) 3109.

[18] J. Kasagi et al., Energetic Protons and alpha Particles Emitted in 150-keV Deuteron Bombardment on Deuterated Ti. J. Phys. Soc. Japan, **64(3)** (1995) 777.

[19] J. Kasagi et al., Low Energy Nuclear Fusion Reactions in Solids. in 8th International Conference on Cold Fusion. 2000. Lerici (La Spezia), Italy: Italian Physical Society, Bologna, Italy

[20] J. Kasagi et al., Strongly Enhanced DD Fusion Reaction in Metals Observed for keV D+ Bombardment J. Phys. Soc. Jpn. 71(2002) 2881.

[21] A. Kitamura et al., D(d,p)T reaction rate enhancement in a mixed layer of Au and Pd, Proc. of ICCF10 (2003) 623.

[22] A. Kitamura et al., Excess heat evolution from nanocomposite samples under exposure to hydrogen isotope gases, *Int. J. of Hydrogen Energy* **43** (2018) 16187.

[23] Y. Iwamura et al., Anomalous heat effects induced by metal nano-composites and hydrogen gas, *J. Condensed Matter Nucl. Sci.* **29** (2019) 119.

[24] Y. Mori et al., New MHE Experiments by D-System, Proc. *Proceedings of the 22nd Meeting of Japan CF Research Society*, JCF22, March 5, 2022, Online Meeting, pp. 1–12.

[25] M. Hasegawa et al., Characteristics of Excess Thermal Power Generation in MHE Experiments by D System, *Proceedings of the 22nd Meeting of Japan CF Research Society*, JCF22, March 5, 2022, Online Meeting, pp. 13–26.

[26] A. Takahashi et al., Rising Characteristics of MHE Power with CNZ Material, *Proceedings of the 23rd Meeting of Japan CF Research Society*, JCF23, March 4-5, Waseda University, Tokyo Japan, pp. 124–130.

[27] T. Yamauchi et al., Detections of He-3 in Ni-based binary metal nanocomposites with Cu in zirconia exposed to hydrogen gas at elevated temperatures, Jpn. J. App. Phys., **64**, (2025) 017004.

[28] T. Kobayashi et al., Estimation of the Heat Generation of the Metal Composite Powder Absorbing the Pulsed Flow of Hydrogen Gas, *J. Condensed Matter Nucl. Sci.* **38** (2024) 96.

[29] T. Kobayashi et al., Temperature and pressure dependence of anomalous heat generation occurring in hydrogen gas absorption by metal powder,” J. Condensed Matter Nucl. Sci. **36** (2022) 318.

[30] T. Kobayashi et al., Development of reaction system with small chamber for fundamental experiments measuring anomalous heat effect," Proc. 20th Meeting of Japan CF Research Society JCF20, Fukuoka, pp. 1–8, 2019.

[31] K. Naitoh et al., Fundamental Experimental Tests toward Future Cold Fusion Engine Based on Point-compression due to Supermulti-jets Colliding with Pulse (Fusine), *J. Condensed Matter Nucl. Sci.*, **24** (2017) 236.

[32] M. Yanagidate et al., Heat measurement in hydrogen desorption experiment using Pd-Ni Sample, *Proceedings of the 23rd Meeting of Japan CF Research Society*, JCF23, March 4-5, 2023, Waseda University, Tokyo, Japan, pp. 148–160.

[33] S. Narita et al., Recent progress of deuterium/hydrogen desorption experiments using Pd-Ni samples, *Proceedings of the 22nd Meeting of Japan CF Research Society*, JCF22, March 5, 2022, Online Meeting, pp. 50–57.

[34] Y. Iwamura et al., Anomalous heat generation that cannot be explained by known chemical reactions produced by nano-structured multilayer metal composites and hydrogen gas, *Jpn. J. Appl. Phys*. **63** (2024) 037001.

[35] Y. Iwamura et al., Anomalous heat burst triggered by input power perturbations observed in Ni-based nanostructured thin films with hydrogen", *J. Condensed Matter Nucl. Sci.* **38** (2024) 269.

[36] Y. Iwamura et al., Progress in energy generation research using nano-metal with hydrogen/deuterium gas, *J. Condensed Matter Nucl. Sci.* **36** (2022) 285.

[37] Y. Iwamura et al., Excess energy generation using a nano-sized multilayer metal composite and hydrogen gas", *J. Condensed Matter Nucl. Sci.* **33** (2020) 1.

[38] J. Kasagi et al., Photon radiation calorimetry for anomalous heat generation in NiCu multilayer thin film during hydrogen gas desorption, J. Condensed Matter Nucl. Sci. **39** (2025) 210.

J. Condensed Matter Nucl. Sci. 41 (2026) 62–72

Research Article

Measurement of Radiant Spectrum for Excess Heat Generation in NiCu and Ni Thin Film During Hydrogen Gas Desorption

J. Kasagi, T. Itoh*

Research Center for Accelerator and Radioisotope Science, Tohoku University, Japan

Y. Shibasaki

Clean Planet Inc., Japan

Y. Iwamura

Yokohama City University, Japan

Abstract

Heat production in Ni-based thin films interacting with hydrogen gas was studied using a radiation calorimeter equipped with a composite photon-detector system. Measurements were performed on pure Ni foil and NiCu composite thin films. Electromagnetic radiation emitted from samples heated to approximately 1100 K in vacuum was recorded over the energy range of 0.05–2.5 eV. In this study, detailed spectra were obtained, particularly in the low-energy region below 0.5 eV. The peak of the thermal radiation spectrum was observed around 0.2 eV, deviating from that expected for simple gray-body radiation. Spectral variations depending on the presence or absence of hydrogen differed between the NiCu and pure Ni samples. The total radiated energy was determined directly from the measured radiation power, without relying on radiation models. The excess heat generated in the NiCu sample was estimated to be approximately 1.1 W. Comparable but slightly smaller excess heat generation was also observed in Ni. Long-term measurements of the NiCu sample demonstrated sustained excess heat production for at least 215 hours, with a decay time exceeding 2000 hours.

Keywords: Metal-Hydrogen system, NiCu multilayer film, H_2 gas desorption, Anomalous heat production, Radiant calorimetry, Radiation power spectrum.

1. Introduction

Much work on the phenomenon of anomalously large heat generation in metal–hydrogen (or deuterium) systems has been reported since the work of Fleischmann and Pons [1]. They observed excess heat during electrolysis of heavy

---

*T. Itoh: also affiliated with Yokohama City University water with a Pd cathode and claimed that the heat produced far exceeded the enthalpy of any chemical reaction and suggested that the underlying cause was the DD fusion reaction, i.e., “cold fusion.” Since then, various experimental approaches have been explored, including not only electrolysis, but also gas loading, ion implantation, and other methods.

In terms of metallic materials, a wide variety of forms have been tested, such as Pd, Ni, and Cu in the form of bulk metal, fine particles, amorphous powders, and nanostructured composite thin films [2], [3]. It is increasingly recognized that the anomalous heat generation may involve a process fundamentally different from conventional nuclear reactions. In particular, the emission of high-energy particles such as gamma rays and neutrons is rarely observed, with most of the released energy appearing as heat.

Since nanostructured composite metals have shown promise as heat-generating materials [4], we have been investigating anomalous heat generation phenomena in metal thin films for several years [5]–[7]. Our group has developed a method to induce large excess heat in composite NiCu thin films exposed to H_2 and D_2 gas. To obtain solid evidence for this heat production, we developed a radiation calorimetry technique. In our experiments, a thin metal film is placed in vacuum and heated to high temperatures [5], [6], where most of the heat transfer from the sample occurs via electromagnetic radiation. Accurate determination of the total heat flow therefore requires measurement of the radiation spectrum over a wide energy range.

In earlier measurements, three spectroscopic instruments with different energy ranges were employed to reconstruct the full spectrum by combining their data. However, in the range below 0.5 eV, only the average intensity between 0.2 and 0.4 eV was recorded, leaving the spectrum incomplete. To address this limitation, we recently incorporated a Fourier-transform infrared (FT-IR) spectrometer, which covers a much broader wavelength region from the far-IR to the near-IR, corresponding to photon energies from 0.004 eV to 0.93 eV.

Obtaining the complete radiation spectrum, including the low-energy region below 0.5 eV, allows us to analyze the data without relying on the previously used gray-body radiation approximation, thereby enabling a more model-independent and quantitatively reliable determination of the generated energy.

2. Detection System for Photon Radiation From Metal Thin Film; BREMS

Figure 1 shows a simplified cross-sectional view of the entire setup, seen from above. The detection system, which we call BREMS (Broad Range ElectroMagnetic wave detection System), consists of a newly introduced FT-IR spectrometer and four previously employed spectrometers. Each detector is directed toward a sample placed at the center of the vacuum chamber. Two thin-film samples are mounted on either side of a ceramic heater suspended from the chamber lid.

The newly installed spectrometer, referred to as FT-IR, is shown on the right side of Fig. 1. It is a Fourier transform spectrometer (INVENIO R, Bruker) that covers the energy range from 0.043 eV to 0.93 eV (wavelength 28.5 – 1.33 μm) in MIR mode and from 0.004 eV to 0.084 eV (wavelength 325 – 14.8 μm) in FIR mode. Photons emitted from the sample enter the FT-IR through a diamond window located 20 cm from the sample, passing through a 10-mm diameter aperture that selects parallel rays. To avoid absorption by H_2O and CO_2 molecules, nitrogen gas is continuously supplied inside the FT-IR, displacing the air.

On the opposite side of the chamber, a SiO2 window transmits photons from the near-IR to the UV range. These photons pass through a focusing lens and are guided into an optical fiber, which is split between two spectrometers; NIR, an FT spectrometer (Hamamatsu C15511) covering 0.5 – 1.13 eV (1.5–2.5 μm), and VL (Visible Light), a multichannel spectrometer (Hamamatsu C10027) covering 1.3 – 4.1 eV (0.3–0.9 μm).

For improved statistical accuracy, all three spectrometers output the average radiant power from multiple scans as a function of wavelength or wavenumber. The acquisition times are $\sim$30 s for NIR, $\sim$50 s for VL, and $\sim$60 s for FT-IR. Photon collection is restricted to within $\sim$10-mm from the sample center.

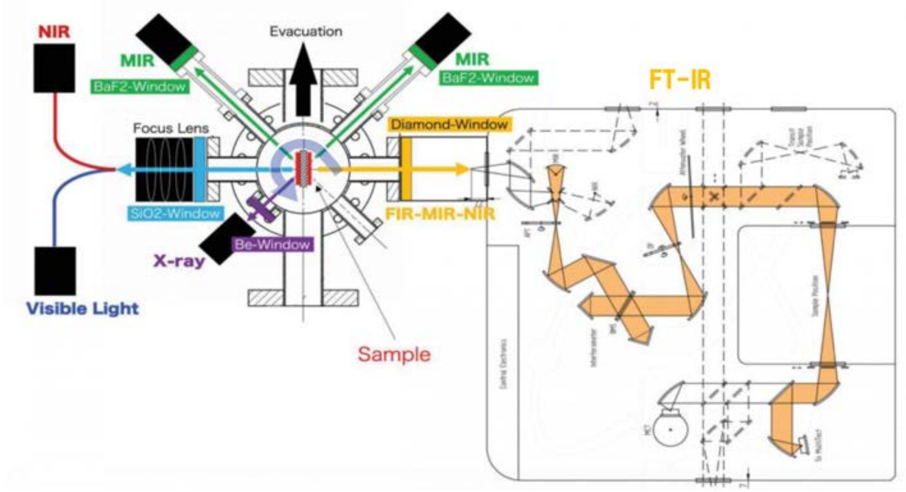

Figure 1. BREMS: Broad Range ElectroMagnetic wave detection System. Cross-sectional view of entire equipment is shown. Photons emitted from the sample, placed at the center of a vacuum chamber, are observed by 5 types of detectors for different energies; FT-IR for 0.043 – 0.93 eV, MIR for 0.21 – 0.41 eV, NIR for 0.5 –1.13 eV, VL (Visible Light) for 1.3 – 4.1 eV and X-ray for larger than 1 keV.

In addition to these two main windows, the vacuum chamber has four auxiliary windows, each at a 60-degree angle to the axis connecting the center of the two windows. Two of them are extended via vacuum pipes to a $\mathrm{BaF_2}$ window 40 cm from the chamber center, and a mid-infrared radiation thermometer (MIR) is installed. The MIR has a nearly constant sensitivity in the 0.21 - 0.41 eV range (3 - 5.5 μm). It is used here as a radiation intensity meter rather than a thermometer. Although it does not provide spectral resolution, it offers two advantages: it covers a relatively wide energy region near the maximum radiation intensity and has a fast time response (< 1 s). Thus, in long-term measurements, it is particularly useful for monitoring radiation power from both sides of the sample simultaneously at intervals as short as 1 s.

Furthermore, X-rays are detected by a silicon drift detector (SDD, Amptek XR-100) positioned outside a Be window, which can measure X-rays down to 1 keV.

Among all the instruments, the FT-IR spectrometer plays the central role in quantitative determination of radiant power, since it covers most of the broad peak region and enables model-free estimation of heat flow. The NIR and VL spectrometers complement this by providing spectral information at higher photon energies, which is essential for deducing the radiation temperature. As shown in Fig. 1, when the FT-IR faces the side-A sample, the NIR/VL spectrometers face the side-B sample. To obtain the whole spectrum, we first measure side A with FT-IR (and side B with NIR/VL), then rotate the sample 180° and repeat the measurement. The spectra from both sides are combined and treated as the total emission from the sample.

Calibration of the FT-IR, NIR, and VL spectrometers was performed using radiation from carbon nanotubes, which act as blackbody radiators. Details are provided in the Appendix.

3. Experimental Procedure

Two types of samples were investigated in the present study:

(1) NiCu sample: Six bilayers of Cu (3.8 nm) and Ni (20 nm) were alternately deposited on a Ni substrate by magnetron sputtering.

(2) pure Ni sample: The Ni substrate used for (1), consisting of 99.9%-purity Ni foil, 0.1 mm thick, with an area of 25 × 25 mm^2. Details of the NiCu sample preparation are provided in Ref. [5], [6].

Each sample thin film was attached to both sides (A and B) of a ceramic heater equipped with an R-type thermocouple. On each side, a 0.3-mm-thick Photoveel plate was placed between the heater and the sample thin film. This was further covered by two Photoveel plates (35 × 35 mm) with a central 20 mm square cutout, and fixed to a holder frame suspended from the chamber lid. Heater power and thermocouple signals were supplied through airtight feedthroughs.

After mounting, the sample was baked in vacuum for three days at $\sim$1150 K and at pressures below 3×10^{-6} Pa.

Base-line measurements: Before introducing H_2 gas, radiation from the sample was measured to obtain baseline spectra without anomalous heat generation. The heater input voltage was varied as V_{in} = 36, 38, 40, 41, and 42 V. Because equilibrium between input power and radiated power required some time, spectra were recorded 1.0 h and at least 4.0 h after setting each voltage. The measurements were repeated for two cycles of V_{in}. These data served to calibrate the radiative power corresponding to zero excess heat.

Excess power measurements: Radiant power during hydrogen desorption was then measured while evacuating the chamber, i.e., during release of absorbed H_2 from the sample. The following sequence was repeated three times for the NiCu sample and twice for the pure Ni sample at V_{in} = 38, 40, and 42 V:

(1) Hydrogen absorption: The chamber was filled with H_2 gas to 200–300 Pa, and V_{in} was set to 28 V, giving a heater temperature $T_C \approx$ 570 K. This condition was maintained for 12–15 h (overnight) without replenishing H_2 gas.

(2) Desorption and radiation measurement: The chamber was evacuated while *Vin* was set to the target value. Full spectra were measured at $\sim$0.5, 2.5, 4.0, and 6.0 h after evacuation. During these intervals, FT-IR continuously monitored the side-A sample, while NIR/VL monitored the side-B sample, with measurements taken every 5 min.

Long-term measurement: After completing the above cycles, a long-term measurement was performed for the NiCu sample at V_{in} = 40 V without hydrogen refilling. In this run, full spectra were not acquired; instead, both side-A and side-B configurations were fixed, and data were recorded for over 200 h. Each detector acquired data every 5 min.

Throughout all measurements, a data logger continuously recorded (at 1 s intervals) the following experimental parameters: heater temperature T_C, MIR outputs from sides A and B, heater voltage V_{in}, heater current I_{in}, chamber pressure, and outer wall temperature.

4. Results and Discussion

4.1. Radiant Spectrum

Figure 2 presents a typical example of thermal radiation emitted from the NiCu sample during H_2 desorption.

Figure 2(a) shows the whole spectrum obtained approximately 6 hours after evacuation at V_{in} = 40 V, with all detector data overlaid. The blue dots represent FT-IR data, while the red dots denote results from the other detectors. The spectral region between 0.2 and 0.8 eV is covered by both FT-IR and MIR/NIR, and the excellent agreement between them is evident from the near-complete overlap. The red curve corresponds to a gray-body fit to the red data points. Below 0.2 eV, however, the observed radiation clearly exceeds the gray-body prediction—a region not

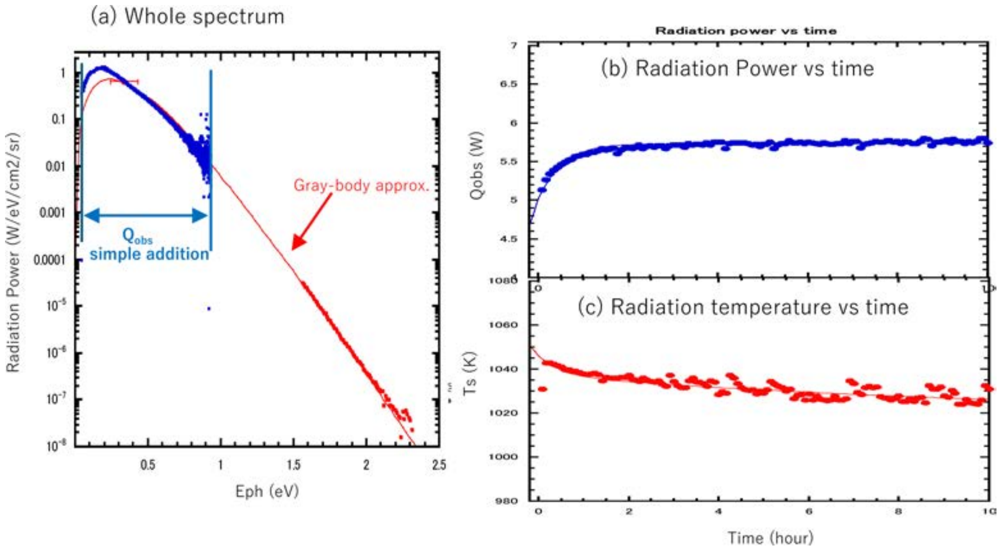

Figure 2. Observed radiation characteristics from the NiCu sample heated up about 1000K. (a) Whole spectrum: overlaid of FT-IR, NIR, VL and MIR spectra. (b) Time dependence of observed radiation power Q_{obs}. (c) Time dependence of radiation temperature T_S.

accessible in our previous measurements. This result demonstrates that the total radiation power estimated by the gray-body approximation in Ref. [7] must be revised. In the following analyses, the radiation power is evaluated by integrating the experimental FT-IR spectra over the energy range indicated by the arrows in Fig. 2(a).

Figure 2(b) plots the integrated radiation power in this range as a function of time. Since the FT-IR monitors only the A-side sample, the values correspond to approximately half of the total emission. Because most of the radiation originates from the heater, the gradual rise reflects the equilibration process between heater input and radiative output. The increase is well described by a time constant of about 0.7 h.

Figure 2(c) shows the radiation temperature T_S, obtained by fitting the red data in Fig. 2(a) with the gray-body model, as a function of time. Unlike the radiation intensity, T_S rises rapidly and then decreases slowly. Two decay constants, a fast component ($\sim$3 h) and a slow component ($\sim$80 h), are required to reproduce the observed behavior.

The contrasting time dependences of radiative power and sample temperature indicate that the gray-body assumption, which relates radiation power to the fourth power of temperature, does not hold. The heater temperature T_C exceeds T_S by $\sim$100 K and shows a similar time dependence, suggesting that variations in heat flow cannot be captured solely by monitoring either T_C or T_S.

4.2. Comparison of Spectra With and Without H_2

Figures 3 and 4 compare radiation spectra obtained with and without hydrogen for the NiCu and pure Ni samples, respectively, both measured at V_{in} = 40 V.

In Figs. 3(a) and 4(a), the black circles denote spectra without H_2, and the red circles those with H_2. Black and red curves represent gray-body fits to the MIR, FIR, and VL data. The derived T_S values are 1020 K (NiCu) and 1020 K (Ni) with H_2, compared with 990 K (NiCu) and 1010 K (Ni) without H_2. Thus, both samples exhibit higher radiation temperatures in the presence of hydrogen, with the increase ΔT being larger for NiCu (ΔT = 30 K) than for pure Ni (ΔT = 10 K).

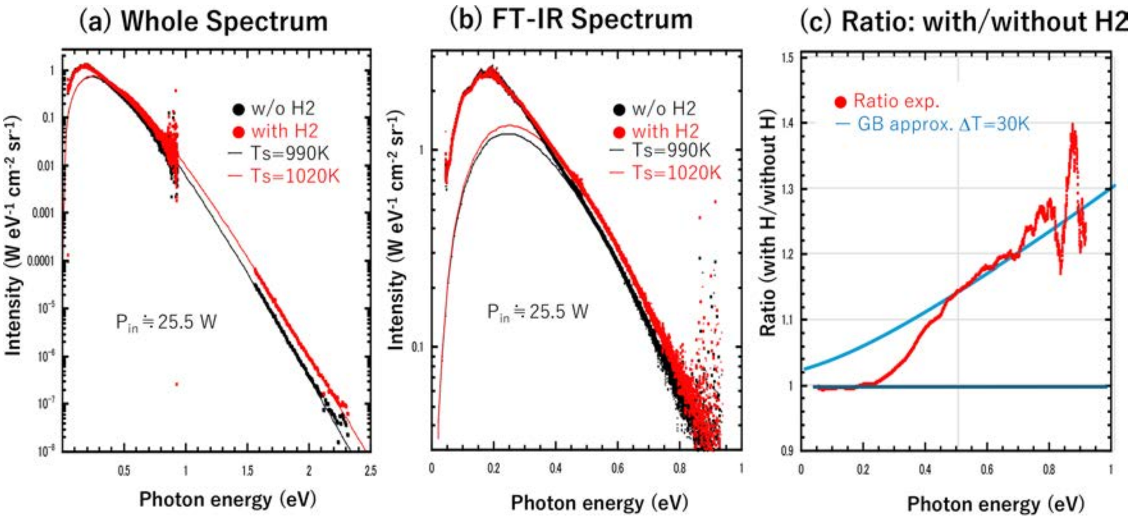

Figure 3. Comparison of radiation intensity for the NiCu sample with and without H_2. (a) Comparison of the whole spectrum. Red circles indicate measurements with hydrogen, and black circles indicate measurements without hydrogen. The red and black lines are calculated for corresponding data by fitting the MIR, NIR, and VL data with a gray-body radiation model. (b) Comparison of only the FT-IR spectrum. (c) Ratio of intensity with hydrogen divided by intensity without hydrogen. Red circles indicate experimental values, and the blue line is the gray-body radiation calculation.

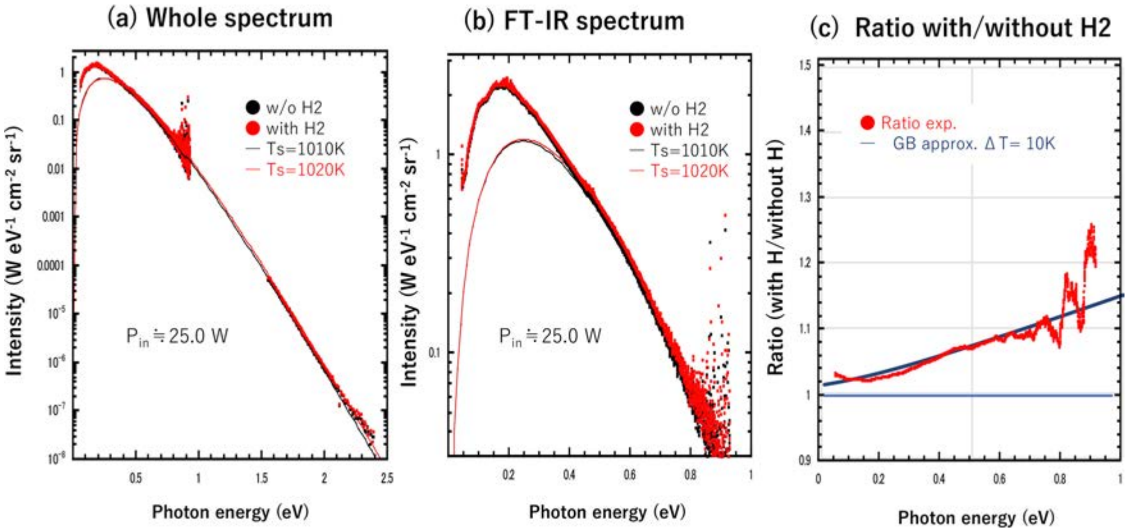

Figure 4. Same as Figure 3, but for pure Ni sample.

Figs. 3(b) and 4(b) compare the FT-IR spectra directly. As noted in Sec. 4.1, the gray-body approximation reproduces the experimental data above 0.5 eV but underestimates the radiation below 0.4 eV. The observed intensity peaks at 0.15–0.2 eV, whereas the gray-body model predicts a maximum around 0.25 eV. In NiCu (Fig. 3), the spectrum with

H_2 is clearly enhanced relative to that without H_2 for photon energy larger than 0.4 eV, but no enhancement below 0.3 eV.

Figs. 3(c) and 4(c) display the ratio of the spectra with H_2 to those without H_2. Red circles show the experimental results averaged over 0.024 eV bins to reduce statistical noise, and the blue lines are gray-body ratios calculated for the corresponding temperature increases. For NiCu, the ratio remains near unity below 0.2 eV, but increases rapidly between 0.2 and 0.4 eV. The gray-body model reproduces the data only above 0.4 eV. Since radiation above 0.5 eV contributes less than 10% of the total power, this discrepancy indicates that the gray-body model overestimates the total emission. In contrast, for pure Ni, the ratio increases monotonically with energy, consistent with a modest 10 K temperature rise predicted by the gray-body model.

The observed radiation Q_{obs} is defined as the FT-IR spectral integral from 0.05 to 0.85 eV multiplied by the angular factor $\pi/2$. For NiCu, the ratio of Q_{obs} with and without H_2 is $\sim$1.04, reflecting strong suppression of radiation below 0.4 eV. For pure Ni, where such suppression is absent, the ratio is larger. These results highlight that quantitative heat-flow evaluation without spectral information can be misleading when the radiative properties change upon hydrogen absorption.

4.3. Evaluation of Excess Power

The excess thermal power is evaluated from Q_{obs} using the heat-flow model of [7]. Two heat sources are considered: heater input P_{in} and sample-generated excess heat Q_{ex}. Heat from the heater flows through the insulating spacer (thermal resistance R_C) to the sample, where it combines with Q_{ex} to yield the total heat flow Q_{tot}. Most of Q_{tot} is dissipated as radiation from the sample (Q_{obs}) and from the holder (Q_H), connected through another resistance R_{SH}. Conductive losses through the supporting rod and reflected radiation are negligible (< 0.08 W). At thermal equilibrium:

$$Q_{tot} = P_{in} + Q_{ex} = Q_{obs} + Q_H = Q_{obs}\,(1 + \frac{Q_H}{Q_{obs}}). \tag{1}$$

This shows that Q_{tot} can be deduced from Q_{obs}, if the ratio of Q_H / Q_{obs} is known. The measurement without H_2 can give the relationship between Q_H and Q_S because of null Q_{ex}.

Figure 5(a) shows Q_H as a function of Q_{obs}, where values of Q_H are obtained from P_{in} – Q_{obs}. Blue circles represent the data for the NiCu sample, and the black circles represent the data for the pure Ni sample. It seems that Q_H increases at a constant rate as Q_{obs} increases. Blue lines in Fig. 5(a) are the results of applying a linear function, $Q_H = a\, Q_S + b$, to each data set. The best fit gives $a = 3.584$ and $b = 0.933$ for the NiCu sample and $a = 2.807$ and $b = 1.071$ for the pure Ni sample. However, this form does not satisfy the condition $Q_H = 0$ at $Q_S = 0$.

Red lines are the best fits when applying the power function, $Q_H = A\, Q_S^m$, which is effective as an approximation function for Q_H for the thermal radiation intensity being proportional to the fourth power of the temperature. The linearity in the measured region is reproduced with the exponential parameter m being 0.72 < m < 0.76 for the NiCu sample and 0.77 < m < 0.81 for the pure Ni sample. Nevertheless, within the observed range, the linear approximation is sufficiently accurate and was adopted for further analysis:

$$Q_{tot} = \alpha + \beta\, Q_{obs} \tag{2}$$

$$Q_{ex} = Q_{tot} - P_{in} \tag{3}$$

with $\alpha = 3.584$ and $\beta = 1.933$ for the NiCu sample and $\alpha = 2.807$ and $\beta = 2.071$ for the pure Ni sample.

Control tests confirmed that the holder material (Photoveel) does not absorb hydrogen, and its radiation spectrum remained unchanged (< 0.2% difference). Therefore, Eqs. (2) and (3) were used to determine Q_{ex}.

Figure 5(b) shows Q_{ex} as a function of P_{in}. Red and green circles denote data with H_2 for the NiCu and pure Ni sample, respectively, while blue and black circles denote the corresponding data without H_2. All values were obtained

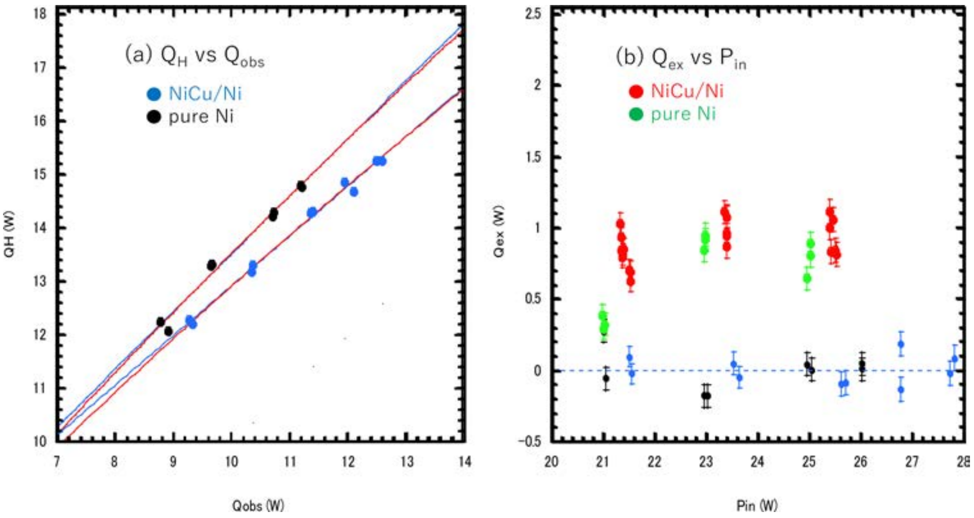

Figure 5. (a) Radiation power emitted from the sample holder Q_H as a function of observed radiation power Q_{obs}. Blue circles are obtained for the NiCu sample, and black ones for the pure Ni sample. (b) Excess power Q_{ex} plotted as a function of heater input power P_{in}. Red circles are obtained for the NiCu sample and green circles are for the pure Ni sample. Data used in the calibration are also shown as blue and black circles.

at least four hours after voltage setting, ensuring thermal equilibrium. The typical uncertainty in Q_{ex} is $\sim$0.08 W (1σ). The results clearly show excess power of $\sim$1 W: $Q_{ex} \approx 1.1$ W for the NiCu sample at $P_{in} > 21$ W and just under 1 W for the pure Ni sample at $P_{in} > 23$ W.

Compared with our earlier report [7], two important differences emerge: (i) the excess power for NiCu is much smaller than previously reported, and (ii) a clear excess is observed for pure Ni. While sample-to-sample variation cannot be excluded, the present inclusion of spectral data below 0.5 eV provides a more accurate evaluation of excess heat. In NiCu, radiation below 0.3 eV is not enhanced by the presence of H_2, whereas for Ni no such suppression is observed.

4.4. Long Term Measurement

Figure 6 shows long-term data for NiCu acquired at V_{in} = 40 V over 215 h, with spectra collected every 5 min without replenishing hydrogen. Because only one side of the sample was monitored, the Q_{ex} values exhibit larger fluctuations than in Fig. 5(b).

The radiation rises to $\sim$1.2 W after $\sim$10 h and then decays gradually—initially faster, and more slowly after $\sim$150 h. We attribute this decrease to depletion of hydrogen fuel within the sample. The time dependence is expressed as:

$$Q_{ex}(t) = \quad (a - b\exp\left(-\frac{t}{\tau_{eq}}\right)) \times (A_F \exp\left(-\frac{t}{\tau_F}\right) + A_S\, exp(-\frac{t}{\tau_S}))^2. \tag{4}$$

The first bracket corresponds to the increase in radiation intensity up to thermal equilibrium, with its time constant τ_{eq}. The second bracket corresponds to the decrease in H density, with the fast decay time constant τ_F and the slow decay time constant τ_S. Here, we assume that two H atoms are involved in a reaction, and, thus, the reaction rate is the square of the density (although in this case the exponential decay function is an approximation).

The red curve in Fig. 6 shows a fit with a = 0.93, b = 0.46, τ_{eq} = 5.0, A_F = 0.2, τ_F = 90, A_S = 1.0, and τ_S = 2500. The fit reproduces the data well, and extrapolation suggests energy production could continue for $\sim$4000 h

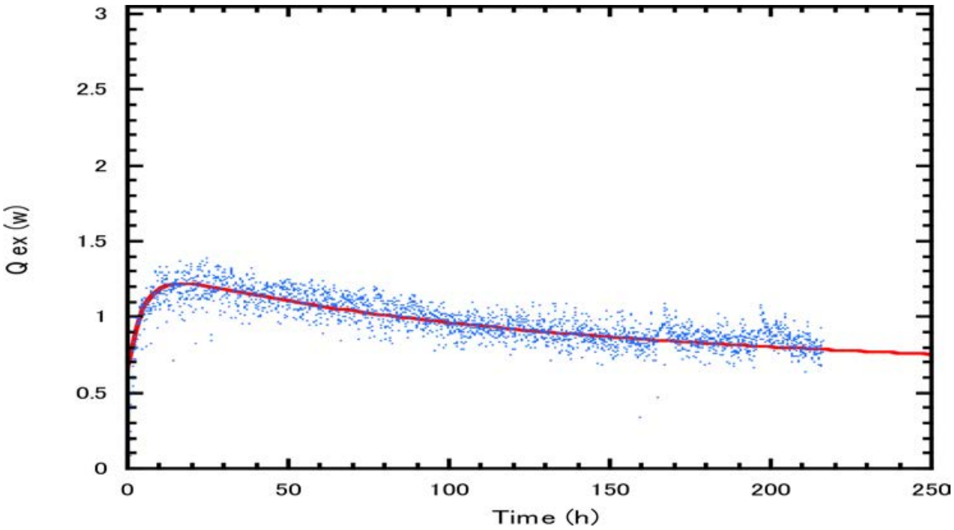

Figure 6. Excess power Q_{ex} as a function of time *t*. The blue dots are data from measurements taken every 5 minutes for 215 hours on one side of the sample. The red line is the calculated value using equation (4).

until hydrogen is exhausted. The integrated output is 4.26 MJ. The absorbed hydrogen was measured prior to the run, with an upper limit of 1×10^{-4} mol. Assuming full participation, the minimum specific energy is *E*/H > 22 keV per hydrogen atom—5 orders of magnitude greater than any chemical process. The actual value must be much higher, as most absorbed hydrogen is lost by thermal diffusion and thus cannot contribute to the reaction.

5. Conclusions

The present experiment, which expanded the energy range for spectroscopic measurement of radiation, revealed the following findings:

Thermal radiation spectra of both the NiCu composite and pure Ni samples deviate significantly from that of simple gray-body radiation. Unlike the gray-body calculation, where intensity decreases below 0.3 eV, the observed spectra exhibited a continued rise, with a peak at around 0.2 eV.

In the presence of hydrogen, both samples showed an increase in radiation power by several percent, but with distinct spectral features. For the NiCu sample, little enhancement was observed below 0.3 eV, whereas a sharp increase appeared above 0.35 eV. In contrast, the pure Ni sample exhibited a gradual enhancement starting from as low as 0.05 eV.

The total radiation output was determined directly from the observed spectra, without reliance on a gray-body radiation model. The excess heat generation in the NiCu sample was estimated to be approximately 1.1 W, while the pure Ni sample exhibited a slightly lower value.

Long-term measurements over 215 hours demonstrated that excess power generation can persist for extended periods, with a decay time exceeding 2000 hours. The energy released per absorbed hydrogen atom was estimated to exceed 22 keV.

While these results strongly support the occurrence of anomalous heat generation, the measurement of excess energy alone is insufficient to establish whether the origin lies in a novel nuclear process. To provide conclusive evidence, signatures of nuclear reactions must be identified, such as residual nuclei, nuclear γ-rays, high-energy charged

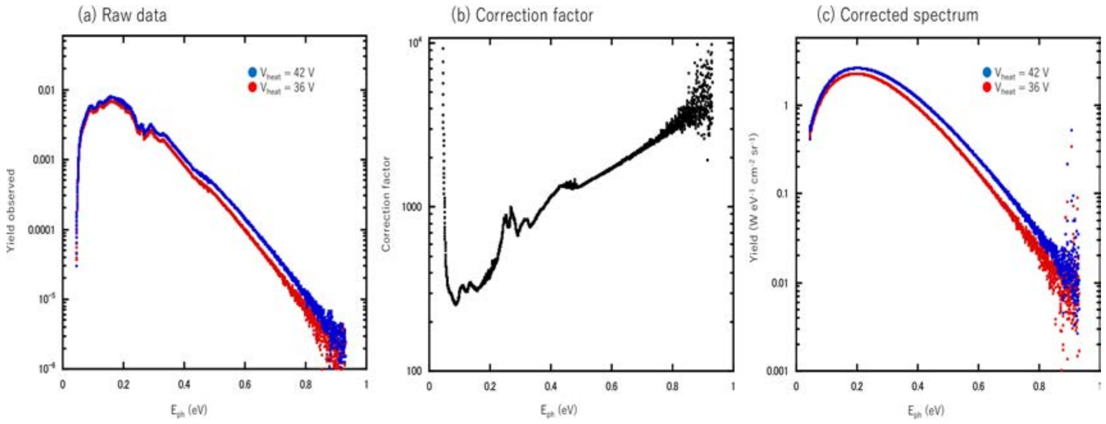

Figure 7. FT-IR detector calibration. (a) Two examples of raw spectra, measured at heater input voltages of 36V (red circle) and 42V (blue circle). (b) Calibration curve obtained using data measured for five different heater input. (c) Calibrated spectrum corresponding to the raw data in (a).

particles, or characteristic X-rays from sample atoms. The advantage of the present experimental system lies in its capability to simultaneously monitor various electromagnetic radiations together with excess heat, offering a powerful tool for further investigation into the nature of this anomalous phenomenon.

Acknowledgements

This work is supported by Clean Planet Inc., and The Thermal & Electric Energy Technology Foundation.

Appendix

The intensity calibration of the three spectrometers, FT-IR, NIR and VL, was performed by setting two sheets of carbon nanotube (CNT) at the sample positions. Since the emissivity of CNT is more than 0.98, the radiation is treated as blackbody radiation; the error due to this is less than 0.3% in the analysis. The blackbody radiation power B_{black} is expressed for the photon with the energy E_{ph} emitted from the surface with the temperature of T as

$$B_{black}(E_{ph},\,T) = \frac{a_1\,E_{ph}^3}{\exp\left(a_2\frac{E_{ph}}{T}\right) - 1}[\mathrm{W\ cm^{-2}\ sr^{-1}\ eV^{-1}}], \tag{A1}$$

where $a_1 = 5.07\times10^3$ [W cm^{-2} sr^{-1} eV^{-4}] and $a_2 = 1.16\times10^4$ [K eV^{-1}].

In the CNT measurement, T is measured as T_{MIR}, the temperature output of the MIR detector with emissivity 1.0. Using this temperature, the absolute intensity of the radiant power is calculated and compared with the measured raw spectrum to obtain a correction factor for each photon energy. For the detectors, FT-IR, NIR and VL, the correction factor $F(E_{ph})$ is determined as

$$F(E_{ph}) = \frac{B_{black}(E_{ph}, T)}{Y_{raw}(E_{ph}, T)}, \tag{A2}$$

where Y_{raw} (E_{ph},T) is a raw yield measured for CNT with temperature T. Since the correction should depends only on E_{ph}, the correction factor finally used is an average of several measurements taken at different temperatures.

The correction includes all the effects; absorption due to the window material and fiber cable, the detection efficiency of the photosensor, and the solid angle of the detection.

As an example of the calibration of the FT-IR detector, we show two spectra in Fig. 7: the raw data at two different temperatures (Fig. 7(a)), the calibration curve obtained using data at five different temperatures (Fig. 7(b)), and the calibrated spectrum (Fig. 7(c)).

References

[1] M. Fleischmann and S. Pons, J. Electroanal. Chem. 261 (1989) 301.
[2] E. Storms, Naturwissenschaften, 97, 861 (2010).
[3] L.O. Freire, D.A.d. Andrade, J. Electroanal. Chem. 903, 115871 (2021).
[4] A. Kitamura, et al., Phys. Lett. A373 (2009) 3109; Int. J. of Hydrogen Energy 43 (2018) 16187.
[5] Y. Iwamura, et al., J. Condensed Matter Nucl. Sci. 33 (2020) 1; ibid., 36 (2022) 285.
[6] T. Itoh et al, J. Condensed Matter Nucl. Sci. 36 (2022) 274.
[7] J. Kasagi et al., arXiv: 2311.18347, J. Condensed Matter Nucl. Sci. 39 (2025) 210–219.

J. Condensed Matter Nucl. Sci. 41 (2026) 73–83

Research Article

Heat Measurement in Hydrogen Absorption into Metal Composite Powder and Thin Films

Tomoki Kawarada, Takuya Kitabayashi, Tomo Nemoto, Saaya Sasaki,
Youichi Takeda, Aiko Shoji, Shinya Narita
Iwate University, Morioka 020-8551 Japan

Abstract

Recent studies have reported excess heat generation during hydrogen absorption–desorption cycles in Cu–Ni composite metals. It has also been suggested that laser irradiation of the sample can enhance the reactions of hydrogen within metals. Considering these findings, we investigated the thermal behavior of hydrogen-loaded Cu–Ni alloys supported on zirconia (CNZ). In absorption experiments with a heater input of 50 W, maximum excess heat of 16 W was observed. Furthermore, when laser irradiation at a wavelength of 793 nm with an output power of 1–6325 mW was applied to the CNZ sample, the excess heat calculated from the sample temperature was positive, whereas that derived from the gas temperature was negative. In addition, hydrogen desorption experiments using Pd–Ni multilayers deposited on a zirconia substrate were carried out. The results showed that excess heat occasionally became negative depending on the heater power, indicating poor reproducibility.

Keywords: H2-gas, Laser irradiation, Cold fusion, Thin films, Powder

---

1. Introduction

In a study of low-energy nuclear reactions in condensed matter, hydrogen absorption in copper-nickel powder with zirconia as the support (CNZ) has been reported to generate excess heat 100–1000 times higher than that expected from the most energy dense chemical reaction [1]–[4]. This suggests new physical phenomena that cannot be explained by the reaction processes in conventional metal–hydrogen systems. In this study, experiments were conducted to confirm the reproducibility of this heat generation phenomenon in a CNZ sample.

Nuclear transmutation has also been reported to occur under laser irradiation [5], [6]. We performed a hydrogen loading experiment on the sample using a laser with a wavelength of 793 nm and varied its output power within the range of 1–6325 mW.

In addition to powder samples, exothermic phenomena in hydrogen absorption and desorption have also been reported for composite metal thin film samples [7]–[10]. Therefore, we are currently performing experiments using composite thin film samples. In this paper, we report the heat generation results for a palladium-nickel multilayer sample deposited onto a zirconia plate.

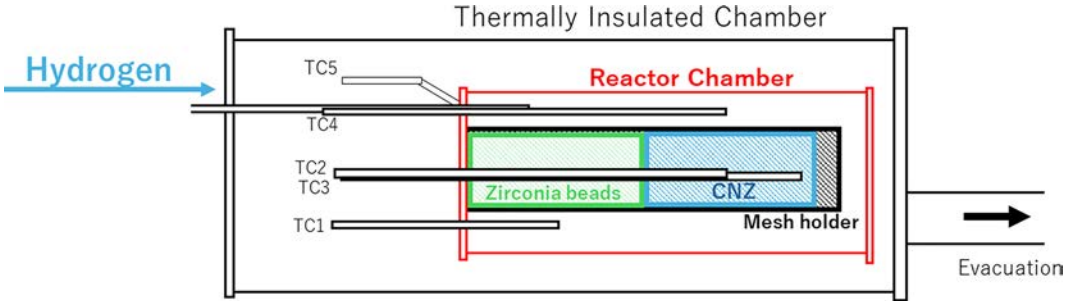

Figure 1. Schematic of experimental setup.

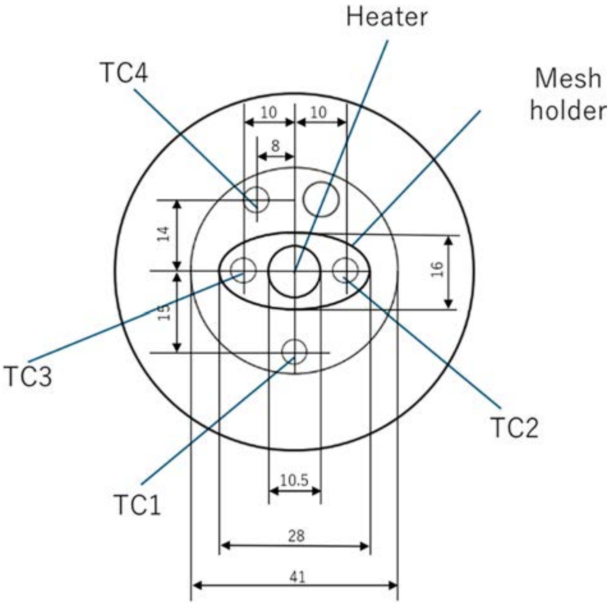

Figure 2. Cross-sectional view of the reactor chamber.

2. Experiment

2.1. Absorption Experiment in CNZ

2.1.1. *Sample*

The sample consisted of a copper–nickel powder supported on zirconia, with a molar ratio of Cu:Ni:ZrO_2 = 1:7:14 with reference to previous studies and a particle size in the range of 75–125 μm. In addition, a reference experiment was conducted using zirconia beads with a particle diameter of 1 mm. In the experiment, 90.5 g of zirconia beads and 61.5 g of the CNZ sample were used, and the lengths when loaded into the mesh holder were approximately 8 cm each.

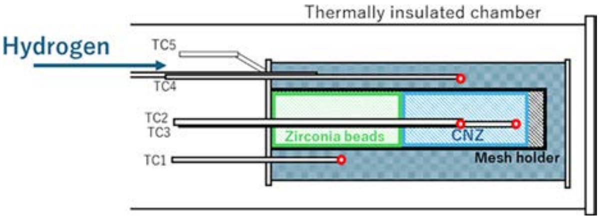

Figure 3. Temperature measurement points.

Table 1. TC positions.

TC1	Hydrogen gas temperature
TC2	Center temperature of CNZ
TC3	Edge area temperature of CNZ
TC4	Hydrogen gas temperature

2.1.2. *Experimental Method*

Figure 1 shows a schematic of experimental setup, and Fig. 2 presents a cross-sectional view of the reactor chamber together with its dimensions. After setting the CNZ and zirconia beads such that the CNZ was positioned at the edge area of the mesh holder (Fig. 2). The outer and reactor chambers were evacuated using a scroll pump to a pressure of a few pascals. The outer chamber served to thermally insulate the system from the surrounding environment Hydrogen was supplied to the reactor chamber at a pressure of 1.6 atm. Subsequently, 50–80 W of constant power was supplied to the heater, and the sample was heated for 6 h. Four thermocouples were installed in the inner chamber to measure the sample and gas temperatures at various locations throughout the experiment (Fig. 3, Table 1). For reference, we performed an experiment using zirconia beads, which do not absorb hydrogen. Subsequently, the heat generated because of hydrogen absorption in the CNZ sample was evaluated by comparing its thermal behavior with that of the zirconia beads.

2.1.3. *Excess Heat Calculation*

Excess heat was estimated from the difference between the temperatures observed in the reference and absorption experiments. The evaluation method was as follows.

1. Plot the temperatures at each heater input in the reference experiment.
2. Fit the data with a quadratic function.
3. Derive the differential coefficient from the fitting curve (y' = dT/dW).
4. Obtain a calibration factor ($k = 1/y'$) from Step 3.
5. Calculate excess heat as $W_{\mathrm{ex}} = k(T_1 - T_0)$.

In Step 5, T_0 denotes the temperature in the reference experiment, and T_1 denotes the temperature in the hydrogen absorption experiment.

2.1.4. *Results and Discussion*

Figure 4 shows the results of the hydrogen absorption experiment conducted with 50 W of heater input. Based on these results, the reduced temperature gradient observed during the initial phase (0.8–2.0 h) was associated with an endother-

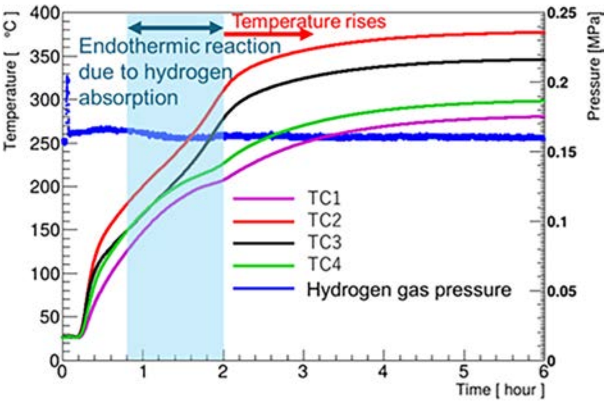

Figure 4. Time dependence of sample temperature and pressure of absorption experiments with a 50 W heater input.

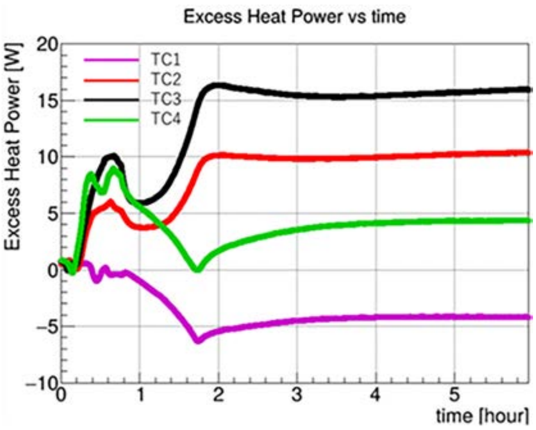

Figure 5. Time dependence of the excess heat with a 50 W heater input.

mic process resulting from the hydrogen absorption into nickel. In contrast, the subsequent temperature increases in the later phase (2.0–6.0 h) suggest the emergence of an anomalous heat effect, indicating a possible transition from hydrogen uptake to heat-generating reactions within the sample.

The results of the absorption and reference experiments with an 80 W heater input are presented in Figures 6 and 7, respectively. The observed temperature differences for each thermocouple were –4.25 °C (TC1), 26.25 °C (TC2), 36.15 °C (TC3), and 8.10 °C (TC4).

The results for excess heat with 50 W of heater input are shown in Fig. 5. The values of excess heat at the end were –4 W for the first thermocouple (TC1), 10 W for TC2, 16 W for TC3, and 4 W for TC4. In this experiment, a negative excess heat signal was observed at TC1, although the cause remains unclear. In contrast, positive excess heat appeared at the other thermocouples. The experiments conducted using the same sample under varying heater inputs over a total of 90 h consistently exhibited excess heat in all cases.

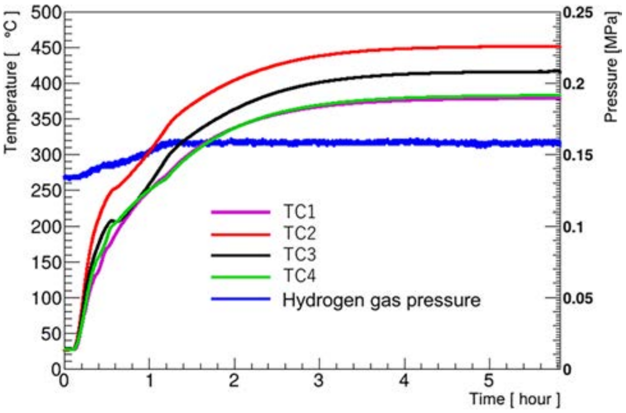

Figure 6. Time dependence of sample temperature and pressure of absorption experiments with an 80 W heater input.

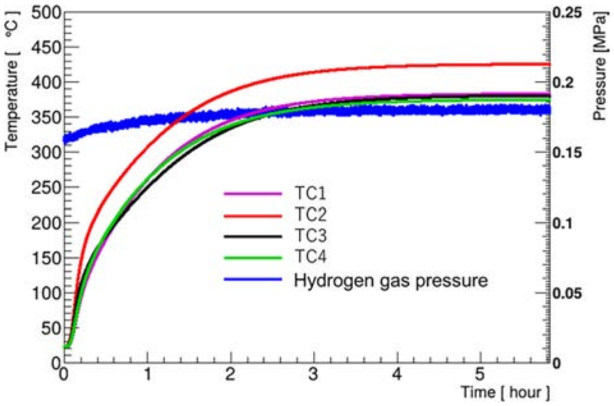

Figure 7. Time dependence of sample temperature and pressure of reference experiments with an 80 W heater input.

Figures 8 and 9 show the relationship between heater input and excess heat at the conclusion of the 6-hour experiment. For the heater input ranges of 50 - 80 W, the excess heat tends to increase with higher input power. This trend suggests that the amount of excess heat may be influenced by the level of energy supplied to the system.

2.2. Laser Irradiation Experiment

2.2.1. *Sample*

As in Section 2.1.1 (Sample), the sample consisted of a copper–nickel powder supported on zirconia, with a molar ratio of Cu:Ni:ZrO_2 = 1:7:14 and particle size in the range of 75 - 125 μm. In addition, a reference experiment was conducted using zirconia beads with a particle diameter of 1 mm.

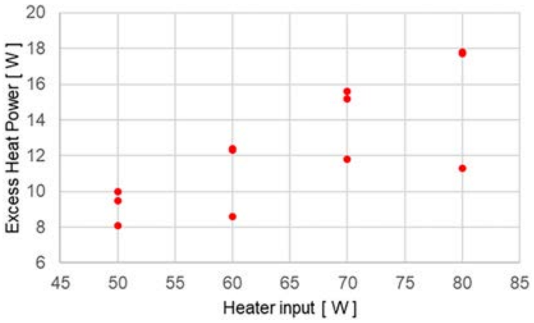

Figure 8. Dependence of excess heat (TC2) on heater input.

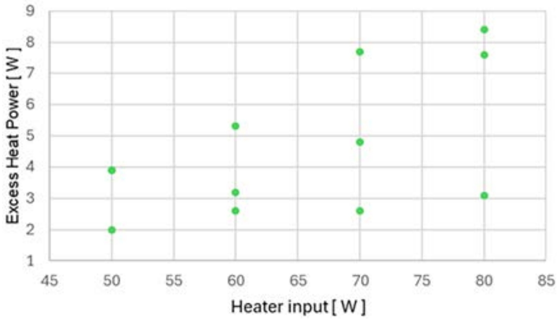

Figure 9. Dependence of excess heat (TC4) on heater input.

2.2.2. *Experimental Method*

A schematic of the laser experiment is shown in Fig. 10. The laser had a wavelength of 793 nm, with the output power set within the range of 1 - 6325 mW. The irradiation was directed toward the vicinity of thermocouple TC2. In this experiment, a 9-hour hydrogen absorption test was conducted under a heater input of 50 W, with laser irradiation applied during the final 3 h.

2.2.3. *Results and Discussion*

Figure 11 shows the result of laser irradiation at 6325 mW. A temperature increase of 28 °C was observed at TC2, which was positioned near the spot irradiated by the laser. The results of the laser irradiation from the reference test are shown in Fig. 12. The laser power was the same as in Fig. 11. However, in this case, it was applied to zirconia beads. Although a temperature increase at TC2 was also observed during laser irradiation in this reference experiment, the rise was approximately 8 °C lower compared to that observed in the CNZ experiment.

Figure 13 shows the resulting excess heat in the 6325 mW laser irradiation experiment. As shown in Fig. 13, excess heat increased by 1.7 W at TC2 and 2.0 W at TC3 during laser irradiation, whereas a decrease of approximately 1 W was observed at TC4. This behavior may be attributed to differences in the physical properties of the CNZ and zirconia beads, particularly in their ability to absorb or reflect the laser light. Similar trends were observed at other laser power levels.

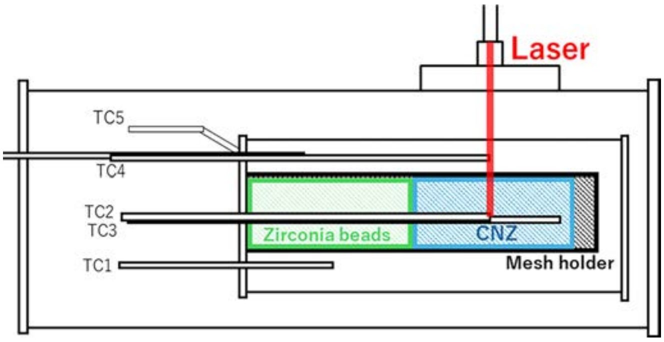

Figure 10. Schematic of laser experiment.

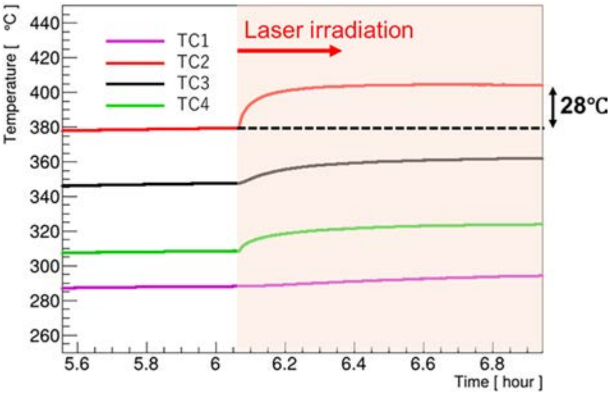

Figure 11. Time dependence of sample temperature with a 50 W heater input and 6325 mW laser irradiation.

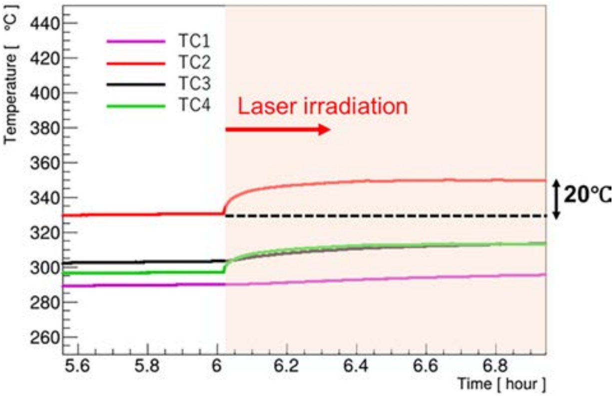

Figure 12. Time dependence of zirconia beads temperature with a 50 W heater input and 6325 mW laser irradiation.

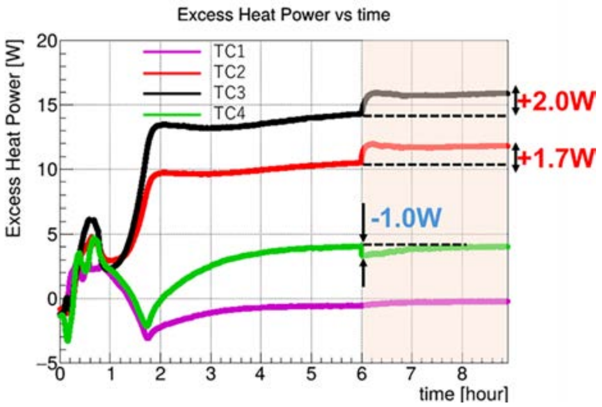

Figure 13. Time dependence of excess heat with a 50 W heater input and 6325 mW laser irradiation.

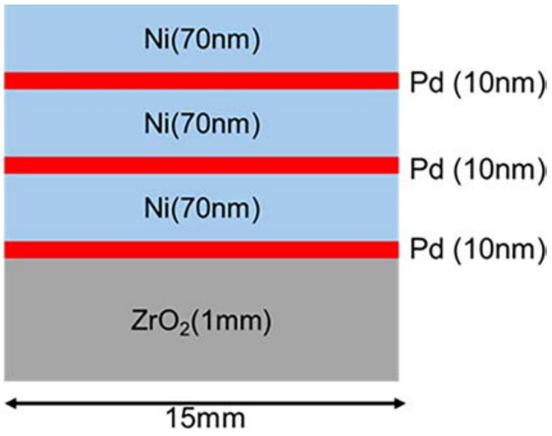

Figure 14. Schematic of sample.

2.3. Hydrogen Desorption Experiment in Multilayer Thin Films

2.3.1. *Sample*

The sample was composed of alternating layers of Pd (∼10 nm) and Ni (∼70 nm) deposited onto a 1 mm-thick ZrO_2 plate (15 × 15 mm^2) by sputtering (Fig. 14).

2.3.2. *Experimental Method*

A schematic of the experimental setup is shown in Fig. 15. The experimental procedure was as follows. First, the sample was baked after evacuation. Subsequently, approximately 250 Pa of hydrogen gas was introduced, and hydrogen absorption occured for 20 h while heating the sample to approximately 180 °C. The chamber was then evacuated to a pressure of a few pascals. Finally, the sample was heated to a temperature in the range of 600–800 °C. As a reference experiment, a zirconia plate was used.

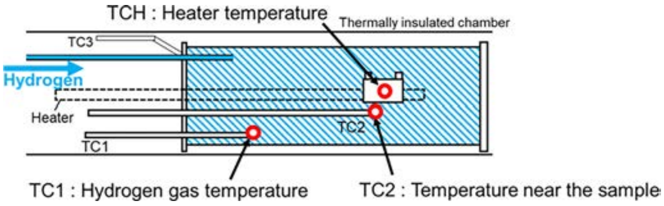

Figure 15. Schematic of the experimental setup.

Table 2. Temperatures reached in each experiment.

Heater Input (W)	Temp at TCH (°C)	Temp at TC1 (°C)	Temp at TC2 (°C)
20	627.90	182.30	216.25
30	722.70	223.00	259.85
40	794.70	257.25	296.15

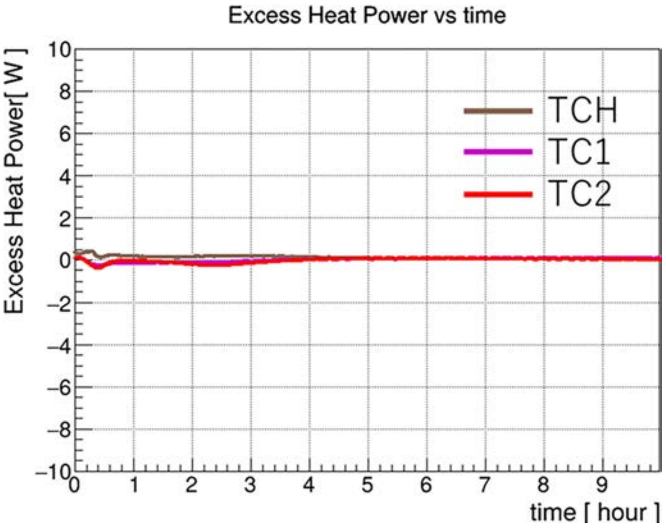

Figure 16. Time dependence of excess heat with a 20 W heater input.

2.3.3. *Results and Discussion*

Table 2 shows the maximum temperatures reached in the experiments at each input power level. Figure 16 presents the excess heat results for the 20 W heater input experiment, Fig. 17 for the 30 W experiment, and Fig. 18 for the 40 W experiment. Focusing on the 30 W experiment, excess heat was observed during the initial 6 h, with a maximum value of 5 W. In contrast, no excess heat was detected in the 20 W experiment, and a heat deficit (negative excess heat) was recorded for the 40 W heater input. Overall, the experiment exhibited low reproducibility, and conclusive evidence for excess heat generation was not obtained.

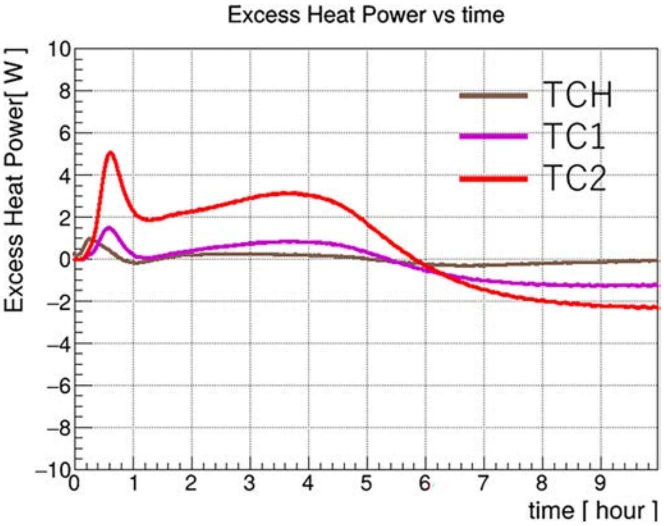

Figure 17. Time dependence of excess heat with a 30 W heater input.

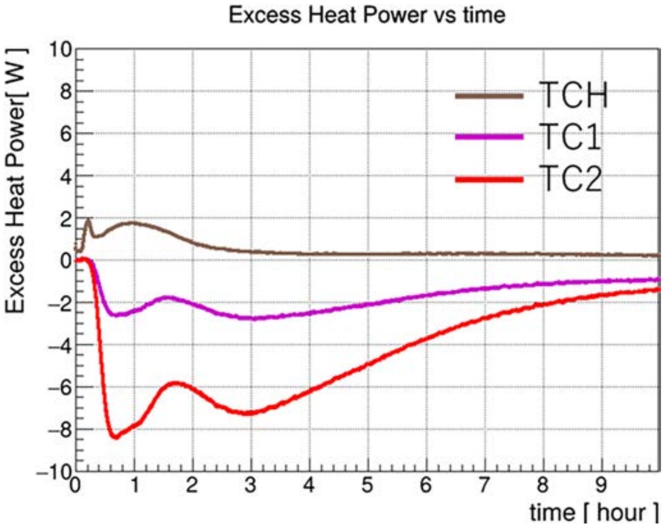

Figure 18. Time dependence of excess heat with a 40W heater input.

3. Summary

In this study, hydrogen absorption and laser irradiation experiments in CNZ and desorption experiments in multilayer thin films were conducted.

In the absorption experiment, excess heat of approximately 4 W, based on hydrogen gas temperature, and 10 W, based on the sample temperature, was observed. Moreover, a certain degree of correlation was identified between the heater input and measured excess heat. Furthermore, the excess heat generation persisted for approximately 90 h using the same sample.

In the laser irradiation experiment, excess heat increased by 1.7 W at TC2 and 2.0 W at TC3 during laser irradiation, whereas a decrease of approximately 1 W was observed at TC4. The negative excess heat observed at TC4 is considered to be due to the higher reflectivity of the zirconia beads compared to CNZ. Therefore, the excess heat observed at TC2 and TC3 can be attributed to their higher optical absorption, and it cannot be conclusively identified as being induced by an anomalous heat generation phenomenon. This suggests that optimization of laser specifications and irradiation conditions may be required, considering the properties of the CNZ and zirconia beads.

In the desorption experiment in multilayer thin films, heat generation was evaluated during hydrogen desorption. Although one instance of heat generation was observed, reproducibility was limited. Further investigations will be conducted to determine the conditions that reliably induce heat generation.

Acknowledgements

This work is supported by The Thermal & Electric Energy Technology Foundation.

References

[1] Y. Miyoshi et al., Proc. of JCF12(2011) 1.
[2] Y. Mori et al., Proc. of JCF22 (2022) 1.
[3] M. Hasegawa et al., Proc. of JCF22 (2022) 13.
[4] A. Takahashi et al., J. Condensed Matter Nucl. Sci. 38 (2024) 295.
[5] Ubaldo Mastromatteo, J. Condensed Matter Nucl. Sci. 19 (2016) 173.
[6] Jean-Paul Biberian, J. Condensed Matter Nucl. Sci. 37 (2023) 9.
[7] Y. Iwamura et al., J. Condensed Matter Nucl. Sci. 4 (2011) 132.
[8] Y. Iwamura et al., Proc of JCF21 (2021) 1.
[9] N. Yanagidate et al., Proc. Of JCF23 (2023) 148.
[10] J. Kasagi et al., J. Condensed Matter Nucl. Sci. 39 (2025) 210.

J. Condensed Matter Nucl. Sci. 41 (2026) 84–89

Research Article

Exothermic Phenomena in Hydrogen Desorption Experiments Using Pd-Ni Samples

Takuya Kitabayashi, Tomo Nemoto, Tomoki Kawarada, Youichi Takeda, Shinya Narita
Iwate University, Morioka 020-8551 Japan

Abstract

In this study, we conducted a hydrogen desorption experiment using a Pd foil sample coated with a Ni membrane to investigate its thermal behavior and hydrogen diffusion characteristics. Two heating methods were employed: direct heating and indirect heating. In the direct heating experiments, transient heat generation was observed 0.5–1.0 hours after applying constant power, accompanied by temperature changes associated with hydrogen release. Comparison with unabsorbed samples suggested that the excess heat was estimated to be up to several hundred milliwatts. On the other hand, in the indirect heating experiments, heat generation was rarely observed, but a heat generation phenomenon was confirmed when a constant power of 1 W was applied. These results suggest that anomalous diffusion during the hydrogen desorption process may induce heat generation, indicating the need for further confirmation of reproducibility and higher-precision evaluation of excess heat.

Keywords: H2-gas, Cold fusion, Metal complex, Nano-structure, Thin film.

---

1. Introduction

Several previous studies on hydrogen/deuterium absorption and desorption in Pd-Ni and Cu-Ni systems have reported the generation of excess heat [1]–[9]. These studies highlighted the following conditions as necessary for such anomalous phenomena:

- Formation of metal complexes (e.g., composite particles, multi-layer structures)
- Presence of nano-structures (e.g., nano particles, thin membranes)

Considering these conditions, we conducted a hydrogen desorption experiment using a Pd foil sample coated with a Ni membrane to investigate its thermal behavior and hydrogen diffusion characteristics. The sample was heated to promote hydrogen desorption, employing two heating methods:

- Direct heating: The heater was in direct contact with the sample.
- Indirect heating method: The sample was fixed to a metal plate, and a heater was used to heat the metal plate. Heat was then transferred from the plate to the sample.

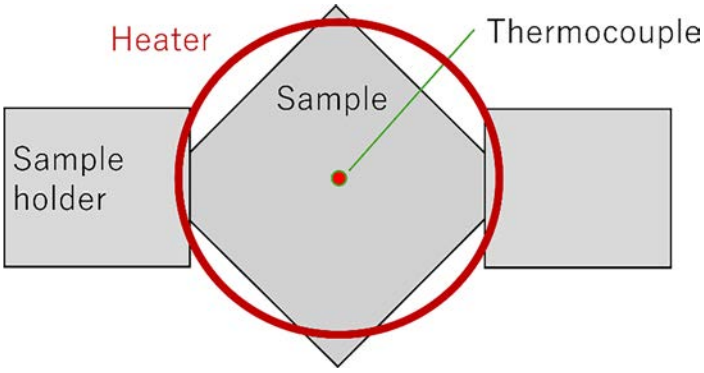

Figure 1. Schematic of direct heating.

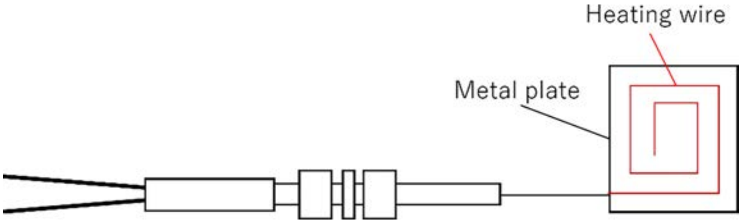

Figure 2. Schematic diagram of indirect heating.

2. Experiment

2.1. Sample

The sample material consisted of a Pd foil (10 × 10 × 0.1 mm) and a Ni membrane (t = ∼100 nm). First, the Pd foil was washed with acetone and annealed at 900 °C for 10 h. Subsequently, the annealed Pd foil was washed with aqua regia to remove any metallic impurities from its surface. A fine structure was formed on the surface of the Pd foil by etching with an Ar+ beam. Subsequently, an Ni membrane was deposited on the etched surface via Ar+ sputtering.

2.2. Hydrogen Loading

A schematic of the experimental setup is shown in Fig. 4.

The Pd-Ni sample was placed in a stainless-steel cell, which was filled with hydrogen gas (purity: 99.99999% or higher) at 5 atm and pressurized for approximately 20 h. The weight of each sample was measured before and after loading, and the loading ratio (H/Pd) was calculated from the weight difference. The electronic balance used in this experiment was a GH-202(A&D Co., Ltd.), with a minimum display of 0.01 mg and a standard deviation of 0.02 mg.

When calculating the loading ratio from the weight, the thin film was considered to have a negligible amount of absorbed hydrogen because its thickness (100 nm) is much smaller than that of the substrate (0.1 mm).

In addition, the gas released between removing the sample from the absorption apparatus and weighing it is not taken into account in the calculation of the loading ratio.

The absorption experiments were repeated 17 times, yielding an average H/Pd ratio of 0.72.

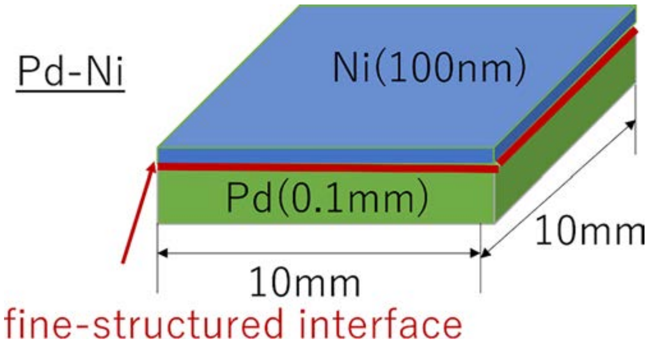

Figure 3. Schematic diagram of sample.

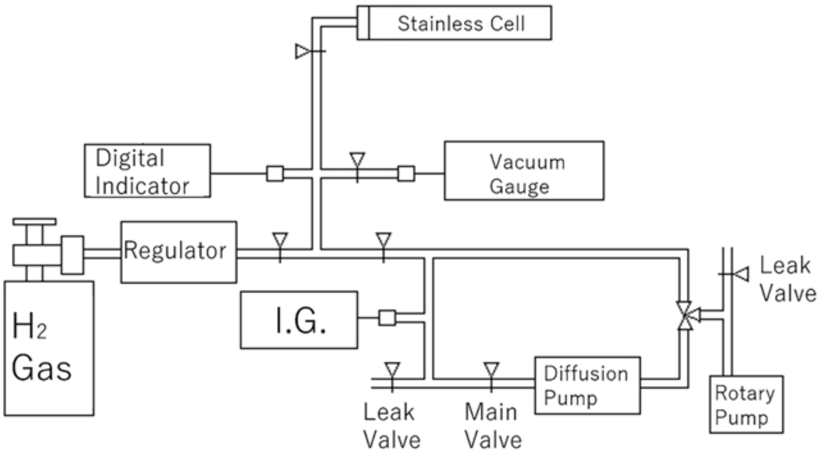

Figure 4. Schematic of the absorption experimental setup.

2.3. Hydrogen Desorption

A schematic of the experimental setup is shown in Fig. 5. The volume of the vacuum chamber in the desorption apparatus is approximately 1.098 L. The sample was placed into a chamber equipped with a TMP, which could be evacuated to $\sim10^{-4}$ Pa. Inside the chamber, the sample was heated by applying constant power to the heater to stimulate hydrogen diffusion. The sample temperature and chamber pressure were continuously monitored for approximately 24 h. A thermocouple was used to measure the temperature, and an ionization gauge was used to measure the chamber pressure. The voltages and currents applied to the heater were recorded during the experiments.

2.4. Blank Experiment

After the desorption experiment, the samples were treated as hydrogen-free for subsequent experiments. The experiment was conducted under the same conditions as the desorption experiment, and the sample was heated for 20 h using the heater.

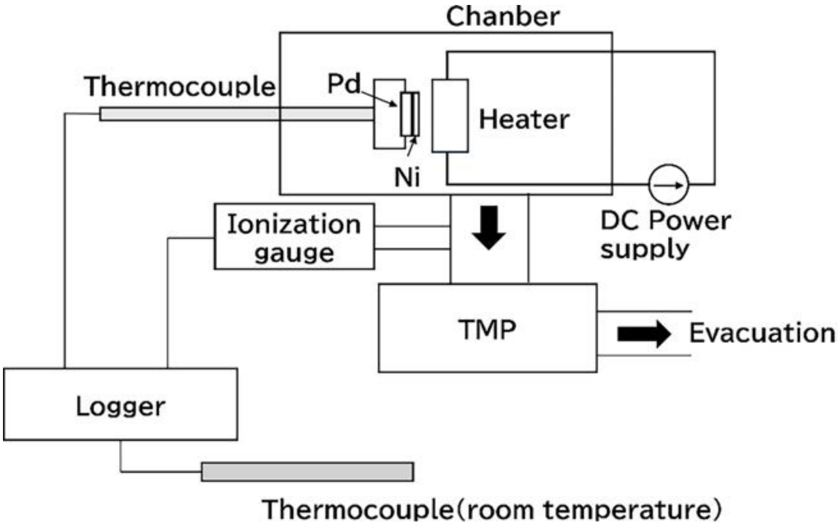

Figure 5. Schematic of the experimental setup.

2.5. Calibration

The power supplied to the heater varied every two hours during the experiment. For example, when 1.2 W was supplied to the heater in the desorption and blank experiments, the output was increased incrementally to 1.3 W, 1.4 W, 1.5 W, and 1.6 W, using 1.2 W as the reference. The corresponding temperature was measured for each power setting, and a calibration curve of temperature versus supplied power was constructed.

3. Results

3.1. Experimental Result 1: Hydrogen Desorption By Direct Heating

The experiments were conducted using a direct heating system. Fig. 6(a) shows the time dependence of the sample temperature and chamber pressure during the desorption experiment (Pd(Ni)-2024-09). Fig. 6(b) presents an enlarged plot of the initial 24 h, and Fig. 6(c) provides an enlarged plot of the initial 4 h of the experiment. Similarly, Fig. 7(a) shows the time dependences of the sample temperature and chamber pressure during the desorption experiment (Pd(Ni)-2024-10), and Fig. 7(b) depicts an enlarged plot of the initial 24 h. Furthermore, Fig. 7(c) shows an enlarged plot of the initial 4 h.

The data obtained from 0 to 24 h corresponded to the desorption experiment, from 28 to 48 h to the blank experiment, and from 52 to 74 h to the calibration experiment. In the desorption phase, transient heat generation was occasionally observed between 0.5 and 1.0 h following the application of constant power. Concurrent pressure variations correlated with the temperature changes were also recorded. These results suggested a possible increase in the surface temperature of the sample during hydrogen release. The unique conditions of the sample may have induced specific hydrogen diffusion, causing an exothermic reaction. This phenomenon was observed in approximately 4 out of 6 trials.

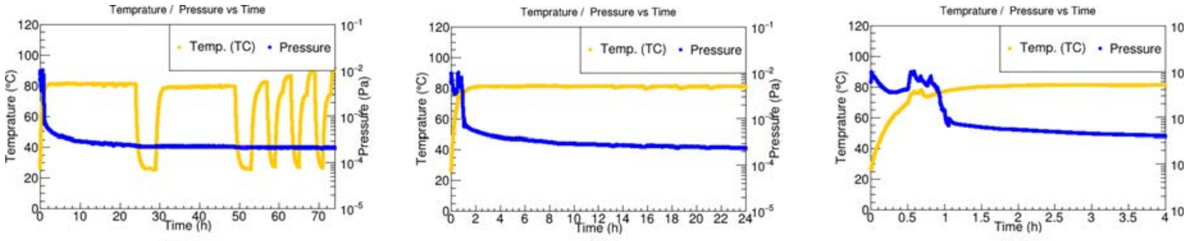

(a) (b) (c)

Figure 6. (a) Time dependence of sample temperature and chamber pressure for the experiment (Pd(Ni)-2024-09) over 74 h. (b) Time dependence of sample temperature and chamber pressure for the experiment (Pd(Ni)-2024-09) over 24 h. (c) Time dependence of sample temperature and chamber pressure for the experiment (Pd(Ni)-2024-09) over 4 h.

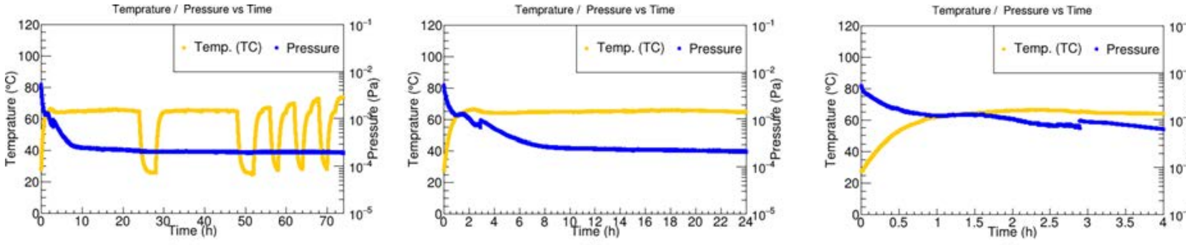

(a) (b) (c)

Figure 7. (a) Time dependence of sample temperature and chamber pressure within the chamber for the experiment (Pd(Ni)-2024-10) over 74 h. (b) Time dependence of sample temperature and chamber pressure for the experiment (Pd(Ni)-2024-10) over 24 h. (c) Time dependence of sample temperature and chamber pressure for the experiment (Pd(Ni)-2024-10) over 4 h.

3.2. Experimental Result 2: Hydrogen Desorption by Indirect Heating

The experiments were conducted using an indirect heating system. Fig. 8(a) shows the time dependences of the sample temperature and chamber pressure during the desorption experiment (Pd(Ni)-2024-13). Fig. 8(b) presents an enlarged plot of the initial 24 h, and Fig. 8(c) shows an enlarged plot of the initial 4 h of the experiment. Similarly, Fig. 9(a) shows the time dependence of the sample temperature and chamber pressure during the desorption experiment (Pd(Ni)-2025-03). Moreover, Fig. 9(b) depicts an enlarged plot of the initial 4 h, Fig. 9(c) shows an enlarged plot of the sample temperature during the initial 4 h of the experiment.

The data from 0 to 24 h correspond to the desorption experiment, from 28 to 48 h to the blank experiment, and from 52 to 74 h to the calibration experiment. In the experiments using an indirect heating system, heat generation phenomena were rarely observed. Pressure fluctuations associated with hydrogen release were recorded. Notably, heat generation associated with hydrogen release was observed when a constant power of 1.0 W was applied. Further investigations are required to clarify the specific conditions under which hydrogen-related heat generation occurs. This phenomenon was observed in approximately 3 out of 11 trials.

4. Summary

Hydrogen desorption experiments were conducted using a sample consisting of a Pd substrate coated with a nickel layer. Two heating methods were employed: direct and indirect. In the using direct heating experiments, heat generation was observed between 0.5 and 1.0 h after the application of constant power. This heat generation was potentially associated with hydrogen desorption. Furthermore, the specific conditions of the sample induced anomalous diffusion

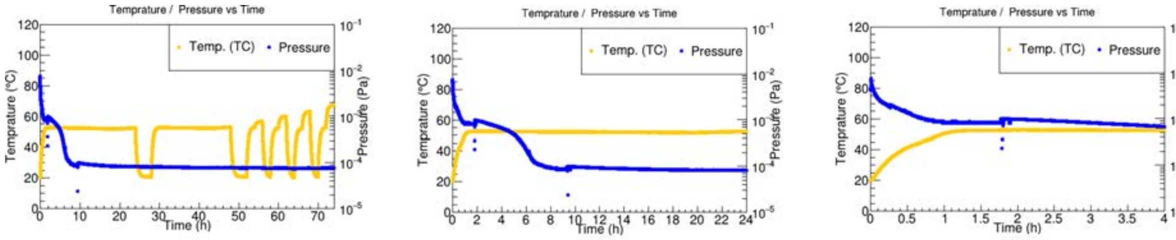

(a) (b) (c)

Figure 8. (a) Time dependence of sample temperature and chamber pressure for the experiment (Pd(Ni)-2024-13) over 74 h. (b) Time dependence of sample temperature and chamber pressure for the experiment (Pd(Ni)-2024-13) over 24 h. (c) Time dependence of sample temperature and chamber pressure for the experiment (Pd(Ni)-2024-13) over 4 h.

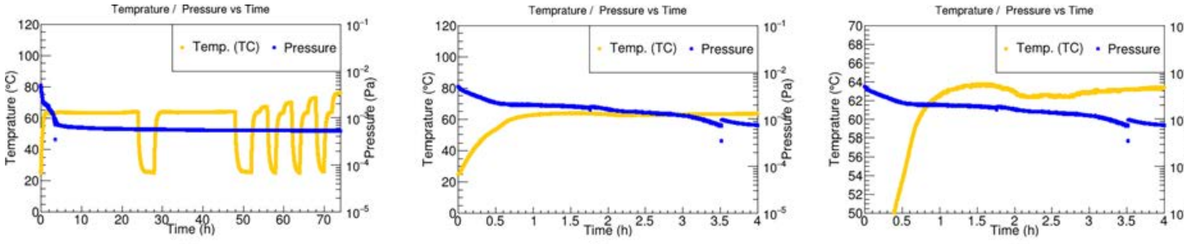

(a) (b) (c)

Figure 9. (a) Time dependence of sample temperature and chamber pressure for the experiment (Pd(Ni)-2025-03) over 74 h. (b) Time dependence of sample temperature and chamber pressure for the experiment (Pd(Ni)-2025-03) over 4 h. (C) Time dependence of sample temperature and chamber pressure for the experiment (Pd(Ni)-2025-03) over 4 h (enlarged view of the sample temperature).

behavior of hydrogen, which in turn triggered an exothermic reaction. Excess power was estimated by a comparison with the temperature measured for the unloaded sample, yielding preliminarily values up to several hundred milliwatts. In contrast, in the indirect heating experiments, heat generation observed in the case of direct heating was rarely detected. However, when a constant power of 1 W was supplied, heat generation phenomena, possibly related to hydrogen desorption, were occasionally observed. Experiments are ongoing to confirm heat generation and improve the accuracy of excess heat evaluation.

Acknowledgement

This work is supported by The Thermal & Electric Energy Technology Foundation.

References

[1] A. Takahashi et al., J. Condensed Matter Nucl. Sci, 33 (2020) 14.
[2] Y. Iwamura et al., J. Condensed Matter Nucl. Sci, 36 (2022) 285.
[3] T. Mizuno and J. Rothwell, J. Condensed Matter Nucl. Sci, 29 (2019) 21.
[4] T. Itoh et al., J. Condensed Matter Nucl. Sci, 24 (2017) 179.
[5] Sato et al., J. Condensed Matter Nucl. Sci, 37 (2023) 111.
[6] P. Ramarao et al., J. Condensed Matter Nucl. Sci, 38 (2024) 357.
[7] A. Kitamura et al., International Journal of Hydrogen Energy 43 (2018) 16187.
[8] J. kasagi et al., arXiv:2311.18347 [physics.ins-det]
[9] Y. Iwamura et al., J. Condensed Matter Nucl. Sci, 33 (2020) 1.

J. Condensed Matter Nucl. Sci. 41 (2026) 90–98

Research Article

Detonation in Hydrogen-Carbon Cluster Heterogeneous Plasma

Klimov A., Pashchina A.
Joint Institute for High Temperature, RAS

Abstract

In this paper we study the plasma-assisted LENR and its detonation in heterogeneous plasmoid (HP) triggered by a magnetic compressor at a static pressure of P_{st} ~1 Bar and higher. This HP consists of cheap carbon nanoclusters and hydrogen ions (protons).

Keywords: LENR detonation, Carbon clusters, Energy balance, Hydrocarbon erosive plasma, Magneto-plasma compressor, pulsed erosive plasma generator (EP).

1. Introduction

It is known that LENR in a mixture of hydrogen and metallic nanoclusters is accompanied by the transmutation of the initial chemical elements and the release of excess thermal energy with a high specific value, on the order of several keV/hydrogen atom [1], [2], [5]–[7]. Thus, LENR is a highly exothermic reaction.

Unfortunately, at the initial moment this energy is in the form of UV and soft X-ray quanta [3].

Interesting questions arise:

1. How can the initial energy of X-ray quanta in LENR be transformed into the thermal energy of metal clusters and hydrogen atoms?
2. Under what conditions can LENR be accelerated and put into detonation mode?

This problem is investigated in the present work. Note that it is very difficult to measure the energy balance in any reactor reliably (due to possible unaccounted energy losses). The method of studying energy release and rates of exothermic chemical reactions using shock waves (SW) in chemical physics is well-known and widely used [4]. During a high-speed chemical process (typical duration several microseconds) behind the shock front in a compressed layer, possible thermal losses in the boundary layer on the walls of the shock tube are usually neglected. The chemical reaction takes place completely in a very short time within the thin shock wave layer, and then released thermal energy is converted to a pressure jump and temperature jump behind the shock wave front. This calorimetric method is more reliable and accurate than other calorimetric methods used in reactors. This method is based on the Rankine-Hugoniot equation [4]. In the stationary detonation mode (Chapman-Jouguet mode), the following relations are obtained:

$$Da\ = \mathrm{q/CpT} \tag{1}$$

$$q = c_pT\frac{\gamma-1}{2\gamma}\left[\frac{p_2}{p_1}\left\{\frac{\gamma+1}{\gamma-1}\frac{\rho_1}{\rho_2}-1\right\}-\frac{\gamma+1}{\gamma-1}\frac{\rho_2}{\rho_1}\right] \tag{2}$$

$$M^2{}_{CJ} = {V_1}^2/{c_1}^2 = 2(\gamma+1)\ q/CpT \tag{3}$$

where:

M_{CJ} – the Mach number of the detonation wave (M_{CHJ} >>1)
P_2, P_1- the pressures behind the SW front and before its front
ρ_2, ρ_1- the density of the gas behind the SW front and before its front
q- the specific thermal energy from the exothermic reaction
C_p– the specific heat capacity
γ- C_p/C_v ratio
T, K- the gas temperature

It follows from formulas (1-3) that measuring the SW velocity and pressure jump and density jump at its front allows us to estimate the ***Da*** number and ***q*** value. Therefore, in our work, the SW method was used to determine the indicated values in the plasma-assisted LENR detonation in a hydrocarbon heterogeneous plasmoid (HP). In our previous works [5]–[7], LENR was observed in a heterogeneous hydrocarbon plasma consisting of carbon nanoclusters and ionized hydrogen (protons). Such an HP was created using a pulsed erosive plasma generator (EP) with a capillary discharge gap. This EP was described in detail in our work [5]. It was shown that this EP creates a metastable energy-saturated HP with a specific energy content of about 100 eV/atom and a typical lifetime of about 0.1-1 seconds. Such an HP was obtained in a capillary discharge gap made of polyethylene (or PMMA) due to erosion of its walls by means of a powerful electric discharge (see below). In such an HP, the transmutation of the initial chemical atoms *C* and *H* was observed, and the formation of final chemical elements such as *Li, Al, Ca, N* and others took place. The transmutation reaction is accompanied by a significant release of thermal energy [5]. In such an EP, sufficiently high values of the COP coefficient = 2-4 have been achieved (the ratio of the output thermal energy in the HP to the input electrical energy spent on its creation), [5], [6].

In this paper, we examine a significant acceleration of LENR in an HP by means of a pulsed pressure jump and temperature jump behind the SW front is discussed. To create such SW, a pulsed magneto-plasma compressor (MPC) was used, in which, with some delay relative to the first current pulse in EP, a second powerful current pulse with an amplitude of about 10 kA and a duration of about 100 μs was additionally created. This SW was used as a detonator in the HP. It has been shown that under certain conditions, a directed detonation (an explosion) can occur in an energy-saturated heterogeneous hydrocarbon plasma (HP).

2. Experimental Setup

A schematic and photos of the experimental setup are shown in Figs. 1 and 2. In this configuration, the EP is combined with the MPC. The EP is shown on the left side of the drawing up to the red line *A1A2*. The MPC generator is located on the right side of the red line.

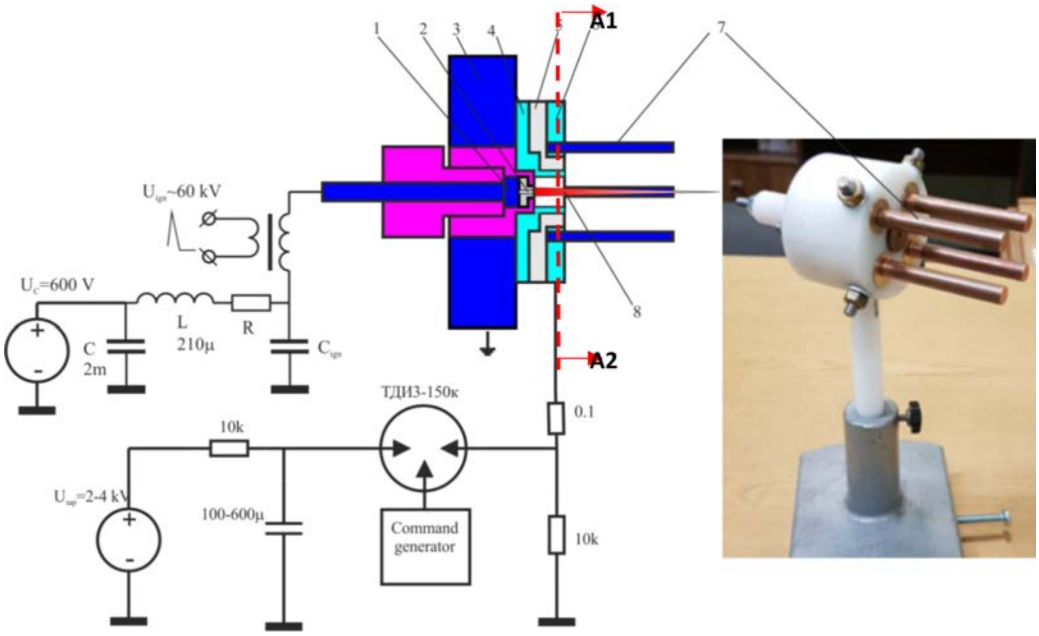

Figure 1. Electrical diagram and general view of the MPC-EP: 1 –the anode of the EP; 2 – capillary discharge channel in the EP; 3 – holder; 4 – cathode of the EP / anode of the MPC; 5 – insulator; 6, 7 – cathode of the MPC; 8 – heterogeneous plasma jet (EP-jet).

Figure 2. MPC-EP and diagnostic instrumentation. 1: MPC-EP, 2: pressure transducers, 3: high voltage probe Tektronix P-3650, 4: high voltage capacitor.

The EP parameters are as follows:

- pulse current	-150 A
- pulse duration	- 4 ms
- capacitor energy storage	80 J
- the working substance in EP	PMMA or **polyethylene**.

MPC parameters are as follows:

- pulse current-	8-16 kA
- pulse duration	about 100 μs
- capacitor energy storage	400-1600 J

To study the shock wave parameters, two pressure sensors (Fig. 2, item 2) were used, placed at specified distances from the MPC-EP (Fig. 2, item 1). During the experiments, the pressure distribution $P_2(X)$ behind the SW front created by the MPC-EP, the average SW velocity $V_{SW}(X)$ and its local velocity were measured in the registration cross-section.

A *Photron FASTCAM Nova S9* high-speed video camera was used to study the structure, as well as the spatial and temporal evolution of a heterogeneous plasmoid (plasma piston) created by the MPC-EP.

The optical spectra of the HP were recorded using an *AvaSpec UL 2048* optical spectrometer. The duration of the spectrum exposure is 2 ms.

3. Main Experimental Results

Typical high-speed video frames are shown in Fig. 3. The first frame shows the formation of an erosive plasma jet (HP) formed by the EP. The typical speed of the head part of such an HP-jet reaches approximately 100 m/s. At time T_0 (MPC ignition), its typical length is 100-150 mm. The typical diameter of the HP-jet reaches 5-10 mm.

The second frame shows the initial moment of discharge initiation in the MPC. A bright white flash from such a discharge is visible. It is important that all four anode electrodes were activated in the MPC simultaneously. Thus, the compression of the HP occurs symmetrically from all sides.

The second frame shows the process of acceleration of the plasma piston created by the MPC along the axis of the installation. A directional detonation mode was implemented. The typical speed of such a piston reached about 1000-2000 m/s.

The method of measuring the pressure field behind the SW front in this experiment is shown in Fig. 2. We used two pressure sensors with linear characteristics as in our previous work [5]. The measurements were carried out in the far wave zone at a distance of L= 300-1000 mm. The distance between the pressure sensors was constant during this experiment. Its value was 50 mm. Using this technique, the local SW velocity and the average SW velocity between the plasma generator and the piezo-transducer were reliably measured. Typical pressure signals behind the SW front recorded by the piezo-transducer are shown in Fig. 4.

Based on the processing of the obtained pressure signals (Fig. 4), a delay time between the moment of the MPC ignition and the moment of registration of a pressure jump behind the SW front can be measured, as well as the average SW speed. It can be seen that the pressure amplitude behind the SW front in the MPC+EP mode exceeds the amplitude of the pressure signal behind the SW front in the MPC mode by **2.5 times** at a distance of 400 mm from the HP generator. It was shown that the EP-generator in single mode creates a weak sound wave only, but no shock wave.

One can see that there is EM noise in the blue signal at the delay time T $\sim$100 μs connected with extra voltage creation by the inductance of MPC power supply at the moment the electric current switches off. One can see that the mean SW velocity is about Vsw = 470 m/s at measuring distance L $\sim$400mm. So, we have a weak shock wave in this distance L $\sim$400mm. Calibration dependence Vsw(L) was obtained in our previous work [5]. It was shown that the SW velocity decreases very quickly with distance L as well as pressure jump behind SW front (due to spherical SW decay at distance L increase). We recalculate pressure jump behind SW front near plasma piston boundary with the

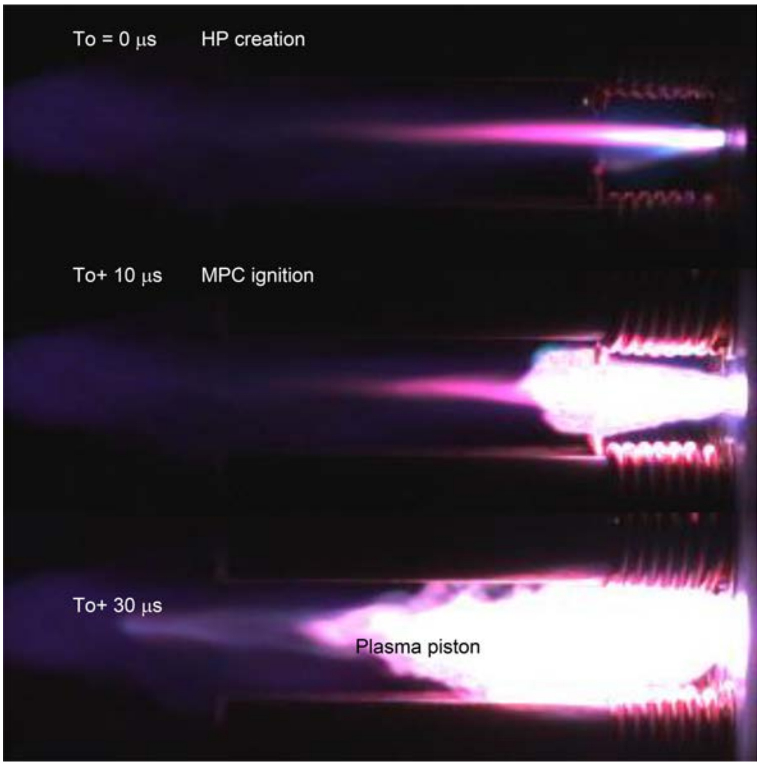

Figure 3. Separated frames of a high-speed video of HP-jet interaction with SW, created by the MPC.

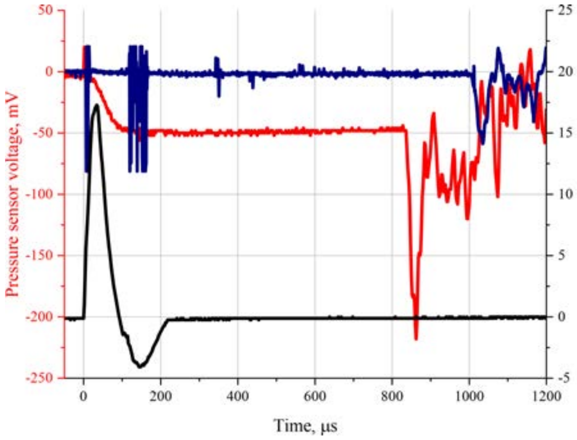

Figure 4. The typical experimental pressure signals behind shock wave (SW) front recorded at 400 mm from the HP generator. Pressure signal behind SW front (red): MPC+ EP mode. Pressure signal behind SW front blue: MPC without EP. MPC Current: black.

help of this dependence and well-known gas dynamic relation:

$$\mathrm{P_2/P_1} = (2\gamma \mathrm{M}^2/\,\gamma + 1) \;+\; (\gamma + 1/\,\gamma - 1).$$

It was found that

1. Mach number of the shock wave near the plasma piston is M ~6, or its velocity V_{SW} ~2100 m/s near "plasma piston" front.
2. The volume of the "plasma piston" is about W= 10 cm^3.

Using well-known gas-dynamic formulas at the shock wave front, one can obtain an estimate of the released energy E_{ch} during the HP explosion.

EP+ MPC mode.

The energy of the explosion can be estimated using the following formula

$$E \;=\; \Delta P_2\, W \;\sim 320\text{ J},\; \Delta \mathrm{P}_2 = \mathrm{P}_2 - \mathrm{P}_1,$$

where P_2/P_1 pressure jump at SW front near the border of the plasma front

MPC (only) mode.

$$E^* \;=\; \Delta P_2{}^*\, W^* \;\sim 120\text{ J}.$$

It can be assumed that the additional LENR energy released in the HP plasma is:

$$E_{ch} = E \;-\; E^* \;=\; 200\mathrm{J}.$$

Note that EP-generator (single mode) creates a weak sound wave only (but not SW). Thus, the contribution of erosive plasma jet created by EP to the total pressure was insignificant.

The estimation of the specific energy $\boldsymbol{q_x}$ released in stimulated LENR at

δM_{ch} = 1.2 mg/ per shot is about

$$\boldsymbol{q_x} = \;\delta E_{ch}\;/\;\delta M_{ch} \;=\; 200\mathrm{J}/1.2\,\mathrm{mg} \;\sim 1.67\;10^8\;\mathrm{J/kg} \;\sim \mathbf{2MeV/atom\,H},$$

at PMMA molecular weight about 100g ($C_5H_8O_2$-monomer)

4. Optical and X-ray Spectroscopy of HP

The optical spectra of the HP were recorded with an AvaSpecUL 2048 optical spectrometer, and are shown in Figs. 5, 6. The optical spectra include lines of highly excited ***H, K, Ni, Na, Li*** atoms, as well as intense continuous radiation spectrum. The presence of the latter one is due to the formation of metallic and carbon nanoclusters inside the EP [3], [4]. Estimating the *black-body* temperature T_6 of metallic nanoclusters by continuous radiation spectra (Wien approximation) leads to values of T_6~3000-4000 K. Part of the total HP's radiation spectrum is shown in Fig. 5. The radiation spectrum contains lines of the Balmer series of hydrogen atom: - $\boldsymbol{H_\alpha}$, $\boldsymbol{H_\beta}$, $\boldsymbol{H_\gamma}$, $\boldsymbol{H_\delta}$, excited carbon ion ***C II*** (products of ablation of the capillary wall), lines of excited atoms and ions of ***Cu*** and ***Zn*** (electrode material), lines of nitrogen ion ***N II*** and oxygen atom ***O I,*** as well as molecular band of radical ***CN.*** The presence of *highly excited optical lines* ***N II*** (498.74-502.57 nm, excitation energy of E*=23.13 eV) and *lines* ***C II*** (426.7 nm, E*= 20.95 eV), *lines* ***C II*** (407.45-407.58, E*=27.41 eV) in the radiation spectrum proves the presence of LENR in HP. It was shown that there is the typical electron temperature $\mathbf{T_e}$**~1-3 eV** in this HP. So, it is very difficult to explain the *highly excited*

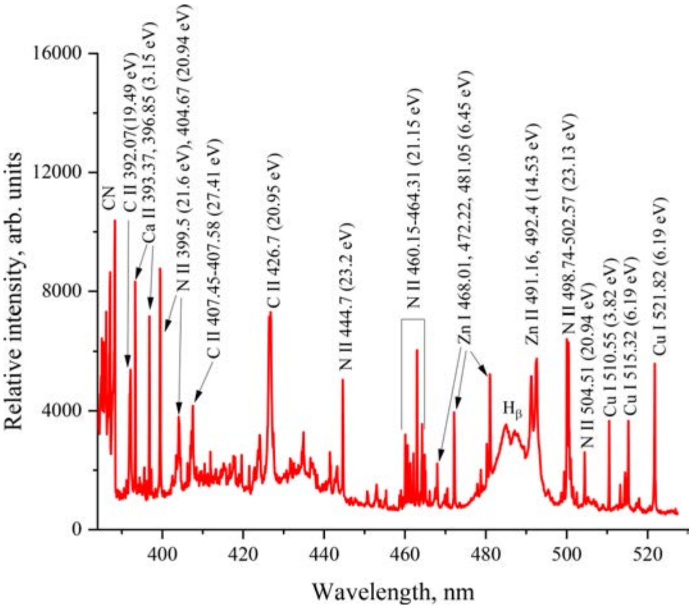

Figure 5. Typical plasma emission spectrum in the MPC+ EP mode in the range $\Delta\lambda$ = 385-530 nm.

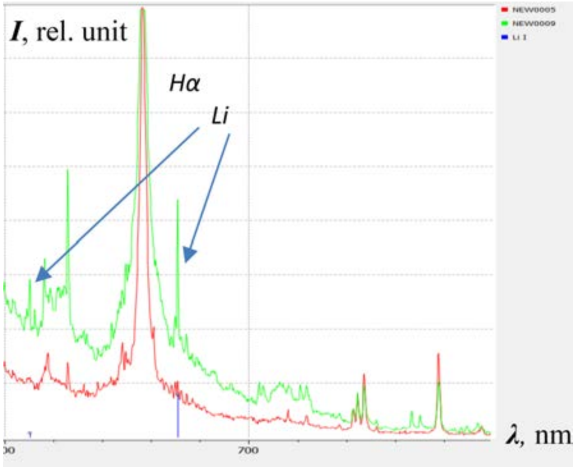

Figure 6. Optical spectra in the HP. MPC+EP mode. Optical range $\Delta\lambda$=600-800 nm. Red- PMMA. Green- PMMA+ $\mathrm{TiD_x}$ (very small concentration). Blue columns – simulation, NIST data.

optical lines by plasma electron impact. We hope to explain this result by LENR between hydrogen ions and carbon clusters in our future experiments.

The X-123 spectrometer detected intense soft X-ray radiation with a quantum energy of the order of E_x $\sim$1-2 keV (fig. 7).

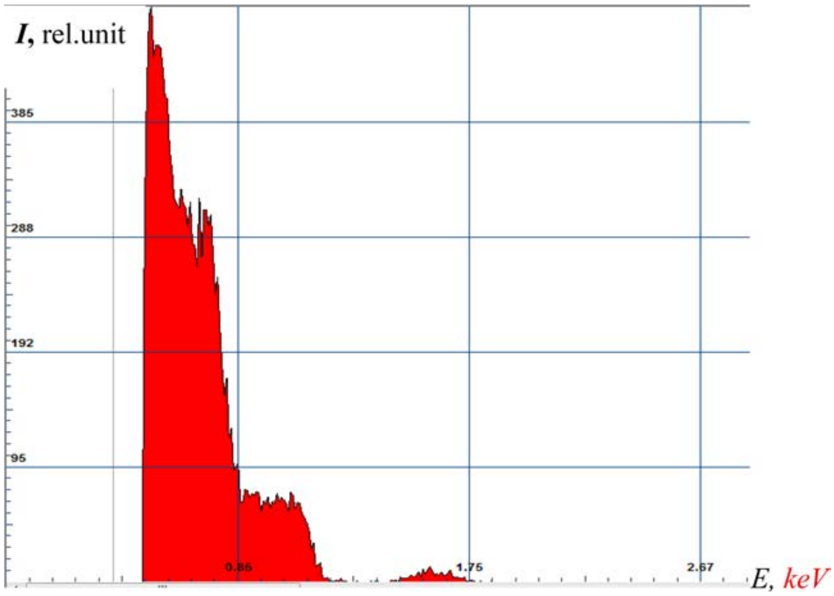

Figure 7. Typical spectrum of soft X-ray radiation from HP.

The radiometer-spectrometer MKS-A03-1 recorded cold neutron flux from the HP. This experimental result requires further study.

5. Conclusion

1. A unique experimental setup MPC-EP was developed. This setup allows us to create a plasma-assisted *LENR and its detonation in heterogeneous plasmoid (HP)* triggered by a magnetic compressor in this installation at a static pressure of P_{st} ~1 bar and higher.
2. This HP consists of *cheap carbon nanoclusters and hydrogen ions (protons).*
3. In this work, the pressure $P_2(t)$ behind the shock wave front created by the MPC-EP and the average and local SW velocities $V_{SW}(t)$ were measured. It was found that a mode of creating a directional explosion of an HP created with an MPC-EP is possible with an optimal time delay between the EP ignition and the MPC ignition. An anisotropic pressure distribution was observed behind the SW front. This result was also confirmed by the optical shadow method.
4. The high average velocity of the plasma piston V_p ~1000-2000 m/s was measured by a high-speed video camera.
5. It was observed that the pressure jump behind the SW front in the joint (MPC+ EP) mode exceeds the pressure jump behind the SW in the MPC mode (without EP) by 2.5-3 times. Assuming that the additional energy release behind the SW front is associated with LENR inside the HP, it is easy to estimate a value for the specific release of reaction energy q_x ~200 kJ/g or 2 MeV/hydrogen atom.

This study was carried out within the State Assignment of the Ministry of Science and Higher Education of the Russian Federation (project No. 075- 00270-24-00).

References

[1] Y. Iwamura, T. Itoh, Jirohta Kasagi, T. Takahashi, S. Yamauchi, M. Saito, S. Murakami, T. Hioki, "Anomalous Heat Burst Triggered by Input Power Perturbations observed in Ni-Based Nanostructured Thin Films with Hydrogen", J. Condensed Matter Nucl. Sci., 38, (2024), pp. 269–287.

[2] Highly Efficient Water Plasma Vortex Reactor for Obtaining of Extra Thermal Energy and Transmuted Chemical Elements 287 Klimov A., Altunin S., Kulikovskii O., J. Condensed Matter Nucl. Sci., 38, (2024), pp. 287–295.

[3] R. Mills, Y. Lu, R. Frazer, "Power Determination and Hydrino Product Characterization of Ultra-low Field Ignition of Hydrated Silver Shots", Chinese Journal of Physics, Vol. 56, (2018), pp. 1667–1717.

[4] F. Bartlme, Combustion Gas Dynamics, M., Energoizdat, 1991, P.237 (in Russian).

[5] Ball Lightning in Laboratory, M., Chemistry, 1994, P.256, (in Russian).

[6] Klimov A., Pashchina A., "LENR- Experiment on Heterogeneous Hydrocarbon Plasma Jet Interaction with Ni-Foil-Target", J. Condensed Matter Nucl. Sci. 36 (2022) 312–317.

[7] Brovkin V., Klimov A., Pashchina A., "Stimulated Detonation of a High- Energy Heterogeneous Plasma Formation Created by a Capillary Erosive Plasma Generator and Magneto - Plasma Compressor", Russian Journal of Physical Chemistry B, 2024, V.18, No.5, pp. 1415–1421.

J. Condensed Matter Nucl. Sci. 41 (2026) 99–112

Research Article

Multiple Scattering, Coherent Resonance, Quantum Flux and Quantum Hydrogen Energy

Xingzhong Li, Changlin Liang, Si Chen, Jian Tian, Bin Liu,
Zhanming Dong, Guisong Huang
Dept. of Physics

Shuxin Zheng
Dept. of Engineering Physics, Tsinghua University, Beijing, CHINA

Abstract

S. E. Koonin's formula and Bethe's calculation on solar energy are combined with the 2-step nuclear resonance caused by multiple scattering in lattice in order to evaluate the resonance effect on the possible low energy nuclear reaction rate. This resonance is justified by the 6 straight lines from 6 laboratories (Fleischmann, Storms, Dennis, Mizuno, Parkhomov, and Tsinghua) in 5 countries. It may explain both Storms' tritium and Miles' correlation between excess power and ^{4}He data. Similar to low energy electron diffraction, the low energy proton diffraction has 3 effects: (1) turns 2-body phase-shift into many-body phase-shift and makes coherent resonance in lattice, i.e. puts many peaks of wave function at many nuclear surfaces simultaneously and replaces the Gamow suppression by Boltzmann factor; (2) many bouncing back and forth motions between interface of 2 films greatly enhance the number of nuclear reactions; (3) reduces the total reflection rate from a set of films in terms of interference between many reflected waves; then, confine the incident wave inside the multiple film system for a much longer time. It is consistent with the correlation between quantum diffusion flux and excess power. This model may further explain 5-peak pattern and the $\sqrt[3]{A}$-law in the nuclear transmutation of metal hydrides (Miley, Mizuno, and Ohmori's data). This is the **Lattice Enhanced Nuclear Resonance** (LENR). It is supposed to appear in the "electron screening potential", and show the 5-peak pattern as well. 3 experiments are suggested to verify this possible nuclear origin in electron screening potential. It may turn metal-hydride a fuel burning with hydrogen together, rather than a furnace for burning hydrogen in it.

Keywords: Koonin's formula, multiple scattering, coherent resonance, lattice enhanced nuclear resonance, 5-peak pattern in electron screening potential, correlation between quantum diffusion flux and excess power, Gamow suppression and Boltzmann factor, low energy electron diffraction, Many-body phase-shift.

---

1. Introduction

Thirty-six years ago, we learned that cold fusion produces excess heat. A few years later we learned that excess heat is correlated with deuterium flux. Now we understand that there are two kinds of flux: classical flux and quantum flux.

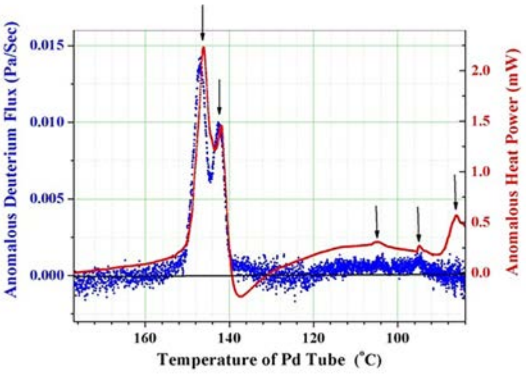

Figure 1. Correlation between anomalous deuterium flux and anomalous heat flow.

Classical flux arises from two-body collisional diffusion, whereas quantum flux results from wave scattering by many bodies in a lattice (i.e., multiple scattering). The excess power is only correlated with this quantum flux. Classical flux decreases with temperature monotonically, but quantum flux has many peaks when the temperature is decreasing. In Fig. 1 the blue line shows the anomalous deuterium flux passing through a thin wall of a Pd tube [1]. When the temperature of the tube drops from ∼180° C to 80° C, the blue line shows many peaks instead of monotonic behavior. We will discuss why there are peaks in anomalous deuterium flux due to multiple scattering, and why these peaks are correlated with excess power due to the wave function peak at the nuclear surface. Then we will propose experimental tests of our model.

2. Quantum Flux Passing Many Films: Wave Superposition and Interference

Wave has a phase, and the superposition principle may lead to partial or complete cancellation of the wave's amplitude. Thus, wave mechanics may explain the peak behavior of transmission. This is the advantage of quantum flux over classical flux. In quantum mechanics, we are dealing with the wave function, ψ first, instead of dealing with the observable quantities directly such as flux, transmission rate, T, and reflection rate, R. We define the incoming and outgoing wave functions as a linear combination of the forward, e^{ikz}, and backward, e^{-ikz}, plane waves in upper plot of Fig. 2:

$$\psi_L = U_L^+ e^{ikz} + U_L^- e^{-ikz}; \tag{1}$$

$$\psi_R = U_R^+ e^{ikz} + U_R^- e^{-ikz}. \tag{2}$$

The matrix, $M[1]$, is used to describe the wave scattering by a thin film:

$$\begin{bmatrix} U_L^+ \\ U_L^- \end{bmatrix} = M[1] \cdot \begin{bmatrix} U_R^+ \\ U_R^- \end{bmatrix} \equiv \begin{bmatrix} m_{11} & m_{12} \\ m_{21} & m_{21} \end{bmatrix} \cdot \begin{bmatrix} U_R^+ \\ U_R^- \end{bmatrix}. \tag{3}$$

When there is more than one thin film, the reflected wave by the first film may superpose on the reflected wave from the second film…etc. They may interfere with each other and may even be cancelled to zero amplitude. This is the origin of the peak behavior in quantum flux. It may be described by matrix algebra as follows. $M\,[N]$, which

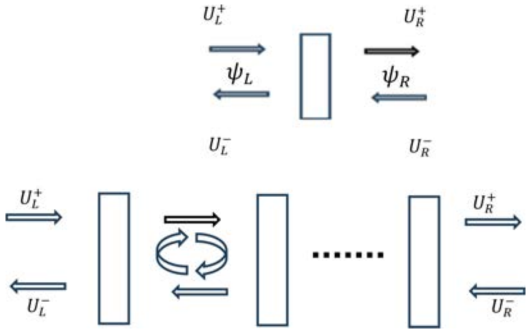

Figure 2. Incoming, outgoing, and reflected waves for a single film (upper) and multiple films (lower).

describes the scattering by N films, may be expressed in terms of the single film parameters as:

$$M\left[N\right] \equiv \underbrace{M[1]\cdot M[1]\cdots\cdot M[1]}_{N} \equiv \begin{bmatrix} M[N]_{11} & M[N]_{12} \\ M[N]_{21} & M[N]_{22} \end{bmatrix}; \tag{4}$$

$$M[N]_{11} = \frac{Sin[N\alpha]}{Sin[\alpha]}m_{11} - \frac{Sin\left[(N-1)\,\alpha\right]}{Sin\left[\alpha\right]}; M[N]_{21} = \frac{Sin[N\alpha]}{Sin[\alpha]}m_{21}; \tag{5}$$

$$\alpha = ArcCos\left[\frac{m_{11}+m_{22}}{2}\right]; \tag{6}$$

The observable physical quantities (reflection rate $R\left[N\right]$, transmission rate $T\left[N\right]$) are related to the square of the absolute value of these coefficients in the wave functions (1) and (2):

$$R\left[1\right] \underbrace{=}_{when\ U_R^-=0} \left|\frac{U_L^-}{U_L^+}\right|^2 = \left|\frac{m_{21}}{m_{11}}\right|^2; \qquad T\left[1\right] \underbrace{=}_{when\ U_R^-=0} \left|\frac{U_R^+}{U_L^+}\right|^2 = \left|\frac{1}{m_{11}}\right|^2; \tag{7}$$

$$R\left[N\right] \underbrace{=}_{when\ U_R^-=0} \left|\frac{U_L^-}{U_L^+}\right|^2 = \left|\frac{M[N]_{21}}{M[N]_{11}}\right|^2; \quad T\left[N\right] \underbrace{=}_{when\ U_R^-=0} \left|\frac{U_R^+}{U_L^+}\right|^2 = \left|\frac{1}{M[N]_{11}}\right|^2. \tag{8}$$

Using Eq. (5), we have:

$$R\left[N\right] = \left|\frac{M[N]_{21}}{M[N]_{11}}\right|^2 = \left|\frac{Sin\left[N\alpha\right]\ m_{21}}{Sin\left[N\alpha\right]\ m_{11} - Sin[(N-1)\alpha]}\right|^2; \tag{9}$$

$$T\left[N\right] = \left|\frac{1}{M[N]_{11}}\right|^2 = \left|\frac{Sin\left[\alpha\right]}{Sin\left[N\alpha\right]\ m_{11} - Sin[(N-1)\alpha]}\right|^2. \tag{10}$$

Even if the reflection rate of a single film is not zero ($m_{21} \neq 0$), the reflection rate of N films may still be zero, as long as $Sin\left[N\alpha\right] = 0$. This is due to the interference among the reflected waves. When all the films are elastic films, $R\left[N\right] = 0$ must come with a perfect transmission, i.e., $T\left[N\right] = 1$. It implies there are many reflections and transmissions between films. Of course, these motions bouncing back and forth are favorable for enhancing the interactions of incoming wave with the target nuclei in each film. Particularly, when the many-body phase-shift, $\delta_m = \frac{\pi}{2}$, the peak of the wave function may reach the surface of the target nucleus. It will further increase the interaction between the incoming wave and target nucleus and enhance the quantum transition probability—the resonant quantum transition.

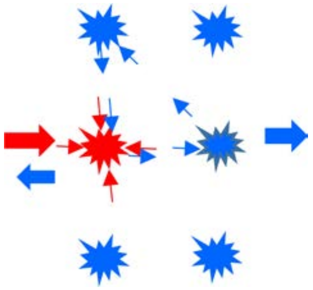

Figure 3. Primary injected wave (red) and secondary scattered wave (blue).

3. The Resonance in a Single Film: 2-Body Phase-Shift δ_2 and Many-Body Phase-Shift δ_m

Multiple scattering happens not only between films, but also inside each film**.** The primary injected wave will be scattered by many scatterers in a film. In Fig. 3, the red incident plane wave will be decomposed to many spherical waves around many scatterers. Each incoming spherical wave will be scattered by an individual scatterer and produce the blue scattered spherical waves. The blue scattered wave will propagate inside the film and will be scattered by other scatterers in the lattice. At thermal energy, the wavelength of the deuteron is 1.3 Å, which is comparable with the crystal constant (palladium's crystal constant is 3.89 Å). Thus, there may be interference between the incident wave and scattered wave as well. This interference may lead to the many-body phase shift, $\delta_m = \frac{\pi}{2}$, even if the 2-body phase shift, $\delta_2 \neq \frac{\pi}{2}$. The wave function of 2-body scattering in quantum mechanics, ψ_2, is expressed by a linear combination of plane wave in z-direction, and a spherical outgoing wave scattered by the scatterer at point $r = 0$:

$$\psi_2 \approx e^{i\,k\,z} + f(\theta,\varphi)\frac{e^{i\,k\,r}}{r}. \tag{11}$$

Many-body scattering in a single film is expressed by:

$$\psi_{ms} \approx \sum_s \{e^{i\,k\cdot r_s} + f(\theta,\varphi)\frac{e^{i\,k\,r_s}}{r_s}\}. \tag{12}$$

Here, ψ_{ms} is the summation of incoming waves and scattered waves around each scatterer at every lattice point, $\boldsymbol{R_s}$. $\boldsymbol{k}$ **is** the wave vector in various directions (k is its magnitude).

$$\boldsymbol{r_s} \equiv \boldsymbol{r} - \boldsymbol{R_s}. \tag{13}$$

$\boldsymbol{r_s}$ is the radius from one scatterer at one of lattice points at $\boldsymbol{R_s}$. Because many scatterers interact with one another, the resulting wave dynamics become highly complex. Fortunately, the electron screening simplifies the situation. Low energy electron diffraction (LEED) assumes a muffin-tin-like potential to describe the potential field [2]. It means that the individual scatterer would not change the potential field of other scatterers, the only change is due to the change of the boundary condition. In 2-body scattering, the scattered wave function propagates to infinity where the potential field is zero. However, in the case of many-body scattering the scattered wave function would meet a lot of boundaries which are the surfaces of other muffin-tins. In 2-body scattering, we use the phase-shift, δ_2, to describe the effect of boundary on the wave function. During the scattering, the incoming plane wave has to be decomposed into many spherical waves with different angular momentum, *l*, because the interaction between the wave and scatterer varies for different angular-momentum due to the variation of the "collimate distance" at one scatterer:

$$e^{i\ k\cdot r_s}=\sum_{l,m}4\pi i^l(-1)^m Y_{l,m}(\Omega_k)j_l(kr_s)Y_{l,m}(\Omega_{r_s}). \tag{14}$$

Here, $j_l(kr_s)$ is the spherical Bessel function. It describes the free motion of the proton outside the muffin-tin region in the film. It is important to notice that

$$j_l(kr)\xrightarrow{kr\ll 1}\frac{(kr)^l}{(2l+1)!!}. \tag{15}$$

It implies that at low energy, the S-wave (*l=0*) would be dominant in the summation (14) because the momentum of deuteron, *k*, is very small. Hence, we may keep S-wave only in our qualitative discussion. This will further simplify the complicated situation. Otherwise, *m* would run over *-l, -(l-1), -(l-2),…(l-1), l* and *l* would run over all integer numbers from 0 to ∞. $Y_{l,m}(\Omega_k)$ and $Y_{l,m}(\Omega_r)$ are the spherical functions in the direction of ***k*** and ***r*.** When *r* is far away from the muffin-tin [2],

$$j_l(kr)\xrightarrow{kr\gg 1}\frac{Sin[kr-\frac{l\,\pi}{2}]}{kr}. \tag{16}$$

It corresponds to a spherical wave in and a spherical wave out without any phase-shift, i.e. $\delta_2=0$. Indeed, the muffin-tin potential would change the wave function, and have an additional outgoing spherical wave $h_l^{(1)}(kr)$. $h_l^{(1)}(kr)$ is the first kind of spherical Hankel function, and has the desired asymptotic behavior as a spherical outgoing wave:

$$h_l^{(1)}(kr)\xrightarrow{kr\gg 1}\frac{(-i)^l}{i\ kr}e^{i((kr-\frac{l\pi}{2})}(1+\frac{il\,(l+1)}{2kr}). \tag{17}$$

It just has the form of the second term in eq. (12). Thus,

$$\psi_{ms}\approx\sum_s e^{i\ k\cdot r_s}+f\,(\theta,\varphi)\,\frac{e^{i\ k\ r_s}}{r_s}=\sum_{s,l,m}\{4\pi i^l(-1)^m Y_{l,m}\,(\Omega_k)\,[j_l\,(kr_s)+t_l\ h_l^{(1)}(kr_s)]Y_{l,m}\,(\Omega_{r_s})\}. \tag{18}$$

When multiple scattering is ignored, the coefficient of the linear combination, t_l , may be expressed by 2-body phase-shift, δ_{2l}, as [2]:

$$t_{2l}\ =ie^{i\delta_{2l}}Sin[\delta_{2l}]. \tag{19}$$

For low energy deuteron, only the S-wave is kept,

$$\psi_{ms}\approx\sum_s\{4\pi Y_{0,0}\,(\Omega_k)\,[j_0(kr_s)+t_{20}h_0^{(1)}(kr_s)]Y_{0,0}(\Omega_{r_s})\}; \tag{20}$$

$$t_{20}\ =ie^{i\delta_{20}}Sin[\delta_{20}]. \tag{21}$$

Here, δ_{20} is defined as 2-body phase-shift with S-wave only. When the other scatterers' effect is included, δ_{20} in t_{20} would be replaced by many-body phase-shift, δ_{m0}.

$$t_{m0}=ie^{i\delta_{m0}}Sin[\delta_{m0}]; \tag{22}$$

$$t_{m0}=\frac{t_{20}}{1-G_{ST}t_{20}}. \tag{23}$$

Eq. (23) shows the many-body phase-shift, δ_{m0}, in terms of 2-body phase-shift, δ_{20}, and G_{ST}. G_{ST} includes all the effects from all the scattered waves from all other scatterers. In the low energy electron diffraction theory [2] G_{ST}

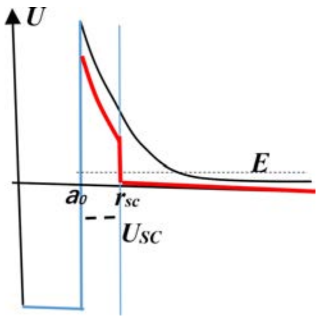

Figure 4. The silo-like potential with electron screening (Red line).

is called the structure factor which is a factor to show the feed-back effect of the scattered wave, $h_0^{(1)}(kr_s)$. When the scattered wave $h_0^{(1)}(kr_s)$ is leaving one scatterer, it becomes incoming waves for all other scatterers inside the film. Every other scatterer would scatter this secondary incoming wave, and produce the third scattered wave which may feed-back to the first scatterer (the red one in Fig. 3). Then, this feed-back incoming wave would be scattered by the red scatterer again. This superposition of waves would continue to form an infinite geometric series with a common ratio, $(G_{ST} \cdot t_{20})$. The details about crystal structure factor, G_{ST}, may be found in any LEED book. Our interest is that G_{ST} will make the many-body phase-shift, $\delta_{m0} = \frac{\pi}{2}$, even if 2-body phase-shift, $\delta_{20} \neq \frac{\pi}{2}$. This is the key point of Lattice Enhanced Nuclear Resonance—The resonance induced by multiple scattering.

When $\delta_{m0} = \frac{\pi}{2}$, $t_{m0} = -1$; then

$$\begin{aligned}\psi_{ms} &\approx \sum_s \{4\pi Y_{0,0}(\Omega_k)\,[j_0(kr_s)+t_{m0}h_0^{(1)}(kr_s)]Y_{0,0}(\Omega_{r_s})\} = \sum_s \{4\pi Y_{0,0}(\Omega_k)\,[j_0(kr_s)-h_0^{(1)}(kr_s)]Y_{0,0}(\Omega_{r_s})\} \\ &= \sum_s \{4\pi Y_{0,0}(\Omega_k)\,[j_0(kr_s)-(j_0(kr_s)+in_0(kr_s)]Y_{0,0}(\Omega_{r_s})\} = \sum_s \{4\pi Y_{0,0}(\Omega_k)\,[-in_0(kr_s)]Y_{0,0}(\Omega_{r_s})\}. \quad (24)\end{aligned}$$

Eq. (24) shows the cancellation of incoming $j_0(kr_s)$ due to interference. $n_0(kr_s)$ is the spherical Neumann function. Its amplitude has the desired behavior—peaked at the muffin-tin surface where kr_s<<1:

$$n_0(kr_s) = -\frac{Cos\,[kr_s\,]}{kr_s}; \quad (25)$$

Now, the question is if this spherical Neumann function would be connected to the irregular Coulomb wave function, $\frac{G_0(kr_s)}{kr_s}$, which is the necessary condition to create a mother state for a resonant transition to the daughter state as we proposed in 2-step nuclear resonance model [3], [4].

4. The Connection of the Wave Function at the Interface Between Coulomb Field and Zero-Field Regions

In multiple scattering model, the potential field outside the electron screening region ($r > r_{SC}$ in Fig. 4) and inside the silo-like region ($a_0 < r < r_{SC}$ in Fig. 4) are shown by red line. The electron screening effect has been treated as an electron screening potential, U_{SC}, which accelerates the incoming positive ion. Indeed, the incident proton energy (E) is conserved in a static electrical field, but its momentum (k_c) inside the down-shifted Coulomb field equals to $\sqrt{\frac{2\mu\left(E-\frac{Ze^2}{4\pi\varepsilon_0 r}+U_{SC}\right)}{\hbar^2}}$, and its momentum outside the silo-like region (k) equals to $\sqrt{\frac{2\mu E}{\hbar^2}}$. $\hbar$ is the reduced Planck Constant, μ is the reduced mass of the deuteron, ε_0 is the dielectric constant of vacuum, Ze is the electrical charge

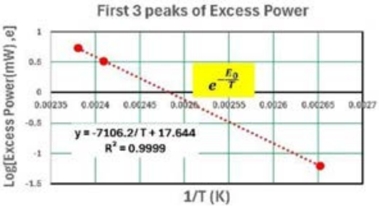

Figure 5. The Boltzmann factor is confirmed by the first 3 points in Fig 1.

of the screening material, U_{SC} is the electron screening potential. Hence, inside the silo-like region the irregular Coulomb function, $G_0(\rho, \eta) \equiv G_0\left(k_C r, \frac{1}{k_C a_C}\right)$. Here, $a_C \equiv \frac{4\pi\varepsilon_0\hbar^2}{\mu Z e^2}$. In order to make a smooth connection between $\frac{G_0(kr_s)}{kr_s}$ and $(-\frac{Cos[kr_s\,]}{kr_s})$ at the interface face ($r = r_{SC}$ in Fig. 4), we have to check if both of them have the same sign for their logarithmic derivative. The logarithmic derivative of $G_0\left(k_C r, \frac{1}{k_C a_C}\right)$ is negative in the region where E is less than the potential energy. However, $Cos\,[kr_s\,]$ has a negative logarithmic derivative only in the region $kr_s < \frac{\pi}{2}$. In LEED, the radius of muffin-tin potential is not strictly defined. Only the phase-shift, δ_2, plays an important role in its effect on other scatterers. If we assume the radius of the silo-like potential, r_{SC}, is in the order of 10^{-14} m, which is less than the radius of the innermost orbit of the electrons for screening material, but is still greater than the nuclear radius of the screening material; then, $k < \frac{\pi}{2r_{sc}}$ for all "cold fusion" experiments which were done at temperature lower than 2000°C. Thus it is sure that the wave function in the zero-field region would be smoothly connected to $G_0\left(k_C r, \frac{1}{k_C a_C}\right)$ at interface, when the phase-shift for multiple scattering, $\delta_{m0} = \frac{\pi}{2}$. In other words, the wave function, $n_0(kr_s)$, would be connected to $G_0\left(k_C r_S, \frac{1}{k_C a_C}\right)$ at interface and makes a peak at the surface of the nucleus of the screening material. This peak-wise wave function produced by multiple elastic scattering within the lattice constitutes the initial state for a transition to the final state (a bound state) to produce the excess power. This excess power is much greater than that in the non-resonance case where the peak of the initial wave function is outside of Coulomb barrier region ($\delta_{m0} \neq \frac{\pi}{2}$). In Appendix, we have shown that the wave function peak at nuclear surface would turn Gamow factor ($e^{-\frac{3380}{T^{1/3}}}$) into Boltzmann factor ($e^{-\frac{E_0}{k_B T}}$). Here, E_0 is the resonance energy, k_B is the Boltzmann constant, T is the temperature in Kelvin. This ($e^{-\frac{E_0}{k_B T}}$) factor is confirmed by the experimental data for the first 3 points in Fig. 1 (see Fig. 5, the effect of heat of formation on heat flow for deuteride in Pd has been deducted.) This temperature-dependence, $e^{-\frac{E_0}{k_B T}}$, has been found in 6 labs of 5 countries [5] as well. Indeed, the slope in Fig. 5 (-7106.2K) is close to that in Pd-D gas loading experiment (-6507.5K) at Tsinghua University [5].

5. Possible Nuclear Reactions at Resonance

When resonance puts the projectile at the surface of target nucleus, there are 2 possible nuclear interactions suggested by experimental results: the weak interaction [6] and the strong interaction [7]. As Bethe pointed out for p+p reactions [8], d+d reaction may produce ^4T through the K-electron capture first; then, ^4T may decay to ^4He. This weak interaction might not affect the calorimetric measurement due to the small coupling constant (see Appendix), and the possible neutrino emission. On the other hand Miles' helium and excess heat correlation measurements show that the strong interaction might produce ^4He directly. S.E. Kooning [9] proposed a method to evaluate the reaction rate by

$$\Lambda = A\ |\Psi_d(a_0)|^2 \tag{26}$$

Here, $A = 1.5\times 10^{-16} cm^3 s^{-1}$ for $d{+}d{\rightarrow}^3He + n \oplus ^3T + p$ reactions. $\Psi_d(a_0)$ is the value of the wave function at the nuclear surface for d+d relative motion(in unit of $cm^{3/2}$). When the reaction rate, Λ, is averaged over Maxwellian distribution using (A14), we have

$$< \Lambda >= A\; I_{resonance} = A * (\frac{\mu}{2\pi k_B T})^{\frac{3}{2}} \left(\frac{a_c}{a_0}\right)^2 \frac{e^2}{4\pi\varepsilon_0 \hbar}\frac{1}{\mu} e^{-\frac{E_0}{k_B T}} \frac{2\pi}{C_2} \tag{27}$$

C_2 is the parameter which determines the energy dependence of the phase shift [4]. Using the **method** in Appendix of reference [4] we have $C_2 = 0.254 keV^{-1}$ for $d + d{\rightarrow}^3He + n \oplus ^3T + p$ reaction in CM system. From Fig. 5, $E_0 = 7106.2\ K$, and from Fig. 1, T= 414.5 K. Eq. (27) gives $< \Lambda > = 1.2 \times 10^{-14} cm^3 s^{-1}$. This reaction rate is for an incident deuteron plane wave normalized to per unit density at infinity. In order to compare with the experimental result in Fig. 1, we need the information about the deuteron flux incident on trapped deuteron in Pd lattice. The deuteron diffusion flux is mainly due to the classical 2-body scattering on the Pd atoms, only the multiple scattering on trapped deuterons may introduce the quantum flux peaks. From Fig. 1, the pressure in the reaction cell changes 0.015 Pa/sec at the first peak. It gives an anomalous flux of $\sim 10^{13}$ deuterons $cm^{-2}s^{-1}$ passing through the thin wall of a Pd tube in a 12.5 ml reaction cell. The thermal speed of the deuteron at 414.5K is $1.85 \times 10^5 cm{\cdot}s^{-1}$. It implies a deuteron density of 10^8 cm^{-3} which is from the multiple scattering on the trapped deuterons. The Pd tube volume is $2.6cm \times \phi 0.4cm \times 0.01cm = 0.033cm^3$. The deuteron loading ratio is $\sim$0.01 at 414.5K and 1.4 atm; hence, the number of the trapped deuterons is $\sim 10^{18}$. Hence, the resonance d+d reaction rate in Pd tube is $\sim 10^{12} s^{-1}$. It implies a measurable excess power at the level of 1 W. Consider the fact that not all the trapped deuterons are involved in this resonant multiple scattering. It seems consistent with the experimental result of 2 mW.

6. The Possible Resonance During the Hopping Process

The application of multiple scattering requires three conditions [10]: (1) The wave length of incident particles is comparable with the crystal constant; (2) The 2-body interaction potential well of the scatterers should not be overlapped each other. There must be a region to separate the individual potential well; (3) There is enough time to have a resonance before the hopping process to destroy this resonance. It seems possible to satisfy these conditions. The de Broglie wave length of a thermal deuteron is about 1 Å, which is comparable with the Pd crystal constant 3.89 Å. The electron screening might provide the separation among the individual potential wells of the scatterers. The phase speed of the thermal deuteron is about $10^5 cm{\cdot}s^{-1}$. It takes $10^{-13}s$ to travel forth and back between the scatterers in the lattice. This travelling time is much shorter than the hopping time (about 100ps [11]). If the quantum transition to a lower state happens before the hopping process, this resonance would be able to enhance this transition. Hagelstein's group [12] has analysed the transition, and answered the question about the gamma radiation as well.

7. The Bouncing Back and Forth Motion Between Thin Films

The reflections between the coating films play a critical role in most of "cold fusion" experiments, because the reflections enhance the total flux. It explains not only the excess power, but also the correlation between the anomalous flux and the excess power. A measurement of the reflection number between the films before the penetration to the next film is the ratio of reflection rate to transmission rate. Using eq. (7), $\frac{R[1]}{T[1]} = |m_{21}|^2$. $|m_{21}|^2$ is calculated in low energy electron diffraction (LEED) theory. It is directly related to many-body phase shift. It is complicated; however, for the case of S-wave dominant in low energy, there is a simple relation based on Optical Theorem. The imaginary part of the forward scattering amplitude, $f\,(0)$, is related to cross-section, σ_0 , and phase shift, δ_0, as

$$Im\left[f\,(0)\right] = \frac{k}{4\pi}\sigma_0 = \frac{1}{k}\left(Sin[\delta_0]\right)^2 . \tag{28}$$

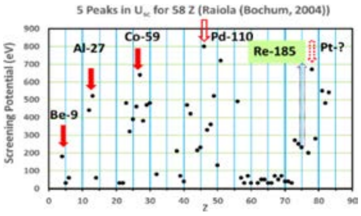

Figure 6. 5-peak pattern in electron screening potential (red arrows).

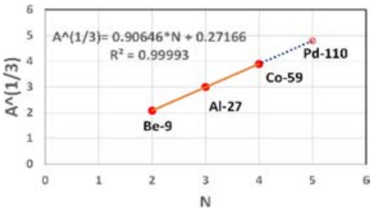

Figure 7. A$^{1/3}$-Plot for the first 3 peaks in U$_{SC}$.

When $\delta_0 = \frac{\pi}{2}$, $Im\left[f\left(0\right)\right]$ reaches its maxima, and $Re\left[f\left(0\right)\right] = \frac{1}{k}Sin\left[\delta_0\right]Cos\left[\delta_0\right] = 0$. It means that the amplitude of forward scattering, $\left|f\left(0\right)\right|$, takes maxima at $\delta_0 = \frac{\pi}{2}$. Since the S-wave is isotropic, so, the back scattering amplitude $f\left(\pi\right)$ takes its maxima as well. Hence when the multiple scattering makes many-body phase shift, $\delta_{m0} = \frac{\pi}{2}$, it also makes $\left|m_{21}\right|^2$ of a single film maximum. Thus, the bouncing back and forth number is maximized while the wave function peak reaches the nuclear surface. For the multiple film case, when we observe the transmission rate, $T[N]$, has a maxima, the corresponding reflection rate, $R\left[N\right] = 1 - T[N]$ is minimized. This implies good confinement in multiple films. It means there will be a lot of bouncing back and forth motions between 2 films before entering the next slot, and it maximizes the number of multiple scatterings. Consequently, the maximum nuclear reaction rate is correlated with the maximum transmission rate as shown by Fig. 1.

8. Multiple Scattering in Electron Screening Experiment

A thin film coating of screening material on a metal substrate is done in all the electron screening experiments. The multiple scattering between this screening material and the substrate might happen when the injected deuterons are slowing down. In Fig. 6 red arrows show a 5-peak pattern in atomic charge number (Z) for electron screening potential, U_{SC}. Prof. Kasagi [13] pointed out that these peak values need an additional mechanism to be explained. Prof. Nagel discovered [14] the similarity between the 5-peak pattern in nuclear transmutation of metal hydrides and in U_{SC}. The multiple scattering might provide an additional reason for the nuclear origin of this 5-peak pattern, because the 2-body phase shift, δ_{20}, in eq. (21) is determined by the boundary condition at the nuclear surface. It should have periodicity in atomic mass number (A). Fig. 7 is the A$^{1/3}$-plot for the first 3 peaks in Fig. 6. Be-9, Al-27, Co-59 are closely on a straight line. It may be extended to the 4-th peak Pd-110, which is in good agreement with Fig. 6. To verify its nuclear origin, we may run the electron screening experiment again using enriched Pd-110 to see if there is any increase in U_{SC}, because the abundance of Pd-110 in natural Pd is only 11.7%. Or, we may detect whether there is any characteristic radiation from Pd-111 in the nuclear product (2.23 MeV $\beta-$radiation with $T_{1/2}$ ~24min. from Pd-111G, and 170 keV $\gamma-$radiation with $T_{1/2}$ ~5.5 hours from Pd-111m) [15]. Iwamura's early device for nuclear transmutation might be used to test if there is any peak flux near 147°C. This can be done by holding that temperature for 17 hours; and then immediately detecting these characteristic β and γ radiations. The positive results of these proposed experiments would confirm not only this coherent resonance mechanism, but also solve the puzzle of missing neutrino or gamma radiation in "cold fusion" because Pd-111G ($5/2^+$) and Pd-111m ($11/2^-$) are high spin nuclei with different parities. Only in many-body coherent quantum transition they might be produced at low energy. This would be compelling evidence of lattice enhanced nuclear resonance.

9. Conclusion

There are 2 kinds of flux. Only the quantum flux caused by multiple scattering is correlated with excess power. The multiple scattering provides an initial mother state for Bethe's weak interaction transition or for Oppenheimer's strong interaction transition. Multiple scattering in lattice has 3 effects: (1) turns a group of 2-body phase shift into many-body phase shift for coherent nuclear resonance; (2) bouncing back and forth motion between thin films enhances the effective incoming flux for coherent quantum transitions; (3) reduces the reflection rate at the surface of multiple films to further enhance the effective incoming flux. It appears as a correlation between quantum flux and anomalous excess power. ***This coherent resonance turns a metal hydride into a fuel burning with hydrogen, rather than a furnace for burning hydrogen in it***. It is a ***Lattice Enhanced Nuclear Reaction.*** It shows a bright future for a quantum hydrogen energy.

Acknowledgements

Many thanks to D. Nagel, G. Miley, T. Passell, F. Will, and J. Rothwell for their important assistance.

Appendix. Gamow Factor is Replaced by Boltzmann Factor for Low Energy Nuclear Resonance

In this appendix we will discuss how to modify Bethe's calculation [8] in order to include the case of resonance.

In the resonance integration the contribution from a resonance depends on both its width and height. In eq. (A1) the width is determined by the coefficient, $Tan\,[K]$, and the height is determined mainly by the irregular Coulomb wave function, G (We keep Bethe's notation [8] in this Appendix for comparison). When the phase-shift, K, passes through the resonance point, $\pi/2$, very quickly with the energy reduction, the energy width of a resonance is very narrow. However, if the resonance height, G, also increases very quickly with the energy reduction; then the resonance effect may still remain. Hence, we need to study the energy dependence of both $Tan\,[K]$, and G value near the nuclear surface when $K \to \frac{\pi}{2}$, in order to evaluate its contribution to the resonance integration.

What should be changed to include the case of resonance in Bethe's calculation [8]? The initial wave function of p-p elastic scattering state in the Coulomb field region outside the nuclear potential well was written as:

$$\Psi_p(r) = \frac{e^{iK} Cos\,[K]\ \ (F + Tan\,[K]\ \ G)}{k\ r}. \tag{A1}$$

Here k is the momentum of the relative motion in the c.m. system, r is the distance between the projectile and the target. At low energy,

$$F = C\varrho\Phi(r); \quad G = C^{-1}\Theta(r). \tag{A2}$$

$$C \equiv \sqrt{2\pi\eta}\, e^{-\pi\eta}; \varrho \equiv k\, r, \eta = \frac{e^2}{4\pi\varepsilon_0\hbar v} \equiv \frac{1}{ka_c};\ a_c \equiv \frac{4\pi\varepsilon_0\hbar^2}{\mu e^2}. \tag{A3}$$

Here, C determines the Gamow suppression. ε_0 is the dielectric constant of the vacuum, $\hbar$ is the Planck Constant divided by 2π, v is the relative velocity between the projectile and the target, e is the electric charge of a proton, μ is the reduced mass of the projectile and the target. $\Phi(\mathrm{r})$ and $\Theta(\mathrm{r})$ are independent of energy, and they are very close to 1 at the surface of nuclear potential $(r = r_0)$. Hence, at low energy,

$$Tan\,[K] = -\left[\frac{F}{G}\frac{\frac{1}{F}\frac{\partial F}{\partial r}-\frac{1}{w}\frac{\partial w}{\partial r}}{\frac{1}{G}\frac{\partial G}{\partial r}-\frac{1}{w}\frac{\partial w}{\partial r}}\right]_{r=r_0} = -2\pi\frac{r_0}{a_c}e^{-2\pi\eta}\left[\frac{\frac{1}{F}\frac{\partial F}{\partial r}-\frac{1}{w}\frac{\partial w}{\partial r}}{\frac{1}{G}\frac{\partial G}{\partial r}-\frac{1}{w}\frac{\partial w}{\partial r}}\right]_{r=r_0}. \tag{A4}$$

$Tan\,[K]$ is very small, unless the denominator, $\left[\frac{1}{G}\frac{\partial G}{\partial r}-\frac{1}{w}\frac{\partial w}{\partial r}\right]_{r=r_0} = 0$. Indeed this is just the resonance condition which was not included in Bethe's calculation (w is the wave function inside the nuclear potential well). Bethe assumes K is small ($\sim$0.0017), and replaces $e^{iK}Cos\,[K]$ by 1 in (A1). However, we are considering now the cases including $K \rightarrow \frac{\pi}{2}$, the replacement, $e^{iK}Cos\,[K] \rightarrow 1$, is no longer valid. Eq. (A1) should be rewritten as:

$$\Psi_p\,(r) = \frac{e^{iK}}{k\,r}\left(Cos\,[K]\;F + Sin\,[K]\;G\right) = \frac{e^{iK}}{k\,r}\left(Cos\,[K]\;F + \frac{1}{\sqrt{1+(Cot\,[K])^2}}\,G\right) \tag{A5}$$

G is much greater than F at the nuclear surface according to (A2) and (A3). Thus, Bethe still keeps G in (A5) in his non-resonance calculation and calls it "resonance effect". Eq. (A5) is now written as:

$$\Psi_p\,(r) = \frac{e^{iK}}{k\,r}C\varrho\left(Cos[K]\Phi + \frac{1}{\sqrt{1+(Cot\,[K])^2}}C^{-2}\varrho^{-1}\Theta\right) \tag{A6}$$

The energy-dependence of the second term in (A6) is very different between the case of resonance and non-resonance. For the case of no resonance, $(Cot\,[K])^2 \gg 1$:

$$\frac{1}{\sqrt{1+(Cot\,[K])^2}}C^{-2}\varrho^{-1} \approx Tan\,[K]\,C^{-2}\varrho^{-1} = Tan\,[K]\,\frac{e^{2\pi\eta}}{2\pi}\frac{a_c}{r_0} \equiv \lambda. \tag{A7}$$

According to (A4), $(Tan\,[K]\,\frac{e^{2\pi\eta}}{2\pi})$ is independent of energy when there is no resonance at low energy. Hence, λ is independent of energy. When the nuclear reaction rate was integrated over the Maxwell distribution of the velocity, the Gamow factor, *C*, in front of $\left(Cos[K]\Phi + \frac{1}{\sqrt{1+(Cot[K])^2}}C^{-2}\varrho^{-1}\Theta\right)$ in (A6) was the only one factor to compete with the Boltzmann factor, $(\frac{\mu}{2\pi k_B T})^{\frac{3}{2}}Exp[-\frac{\mu v^2}{2k_B T}]4\pi v^2 dv$. Here, T is the temperature of the protons, and k_B is the Boltzmann Constant. Since the nuclear reaction rate, $\sigma\,v$, is proportional to the square of the modulus of the wave function; hence, the term involving $|C\,\lambda|^2$ in the integration may be written as:

$$I_{Gamow} = (\frac{\mu}{2\pi k_B T})^{\frac{3}{2}}\int_0^\infty |C\,\lambda|^2\,Exp\left[-\frac{E}{k_B T}\right]\frac{2\pi}{\mu}vdE = (\frac{\mu}{2\pi k_B T})^{\frac{3}{2}}\int_0^\infty |\lambda|^2\,\frac{2\pi\eta}{e^{2\pi\eta}}Exp[-\frac{E}{k_B T}]\frac{2\pi}{\mu}vdE. \tag{A8}$$

Here, $E = \frac{\mu v^2}{2}$ is the kinetic energy. The integrand in (A8) is a product of two factors: an exponentially decreasing $Exp\left[-\frac{E}{k_B T}\right]$, and an exponentially increasing $\frac{1}{e^{2\pi\eta}}$ with E. Their product has a peak at

$$E_G = (\frac{\mu}{2}(\pi\frac{e^2}{4\pi\varepsilon_0\hbar}k_B T)^2)^{\frac{1}{3}}. \tag{A9}$$

Using the steepest descent method, in the case of p-p reaction without resonance Bethe obtained the integration of the famous Gamow peak.

$$I_{Gamow} = 2{*}3^{-\frac{5}{2}}\;(\lambda)^2\;(\frac{3380}{(T)^{\frac{1}{3}}})^2\;(Exp[-\frac{3380}{(T)^{\frac{1}{3}}}]).(T\text{ is in units of Kelvin}) \tag{A10}$$

In the case of resonance, $K \to \frac{\pi}{2}$, $Cot\left[K\right]^2 \to 0$, $\frac{1}{\sqrt{1+(Cot[K])^2}} \to 1$. The C^{-2} in the coefficient of the second term in (A6) defeats not only the Gamow suppression (C), but also the narrowness of resonance width, when the reaction rate is integrated over the Maxwell distribution of the velocity.

$$I_{resonance} = (\frac{\mu}{2\pi k_B T})^{\frac{3}{2}} \int_0^\infty \left| \frac{1}{\sqrt{1+\left(Cot\left[K\right]\right)^2}} \left(\frac{e^{2\pi\eta}}{2\pi}\right) \frac{a_c}{r_0} \right|^2 C^2 Exp[-\frac{\mu v^2}{2k_B T}] 4\pi v^2 dv. \tag{A11}$$

Here, we have to carefully consider the energy dependence of the phase shift, K. This information may be extracted from the experimental data of the fusion cross-section at low energy. Based on the Evaluated Nuclear Data Files (ENDF) in the National Nuclear Data Center (NNDC), a comprehensive study of the nuclear fusion cross-sections (see the Appendix in reference [4]) at the low energy showed that for the interaction between two charged nuclei at low energy, $Cot\left[K\right]$ may be approximated by a product of two factors: a fast changing factor, $(\frac{e^{2\pi\eta}}{2\pi})$, and a slow varying factor, $C_2\left(E-E_0\right)$:

$$Cot\left[K\right] = (\frac{e^{2\pi\eta}}{2\pi})\, C_2\left(E-E_0\right). \tag{A12}$$

Here E_0 is the resonance energy, and C_2 is a constant from p-p elastic scattering data. Therefore.

$$\begin{aligned} I_{resonance} &= (\frac{\mu}{2\pi k_B T})^{\frac{3}{2}} \int_0^\infty \left| \frac{1}{\sqrt{1+\left(\left(\frac{e^{2\pi\eta}}{2\pi}\right) C_2\left(E-E_0\right)\right)^2}} \left(\frac{e^{2\pi\eta}}{2\pi}\right) \frac{a_c}{r_0} \right|^2 \frac{2\pi}{e^{2\pi\eta}} \frac{e^2}{4\pi\varepsilon_0\hbar} Exp[-\frac{\mu v^2}{2k_B T}] 2\pi \frac{1}{\mu} dE \\ &= (\frac{\mu}{2\pi k_B T})^{\frac{3}{2}} \int_0^\infty \frac{1}{1+\left(\left(\frac{e^{2\pi\eta}}{2\pi}\right) C_2\left(E-E_0\right)\right)^2} (\frac{a_c}{r_0})^2 \left(\frac{e^{2\pi\eta}}{2\pi}\right) \frac{e^2}{4\pi\varepsilon_0\hbar} Exp[-\frac{E}{k_B T}] \frac{2\pi}{\mu} dE. \end{aligned} \tag{A13}$$

The integrand of (A13) has a very sharp peak near the energy, E_0, as shown in Fig. A1. The height of the peak is determined by the numerator which is proportional to $\left[e^{2\pi\eta} Exp[-\frac{E}{k_B T}]\right]_{E=E_0}$ and its width is determined by the denominator which is in the order of $\frac{1}{\left(\frac{e^{2\pi\eta}}{2\pi}\right) C_2}$. It is clear that the resonance effect is high enough to overcome the Gamow suppression. Although the width of the resonance peak is decreasing with the resonance energy, E_0, the sharply increasing peak height still contributes enough to overcome both the Gamow suppression and the narrowness of the resonance. The resonance peak acts just like a Delta-function to evaluate the specific value of the integrand after the integration. Using the deepest descent method again:

$$I_{resonance} = (\frac{\mu}{2\pi k_B T})^{\frac{3}{2}} \left(\frac{a_c}{r_0}\right)^2 \frac{e^2}{4\pi\varepsilon_0\hbar} \frac{1}{\mu} e^{-\frac{E_0}{k_B T}} \frac{2\pi}{C_2}. \tag{A14}$$

New features of low energy resonance. The resonance makes G dominant in the linear combination of the wave functions (A1). Hence, *the modulus of the wave function peaks at the surface of nuclear potential well;* and two new features appear:

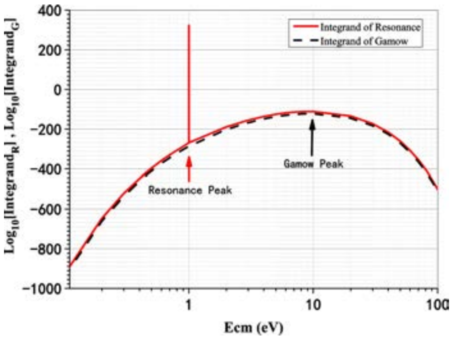

Figure A1. Solid line is the integrand of the resonance integration in (A13). The dashed line is the integrand of the Gamow integration in (A8). E_0=1.0 eV and C_2=0.00164 keV^{-1}. λ=4.80, and T=1000K.

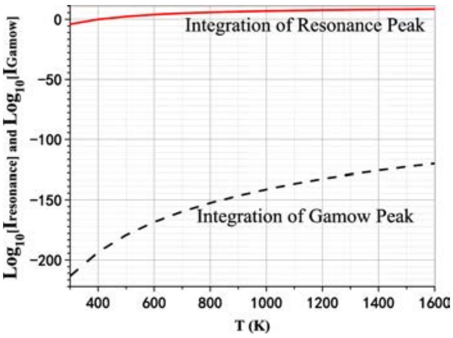

Figure A2. Comparison between the resonance integration $I_{\mathrm{resonance}}$ (Solid line) and I_{Gamow} (Dashed line). E_0=1.0 eV, C_2=0.00164 keV^{-1}, λ=4.80.

A. Gamow Suppression Disappears in the Resonance Integration

The Gamow factor is overcome by a resonance even if the resonance is at very low energy. Fig. A1 shows that two integrands in (A8) and (A13) are mostly similar in the logarithmic scale. The big difference appears only in the resonance region around $E = E_0$. When the resonance energy , E_0, is getting lower, the resonance peak height is getting higher as $e^{2\pi\eta}$ while the width of the resonance is getting narrower as $\frac{1}{e^{2\pi\eta}}$. The resonance peak is always high enough to keep the integration of resonance large, overcoming the Gamow suppressing factor. It will enhance the nuclear reaction rate greatly, particularly at low temperatures. Fig. A2 gives the comparison between two integrations $I_{resonance}$ in (A14) and I_{Gamow} in (A10) in logarithmic scale. The solid line is $I_{resonance}$ which is much greater than the I_{Gamow}, shown by the dashed line. The resonance overwhelms the Gamow suppression in the evaluation of the integral $I_{resonance}$.

B. The Evidence of a Low Energy Resonance

The major temperature dependence of the integration of resonance in (A14) is an exponential function, $e^{-\frac{E_0}{k_B T}}$ (The Boltzmann factor). This temperature dependence is a typical straight line in a semi-logarithmic plot, when $\frac{1}{T}$ is used as the abscissa. We may use this exponential dependence to identify a low energy resonance. This dependence has been found in 6 labs in 5 countries [5], and in Fig. 5 as well.

Discussion. Bethe proposed a two-step p-p reaction model: elastic scattering first to form a mother state; then followed by a nuclear transition from the mother state to a daughter state. This model makes low energy resonance feasible in the first step, and is favorable to the second transition to a bound state because the resonance keeps two charged particles closer even if the Coulomb barrier is high and the energy of the projectile is very low.

This model was proposed for p-p reaction; however, it might be applied to the case with higher charge number (Z). We should expect to observe this low energy resonance in a hydrogen-loaded metal as well.

The resonance puts the peak of the wave function at the surface of nuclear potential; hence, it enhances the interaction between the projectile and target. This effect is getting higher when the energy of projectile is getting lower. Indeed, when the energy is much lower than 1 eV, the projectile might be interacting with more than one target nucleus in a crystal of metal. Hence, the multiple scattering must be involved.

Indeed, the reaction rate, $\langle \sigma v \rangle$, in this 2-step model is mainly determined by the volume of the overlapping between the initial and final wave function, and the coupling constant: $(g\, b^3)$. Here g $\sim 10^{-4}$ sec^{-1}, is the Fermi coupling constant for weak interaction in Bethe's solar energy model; b$\sim 10^{-15}$m, is the scale of extension beyond the nuclear potential well for a neutron [8]. Hence $\langle \sigma v \rangle$ for 2-body nuclear fusion is still very small, even if the I_{Gamow} is replaced by $I_{resonance}$. Thus, we have to consider the strong interaction and the multiple scattering effect to enhance further the reaction rate, $\langle \sigma v \rangle$, in order to meet the experimental data.

References

[1] X. Z. Li, B. Liu, J. Tian, Q. M. Wei, R. Zhou, and Z. W. Yu, "Correlation between abnormal deuterium flux and heat flow in a D/Pd system", *J. Phys. D: Appl. Phys.* **36** (2003) 3095–3097.

[2] J. B. Pendry, Low Energy Electron Diffraction, Academic Press, (London and New York) 1974.

[3] X. Z. Li, Z. M. Dong, C. L. Liang, and G. S. Huang. "Resonant Surface Capture Model." *Journal of Condensed Matter Nuclear Science,* **29** (1) 2019: 440–52. https://doi.org/10.70923/001c.72523.

[4] X. Z. Li, C. L. Liang, G. S. Huang, B. Liu, J. Tian, S. Chen, Y. Chen, Z. M. Dong, and S. X. Zheng. 2025. "Cubic Root ($\sqrt[3]{A}$)—Law in Nuclear Transmutation of Metal Hydrides", *Journal of Condensed Matter Nuclear Science*, **39** (March,2024):322–45. https://doi.org/10.70923/001c.134020.

[5] D. J. Nagel, "Experimental Status of LENR", *ARPA-E Workshop on Low-Energy Nuclear Reactions*," p.16, 21-22 October 2021.

[6] Ed. Storms, "A New and Improved Understanding of Cold Fusion Based on the Observed Behavior," Presentation at ICCF26, Morioka City, Japan, May 26-30, 2025.

[7] M. Miles, and P. L. Hagelstein, "Consistency of helium production with the excess power in the palladium-D_2O electrochemical system". *Journal of Electroanalytical Chemistry*, 2025. **977**: p. 118786.

[8] H. A. Bethe, and C. L. Critchfield, "The formation of deuterons by proton combination", *Phys. Rev.* **54** (1938) 248-254.

[9] S. E. Kooning, and M. Nauenberg, "Calculated fusion rates in isotopic hydrogen molecules", *Nature*, **339**, 690-691 June 1989 DOI: 10.1038/339690a0.

[10] A. Gonis, and W.H. Butler, Multiple Scattering in Solids, Springer-Verlag, New York,1999.

[11] R.R. Arons, Y. Tamminga, "On the Diffusion of H and D in Pd between 50 and 300° K," *Physica Status Solidi (B),* vol. 40, issue 1, pp. 107-112.

[12] P. L. Hagelstein, F. Metzler1, M. K. Lilley, J. F. Messinger1, and N. Galvanetto1, "Models for nuclear fusion in the solid state," arXiv:2501.08338v2.

[13] J. Kasagi, Y. Honda, K. Fang, Screening energy for low energy nuclear reactions in condensed matter, Cold Fusion-Advances in Condensed Matter Nuclear Science, Edited by Jean-Paul Biberian, Elsevier 2020, p.167-187.

[14] D. J. Nagel, "Potential Correlations between Apparent Peaks in LENR Transmutation Data and Deuteron Fusion Screening Data", *Journal of Condensed Matter Nuclear Science*, **39** (March 2024):295–321. https://doi.org/10.70923/001c.134019.

[15] J. B. Natowitz and R. L. Wolke, "Isomeric Cross Sections and Yield Ratios of (d, p) Reactions below 15 MeV", *Phys. Rev.* **155** (1967),1352-1361.

J. Condensed Matter Nucl. Sci. 41 (2026) 113–116

Research Article

Preloaded NANOR®-Tech Trumps the “TDK Energy Solution”

Mitchell R. Swartz, Gayle M. Verner

JET Energy, Inc., Wellesley, MA USA ©

Abstract

Cold fusion (Lattice Assisted Nuclear Reactions: LANR) driven systems can deliver clean, large levels of energy production (through heat) which enable competing and superior handling properties and portability.

Keywords: Fusion, Nanor, Phusor, Power density, Energy density, Zirconium oxide

1. Introduction

TDK, a large Japanese electronics company, purports their new lithium oxide-based solid electrolyte energy production component replaces coin-shaped cell batteries. Further technical details were sought after their recent announcement which received good media reviews on-line, such as by Hackaday:

> *“While the energy density is high, keep in mind that the batteries of this type are usually tiny, so the total actual power available is probably not very high. Tiny batteries are definitely a thing. We are always hearing about breakthroughs, but we always wonder if and when we’ll see actual products.”*

The TDK battery competes with cold fusion and CF/LANR-derived systems, which deliver clean, large levels of energy production and density. High energy density is important which is why cold fusion (Lattice Assisted Nuclear Reactions: LANR) will be an oncoming contender.

As we show below, by contrast to simple batteries, the recent generations of CF/LANR energy production devices [which have preloaded ZrO_2-PdNiD nanomaterial at their core] demonstrate significant energy and power densities.

2.1. Background: Cold Fusion/LANR is Absolutely Real

Thirty-seven years of solid sterling evidence shows conclusive experimental LANR data proving excess heat of a nuclear origin, as reported by multiple groups. Loaded deuterons in PdD (often under difficult-to-achieve conditions) couple together in these active systems to generate *de novo* ^{4}He, loss of D, unique antiStokes and RF Deuterium-line emission signatures and considerable excess heat.

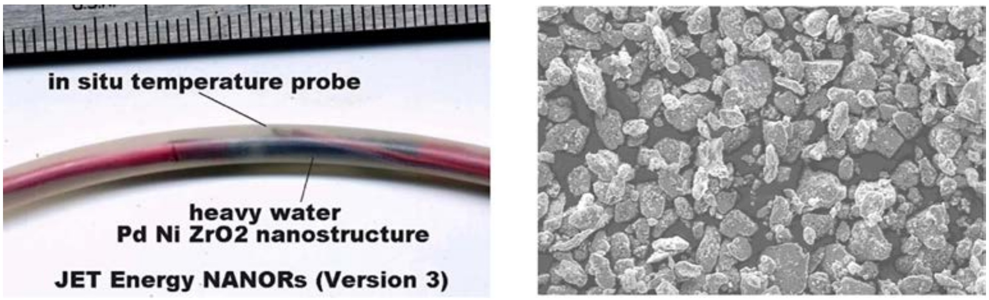

Figure 1. (left) –NANOR®-type Component; Series 3 NANOR®-type LANR component, (right) dry and preloaded ZrO$_2$-PdNiD nanostructured core material.

2.2. LANR has Progressed in Many Ways

Working CF/LANR systems led to open demonstrations (2 at MIT), academic courses, and new discoveries with advancements from BOTH aqueous solution systems and dry pre-loaded nanomaterial CF/LANR components.

Also, working CF/LANR systems now have increased incremental power gains (reflecting efficiency). Development of CF/LANR-specific diagnostics (antiStokes and RF emissions) and properties (quantum computers) now exist also.

2.3. Background-NANOE®-Type LANR Components

NANOR®-type LANR Components are a new generation of CF/LANR quantum electronic devices exhibiting large and reproducible energy gains. Most importantly, the activation of LANR is, for the first time, separated from loading. The core is ZrO$_2$PdNiD [Zr ($\sim$66%), Ni (0-30%), and Pd (5-25%) by weight] with additional D. The PdNiD nanostructured core islands are electrically isolated by the zirconia (ZrO$_2$) dielectric.

These NANOR®-type preloaded components are dry, sealed into an electrically conductive (high impedance) configuration, enabling superior handling properties and useful portability. The self-contained two electrical terminals NANOR®-type LANR components are fully preloaded with deuterons. They are $\sim$2 cm in length, with 30 to 400 milligrams of an active LANR nanocomposite ZrO$_2$-PdD core. The power density $\sim$19.50 watts/gram of nanostructured material, that improves their already superior handling and portability properties.

3. Experimental – Electric Power Drive

To accurately measure excess heat (XSH) in LANR, careful sequencing of input power to both the component and the ohmic control is required. We use precision-controlled power sources like a Keithley current source, Tekpower TP3005P, with DAQ monitoring. Analysis of the delivered and applied precise step functions yield calorimetry. For each step pulse, the electrical dissipation (V*I) is maintained over a long period of time. The results are confirmed by long-term time integration, which rules out false positives.

4.1. Result -Active Dry Preloaded ZrO$_2$-PdNiD LANR Component

The next figure shows the applied input voltage and resulting incremental power gain for NANOR®-type Component N5-02A, calibrated by an ohmic control resistor in Run EJan01A. Note how many orders of magnitude the incremental power gain realized from the active NANOR®-type component, compared to the ohmic control. Achieving these high

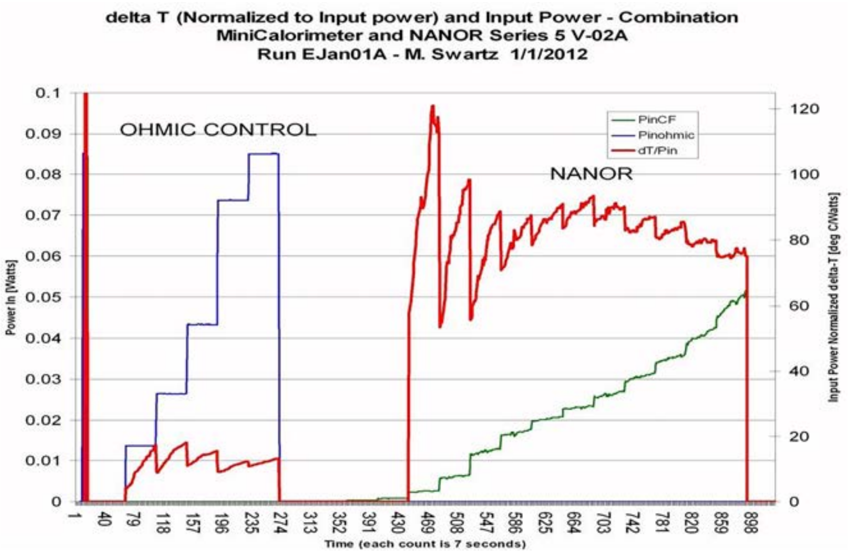

Figure 2. Preloaded NANOR® V-02A – Shown are the applied input voltage and resultant incremental power gain for NANOR®-type Component N5-02A, calibrated by an ohmic control resistor in a previous run (EJan01A).

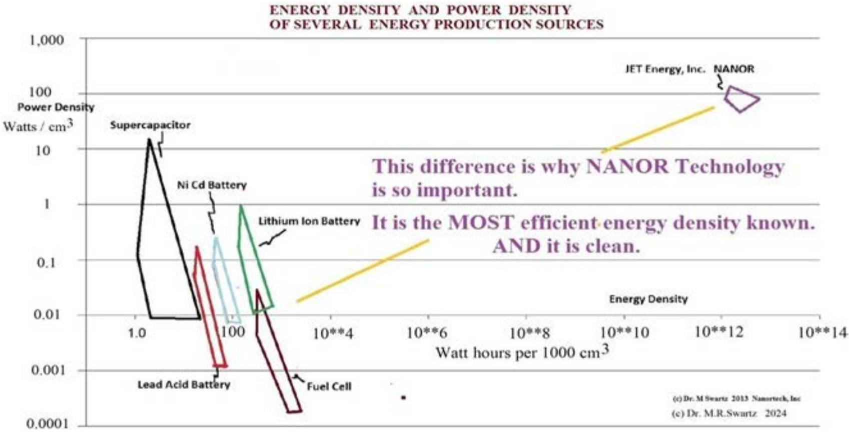

Figure 3. Power Density and Energy Density for several Energy Production and Energy Storage Systems including CF/LANR NANOR®-type Components.

incremental power gains has required improved alloys and their loading by deuterons, followed by careful avoidance of possible electric avalanches, thereby extending the duration of the heat production cycles.

4.2. Results - Range of Energies and Power Densities Available

The next cumulative graph [Figure 3] shows the range of energy densities and power densities available by several energy production and energy storage systems. CF/LANR energy production devices [which include NANOR®-type components with their preloaded ZrO_2-PdNiD nanomaterial at the core] demonstrate significant energy and power densities.

5. Conclusion: LANR is Important

LANR's fuel is abundant, larger and more available than all the Earth's oil reserves. Its energy production is clean, quiet, and so efficient that in the future, LANR will energize engines, motors, and electrical generators enabling transportation, improved health with new and improved opportunities.

Acknowledgements

The authors thank Joshua Gyllinsky and Susan Woods for helping these long-term efforts. NANOR® and PHUSOR® are registered trademarks. The IP technology described here is protected by US patents issued and pending.

References

[1] Williams, A, TDK Claims Solid State Battery With 100X Energy Density", Hackaday, June 18, 2024. https://hackaday.com/2024/06/18/tdk-claims-solid-state-battery-with100x-energy-density/

[2] Swartz M. R., Hagelstein P.I., Demonstration of Energy Gain from a Preloaded ZrO_2– PdD Nanostructured CF/LANR Quantum Electronic Device at MIT, J. Condensed Matter Nucl. Sci. 13, 516 (2014).

[3] Swartz M. R., Verner G., et al., Energy Gain From Preloaded ZrO_2–PdNi–D Nanostructured CF/LANR Quantum Electronic Components, J. Condensed Matter Nucl. Sci. 13, 528, (2014).

[4] Swartz, M., P. Hagelstein, G. Verner, "Impact of Electrical Avalanche Through a ZrO_2-NiD Nanostructured Component on its Incremental Excess Power Gain", ICCF-19, JCMNS, 19, (2016).

[5] Swartz, M. R, Comparison of NANOR-type LANR Components to ^{238}Pu as a Heat Source for Space Flight, J. Condensed Matter Nucl. Sci, vol 29, 238 (2019).

[6] Swartz, M. R., Synchronization of Vacancy-Loaded Deuterons Enables Successful LANR Mass-Energy Transfer, JCMNS, Proceedings of ICCF24, vol. 38, 147 (May 2024).

[7] Swartz M. R., Achieving Very High Increment Power Gain, J. Condensed Matter Nucl. Sci, (ICCF-25).

J. Condensed Matter Nucl. Sci. 41 (2026) 117–120

Excess Power Gain Using Deuterated Niobium

Mitchell R. Swartz

JET Energy, Inc., Wellesley, MA USA

Abstract

The incremental excess power gain in LANR using the niobium [Nb] Phusor®type component in D_2O, vs platinum as the anode [with a very high impedance solution] was $\sim 2.88 +/- 0.21$, compared to the ohmic control ($\sim$1). Nb offers a possible alternative to palladium, with Nb having unique magnetic and high temperature properties.

Keywords: Niobium, Power gain, Excess heat, Ohmic control, Impedance, Phusor.

1. Introduction – Niobium

Niobium [Nb; Figure 1] offers a new alternative and option to use with Lattice Assisted Nuclear Reactions [CF/LANR]. These opportunities are discussed here.

Although niobium was discovered in 1734 by John Winthrop in Massachusetts [Figure 2], that initial, critical ore sample sat “waiting” in the British Museum until 1801. In 1801, Charles Hatchett reported on this new element, which he noted was like tantalum, and which he initially named ‘columbium’. However, this element, and the metals and alloys which it forms, are actually very complex.

2.1. Background - Niobium

Niobium from the Earth’s crust is one stable isotope, ^{93}Nb. Nb is a soft, ductile metal, usually with impurities. It is gray and becomes blue greenish color when exposed to air at room temperature. Nb has a body-centered cubic lattice, however the structure may change because Nb can become anomalous on both thermal heating and spatial expansion. Importantly Nb is anti-corrosive after it forms oxide layers.

2.2. Background – Complexity of Niobium Metallurgy Today

Today, niobium metallurgy is much more complicated. Now, more than a score of Nb radioisotopes exist, and have been synthesized with atomic masses 81 to 115. Paramagnetic niobium has the largest magnetic penetration depth of all elements. It is central to superconducting based technologies, including high-Q radio frequency cavities, and resonators used for quantum computing and gravitational wave detectors. Nb is one of only three elements forming Type II superconductors [with vanadium and technetium]. Niobium becomes a superconductor at 9.2 K, but its hydride phases show no sign of superconductivity down to 1.3 K.

Figure 1. Niobium is an elemental metal with interesting properties.

Figure 2. Gov. John Winthrop (Massachusetts), and Charles Hatchett (British chemist), uncovered and examined the first niobium samples.

3. Experimental - Niobium in LANR

Pertaining to LANR, entry of D in Nb has recently been re-examined. Today, we report that the results of several well-controlled experiments prove that LANR-derived excess heat can be obtained from electrically driven deuteron-loaded niobium. As will be shown below, in one experimental run, we used a five-electrode calorimetric cell containing heavy water which had a platinum anode and both separate nickel and niobium cathodes, and an ohmic control. Each were contained within the same thermal and electrical driving system.

3.1. Experimental–Electric Power Drive

To accurately measure excess heat (XSH), careful sequencing of input power to both the component and the ohmic control is required. We use precision-controlled power sources like Keithley current sources, Tekpower TP3005P, etc. with DAQ monitoring. Analysis of the delivered and applied precise step functions yield calorimetry. For each step pulse, the electrical dissipation (V*I) is maintained over a long period of time. The results are confirmed by long-term time integration, which rules out false positives. Some other possible electrical errors are minimized by the boron nitride (acting as an electrical insulator).

3.2. Experimental–Ohmic Control

Good, calibrated measurements require a timely compared ohmic control. For each step pulse, the thermal ohmic control and then the components are examined by constant input power. This provides heat at a constant rate, with electrical dissipation (V*I) maintained over a long period of time.

Experimentally, the ohmic control is first used and compared to an active NANOR®-type component. The advantage of using an ohmic control square wave immediately before the CF/LANR run is that one can also simultaneously check and compare the performance of the calorimeter's analysis. The algorithm converts the thermometry to ohmic control-calibrated calorimetry.

Confirmation of the algorithm is made by checking the appearance of the output heat from the ohmic control. If it does not produce the applied square wave then the system is flawed and thus, ohmic calibration is important in several ways. In addition to calibrating the calorimeter, it also establishes the baseline by first measuring and observing the response of the ohmic control.

3.3. Experimental–Impedance and Power Matching

As electrical engineers, we match the electrical input power to both the ohmic control and the LANR component ["effective power bracketing"]. Such electrical input power bracketing is required to accurately measure the "excess power". However, in any real setup, the electrical impedance of the NANOR®-type component changes with time, because of history, hysteresis, and possible electrical avalanche, which misses the working LANR if the voltage is excessive. Therefore, we also attempt to match electrical input power by adjusting the voltage as necessary.

In addition, there is some time variance of electrical resistivity that occurs for ohmic controls as well, due to use and changing temperature, but that is minimal and second order. Finally, the use of energy, obtained through time integration of the power, is necessary to also prove that the analytic system is correct, and to rule out phase changes.

3.4. Experimental Methods–Calorimetry

In summary, the experimental setup included calorimetry, and bracketing of the NANOR®-type component with ohmic controls in time and by input electric power applied, and time integration to rule out false positives. The ensemble [components, controls, sensors, additional thermal mass] is examined by thermometry before, during, and after electrical drive, and calibrated by the thermal ohmic control. Calorimetry is then determined by analysis of the dynamic changes of temperature at several locations. Confirmation of the algorithm, checking for linearity and time-invariance, and calibrating the output of the component under test, is made by reproducing the heat generated from a square wave sent to an ohmic control. Also, confirmation of results is made by long-term time integration.

4. LANR RESULTS: Niobium PHUSOR®-type LANR Component

The next Figure [Figure 3] shows both the Input Power and Input Power-Normalized Output Thermal Powers [Watts/cm^2/Pin], for both a Nickel Phusor®-type cathode, and an ohmic control, and a Niobium Phusor®-type cathode. The nickel Phusor®-type component was also included as an additional excess-heat producing control, and for that the incremental power gain was $3.76 +/- 0.23$.

There was excess heat for the deuteron loaded niobium in heavy water loaded versus a platinum anode. The incremental excess power gain for the niobium Phusor®-type component was $2.88 +/- 0.21$ compared to the ohmic control ($\sim$1).

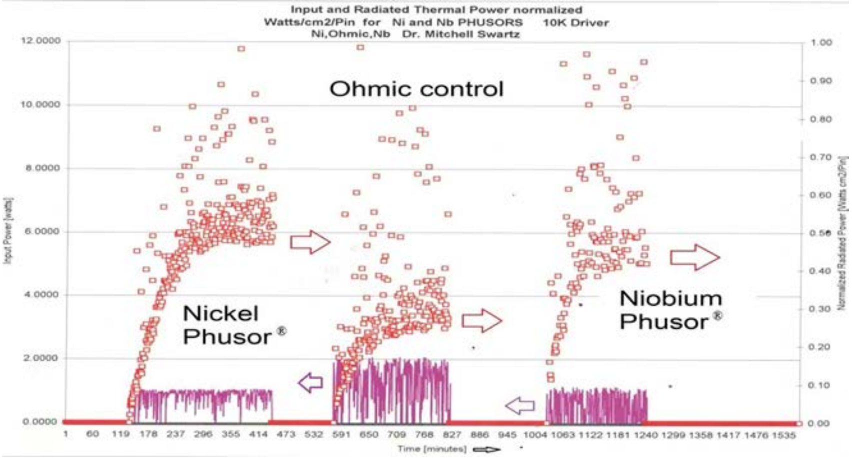

Figure 3. Loaded Niobium Produces Excess Heat – The graph shows the Input Powers and Input Power-Normalized Output Thermal Powers [Watts/cm^2/P$_{\text{in}}$] for both a Nickel cathode, an ohmic control, and a Niobium Phusor®-type cathode.

5. Conclusion

The incremental excess power gain for the niobium Phusor®-type component in D_2O, vs platinum as the anode, with a very high impedance solution, was $\sim 2.88 +/-0.21$ compared to the ohmic control.

LANR's fuel is abundant, larger and more available than all the Earth's oil reserves.

Its energy production is clean, quiet, and so efficient that in the future, LANR will energize engines, motors, and electrical generators enabling transportation, improved health and new and improved opportunities.

Niobium has a future in LANR both because it is an option to palladium and nickel, and because it also offers unique magnetic, high temperature, and now excess heat (XSH) opportunities. It may offer features to LANR unexpected today, including possibly making it easier, more efficient, and/or cheaper to use.

Acknowledgements

The author thanks Gayle Verner, Alex Frank, Joshua Gyllinsky, Raymond Kurzweil, Aaron Kleiner, Michael Staker, Peter Hagelstein, Jeffery Shapiro, Brian Ahern, Jeff Driscoll, Christy Frazier, and Susan Woods for their help, encouragement, support and suggestions.

This effort has been supported by JET Energy Inc. NANOR® and PHUSOR® are registered trademarks.

The IP technology described here is protected by US patents issued and pending.

References

[1] Qi Dan, Ru Tang & Xiaohong Chen, Effect of Deuterium Loading on Permeation of Deuterium Through Niobium at Relative Low Pressure, Journal of Fusion Energy, Volume 43, article number 53, (2024).

[2] Abdulaziz Abogoda, W. A. Shelton, I. Vekhter, and J. A. Sauls, Hydrogen and Deuterium Tunneling in Niobium, https://arxiv.org/pdf/2409.09014 https://www.firstpost.com/world/what-is-niobium-alloy-that-china-is-claiming-abreakthrough-in-13850701.html

[3] Swartz, M., "Survey of the Observed Excess Energy and Emissions In Lattice Assisted Nuclear Reactions", Journal of Scientific Exploration, 23, 4, 419–436 (2009).

[4] Swartz, M. R., Synchronization of Vacancy-Loaded Deuterons Enables Successful LANR Mass-Energy Transfer, JCMNS, Proceedings of ICCF24, Vol. 38, 147 (May 2024).

J. Condensed Matter Nucl. Sci. 41 (2026) 121–126

Research Article

Ordinary H-Humidity Can Inactivate D-Loaded CF/LANR Components

Mitchell R. Swartz, Gayle M. Verner

Nanortech, Inc., Wellesley, MA 02481, USA

Peter L. Hagelstein

Massachusetts Institute of Technology, Cambridge, MA 02139, USA

Abstract

Ordinary H-humidity can alter CF/LANR D-derived reactions, inactivating them, thus impacting both incremental excess power gain and the electrical resistivity. Ordinarily it can completely quench the desired XSH from D-loaded components. Preventing this unwanted H-humidification will engineer better CF/LANR systems.

Keywords: Humidity, Inactivation, Nanor, Zirconium oxide, Excess heat, Ohmic control

---

1. Introduction

The desired result from successful Lattice Assisted Nuclear Reactions [CF/LANR] is the generation of ‘excess heat’ [XSH]. The amount is described by the measured incremental power gain [“the sample activity”]. The production of excess heat [“XSH”] is generally accomplished in conventional CF/LANR systems, usually aqueous [1]–[3], [9]–[11], or by dry deuteron-preloaded ZrO_2-PdD and ZrO_2-PdNiD nanomaterial core NANOR®-type components [4]–[6]. Unfortunately, in the later materials, XSH is quenched by excessive ordinary H-humidity, and in a very complicated way. We report that this unexpected type of CF/LANR inactivation can be significant and irreversible. This causes a major impact both on the incremental excess power gain and the electrical resistivity of previous working NANOR®-type components. This new technologic tip is very important because these dry, very highly preloaded NANOR®-type LANR components are the future of clean efficient energy production – and we must attend to this discovered problem.

2. Background –NANOR®-type LANR Components

NANOR®-type LANR Components are a new generation of CF/LANR quantum electronic devices exhibiting considerable reproducible energy gain. Most importantly, the activation of LANR is, for the first time, separated from

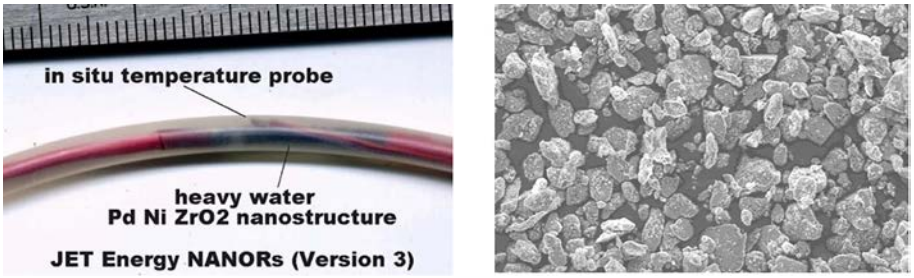

Figure 1. NANOR®-type Component; (left) Series 3 NANOR®-type LANR Component, (right) Dry, preloaded ZrO_2-PdNiD nanostructured core material.

loading. Also, these NANOR®-type preloaded components are dry and sealed into an electrically conductive (high impedance) configuration, enabling superior handling properties and useful portability. The self-contained two electrical terminals NANOR®-type components are fully preloaded with deuterons. They are ∼2 cm in length, with 30 to 400 milligrams of a LANR active nanocomposite ZrO_2-PdD core. The core is ZrO_2-PdNiD [Zr (∼66%), Ni (0-30%), and Pd (5-25%) by weight] with additional D. The PdNiD nanostructured core islands are electrically isolated by the zirconia (ZrO_2) dielectric.

The power density ∼ 19.50 watts/gram of nanostructured material helps their already superior handling properties and portability.

3. Experimental – Electric Power Drive

To accurately measure XSH, careful sequencing of input power to both the component and the ohmic control is required. We use precision-controlled power sources like Keithley current sources, Tekpower TP3005P, etc. with DAQ monitoring. Analysis of the delivered and applied precise step functions yield calorimetry. For each step pulse, the electrical dissipation (V*I) is maintained over a long period of time. The results are confirmed by long-term time integration, which rules out false positives. Some other possible electrical errors are minimized using boron nitride (acting as a heat transporting electrical insulator).

4. Experimental – Ohmic Control

Also, ohmic controls should always be used. Good, calibrated measurements require a timely, compared ohmic control. For each step pulse, the thermal ohmic control and then the components are examined by constant input power. This provides heat at a constant rate, and the electrical dissipation (V*I) is maintained over a long period of time. Experimentally, the ohmic control is first used and compared to an active NANOR®-type component. The advantage of using an ohmic control square wave immediately before the CF/LANR run is that one can also simultaneously check – and compare - the performance of your calorimeter's analysis. The algorithm converts the thermometry to ohmic control-calibrated calorimetry. Confirmation of the algorithm is made by checking the appearance of the output heat from the ohmic control. If it does not produce the applied square wave, then the system is flawed.

The ohmic calibration also establishes the baseline calorimetric response by first measuring and observing the response of the ohmic control.

5. Experimental – Impedance and Power Matching

As electrical engineers, we match the electrical input power to both the ohmic control and the LANR component [“effective power bracketing”]. Such electrical input power bracketing is required to accurately measure the “excess power”. In any real setup, the electrical impedance of the NANOR®-type component changes with time, because of history, hysteresis, and possible electrical avalanche (missing the working LANR) if the voltage is excessive. Therefore, we also attempt to match electrical input power by adjusting the voltage as necessary.

In addition, there is some time variance of electrical resistivity that occurs for ohmic controls as well, due to use and changing temperature, albeit minimal and second order. Finally, the use of energy, obtained through time integration of the power, is necessary to also prove one’s analytic system is correct, and to rule out phase changes, such as observed in some early setups.

6. Experimental Methods – Calorimetry

In summary, the experimental setup included calorimetry, and bracketing of the NANOR®-type component with ohmic controls in time and by input electric power applied, and time integration to rule out false positives. The ensemble [components, controls, sensors, additional thermal mass] is examined by thermometry before, during, and after electrical drive, and calibrated by the thermal ohmic control. Calorimetry is then determined by analysis of the dynamic changes of temperature at several locations.

Confirmation is made by long-term time integration. Confirmation of the algorithm, checking for linearity and time-invariance, and calibrating the output of the component under test, is made by reproducing the heat generated from a square wave sent to an ohmic control.

7. Result – No Additional H Humidity Active Dry Preloaded ZrO_2-PdNiD NANOR®-type LANR Component

The next Figure [Figure 2] shows the applied input voltage and resultant incremental power gain for NANOR®-type Component N6-33ACL131C2, calibrated by an ohmic control resistor in Run EJan30B. Incremental power gained many orders of magnitude from the active NANOR®-type component compared to the ohmic control.

The next Figure [Figure 3] thereafter shows the applied input voltage and resultant incremental power gain for NANOR®-type Component N5-02A, calibrated by an ohmic control resistor in Run EJan01A. Incremental power gained many orders of magnitude from the active NANOR®-type component compared to the ohmic control.

Achieving these high incremental power gains has required improved alloys and their loading by deuterons and then meticulous avoidance of electric avalanches while extending the duration of the heat production cycles.

8. Ordinary H-Humidity Inactivates D-Loaded CF/LANR Component

The next figure shows the impact of ordinary hydrogen through H-humidity. Observe the losses of electrical resistivity and the desired XSH-activity. Observe how the initial steady electrical resistance decreased irregularly but significantly from the presence of H-humidity. Fortunately, each time the XSH-activity and the electrical resistivity finally returned to their baselines; therefore, this is marked as ‘stable operation’, and here indicated by black lines.

Loss of Electrical Resistivity and Desired XSH-activity for NANOR® 8-2 as a function of Ordinary H-Humidity

The ordinary H-humidity at MIT was significant and clearly changed the results. The next figure [Figures 4 & 5] shows a case of irreversible XSH loss from H-humidity. In this case, at higher humidity, there is final permanent decline of both electrical resistance and desired XSH-activity. This unwanted final loss of the desired excess heat in

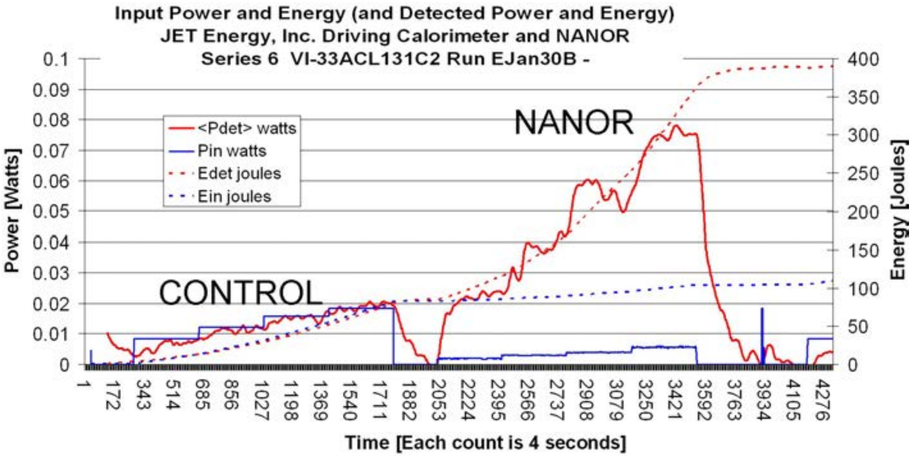

Figure 2. Active Preloaded Dry NANOR®-type LANR/CF Components are Working Systems Which Reproducibly Produce Excess Heat - This component's input and heat output are shown along with both an ohmic control "CONTROL" and calibration pulses.

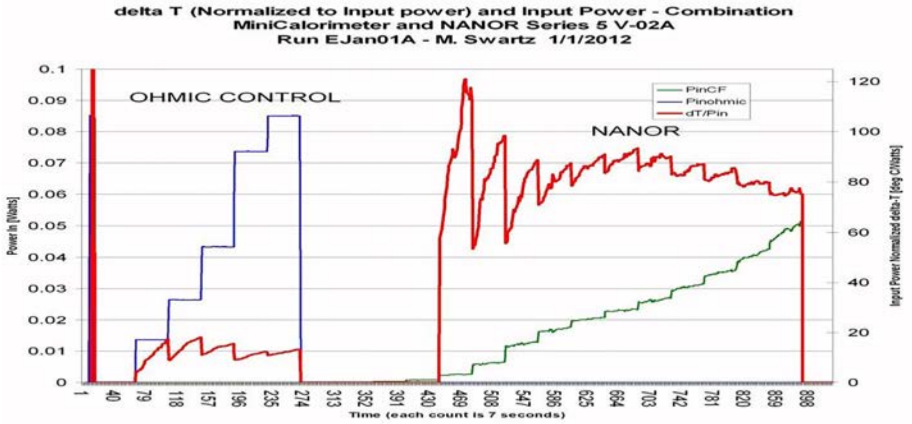

Figure 3. Active NANOR®-type LANR/CF Component N5-02A Producing Excess Heat - This component's input and heat output are shown along with both an ohmic control and calibration pulse.

Run EF9-160410A, with the temperature measured at the heat sink location, is apparent even though the NANOR®-type LANR component was initially active (orange region). **Conclude that H-Humidity Can Irreversibly Inactivate D-Loaded CF/LANR Components.**

The desired XSH first generated is shown in orange. Its difference from the control [in green] is obvious. The inactivation from ordinary hydrogen (through H-humidity) is shown (blue), with dramatic loss of XSH. Note that ordinary hydrogen made the LANR component lose the XSH, then saliently matching the output heat of the ohmic control.

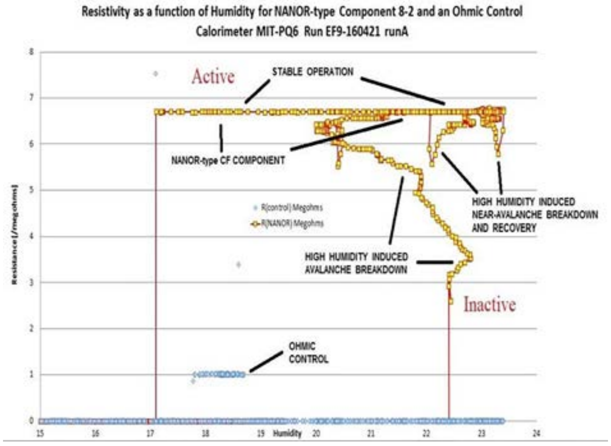

Figure 4. Ordinary H-Humidity Can Inactivate This D-Loaded CF/LANR Component.

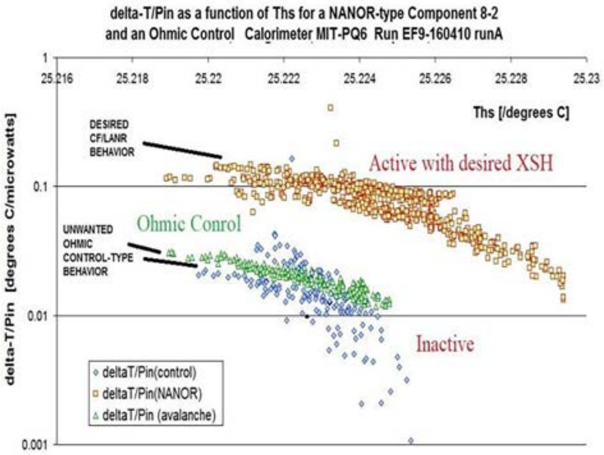

Figure 5. Loss of Both Electrical Resistivity and the Desired XSH-activity for NANOR® 8-2 after it was intentionally targeted with increased Ordinary H-Humidity.

9. IMPORTANT RESULT - Two Modes for CF/LANR

Thus, it is clearly seen that there are two modes. Further, there is an inactivation fall off produced by high humidity when ordinary water is inadvertently introduced. The final unwanted H-induced loss is seen as the undesired XSH-missing blue region. Ordinary H-humidity can partially or completely quench the desired XSH from D-loaded components, with a reduction of component electrical resistance. This negative transformation by inactivation of an LANR component is quite serious. Preventing or resolving this issue will improve engineering and help commercialize these systems.

Side reactions which potentially quench or inactivate the desired reactions must be understood and controlled. This new inactivation of the desired XSH is beyond H merely preventing D entry into metal during loading, as previously known. It is also beyond the temporary inactivation loss of power gain made by NANOR®-type components driven above the breakdown ["avalanche"] voltage, and the partial inactivation observed as the electrical avalanche threshold is approached.

This new, often irreversible, inactivation, was only uncovered using larger core volume components at MIT, where the ordinary H-humidity changes in the laboratory building were significant.

10. Conclusion: Ordinary H Can Inactivate D-Loaded Components

LANR NANOR®-type components enable a future of clean energy production. However, ordinary H-humidity can partially or completely quench the desired XSH, and will alter component electrical resistance, too. This loss of the desired XSH is beyond H merely preventing D entry into metal during loading, as previously known.

Thus, there are more than two modes of activity ["off" and "on"] between which there is a range of inactivation decline that can be produced by ordinary water from high-humidity environments.

LANR's fuel is abundant, and it is likely that clean, quiet, LANR engines & motors systems will drive electrical generators to provide propulsion and transportation. There is more available energy from LANR than from all the Earth's oil reserves – but these experiments have revealed that H-humidity can produce excess heat/power quenching and must be considered as a possible negative factor.

Acknowledgements

The authors acknowledge and thank Jeffery Shapiro, Alex Frank, Joshua Gyllinsky, Susan Woods, and Florian Metzler, for their help, encouragement, support and suggestions. This effort has been supported by JET Energy Inc.

This effort has been supported by JET Energy Inc. NANOR® and PHUSOR® are registered trademarks. The IP technology described here is protected by US patents issued and pending.

References

[1] Swartz, M. R., Brian Ahern, Charles Haldemann and Alan Weinberg, Excess Heat is Linked to Deuterium Loss in an Aqueous Nickel LANR [1] System, Proc. ICCF-21, J. Condensed Matter Nucl. Sci, Vol 29, 169 (2019).

[2] Swartz M., Excess Power Gain using High Impedance and Co-depositional LANR Devices Monitored by Calorimetry, Heat Flow, and Paired Stirling Engines, Proc. ICCF14, 1, (2008), p 123; ISBN: 978-0-578-06694-3, 123, (2010).

[3] Swartz, M., Photoinduced Excess Heat from Laser-Irradiated Electrically Polarized Palladium Cathodes in D_2O, Condensed Matter Nuclear Science, Proc. ICCF-10, ISBN 981-256-564-6, 213–226 (2006).

[4] Swartz M. R., Achieving Very High Increment Power Gain, J. Condensed Matter Nucl. Sci , (ICCF-25).

[5] Swartz, M. R, Oscillating Excess Power Gain and Coerced Magnetic Domains in MNANOR®-type CF/LANR Components, J. Condensed Matter Nuclear Sci., 22, 35–46 (2017).

[6] Swartz, M. R, G. Verner, J. Tolleson, P. Hagelstein, Dry, preloaded NANOR®-type components, Current Science, 108, 4, 595 (2015).

[7] Swartz M. R., Hagelstein P.I., Demonstration of Energy Gain from a Preloaded ZrO2–PdD Nanostructured CF/LANR Quantum Electronic Device at MIT, J. Condensed Matter Nucl. Sci. 13, 516 (2014).

[8] Swartz M. R., Verner G., et al., Energy Gain From Preloaded ZrO_2–PdNi–D Nanostructured CF/LANR Quantum Electronic Components, J. Condensed Matter Nucl. Sci. 13, 528, (2014).

[9] Swartz, M., Survey of the Observed Excess Energy and Emissions In Lattice Assisted Nuclear Reactions, Journal of Scientific Exploration, 23, 4, 419–436 (2009).

[10] Swartz, M. R., Synchronization of Vacancy-Loaded Deuterons Enables Successful LANR Mass-Energy Transfer, JCMNS, Proceedings of ICCF24, Vol. 38, 147 (May 2024).

[11] Swartz, M. R, Aqueous and Nanostructured CF/LANR Systems Each have Two Electrically Driven Modes, Proc. ICCF-21, Fort Collins, Co.6/3/18 (2018), J. Condensed Matter Nucl. Sci, Vol 29, 177 (2019).

J. Condensed Matter Nucl. Sci. 41 (2026) 127–134

Research Article

Coenergy Enables Force Calculations and Loading Measurement

Mitchell R. Swartz, Joshua C. Gyllinsky

JET Energy, Inc., Wellesley, MA USA

Abstract

Coenergy is used to include magnetic fields in linear, conservative systems. It permits easy derivation of force. With an additional technique, it enables loading measurements without interrupting the electrical current flow. Coenergy analysis can also measure induced and remnant magnetization in NANOR®-type CF/LANR components.

Keywords: NANOR, LANR, Fusion, Loading, Magnetoelectric, Coenergy, Ohmic control

1. Introduction – Coenergy Is Key to Understanding LANR Systems

Thirty-seven years of sterling evidence shows conclusive LANR data proving its excess heat is of a nuclear origin, in both aqueous [1]–[3] and dry, preloaded [4]–[8] cold fusion/lattice assisted nuclear reaction systems and components. Successful cold fusion (LANR) therefore begins (and continues) with loading; the metallurgy is complex and well-studied [9]–[10].

Future LANR investigations will be helped by considering coenergy. The coenergy quantity [W'$_{\mathrm{m}}$] is an alternate definition of the energy term in linear, conservative systems [11], and it is used in continuum electromechanics, electrophysics and electrical engineering to include magnetic fields. With the additional techniques shown below, it also enables loading measurements without interrupting the electrical current flow, and the measurement of induced and remnant magnetization in NANOR®-type CF/LANR components.

The reasons for this are that the mechanical forces are easily derived from a simple spatial derivative, of the following equation used.

$$\mathrm{W}'_{\mathrm{m}} \;=\; 1/2\,\mathrm{m}\,*\,\mathrm{H}^2$$

Because the derivation of force in magnetostatic system is simply the negative spatial gradient, which enables a fusion cathode to have its mass (and therefore deuteron population) is measured *in situ* without interrupting the electrical current flow. Therefore, increasing the cathode mass by loading will decrease the frequency of a vibrating cathode. The equation of motion, with terms including magnetostriction, is

$$\frac{d^2x}{dt^2} = -\left[K * x\right] - \frac{[Bo]^2}{2 * \mu^2}\left[\mathit{\Delta}\mu + \left[(-\mathit{\Delta}\rho) * \left(\frac{\delta\mu}{\delta\rho}\right)\right]\right]$$

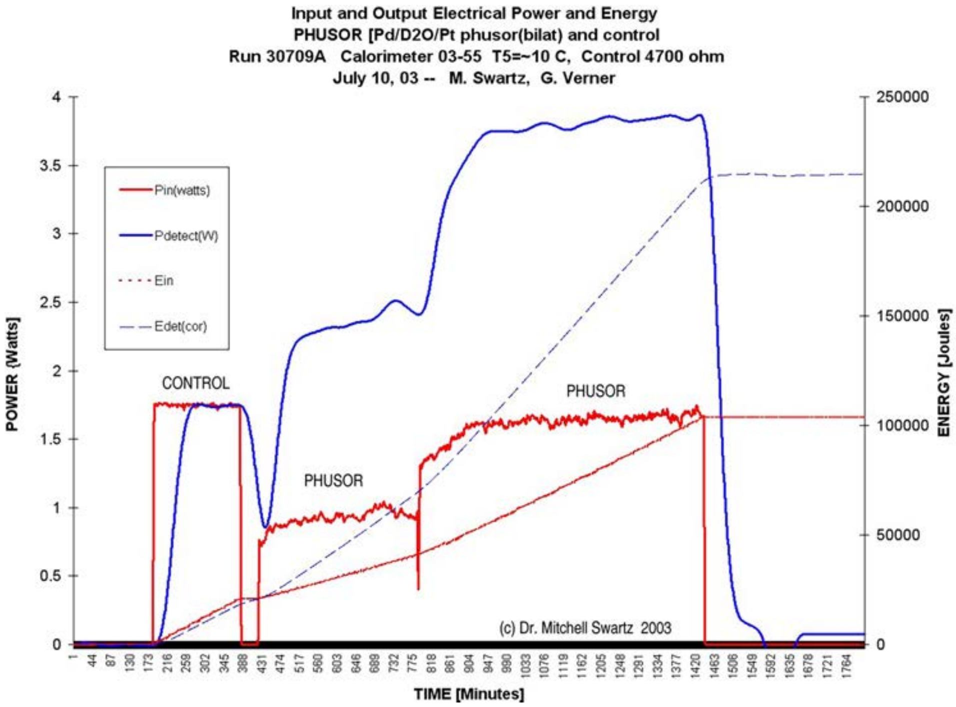

Figure 1. Active Aqueous Pd/D$_2$O/Pt Systems Reproducibly Produce Excess Heat. Shown is the input electrical power (red lines), and heat output (blue lines), to the ohmic control and to the aqueous heavy water PHUSOR$^{®}$-type system, as a function of time. Also shown is the input and output electrical energies (the blue and red dashed lines).

The solution of the equation has an amplitude, and natural frequency, of

$$\frac{[Bo]^2}{2 * V * \rho * \mu^2 * K * \sqrt{(\omega_0^2 - \omega)}} * \left[\Delta\mu + \left[(-\Delta\rho) * \left(\frac{\delta\mu}{\delta\rho}\right)\right]\right]$$

$$\omega_0 = \sqrt{\frac{K}{\rho * V}}$$

The magnetoelectric term at the end of the equation above is similar to that term from conventional dielectrophoresis. In the equation, K is representing the first order spring constant, which arises from the frictional force exerted back on the cathode.

2. Background: COLD FUSION/LANR is ABSOLUTELY REAL

Loaded deuterons in PdD (often under difficult-to-achieve conditions) couple together in these active systems thereby fusing to generate *de novo* ^{4}He and considerable excess heat [with an example shown in Figure 1], and with loss of D and generation of unique optical antiStokes and RF [Deuterium-line] emission signatures.

Figure 1 shows these reproducible Excess heat (XSH) results with clear comparisons to ohmic control. Excess heat was not seen in any of the ohmic controls. However, there is LANR activity. Excess power (beyond that applied)

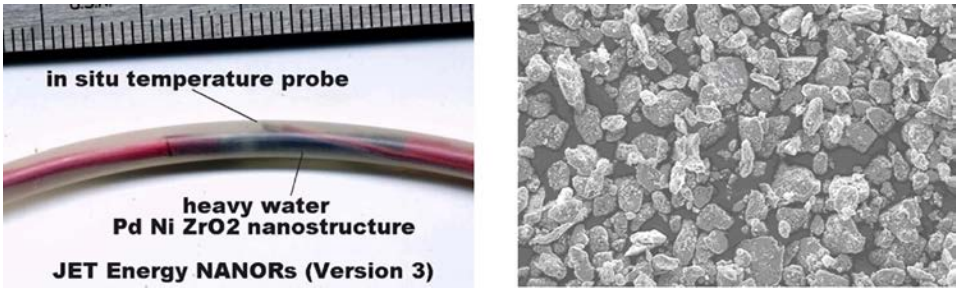

Figure 2. NANOR®-type Preloaded CF/LANR Component. (left) Series 3 NANOR®-type LANR Component, (right) Dry, preloaded ZrO_2-PdNiD nanostructured core material.

can be easily seen. Notice closely that the energy curves rise in parallel for the ohmic control when there is no excess heat, but not if excess heat is being produced. Note that with XSH the incremental (excess) energy curves rise in a supra-linear way when constant input is applied.

3. Background IMPORTANT: Loading is KEY to LANR Success Including With NANOR®-type LANR Components

NANOR®-type LANR components are a new generation of dry, CF/LANR nanomaterial PdD (and sometimes with PdNiD) quantum electronic devices, sealed into an electrically conductive (high impedance) configuration, exhibiting considerable energy gain. Most importantly, the activation of the cold fusion/lattice assisted nuclear reaction is, for the first time, separated from loading.

4. Experimental –ZrO_2-PdNiD NANOR®-type LANR Component

These important, novel devices feature two terminals with a cylindrical shape and active CF/LANR core and self-contained superior handling properties enabling portability and transportability [Figure 2]. Thus, they are incredibly useful and have demonstrated a more reproducible CF/LANR behavior. The self-contained two electrical terminals NANOR®-type components are fully preloaded with deuterons. They are ∼2 cm in length, with 30 to ∼ 400 milligrams of a LANR active nanocomposite ZrO_2-PdD core. The core is ZrO_2-PdNiD [Zr (∼66%), Ni (0-30%), and Pd (5-25%) by weight] with additional D. The PdNiD nanostructured core islands are electrically isolated by the zirconia (ZrO_2) dielectric. Their power density ∼19.50 watts/gram of nanostructured material helps their already superior handling properties and portability.

5. Experimental - Electric Power Drive

Calibrated measurements require a timely compared ohmic control. For each step pulse, the thermal ohmic control and then the components are examined by driving them with a constant input power. This provides heat at a constant rate, along with the electrical dissipation (V*I), which are maintained over a long period of time.

Ohmic calibration is important in several ways. In addition to calibrating the calorimeter, it also establishes the baseline by first measuring and observing the response of the ohmic control. We match the electrical input power to both the ohmic control and the LANR component. Measurement of energy, obtained through time integration of the power, is necessary to also prove one's analytic system is correct, and to rule out phase changes. Several types

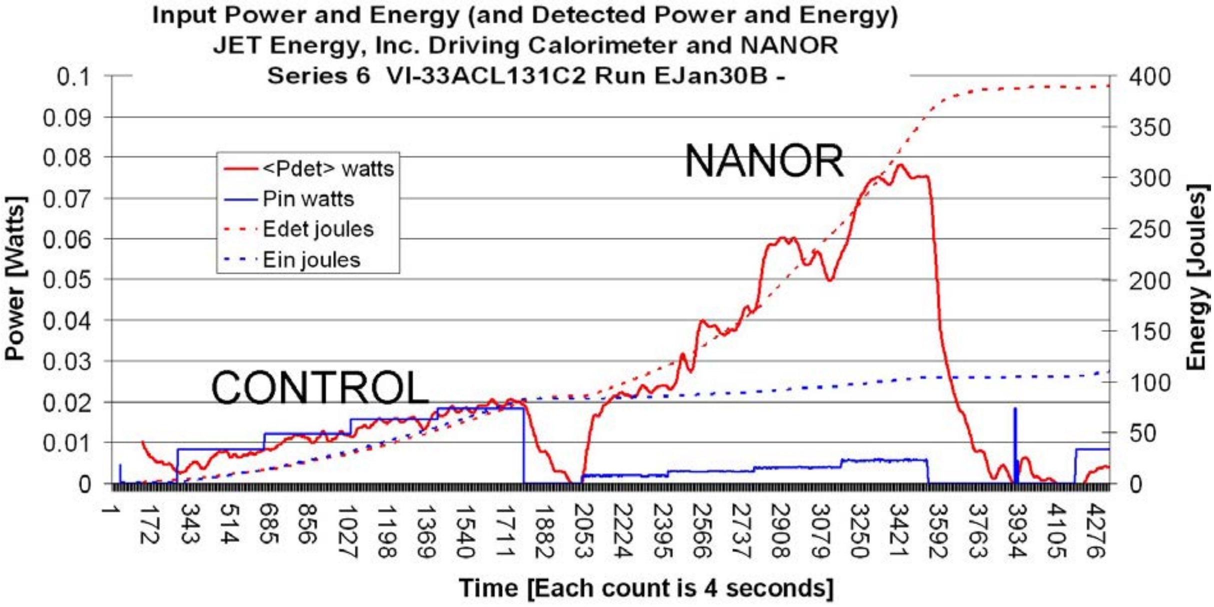

Figure 3. Preloaded, Dry NANOR®-type Component Reproducibly Produces Excess Heat. - Shown are the input electrical power (red lines), and heat output (blue lines), to the ohmic control ["CONTROL"] and to a Deuteron-preloaded, dry NANOR®-type Component as a function of time. Also shown is the input and output electrical energies (the blue and red dashed lines).

of temperature detection methods are used while electrically driving the system. In addition to our publications, we include custom DS18B20 temperature sensors.

6. Results - Active Dry Preloaded NANOR®-type LANR Component

Figure 4 below, shows the applied input voltage and resultant incremental power gain for NANOR®-type Component N5-02A, calibrated by an ohmic control resistor in run EJan01A. Note how many orders of magnitude the incremental power gain [excess heat ["XSH"]] realized from the active NANOR®-type component compared to the ohmic control. Achieving these high incremental power gains has required improved alloys and their loading by deuterons, followed by meticulous avoidance of electric avalanches and extending the duration of the heat production cycles. Cathode vibration enables hydrogen (or deuteron) loading measurement. Furthermore, other benefits arise from an arrangement enabling an external magnetic field.

Figure 3 shows a salient excess heat (XSH) result for the NANOR®-type component compared to the ohmic control. Excess heat was not seen with any of the ohmic controls. However, there is obvious desired LANR XSH-generating activity, and the excess power can be easily seen, as it is far beyond the input power applied.

Upon close observation, one can also see that the energy curves rise in parallel for the ohmic control, unlike later when excess heat was actually produced by CF/LANR. Note that with XSH, the incremental (excess) energy curves rise in a supra-linear way when constant input is applied to the NANOR®-type component.

Also, in Figure 4, it is shown that there is a clear increased temperature rise for the NANOR®-type component compared to the ohmic control – even with less input power.

There is thus a clear, salient result demonstrating the desired excess heat with its temperature generating activity.

Again, it is important to note that such excess temperature rise was NOT seen with any of the ohmic controls.

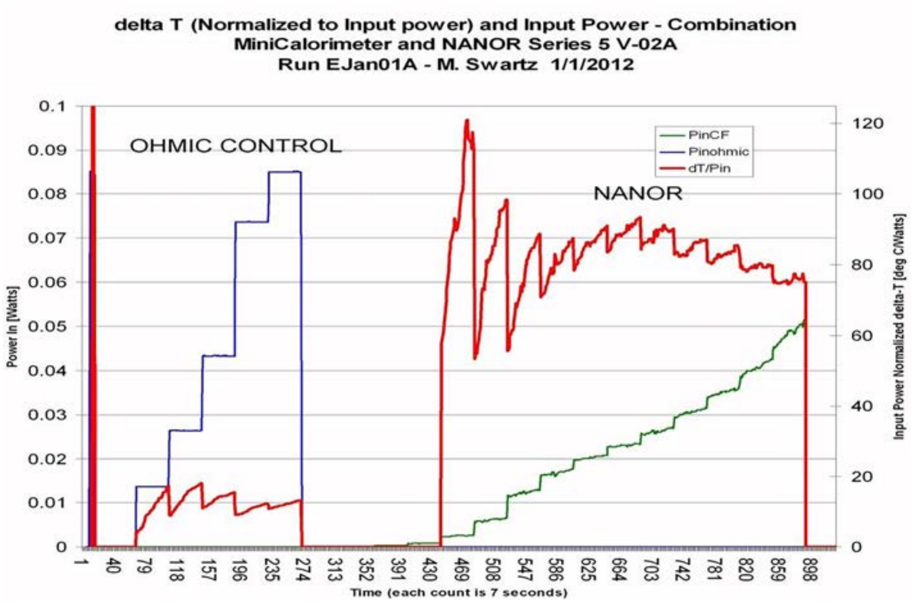

Figure 4. Preloaded Pd-NANOR® V-02A Reproducibly Produces More Heat. Shown are the input electrical power (blue and green lines), and the generated temperature (red lines), to the ohmic control [“CONTROL”] and to a Deuteron-preloaded, dry NANOR®-type component, as a function of time.

7. Results - Vibration of Electrode To Monitor Loading

A palladium electrode has the unique property of internally filling ("loading") with hydrogen, as a sponge fills with water. A ‘vibrational electrode’ can be monitored for its natural frequency revealing information about the electrode, including "how much" hydrogen has been loaded (through the mass change; see Figures 5 and 6). Monitoring of hydrogen, or deuteron, loading used to be complicated and invasive and actually stopped the desired reactions underway.

However, electrically uncoupling the electrode [“effectively pulling the plug” and stopping the reaction], cross-contaminating the cathode and the laboratory by physically removing the electrode, drying it off, and actually weighing it on a scale, before returning it to the disrupted electrical circuit – is no longer required.

By contrast, vibrational in situ monitoring is non-invasive and does not disturb the reactions - features of great and significant utility. This cathode vibration enables hydrogen (or deuteron) loading measurement.

Furthermore, other benefits arise from an arrangement enabling an applied external magnetic field. In addition to inducing a vibrational frequency of the cathode, the magnetic field can be used to increase the incremental power gain or collect a product.

8. Results - Coenergy Analyses Can Reveal the Force Induced, and Remnant Magnetization of Nanomaterial LANR Components

In addition, by this process, LANR domains can also become magnetic, interact, and can be followed over time. This is shown in Figure 7. LANR’s fuel is abundant. Clean, quiet, and LANR engine-motor systems will drive electrical generators to provide propulsion and transportation. There is more available energy from LANR than from all the Earth’s oil reserves.

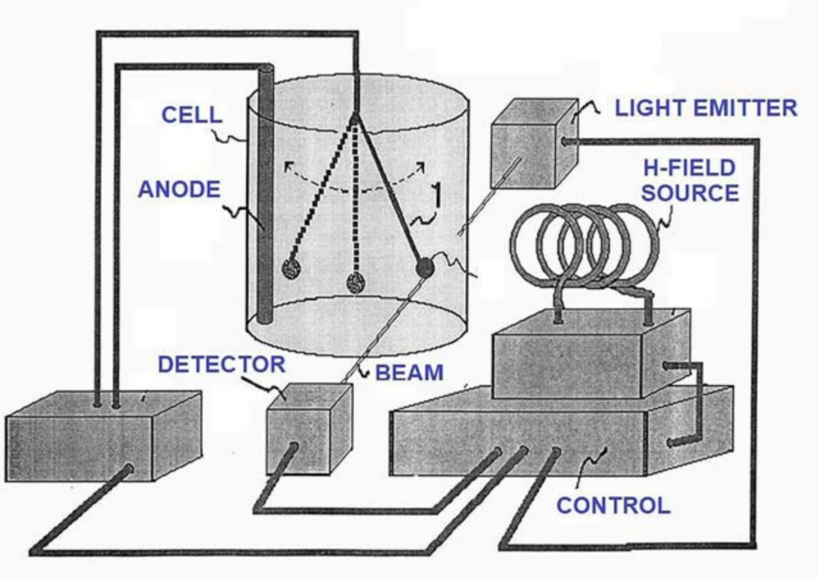

Figure 5. Apparatus and Process To Monitor Electrode Loading By Vibration. Serial No.: 16/501,347; a Continuation of SN 07/371,937, Filed 06/27/1989.

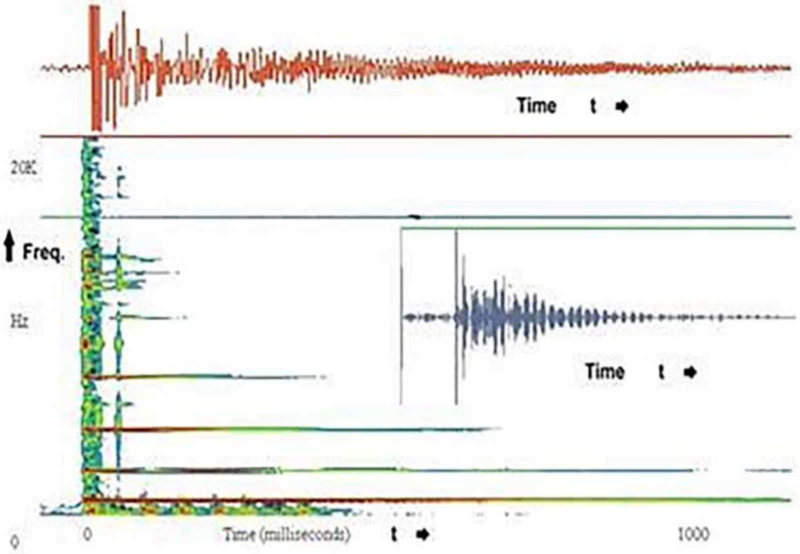

Figure 6. Coenergy Drives and Then Enables Measurement of Loading - The Vibrating Cathode, its Fourier Transform, and calibration, are shown. The cathode was #92505bjNi-B2 immersed in ordinary water. Short-lived vibrational modes are revealed here by FFT. A calibration signal was also inserted at 17,390+/-53 Hz (blue horizontal line, approximately half-way up the image). The sampling rate was ∼100 kilohertz.

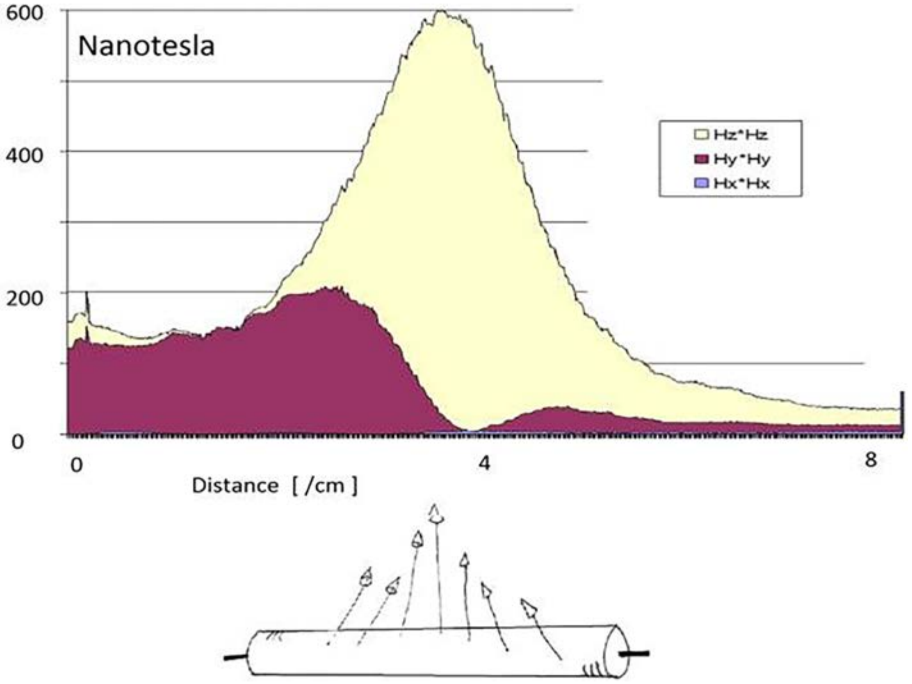

Figure 7. Coenergy Analysis can Reveal the Force Induced, and the Remnant Magnetization Coenergy Enables Measurement Induced Magnetic Microdomains. Magnetic Domains in this run used NANOR®-type component N7-8M and were detected [magnetization in nanotesla] as shown long after it was previously operated. The measured vectorial magnetization scan is shown along the component's entire body in the inset, below the graph.

9. Conclusion – Coenergy has Multiple Uses in CF/LANR

The secret of successful LANR/CF is deuteron loading into palladium (or other alloys). Measuring that loading can be made easily by an electrode vibration, which reveals the mass of the electrode. That electrode vibration can be ephemeral and can be initiated in oscillation by a magnetic field. The coenergy analysis can also reveal the induced force and help measure any remnant magnetization.

Acknowledgements

The authors thank Gayle Verner, Alex Frank, Raymond Kurzweil, Aaron Kleiner, Michael Staker, Peter Hagelstein, Jeffery Shapiro, Brian Ahern, Jeff Driscoll, and Susan Woods, for their help, encouragement, support and suggestions. This effort has been supported by JET Energy Inc. NANOR® and PHUSOR® are registered trademarks. The IP technology described here is protected by US patents issued and pending.

References

[1] Swartz, M. R., Brian Ahern, Charles Haldemann and Alan Weinberg, Excess Heat is Linked to Deuterium Loss in an Aqueous Nickel LANR [1] System, Proc. ICCF-21, J. Condensed Matter Nucl. Sci, Vol 29, 169 (2019).

[2] Swartz M., Excess Power Gain using High Impedance and Co-depositional LANR Devices Monitored by Calorimetry, Heat Flow, and Paired Stirling Engines, Proc. ICCF14, 1, (2008), p 123; ISBN: 978-0-578-06694-3, 123, (2010).

[3] Swartz, M., Photoinduced Excess Heat from Laser-Irradiated Electrically Polarized Palladium Cathodes in D_2O, Condensed Matter Nuclear Science, Proc. ICCF-10, ISBN 981-256-564-6, 213–226 (2006).

[4] Swartz M. R., Achieving Very High Increment Power Gain, J. Condensed Matter Nucl. Sci, (ICCF-25).

[5] Swartz, M. R, Oscillating Excess Power Gain and Coerced Magnetic Domains in MNANOR®-type CF/LANR Components, J. Condensed Matter Nuclear Sci., 22, 35–46 (2017).

[6] Swartz, M. R, G. Verner, J. Tolleson, P. Hagelstein, Dry, preloaded NANOR®-type components, Current Science, 108, 4, 595 (2015).

[7] Swartz M. R., Hagelstein P.I., Demonstration of Energy Gain from a Preloaded ZrO_2– PdD Nanostructured CF/LANR Quantum Electronic Device at MIT, J. Condensed Matter Nucl. Sci. 13, 516 (2014).

[8] Swartz M. R., Verner G., et al., Energy Gain From Preloaded ZrO_2–PdNi–D Nanostructured CF/LANR Quantum Electronic Components, J. Condensed Matter Nucl. Sci. 13, 528, (2014).

[9] Swartz, M., Survey of the Observed Excess Energy and Emissions In Lattice Assisted Nuclear Reactions, Journal of Scientific Exploration, 23, 4, 419–436 (2009).

[10] Swartz, M. R., Synchronization of Vacancy-Loaded Deuterons Enables Successful LANR Mass-Energy Transfer, JCMNS, Proceedings of ICCF24, Vol. 38, 147 (May 2024).

[11] Swartz, M. R, Aqueous and Nanostructured CF/LANR Systems Each have Two Electrically Driven Modes, Proc. ICCF-21, Fort Collins, Co.6/3/18 (2018), J. Condensed Matter Nucl. Sci, Vol 29, 177 (2019).

[12] Woodson, Herbert H., James R. Melcher, Electromechanical Dynamics, Part II: Fields, Forces, and Motion, Massachusetts Institute of Technology: MIT OpenCourseWare, p. 464; http://ocw.mit.edu

J. Condensed Matter Nucl. Sci. 41 (2026) 135–144

Research Article

High Incremental Power Gain is the Future of CF/LANR

Mitchell R. Swartz, ScD, EE, MD

JET Energy, Inc., Wellesley, MA USA

Abstract

In 2003, we demonstrated PHUSOR®-type aqueous D_2O components with incremental power gains circa 480%. And in 2012, with NANOR®-type ZrO_2NiPdD components, we showed open demonstration systems running for three months with incremental power gains of ~ 80. The incremental power gains of CF/LANR have improved to more than 10^4 to 10^6 from preloaded, active NANOR®-type components, calibrated by ohmic controls. The important result for very successful LANR/CF applications is now revealed: large incremental power gain with 1 microwatt in, then circa 10 watts out.

Keywords: NANOR, PHUSOR, Power gain, Efficiency, Loading, Ohmic control, LANR

---

1. Introduction - COLD FUSION/LANR is ABSOLUTELY REAL

Thirty-seven years of solid evidence shows conclusive experimental LANR data proving that CF/LANR excess heat is of a nuclear origin. Multiple groups have also confirmed this. Working LANR components/systems now exist in BOTH aqueous solutions and dry pre-loaded nanomaterials and have led to open demonstrations (2 at MIT) and courses with new discoveries. Loaded deuterons in PdD (often under difficult-to-achieve conditions) couple together in these active systems to generate de novo ^{4}He, loss of D, unique antiStokes and RF Deuterium-line emission signatures, and considerable excess heat. Development of CF/LANR-specific diagnostics including antiStokes and RF emissions, and quantum computers now exist, too; these systems have increased incremental power gain, reflecting gains in efficiency.

2. LANR Efficiency is Improving

In the past, we have shown PHUSOR®-type aqueous D_2O components in 2003 (with power gains circa 480%) and with NANOR®-type ZrO_2NiPdD components in 2012 (with power gains of ~ 80 using applied magnetic fields). In the future, we need higher CF/LANR incremental gains, and meticulous effort has now obtained very high levels of incremental power gains, more than 10^4 to 10^6. These incremental power gains were obtained from the preloaded, active NANOR®-type components and were calibrated by ohmic controls where the power gain is ~ 1.

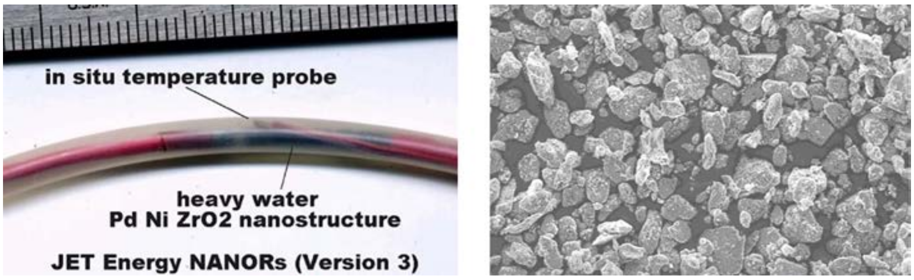

Figure 1. NANOR®-type Component; (left) Series 3 NANOR®-type LANR Component, (right) Dry, preloaded ZrO_2-PdNiD nanostructured core material.

3. Background –NANOR®-type LANR Components

NANOR®-type LANR Components are a new generation of CF/LANR electronic devices exhibiting considerable incremental energy gain. Most importantly, the activation of the cold fusion/lattice assisted nuclear reaction is, for the first time, separated from loading. Also, these NANOR®-type preloaded components are dry and sealed into an electrically conductive (high impedance) configuration.

These important, novel devices feature two terminals with a cylindrical shape and active CF/LANR core and self-contained superior handling properties enabling portability and transportability. Thus, they are incredibly useful and have demonstrated a more reproducible CF/LANR behavior.

The self-contained two electrical terminals NANOR®-type components are fully preloaded with deuterons. They are ∼2 cm in length, with 30 to ∼ 400 milligrams of an LANR active nanocomposite ZrO_2-PdD core, which is ZrO_2-PdNiD [Zr (∼66%), Ni (030%), and Pd (5-25%) by weight] with additional D. The PdNiD nanostructured core islands are electrically isolated by the zirconia (ZrO_2) dielectric. The peak achieved excess power density ∼19.5 watts/gram of nanostructured material improves their already superior handling properties and portability.

4. Experimental – Electric Power Drive in LANR

To accurately measure XSH, careful sequencing of input power to both the component and the ohmic control is required. Each are contained within the same thermal and electrical driving system. We use precision-controlled power sources like Keithley current sources, Tekpower TP3005P, etc. with DAQ monitoring. Analysis of the delivered and applied precise step functions yields accurate calorimetry. For each step pulse, the electrical dissipation (V*I) is maintained over a long period of time. The results are confirmed by long-term time integration, which rules out false positives. Other possible electrical errors are minimized by the boron nitride acting as an electrical insulator.

5. Experimental – Ohmic Control

Good, calibrated measurements require a timely compared ohmic control. For each step pulse, the thermal ohmic control and then the components are examined by constant input power. This provides heat at a constant rate, with electrical dissipation (V*I) maintained over a long period of time.

Experimentally, the ohmic control is first used and compared to an active NANOR®-type component. The advantage of using an ohmic control square wave immediately before the CF/LANR run is that one can also simultaneously check – and compare - the performance of your calorimeter's analysis. The algorithm converts the thermometry to ohmic control-calibrated calorimetry. Confirmation of the algorithm is made by checking the appearance of the output heat from the ohmic control. Thus, ohmic calibration is important in several ways. In addition to calibrating the calorimeter, it also establishes the baseline by first measuring and observing the response of the ohmic control.

6. Experimental – Impedance and Input Power Matching

As electrical engineers, we match the electrical input power to both the ohmic control and the LANR component [“effective power bracketing”]. Such electrical input power bracketing is required to accurately measure the “excess power”. However, in any real setup, the electrical impedance of the NANOR®-type component changes with time, because of past history, hysteresis, and possible electrical avalanche (missing the working LANR) if the voltage is excessive. Therefore, we also attempt to match electrical input power by adjusting the voltage as necessary.

In addition, there is actually some time variance of electrical resistivity that occurs for ohmic controls as well, due to use and changing temperature, but that is minimal and second order. Finally, the use of energy, obtained through time integration of the power, was both used and is actually necessary to also prove one’s analytic system is correct, and to rule out phase changes.

7. Experimental Methods – Calorimetry

In summary, the experimental setup includes calorimetry, and bracketing of the NANOR®-type component with ohmic controls in time and by input electric power applied, and time integration to rule out false positives. The ensemble [components, controls, sensors, additional thermal mass] is examined by thermometry before, during, and after electrical drive, and calibrated by the thermal ohmic control. Calorimetry is then determined by analysis of the dynamic changes of temperature at several locations. Confirmation of the algorithm, checking for linearity and time-invariance, and calibrating the output of the component under test, is made by reproducing the heat generated from a square wave sent to an ohmic control. Also, confirmation of results is made by long term time integration, ruling out several types of possible errors, such as from a phase change.

8. Result –Dry Preloaded NANOR®-type LANR Component

As a result of this meticulous effort, we have now found there can be obtained very high levels of incremental power gain. Different paradigms were used which demonstrate reproducibility several ways. In each example, the paradigm has the ohmic control matched with respect to input power to the NANOR® type component.

Note how many orders of magnitude improvement of the incremental power gain [excess heat [“XSH”]] resulted from the active NANOR®-type component as compared to the ohmic control. Achieving these high incremental power gains has required improved alloys and their loading by deuterons; and then meticulous avoidance of electric avalanches and extending the duration of the heat production cycles.

9. Incremental Power Gain in Series 10 NANOR®-type CF/LANR Components

In Figure 2, the incremental power gain obtained from the preloaded, active NANOR®-type Component N10-1G4 in Run E181-221206A is many orders of magnitude greater when compared to the ohmic control. Shown are the input electrical power (blue and purple dots), and heat output (blue dots), to the ohmic control [“CONTROL”] and to a Deuteron-preloaded, dry NANOR®-type component as a function of time. Also shown are the input and output electrical energies (the yellow and red lines).

Figure 2 shows saliently the desired Excess heat (XSH) which resulted for the NANOR®-type component compared to the ohmic control. Excess heat was not seen with any of the ohmic controls. Note how many orders of magnitude

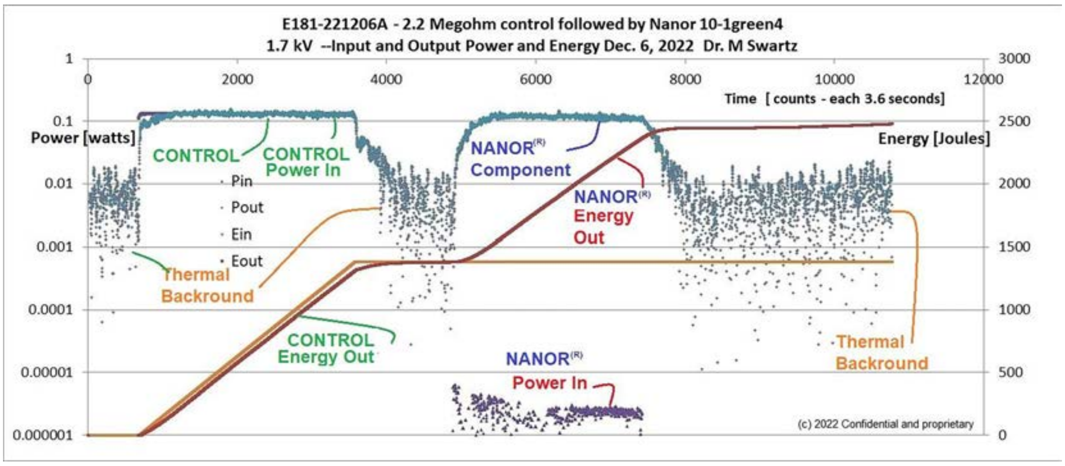

Figure 2. Input and Output Powers and Energies from an Electrically Driven Ohmic Control and then NANOR® N10-1G4, and the Thermal Background. The graph shows the response of NANOR®-type Component N10-1G4, and an ohmic control, in Run E181-221206A. The horizontal axis is time, and here is labeled by counts; with each being 3.6 seconds.

the electrical input to the NANOR®-type component was below the thermal background. The incremental CF/LANR power gain is about 6 x 10^4. The time constant, when the NANOR® was turned on, is about 1500 sec.

In a different run, the results of which are shown in the Figure 3, the input and output electrical powers, and resulting energies, from an electrically driven ohmic control resistor followed by NANOR® N10-1G4, again demonstrate working LANR/CF; large Incremental Power Gains in CF have been achieved reproducibly by these dry, preloaded LANR components.

For further control and proof, Figure 3 also shows the thermal background power. In Figure 3, note how many orders of magnitude the electrical input to the NANOR®-type component N10-1G4 was below the thermal background. Yet even that tiny input has, by LANR, produced very large energy output (logarithmic right axis), far in excess of the input energy. The incremental power gain obtained from the preloaded, active NANOR®-type component is many orders of magnitude greater than the ohmic control in Run E181221130A. The incremental CF/LANR power gain is about 9 x 10^4.

10. Incremental Power Gain Shown Several Ways for LANR Components

The next figure shows the input electrical power and resulting incremental power gain for NANOR®-type Component N10-1G4 and an ohmic control, in Run E181-221201A. The power gain for the ohmic control is 1. By contrast, yet even with a smaller input power, notice that LANR has produced a very large incremental power gain (on the right-hand axis). Notice that the incremental power gain obtained from the preloaded, active NANOR®-type component is many orders of magnitude larger compared to the ohmic control. The difference reflects the excess heat actually achieved in this LANR system.

11. Incremental Power for Series 7 NANOR®-type LANR Components

The next Figure shows the input electrical power delivered to an ohmic control and then NANOR®-type component N7-24. The Figure also shows the resulting mechanical response of some neighboring Nitinol. Excess power (beyond

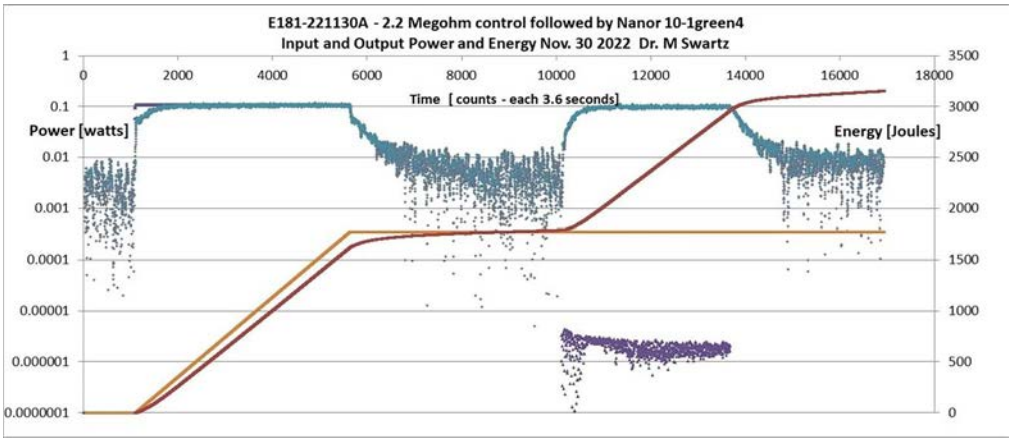

Figure 3. Input and Output Powers and Energies from an Electrically Driven Ohmic Control and then NANOR® N10-1G4, and the Thermal Background. This graph shows the response of NANOR®-type Component N10-1G4, and an ohmic control, in Run E181-221130A. The horizontal axis is time, and here it is labeled by counts with each being 3.6 seconds.

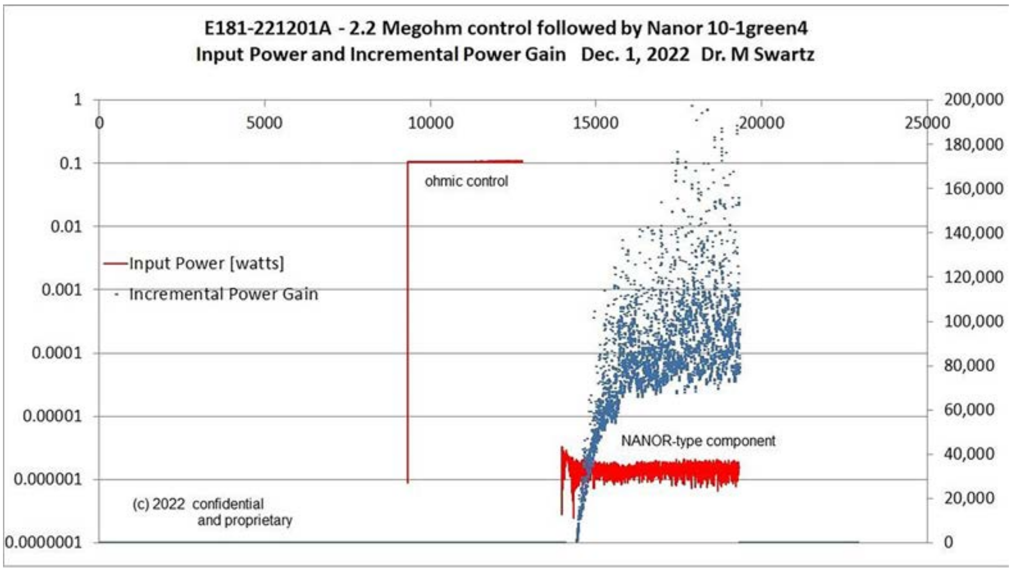

Figure 4. Input Power and Incremental Power Gain for NANOR®-type Component N101G4 and an ohmic control in Run E181-221201A. This graph shows the Input Power and Incremental Power Gains in response to an ohmic control and NANOR®-type Component N10-1G4 in Run E181-221201A.

that which was applied) can be easily seen for the preloaded ZrO_2-PdD. This demonstrates that there was salient LANR activity by NANOR®-type Component N7-24 in Run E127-201009A. In Figure 4, it can also be seen that one can measure and discern the differential response between the ohmic control and a NANOR®-type component where both are physically and thermally attached to the nitinol and thermocouple.

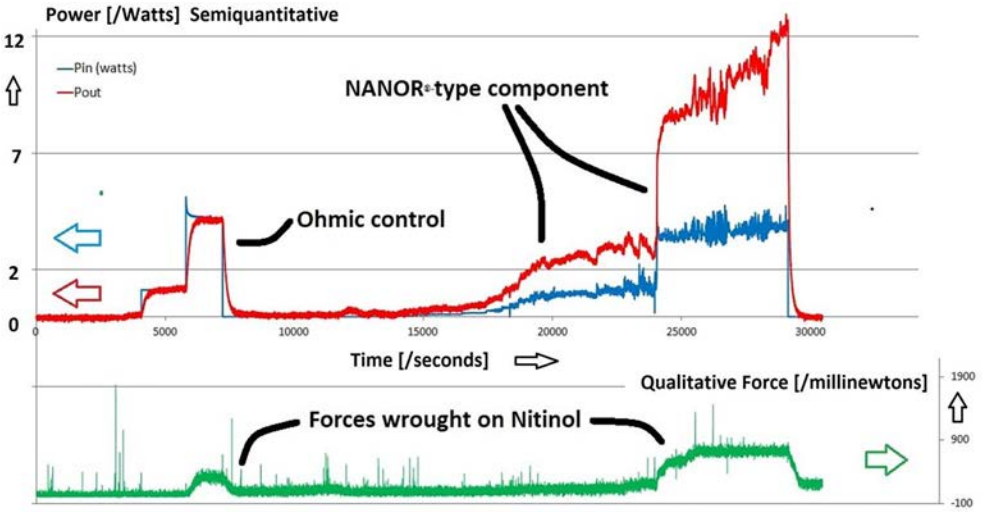

Figure 5. Input Electrical Power delivered to an Electrically Driven Ohmic Control and then NANOR®-type component N7-24 in Run E127-201009A and the Resulting Output Thermal Power and the Mechanical Response on Neighboring Nitinol. Shown is the input (blue) and output (red) electrical power from the Ohmic Control and NANOR® N7-24 as a function of time. Also shown is the response of neighboring accelerometer (shown as the RMS force in green on the lower curve) which was the force wrought by the heat of each upon the nitinol.

12. Incremental Power Gain was Reproducibly Large for Series 7 Components

Figure 6 shows the applied input voltage and the resulting incremental power gain for an ohmic control and then NANOR®-type Component N14-7, after it was fully deuterated. Note how many orders of magnitude the incremental power gain increased compared to the control. A massive incremental power gain was obtained from the preloaded, active NANOR®-type component compared to the ohmic control where the power gain was only 1. Notice that the incremental power gain of the NANOR®-type component, even though initially very high, falls even as the input voltage across it increases. This decrease in incremental power gain, with applying increased voltage, is important.

13. Large Power Gains for Series 7 NANOR® Devices Shown Several Ways

Figure 6 shows the applied input voltage and the resultant incremental power gain for an ohmic control resistor and the NANOR®-type Component N14-7, after it was fully deuterated. Note how many orders of magnitude the incremental power gain realized when obtained from the preloaded, active NANOR®-type component compared to the ohmic control where the power gain was only 1.

14. Large Reproducible Incremental Power Gain Shown Several Ways

Figure 8 shows the elicited delta-T and the calculated incremental power gain for an ohmic control resistor and then NANOR®-type Component N14-7, after it was fully deuterated. Note how many orders of magnitude the incremental power gain from the NANOR®-type component was compared to the ohmic control, where the delta-T is barely noticeable, and the power gain is about 1.

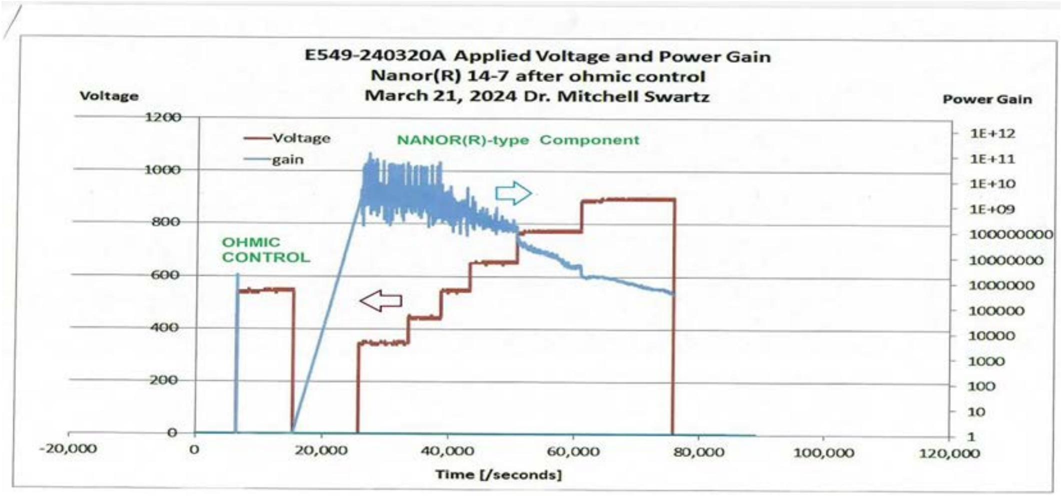

Figure 6. Applied Input Voltage and the Resulting Incremental Power Gain For an Ohmic Control and NANOR®-type Component N14-7 in Run E549-240320A. The horizontal axis is labeled in seconds. The ohmic control was driven prior to the LANR component. The applied input voltage and the calculated effective incremental power gain of both the ohmic control and the LANR component are read off the left-hand voltage axis and the right hand logarithmic incremental power gain axis, respectively.

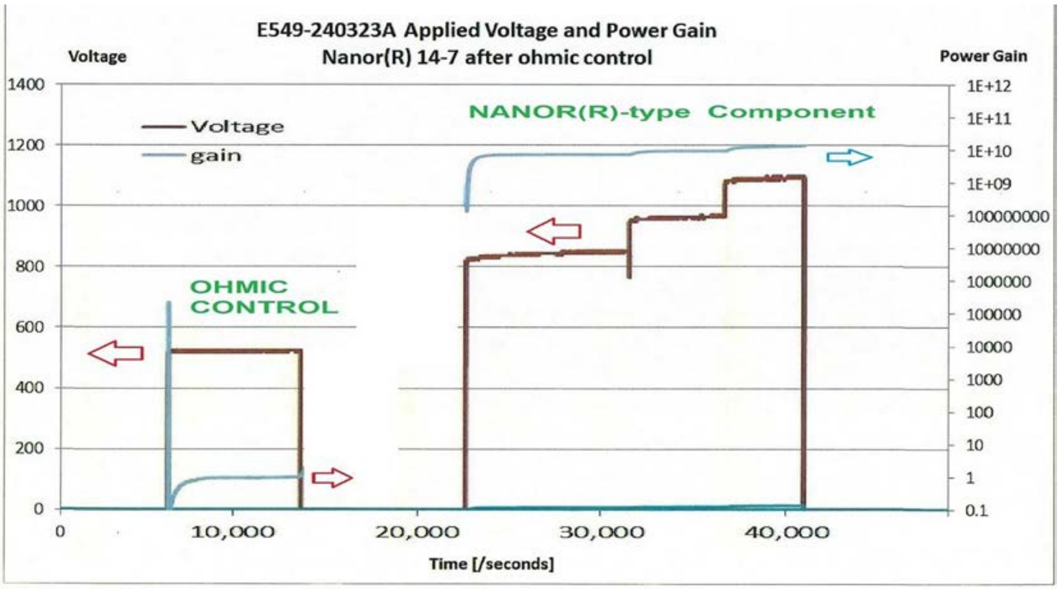

Figure 7. Applied Input Voltage and the Incremental Power Gain For an Ohmic Control and NANOR®-type Component N14-7 Fully Loaded. This graph shows the response of NANOR®-type Component N14-7, and an ohmic control, in Run E549-240323A. The horizontal axis is labeled in seconds.

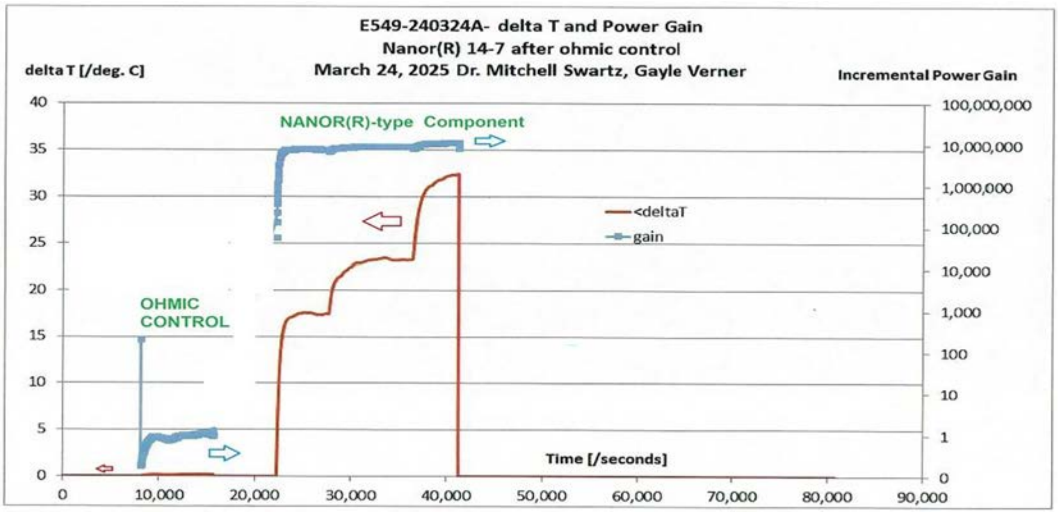

Figure 8. Elicited delta-T and the Incremental Power Gain For an Ohmic Control and NANOR®-type Component N14-7 in Run E549-240324A. The horizontal axis is labeled in seconds.

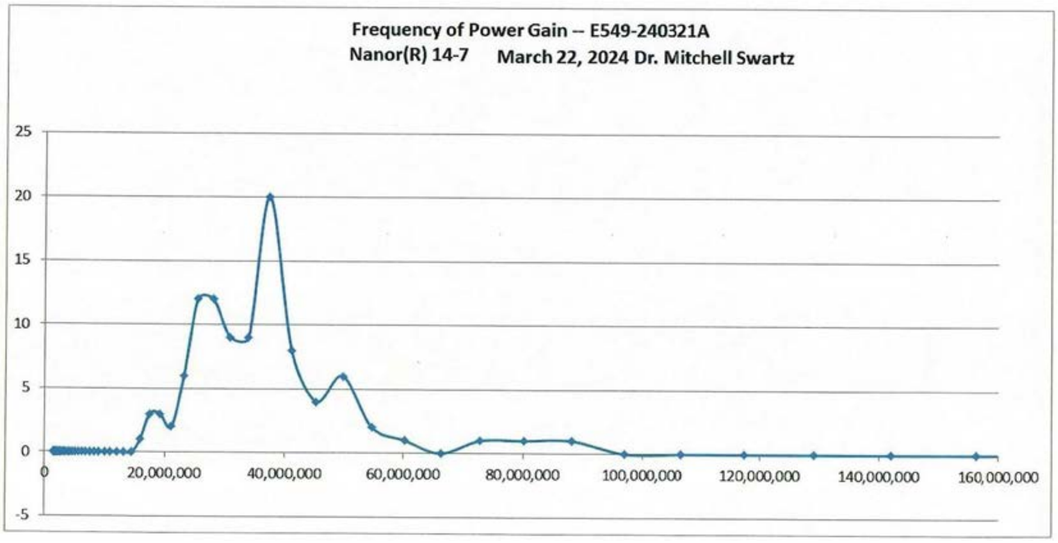

Figure 9. Frequency of Power Gain for Component N14-7 During Run E549-240321A. This is a histogram of the incremental power gain results during Run E549-240321A.

15. Histogram of Incremental Power Gain is Very Interesting

Figure 9 shows the histogram of power gain measured for NANOR®-type Component N14-7 during run E549-240321A. The histogram reveals the number of times during the run, that each incremental power gain (listed on the x-axis) was seen. This diagnostic idea is novel and was suggested by Engineer Physicist John Wallace.

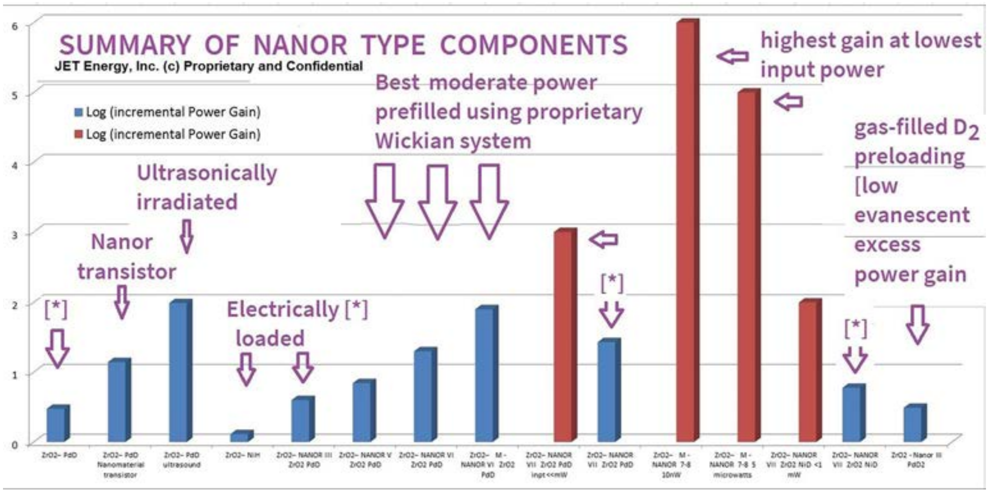

Figure 10. JET Energy: Energy Production Summary of NANORS, Summary of Incremental Power Gain For Thousands of LANR Experiments. This graph of Incremental Power Gain (on a logarithmic vertical axis) shows the results of hundreds of LANR experiments over more than three decades. Much has been learned.

16. Evolution of Incremental Power Gain

Figure 10 summarizes much of the data on incremental power gain for NANOR$^{®}$type Components. Loading by gas, and by electrochemistry, and especially the novel Wickian technology have all been used successfully.

17. Conclusion - Large Incremental Power Gains Available

Very high incremental power gain excess heat [“XSH”] reproducibly elicited by clean CF/LANR energy production is achievable now. Dry, preloaded LANR NANOR$^{®}$-type components produce orders of magnitude greater energy than ohmic controls, for the same electrical input. The highest peaks of ‘excess heat’ & energy production are a road far ‘less traveled’ in this field because success has been difficult to achieve, and required improved loading of deuterons, with meticulous avoidance of unwanted electric avalanche flows. The important result of these studies is the discovery of how successful LANR/CF applications can be achieved by utilizing the very large incremental power gain with 1 microwatt in, then with $\sim$ 10 watts out. Thus, dry preloaded LANR NANOR$^{®}$-type components, bundled in groups, appear to enable a future of clean energy production poised to enable and enhance future demonstrations, technical improvements, and then entry to real commerce.

18. Conclusion – Incremental Power Gains Have Increased Over Time

The incremental power gains (ratio of the actual excess heat to the input energy) of CF/LANR have improved, with much greater incremental gain than was realized with the PHUSOR$^{®}$-type aqueous D_2O components in 2003 (such as at the ICCF-10 open demonstration - with gains $\sim$ 480%), or with the NANOR$^{®}$-type ZrO_2NiPdD components in 2012 (at the MIT IAP Course, then with a gain of 12x (1200%), later increased to a gain of $\sim$ 80x with magnetic fields applied synchronously). Now, this report augments those levels with even higher achievable LANR incremental power gains.

19. Very Large Incremental Power Gain Offers Opportunity

Ultimately, toward the future, commerce and technically engineered improvements may require even larger values of incremental power gain [output power divided by the input power]. Very high incremental power gain is achievable now. Dry, preloaded LANR NANOR®-type components produce orders of magnitude greater energy than ohmic controls, for the same electrical input.

The highest peaks of ‘excess heat’ & energy production are difficult to achieve. The secret of very successful LANR/CF for applications is now revealed: large incremental power gain with 1 microwatt in, then $\sim$ 10 watts out. In CF/LANR’s future, we will also need improved alloys with lattices capable of longer durations than these XSH-production runs, with reduced loss of the active alloy.

Clean, quiet, LANR engines and motors systems will drive electrical generators to provide propulsion and transportation; there is more available energy from CF/LANR devices than from all of the earth’s oil reserves.

Acknowledgements

The author thanks Gayle Verner, Susan Woods, Alex Frank, Thomas Farina, Isidor Straus, Joshua Gyllinsky, Raymond Kurzweil, Aaron Kleiner, Peter Hagelstein, Brian Ahern, Jeff Driscoll, John Wallace, Michael Staker, Andrew Muelenberg, Brian Josephson, Dennis Cravens, Dennis Letts, Florian Metzler, Frank Gordon, Lawrence Forsley, Pamela Mosier-Boss, Louis DeChiaro, Jean-Paul Biberian, David Nagel, Win Cuthbert, Carl Page, and Christy Frazier. NANOR® and PHUSOR® are registered trademarks. The LANR technology described here is protected by patents.

References

[1] Swartz, M. R., Brian Ahern, Charles Haldemann and Alan Weinberg, Excess Heat is Linked to Deuterium Loss in an Aqueous Nickel LANR [1] System, Proc. ICCF-21, J. Condensed Matter Nucl. Sci, Vol 29, 169 (2019).

[2] Swartz M., Excess Power Gain using High Impedance and Co-depositional LANR Devices Monitored by Calorimetry, Heat Flow, and Paired Stirling Engines, Proc. ICCF14, 1, (2008), p 123; ISBN: 978-0-578-06694-3, 123, (2010).

[3] Swartz, M., Photoinduced Excess Heat from Laser-Irradiated Electrically Polarized Palladium Cathodes in D_2O, Condensed Matter Nuclear Science, Proc. ICCF-10, ISBN 981-256-564-6, 213226 (2006).

[4] Swartz M. R., Achieving Very High Increment Power Gain, J. Condensed Matter Nucl. Sci, (ICCF-25).

[5] Swartz, M. R, Oscillating Excess Power Gain and Coerced Magnetic Domains in NANOR®-type CF/LANR Components, J. Condensed Matter Nuclear Sci., 22, 35-46 (2017). [6] Swartz, M. R, G. Verner, J. Tolleson, P. Hagelstein, Dry, preloaded NANOR®-type components, Current Science, 108, 4, 595 (2015).

[6] Swartz M. R., Hagelstein P.I., Demonstration of Energy Gain from a Preloaded ZrO_2–PdD Nanostructured CF/LANR Quantum Electronic Device at MIT, J. Condensed Matter Nucl. Sci.13, 516 (2014).

[7] Swartz M. R., Verner G., et al., Energy Gain From Preloaded ZrO_2–PdNi–D Nanostructured CF/LANR Quantum Electronic Components, J. Condensed Matter Nucl. Sci. 13, 528, (2014). [9] Swartz, M., Survey of the Observed Excess Energy and Emissions In Lattice Assisted Nuclear Reactions, Journal of Scientific Exploration, 23, 4, 419–436 (2009).

[8] Swartz, M. R., Synchronization of Vacancy-Loaded Deuterons Enables Successful LANR Mass-Energy Transfer, JCMNS, Proceedings of ICCF24, Vol. 38, 147 (May 2024).

[9] Swartz, M. R, Aqueous and Nanostructured CF/LANR Systems Each have Two Electrically Driven Modes, Proc. ICCF-21, Fort Collins, Co.6/3/18 (2018), J. Condensed Matter Nucl. Sci, Vol 29, 177 (2019).

J. Condensed Matter Nucl. Sci. 41 (2026) 145–152

Research Article

The Biophysical Reasons, Physical Mechanism and Experimental Implementation of Iodine to Xenon Transmutation in Biological Systems

Vladimir I. Vysotskii

Taras Shevchenko National University of Kyiv, Ukraine

Alla A. Kornilova

member of Condensed Matter Nuclear Science Society

Sergey N. Gaydamaka

AVSystems Inc., 54, Harpsichord TPKE, Stamford, USA

Abstract

The biophysical and nuclear-physical prerequisites for the transmutation of iodine into xenon in growing microbiological systems are considered. The experimental studies have shown that in the presence of external biochemical action, formed by the influence of a small admixture of heavy water to a water-containing nutrient medium, such nuclear transmutation takes place. It is shown that the most probable mechanism for stimulating such nuclear fusion is associated with the formation of local shock acoustic vibrations associated with DNA breaks due to the action of heavy water. The action of such shock vibrations can lead to the formation of coherent correlated states of nearby protons and the generation of short-term intense energy fluctuations, the amplitude and duration of which are sufficient to implement nuclear fusion.

Keywords: LENR, Coherent correlated states, Biological transmutation of isotopes

---

1. Introduction

The traditional description of the process of low-energy isotope transmutation is limited to the substantiation of the physical mechanism for overcoming the Coulomb barrier. In such reactions, the influence of the environment on the conditions for LENR implementation can be quite significant and selective, but not “motivated”.

Previous studies have shown that extending the basic LENR concepts to biological systems leads to the conclusion that such fusion can selectively respond to an objective “demand” for the possibility of generating a specific nuclear reaction. In particular, with a specially created deficit of iron in the nutrient medium in which growing microorganisms are located and developed, the

$$Mn^{55} + d = Fe^{57} \text{ and } Na^{23} + P^{31} = Fe^{54} \tag{1}$$

fusion reactions are implemented very effectively in the presence of the necessary isotopes in the environment (accordingly Mn^{55} and H^2 or Na^{23} and P^{31}) [1]–[4]. These features are due to the fact that iron is a vital microelement and, in its absence, the growth of microcultures becomes impossible. Such conditions are associated with the general functional features of LENR in growing biological systems [1]–[4].

The paper presents for the first time the results of a study of selective-functional methods for stimulating similar nuclear processes associated with the fusion of xenon in biological systems. These methods depend on specific conditions that must be sufficiently met.

It is well known that xenon is not a vital micro- or macroelement and is not their biochemical analogue. On the other hand, it is well known (e.g. [5]) that xenon has unique protective and healing properties, which are widely used in modern medicine and in the treatment of animals.

The traditional clinical method of using xenon as the most effective and safe anti-stress drug is associated with its external introduction into a living organism (for animals and humans – into the respiratory tract). Xenon reduces the amount of free radicals, has a neuroprotective effect, blocks some receptors, stimulates the hormonal system, etc. On the other hand, it seems quite strange that this chemically neutral gas – the concentration of which in the atmosphere is very small, and which is not a vital micro and macro element – is such an anti-stress factor. Yet effectiveness of xenon has been established by many millions of years of biological evolution.

This dilemma can only be successfully resolved if a given living organism can automatically synthesize xenon as a defensive response. Such a radical explanation cannot be based on chemical and biochemical processes, and is impossible from the point of view of physiology, anatomy and biochemistry. Potentially it must have a nuclear-physical basis that can justify the nuclear fusion of xenon

$$I^{127} + p = Xe^{128} \tag{2}$$

under critical conditions.

An alternative method for hypothetically producing xenon in a living biological system could involve a different reaction

$$I^{127} + d = Xe^{129}, \tag{3}$$

leading to the formation of a heavier stable isotope of xenon. The probability of this reaction is significantly lower due to two obvious factors: the low concentration of deuterium in the aqueous environment of a living organism (0.015% in pure water and 2% in the experiment described here) and the significantly lower probability of tunneling for the heavier deuterium nucleus compared to a proton.

The final energy of these reactions is released in the form of several gamma quanta. In different types of living systems, these can be places of maximum iodine concentration. In particular, in chordate animals, the most probable mechanism of xenon creation is associated with fusion reaction on the surface or in the volume of the thyroid gland, where iodine atoms are localized. There are good reasons to believe that the unique anti-stress potential of xenon exists even with the development of microbiological associations.

2. Experiments on Xenon Fusion in Microorganisms

In our experiments, a syntrophic association of mold fungi that grew on high concentrations of chromium at room temperature was used. Glucose (about 5 *g/l*) was used as a carbon substrate of the energy source. The remaining macro- and microelements were provided by autolysis of dead cells of the original syntrophic association.

Figure 1. Dry-air granules from an anaerobic syntrophic association before loading into bioreactors.

To select microorganisms with multiple resistance, a programmable temperature gradient from 20° C to 90° C for 7 days was used. Then, this group of microorganisms (a consortium) was incubated, and the system was maintained in sealed conditions at a stable temperature (20-22° C) for 3 months. As a result, a consortium of thermotolerant anaerobic polyextremophiles was obtained, capable of syntrophy in life-suppressing conditions, limited availability of substrates, as well as macro- and microelements. The biomass obtained from this process (Fig. 1) was inoculated into sealed bioreactors with an argon atmosphere simulating anaerobic conditions and allowing the analysis the biogas composition. Iodine (total content in the medium was 100, 50 and 10 *mg/l*) and distilled water with a controlled addition of D_2O (2%) were added to the liquid (H_2O-based) nutrient medium of the experimental bioreactors.

In these final (nucleus-focused) experiments, the main chemical elements in the liquid medium containing the biomass were *S, N, C, O*, and *D*. The only source of carbon in this medium was glucose (2 *g/l*). The incubation temperature was 20-22°C, which corresponded to the optimum for the consortium formed over 3 months. The incubation duration was 7 days. An indirect assessment of metabolism was determined by the release of CO_2 into the gas phase. Metabolic activity in the bioreactor was regulated by changing the concentration of potassium.

The main stress factor in these experiments was the presence of a small impurity of heavy water D_2O, which inhibits the process of DNA replication, cell division and, ultimately, the growth of the syntrophic association of mold fungi. This influence is associated with various factors which will be briefly discussed below.

Two views of closed bioreactors with different iodine concentrations at the beginning (left) and after the end of the experiment (right) are shown in Fig. 2. The contents of the cuvettes differed in key components (from left to right): *K* (100 *mg/l*), *I* (100 *mg/l*), *K* and *I* (100 *mg/l*), *I* (50 *mg/l*), *K* and *I* (50 *mg/l*), *I* (10 *mg/l*), *K* and *I* (*10 mg/l*).

Determination of *Xe* content in the gas phase of hermetically sealed bioreactors without sampling was carried out by non-invasive measurement through the glass walls of the bioreactor (3 mm thick) using a portable X-ray fluorescence analyzer SciAps X-505.

The following operating mode of this device was used. An *Au* anode (50 *kV*, 200 μA) was used to generate hard X-ray radiation capable of passing through glass and exciting *Xe* and a filter (for heavy elements) to minimize the reflection from the glass. The measurement time was 600 seconds to increase sensitivity. The device was pressed tightly against the glass wall of the bioreactor in the gas space zone (see Fig. 3).

Experiments on studying the transmutation of iodine into xenon lasted 7 days. It was found that a small concentration of iodine (10 *mg/l*) did not suppress the growth and metabolic activity of the microcultures used, which in the

Figure 2. Two views of the system of closed bioreactors with an identical syntrophic community of mold fungi at different initial concentrations of iodine at the beginning and after the end of the experiment. Each pair of duplicate bottles contained 100, 50 and 10 *mg/l* of Iodine and 2% of heavy water.

Figure 3. Detection of xenon in a bioreactor using an X-ray spectrometer SciAps X-505.

process of their development produced xenon as a by-product when using iodine in internal metabolic processes under stress conditions. In bioreactors with iodine content of 50–100 *mg/l*, metabolic activity decreased by 90–95% or more.

The fragment of the gas composition spectrum (with *Xe* resonance peaks in the range of λ=823-828 *nm*) in a bioreactor with an initial iodine concentration of 10 *mg/l* is shown in Fig. 4.

During additional analysis of this gas composition, a peak at an energy of 29.77 *keV* was also recorded. This peak corresponds to the K_α line of xenon.

The detection of resonance peaks of *Xe* at wavelengths of 823.16, 828.01 and 826.65 *nm* and at energy of 29.77 *keV* confirms the occurrence of fusion reactions (2) or (3) in the bioreactor.

In control experiments (without the presence of iodine or in the presence of iodine and the absence of heavy water) these xenon X-ray resonances in similar biosystems and in a closed air space inside the bioreactor were completely absent.

The peculiarity of this device is the presence of spectral lines of *Fe* and *Mn* in the spectrum, which is due to the presence of an iron edging of the measuring window of the X-ray fluorescence analyzer.

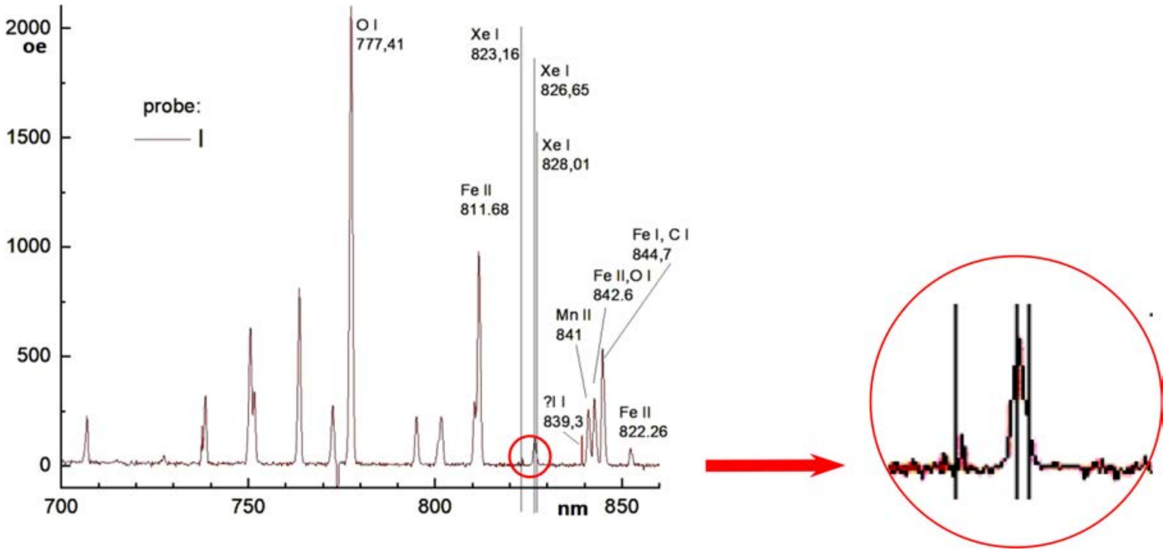

Figure 4. Spectrum of the gas environment and measurement of xenon in the airspace of a closed bioreactor 7 days after the start of the experiment. The initial aqueous environment of the bioreactor contained an admixture of 2% D_2O and iodine in the amount of 10 *mg/l*.

3. Possible Physical and Biophysical Mechanisms of I to Xe Nuclear Transmutation in Microbiological Systems

The mechanism can be explained by nuclear fusion in the microfungi system in the presence of an external influence on this biostructure is associated both with the general (physical) conditions for the implementation of LENR, and with consideration of the specifics of biological processes, and their possible influence on the process of interaction of nuclei.

In our opinion, one of the most realistic self-regulating mechanisms for the production of fusion reactions (2) and (3) may be associated with the self-regulating processes of forming coherently correlated states (CCS) of protons in interatomic potential wells of small size (nanowells) near or inside the volume of changing biomolecules. This process constantly occurs in living organisms (for example, during DNA replication or biological cell division in the aqueous environment of biological systems). This leads to the formation of very intense and relatively long-lasting fluctuations in the energy and momentum [6], [7]

$$\delta E \geq \hbar/2\delta t\sqrt{1-r_{E,t}^2}, \tag{4}$$

$$\delta p \geq \hbar/2\delta x\sqrt{1-r_{p,x}^2} \tag{5}$$

of protons located in these nanowells [8]–[10]. These characteristics of living systems differ fundamentally from the static structure of inanimate matter.

Such CCS states with a large correlation coefficient $|r| \to 1$ and coefficient of correlation efficiency $G = 1/\sqrt{1-r^2}$ can be created with different types of modulation of the parameters of the potential well in which the particle in question (for example, a proton) is located. In particular, such a process occurs during a rapid, monotonic, unidirectional expansion or compression, or a reversible, pulsed compression and subsequent expansion of this potential well, leads to mutual phasing of the quantum superposition of the eigenwave functions of a particle (e.g., a proton) located in this well. This is a direct result of the standard quantum mechanical analysis of the dynamic state of a particle in a non-stationary potential well [9]–[13]. One of the effective sources of such rapid deformation is the action of a local microshock acoustic wave on neighboring atoms forming a potential well for the proton in question.

In real aqueous environments, such as those at room temperature, these energy fluctuations can correspond to very large values.

The duration of the proton's correlated state after its rapid formation is many orders of magnitude longer than the proton's oscillation period in the potential well under consideration [11]–[13]. This time is sufficient for it to pass through the Coulomb potential barrier of the neighboring nucleus.

When a proton is localized in a typical interatomic or intermolecular potential nanowell of size $a \approx 2 - 5\,\mathring{A}$, the energy fluctuation in such a correlated state reaches a very large value

$$\delta E = \frac{(\delta p_x)^2}{2M_p} \geq G^2_{p_x x}\hbar^2(2N+1)/8M_p(\delta \mathrm{x})^2 \geq 20 - 50\,keV \qquad (6)$$

Here, $\delta x \approx a/2$, M_p is proton mass, N is the number of the energy level of the proton in this potential nanowell before the impact of the local shock wave ($N \approx 10 - 30$ at room temperature of the liquid environment) [13].

The presence of such very large fluctuations in the energy of a proton located near the I^{127} isotope in the region of action of a local shock wave leads to a very significant increase in the probability of the tunneling effect

$$D_{r\to 1} \approx \exp\left\{-\frac{2\sqrt{1-r^2}}{\hbar}\int_R^{R+L(E)}\sqrt{2\mu_p\{V(q)-E\}dq}\right\} = (D_{r=0})^{\sqrt{1-r^2}} \equiv \sqrt[G]{D_{r=0}} \qquad (7)$$

and, accordingly, to a high probability of generating a nuclear fusion reaction (2).

Here μ_p is the reduced proton mass, *R* is the radius of I^{127} isotope, *L(E)* is the width of the Coulomb potential barrier $V(q)$ at average particle energy $E \approx kT$.

From this formula it follows that when $r \to 1$ and *G* >> 1 we have $D_{r\to 1} \to 1$ at low average energy of the proton.

A detailed description of such processes is discussed and presented in [9], [13].

It is fundamentally important that the formation of a coherent correlated state of a specific particle (e.g., a proton) with the subsequent generation of very large fluctuations in its energy and momentum is associated with quantum interference processes in the system of quantum eigenstates of the particle in question in a local potential nanowell. This process does not require the collective influence of the environment on the equivalent oscillator to occur. In this case, the process within this oscillator also has no impact on the environment, which is critical for maintaining the viability of living organisms.

Another significant difference in features compared to LENR reactions stimulated by short-term energy (4) and momentum (5) fluctuations is that this process is not accompanied by a net transfer of this momentum fluctuation to the reaction products and the environment. This is due to the general law of conservation of momentum – this momentum appears for a short time $\delta \mathrm{t}$ the existence of a fluctuation, and then disappears completely. In contrast, "standard" reactions involving real (rather than virtual) accelerated particles with high momentum result in a net transfer of this real momentum to the reaction products.

The features discussed here for the implementation of LENR at low temperatures during rapid deformation of a model potential are closely related to purely physical properties of the interaction of nuclear particles in an abstract physical system (for example, a metal hydride). Importantly, similar processes can occur at the microlevel not only in such laboratory or natural physical systems, but also within the volume of a biological system, provided the same conditions are met at the local atomic or micromolecular levels.

The physical mechanism that leads to the formation of a local shock wave and, accordingly, to the formation of a coherent correlated state is associated, in particular, with the specificity of the DNA replication process in growing microorganisms in an aqueous environment (including in the syntrophic community of mold fungi under consideration).

It is well known that the standard period $L_{DNA} = 0.34\ nm$ of the spatial structure of the arrangement of nucleotide pairs in any DNA is in very good agreement with the spatial near-surface microstructure of the mutual arrangement of water molecules surrounding the DNA [14]. This structure of water is associated with the formation of clathrate hydrates formed from water molecules in the area near any surface. This complete and mysterious spatial alignment is maintained throughout the entire DNA double helix, which contains more than one billion consecutive periods.

There are fundamental studies (for example, [15], [16]) that consider a very convincing version that ordinary water H_2O was an effective matrix on which the first DNA molecules were formed about 3.8 billion years ago. The size of a heavy water molecule D_2O or *HDO* is slightly smaller than that of light water H_2O due to the different masses of hydrogen and deuterium atoms. This leads to a slight change in the spatial structure of surface water near DNA. In the case of the presence of heavy water molecules near the DNA surface, a slight mismatch of the spatial structures of water and DNA occurs, which over an interval of about 80-100 periods L_{DNA} leads to the appearance of strong tearing electric fields acting on the DNA surface (on sugar-phosphate backbone) and associated with the electric dipole moments of water molecules. During the process of DNA replication, which is a necessary element preceding cell division, such external electric fields lead to rapid mechanical DNA breaks, which leads, in particular, to the formation of local acoustic waves and a local shock waves in the volume of water surrounding the area of the DNA break.

The process of automatic formation of such CCS [8]–[13] can be stimulated by the action of such local acoustic waves and local shock waves on protons caused by physiological stress in response to an abnormal external effect (for example, partial replacement of H_2O with D_2O or *HDO*). Similar processes can also occur in more complex biosystems (e.g. animals or humans) under the influence of various factors of external or internal influence, leading to a stressful state.

This mechanism of stimulating nuclear fusion by adding heavy water to a working cell containing growing syntrophic association of mold fungi is in good agreement with the fundamental laws of nuclear physics and biophysics.

In the future, we plan to continue a detailed study of mechanisms of formation of stress reactions of biosystems and other possible processes associated with the combination of biophysical and nuclear-physical effects in living biosystems. In future complex experiments, we will study the isotopic composition of the detected xenon to fully identify the reaction occurring in the experiment reported here ((2) or (3)). We also plan to conduct further synchronous measurements of gamma radiation, which is the main mechanism of energy release in reactions (2) and (3) when heavy water acts on a biological system. Similar studies will include analysis of possible acoustic vibrations in the volume of the working environment during these experiments. We also plan to conduct similar and more detailed studies using other methods of stress generation, not only in fungi or microorganisms, but also in mice and other animals.

References

[1] V.I. Vysotskii, A.A. Kornilova. Nuclear fusion and transmutation of isotopes in biological systems, MIR Publ. House, 2003, 302 p.

[2] V.I. Vysotskii., A.A. Kornilova. Nuclear transmutation of stable and radioactive isotopes in biological systems. Book, Pentagon Press, India, 2010, 187 p.

[3] V.I. Vysotskii, A.A. Kornilova. Transmutation of stable isotopes and deactivation of radioactive waste in growing biological systems. *Annals of Nucl. Energy*, **62** (2013) 626–633.

[4] Vladimir Vysotskii, Alla Kornilova. Effective LENR and transmutation of stable and radioactive isotopes in growing biological systems. Cold Fusion. Advances in Condensed Matter Nuclear Science, Ed. by J.-P. Biberian, Elsevier, Chapter 12, pp. 205–232, 2020.

[5] Wenwu Liu, Ying Liu, Han Chen et al. Xenon preconditioning: molecular mechanisms and biological effects. *Med. Gas Res.* 2013, Jan 10;3:3.

[6] E.Schrödinger, Heisenbergschen Unschärfeprinzip, Ber. Kgl. Akad. Wiss., S24, 1930, 296.

[7] P. Robertson, *Phys. Rev.* A, **35** (1930), 667.

[8] V.I. Vysotskii, M.V. Vysotskyy. Coherent correlated states and low-energy nuclear reactions in non stationary systems. *European Phys. Jour*. A49, issue 8: 99 (213) 1–12.

[9] V.I. Vysotskii, M.V. Vysotskyy, Universal mechanism of LENR in physical and biological systems on the base of coherent correlated states of interacting particles. Book, Cold Fusion. Advances in Condensed Matter Nuclear Sci., Ed. by J.-P. Biberian, Elsevier, Chapter 17, pp.333–369, 2020.

[10] V.I. Vysotskii, M.V. Vysotskyy, Features of correlated states and a mechanism of self-similar selection of nuclear reaction channels involving low-energy charged particles, *J. Exp. Theor. Phys.*, **128** (2019) 856–864.

[11] V.I. Vysotskii, M.V. Vysotskyy, The formation of correlated states and optimization of the tunnel effect for low-energy particles under nonmonochromatic and pulsed action on a potential barrier, *J. Exp. Theor. Physics*, **121** (2015) 559–571.

[12] V.I. Vysotskii, M.V. Vysotskyy, Formation of correlated states and tunneling for a low energy and controlled pulsed action on particles, *J. Exp. Theor. Physics*, **125** (2017) 195–209.

[13] V.I. Vysotskii, M.V. Vysotskyy, Current status of the coherent correlated states for explanation of LENR, *J. Condensed Matter Nucl. Science.* **39** (2025) 165–184.

[14] A.A. Pinchuk, V.I. Vysotskii. Long-range intermolecular interaction between broken DNA fragments, *Phys. Rev E*, **63**, No. 3 (2001) 31904–31910.

[15] B. Jacobson, Hydration Structure of deoxyribonucleic acid and its physico-chemical properties. *Nature* **172** (1953) 666–667. https://doi.org/10.1038/172666a0

[16] J. Depireux, D. Williams, Influence of deoxyribonucleic acid on the intermolecular structure of water. *Nature* **195** (1962) 699–700. https://doi.org/10.1038/195699b0

J. Condensed Matter Nucl. Sci. 41 (2026) 153–163

Research Article

Temperature Effects and Transmutations With High Frequency Induction

Heinz B. Winzeler
ecoengineering dr. winzeler, Winterthur-Zurich, Switzerland

Abstract

A compact quartz-glass reactor combining inductive heating and excitation with high magnetic fields was developed to study hydrogen-metal interactions and potential low-energy nuclear phenomena. Experiments with palladium-coated and pure nickel foils produced repeatable activation upon gradual pressure reduction and deactivation by short hydrogen pulses. In the active state, identical output temperatures were maintained with substantially less electrical input, with coefficients of performance ranging from 1.4 to 2.4. Surface analysis by scanning electron microscopy revealed localised melting and pore formation, while energy-dispersive X-ray spectroscopy showed significant compositional changes, including the appearance of elements such as carbon, oxygen, aluminium and silicon. The results demonstrate reproducible excess heat under well-defined conditions and surface changes consistent with nuclear processes, making the reactor a versatile platform for systematic LENR research and scale-up.

Keywords: High-frequency induction, Hydrogen-metal system, Excess heat, Transmutation, Dynamic insulation

1. Introduction

Hydrogen-metal systems have received increasing attention due to their potential to produce clean energy and transmute elements under mild and unconventional conditions [1], [2], [3]. This study presents the results of experiments involving various material configurations. Our experiments are based on the hydrogen-metal gas-phase system discovered by Italian physicists Sergio Focardi and Francesco Piantelli in 1989 [4]. This system was discovered independently in the same year that Fleischmann and Pons observed the electrolysis effect in the USA. Both processes generate nuclear energy without radioactivity. The nuclear nature of the processes was demonstrated by the presence of specific signatures [5]. Piantelli and Focardi's process received little attention at the time. The author considers it to be the more promising of the two.

2. Reactor Design and Methodology

2.1. Reactor Concept

The reactor is made of quartz glass, allowing both induction heating and optical interaction. It is sealed at the bottom with a flange which allows for the easy exchange of reactants. It contains feedthroughs for sensors and gas at ambient temperature. A central tube that is open to the atmosphere at the bottom contains the temperature sensors. The sensors can be moved freely during the reaction, enabling temperature profiles to be recorded.

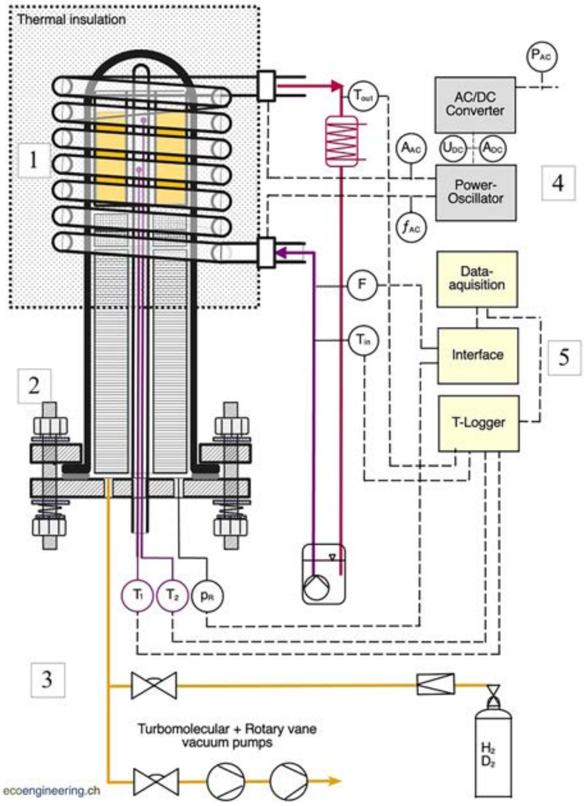

Figure 1. Schematic of the LENR reactor system.

Table 1. Features of the reactor concept.

1.	Hot reaction zone surrounded by a high-frequency induction coil: all energy is coupled inductively (no wiring in the hot zone)
2.	Cold flange with sensor- and gas feedthroughs
3.	Vacuum and gas supply for controlled atmosphere conditioning
4.	Power supply, HF oscillator
5.	Measurement and control system

Fig. 1 shows the P&I diagram of the overall system. Its special features are listed in Table 1. The intellectual property is described in two patents [6] and [7].

A coil is wound around the upper, hot reaction zone. A power oscillator generates an alternating electromagnetic field within the reaction chamber. This heats the reaction material inductively, stimulating interaction between the hydrogen and the metal lattice through the generation of high local currents, all without direct contact.

The induction frequency used was in the range of 102 ±2 kHz.

Fig. 2 shares the principle of dynamic insulation whose function is described under section 2.3

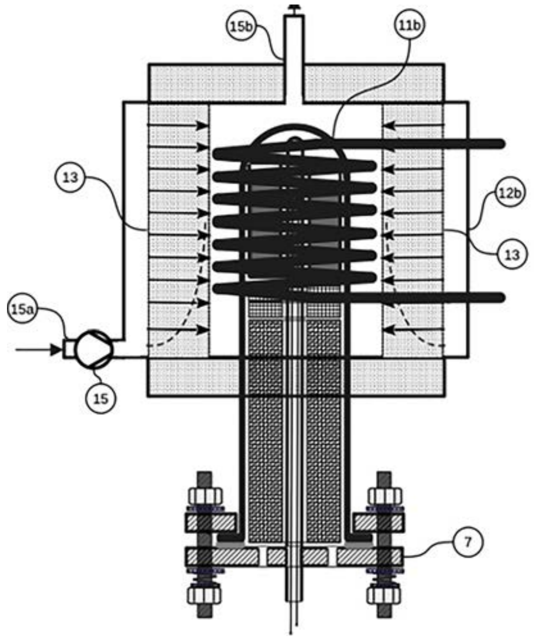

Figure 2. Dynamic insulation.

2.2. Process Equipment, Sensors, Control and Safety Monitoring

Vacuum pumps**:** Rotary vane Alcatel Pascal ACS 2005SD and Turbomolecular Alcatel ATP 80; Flow calibration: Microbalance Mettler Toledo, PM489 DeltaRange 1 mg - 400 g; Valves: Swagelok SS-DS6MM for vacuum and SS-6BRG-MM for hydrogen; 3 piston reciprocating pump for cooling circuit**;** inline filter: Distrelec AG; ZFC75 (04.2023), pressurized gases: H_2 (Linde AG), 10 L, 150 bar, 99.99%; D_2 (Sigma Aldrich), 2 L, 20 bar with pressure reducer 300/1.5 bar (Gloor AG)

Professional components are used for the sensors, pumps and valves. For example: pressure: NXP 100 kPa type MPX2100DP; water flow rate: Digmesa Nano Flowmeter (0.05–0.4 l/min), nozzle (1.1 mm), 49,000 pulses/L, 40 s^{-1}. A 4-channel temperature logger (PCE-T390-4) calibrated and compensated, with an SD card is used with temperature K-type sensors GG-K-30 SLE glass fibre (-30 to 760/1000 °C).

Data acquisition and control: ProfiLab-Expert in combination with a LabJack interface. All the electronics for data acquisition, high-frequency technology, control and safety elements were developed and programmed in-house by team members. Radiation values were continuously measured and recorded using a certified and calibrated device (Gamma-Scout, model Alert) to determine and record any α, β and γ radiation.

2.3. Extraction of Energy - Static and Dynamic Insulation

As shown in Fig. 1, the inductor is designed as a tubular coil through which coolant flows. It acts both as an inducer and a heat exchanger, absorbing and dissipating the heat of the reaction. The hot zone of the reactor is enclosed by static insulation to minimise heat loss.

Fig. 2 shows the reactor equipped with dynamic insulation. The induction coil is made of solid wire and is surrounded by a fluid-permeable insulating material through which a heat transfer fluid (e.g. air) is conducted from the outer containment to the reactor wall. In a counterflow this fluid dissipates the heat emitted by the reactor core and transfers the heat energy to an external recipient with practically no loss.

2.4. Materials and Procedures

2.4.1. *Reaction materials*

Nickel foil rings measuring 20 × 8 × 0.1 mm were electrolytically plated in a bath containing 80 % by weight palladium and 20 wt-% nickel. The resulting thickness of the palladium/nickel layer was 2.6 $\pm$ 0.03 μm (Fischerscope X-ray XDV). The total mass of the reaction material was 3.01 g, while the amount of palladium in the reactor was around 205 mg. For surface composition reference is made to section 3.4.2. Plain Ni foils see section 3.5

2.4.2. *Preconditioning*

To remove volatile impurities, a stack of metal rings was pretreated in two stages in the reactor, while the inductor winding was water-cooled: The material was baked under a vacuum of $\sim$2 Pa for 8 hours using a rotary vane vacuum pump at 200–300 °C. Heating was then continued for a further six hours under a high vacuum of $\sim$10 mPa using a rotary vane pump and a turbomolecular pump in series. The temperature was gradually increased from 300 to 500 °C.

2.4.3. *Adsorption of hydrogen*

Hydrogen adsorption occurred in cycles of evacuation to 3 mbar and refilling with hydrogen to 0.8 bar. This procedure was repeated four times at 200 °C. The hydrogen loading in the palladium-coated nickel reactant was maintained at temperatures within the range of 190–300 °C and at H_2 pressure typically between 0.5 and 0.8 bar. The H_2 pressure decreased from 0.9 bar to 0.45 bar within 42 hours.

3. Experimental Results

3.1. Temperature Effects

The relationship between temperature, DC input power for induction, and hydrogen pressure was recorded for palladium/nickel-coated nickel foil over a period of approximately 2,000 hours (see Fig. 3).

Three distinct temperature effects appear each with a controlled, slow reduction in H_2 pressure (green curve). This triggers a steady rise in temperature. Significant and repeatable temperature increases are typical of the experiments involving a Ni-Pd stack in a high-frequency field (see the red curves for T_{R1} and T_{R2} with K-type sensors 10 mm apart). With a constant electrical input power of either 24 or 30 W, this indicates an exothermic process (see section 3.3). Each increase of temperature ends with a sharp kink, marked with black arrows, before transitioning to a long-lasting constant level. A short H_2 pulse stops the temperature anomaly and returns the reactor temperature to its initial value.

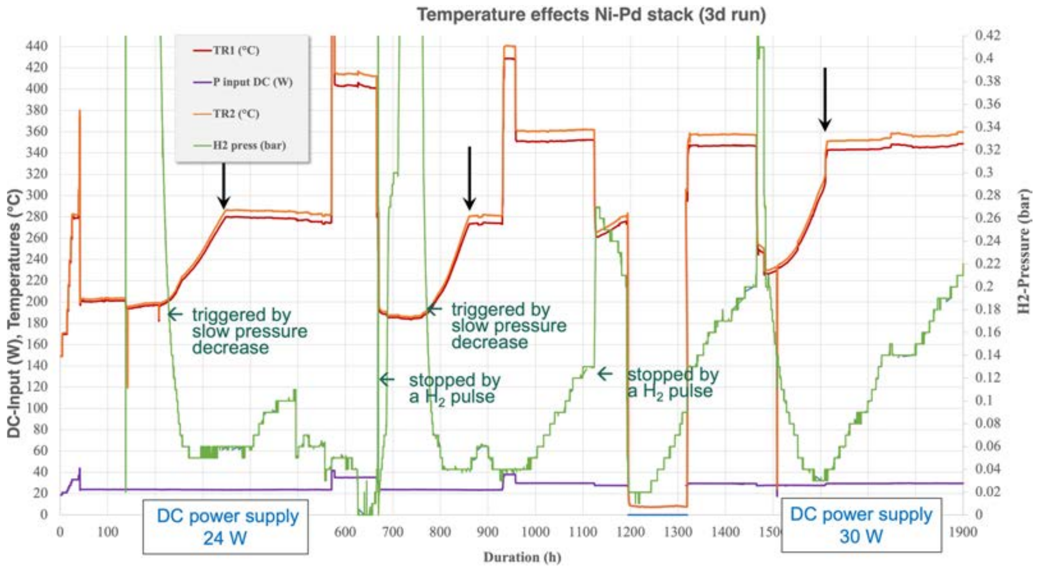

Figure 3. Test procedure over 2000 hours.

Another peculiarity is that once a constant temperature is reached, the gas pressure rises. A sudden leak can be ruled out as the pressure remained constant for around 120 hours and the system underwent repeated vacuum tests. Further clarification is needed to determine whether this could be a reaction product.

3.2. Starting and Stopping the Effect

Reducing the H_2 pressure slowly to below 100 mbar triggers the effect. The temperature increased by 80 K at a constant power input of 24 W DC, rising from 200 to 280 °C and by 120 K at a constant power input of 30 W DC rising from 230 to 350 °C. It takes about 120-150 hours for the temperature to rise to a constant activated state, which is a kind of stable equilibrium. After the distinct kink it remains there for weeks as shown in Fig. 3, for example, from 340 to 500 hours.

After exposing the system to a short H_2 pressure pulse of around 300 mbar, the temperature returns to its initial value within a few minutes.

3.3. Excess Heat

Measurements indicate consistent power gain under specific activation conditions.

Figure 4 shows the results of the step tests, comparing the reactor temperatures before (‘inactive) and after activation (‘activated) as a function of the power supplied to the inductor. Two example points illustrate the differences between the inactive (orange curve) and active (red curve) states. The temperature of 280 °C is reached at 23 W instead of 33 W and that of 380 °C is reached at 31.5 W instead of 44 W. This indicates that, after activation, the system requires 10–12.5 W less electrical power to reach the same reactor temperature. This equates to a 28% decrease in required electrical heating at 380 °C. Excess heat is generated with a coefficient of performance (COP) of approximately 1.4.

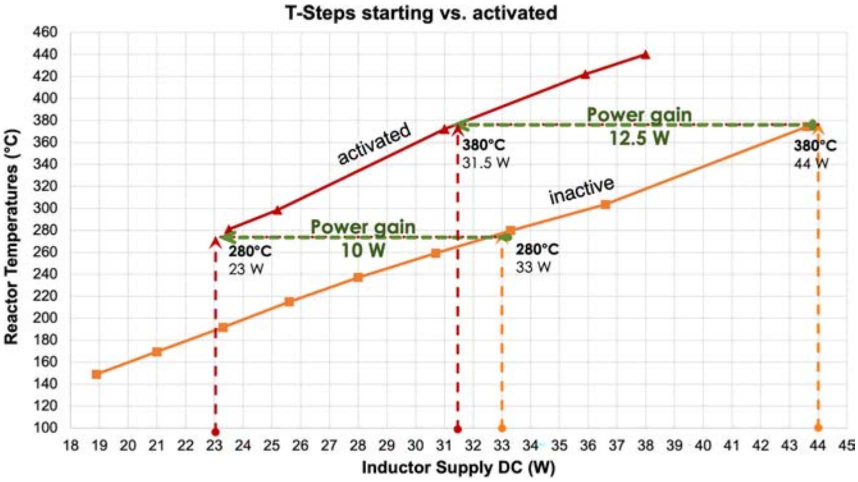

Figure 4. Reactor temperatures as a function of the power supplied to the induction generator.

3.4. Surface Morphology and Composition

Scanning electron microscopy (SEM) and energy-dispersive X-ray analysis (EDX) were used to analyse the palladium-nickel-coated (Ni) foils of the initial material as well as the material that had reacted after thermal treatment under H_2. These analyses were carried out at the Nanoimaging Lab of the Swiss Nanoscience Institute at the University of Basel.

3.4.1. *Surface imaging by scanning electron microscopy (SEM)*

Scanning electron microscopy (SEM) reveals striking changes to the surface, including localised zones of melting and a pattern of scattered holes (Fig. 5 and 6). In a few cases, some of these holes appear to be aligned along crystal boundaries. Since palladium has a melting point of 1550 °C, it is melting and recrystallising locally around these holes at average reactor temperatures of 200 to 500 °C. These zones may be nuclear-active environments.

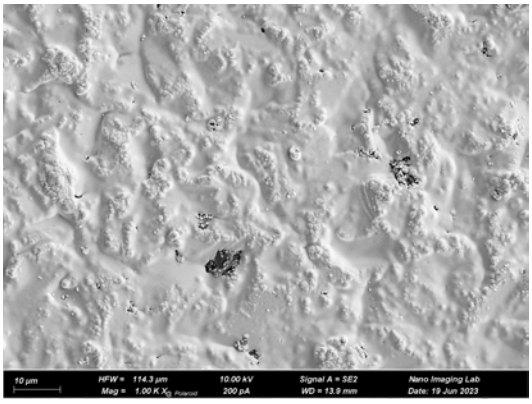

Figure 5. SEM of Pd/Ni coated Ni-foil before.

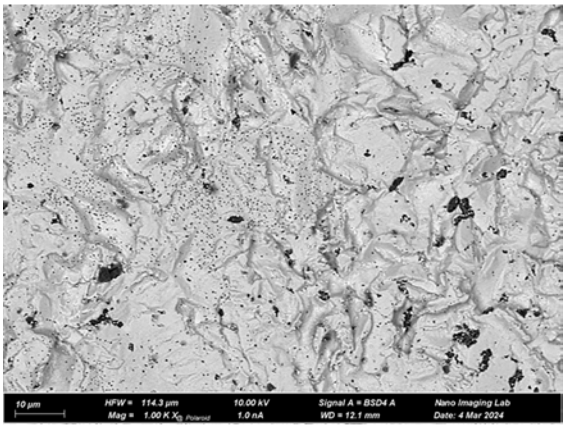

Figure 6. After reaction.

3.4.2. *Surface composition by energy dispersive X-ray analysis (EDX)*

Pre- and post-reaction samples show significant differences in element composition. New elements, such as C, O, Si and Al, were analysed with substantial weight percentages at the surfaces (Fig. 7 and 8).

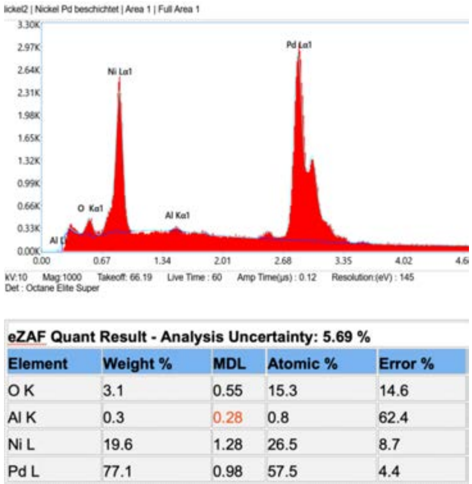

eZAF Quant Result - Analysis Uncertainty: 5.69 %

Element	Weight %	MDL	Atomic %	Error %
O K	3.1	0.55	15.3	14.6
Al K	0.3	0.28	0.8	62.4
Ni L	19.6	1.28	26.5	8.7
Pd L	77.1	0.98	57.5	4.4

Figure 7. EDX Analysis before.

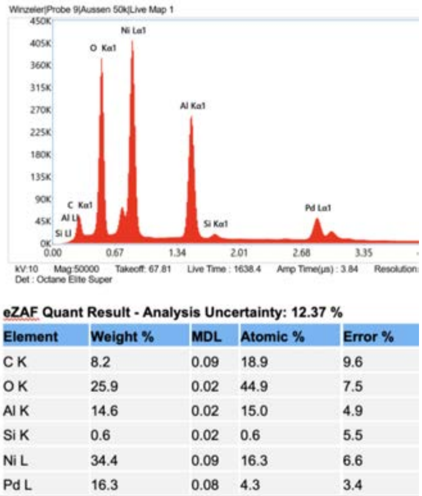

eZAF Quant Result - Analysis Uncertainty: 12.37 %

Element	Weight %	MDL	Atomic %	Error %
C K	8.2	0.09	18.9	9.6
O K	25.9	0.02	44.9	7.5
Al K	14.6	0.02	15.0	4.9
Si K	0.6	0.02	0.6	5.5
Ni L	34.4	0.09	16.3	6.6
Pd L	16.3	0.08	4.3	3.4

Figure 8. After reaction.

In addition to isolated areas that remained inactive, melt zones and perforated surfaces yielded the following analysis values (Table 2):

Table 2. Elements on the surface of the probes after reaction.

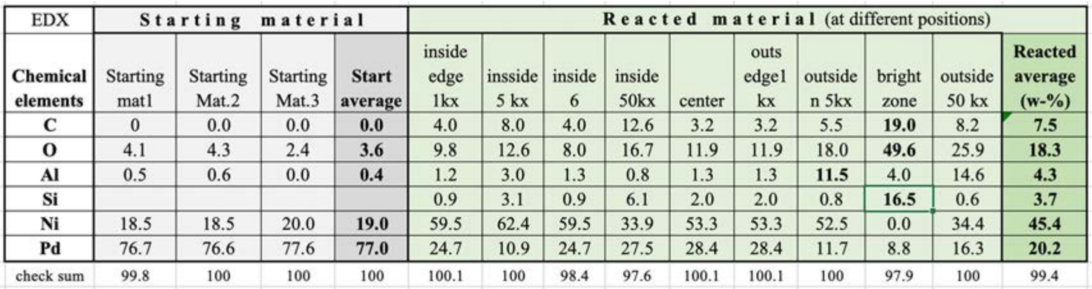

EDX	Starting material				Reacted material (at different positions)									
Chemical elements	Starting mat1	Starting Mat.2	Starting Mat.3	**Start average**	inside edge 1kx	insside 5 kx	inside 6	inside 50kx	center	outs edge1 kx	outside n 5kx	bright zone	outside 50 kx	**Reacted average (w-%)**
C	0	0.0	0.0	**0.0**	4.0	8.0	4.0	12.6	3.2	3.2	5.5	**19.0**	8.2	**7.5**
O	4.1	4.3	2.4	**3.6**	9.8	12.6	8.0	16.7	11.9	11.9	18.0	**49.6**	25.9	**18.3**
Al	0.5	0.6	0.0	**0.4**	1.2	3.0	1.3	0.8	1.3	1.3	**11.5**	4.0	14.6	**4.3**
Si					0.9	3.1	0.9	6.1	2.0	2.0	0.8	**16.5**	0.6	**3.7**
Ni	18.5	18.5	20.0	**19.0**	59.5	62.4	59.5	33.9	53.3	53.3	52.5	0.0	34.4	**45.4**
Pd	76.7	76.6	77.6	**77.0**	24.7	10.9	24.7	27.5	28.4	28.4	11.7	8.8	16.3	**20.2**
check sum	99.8	100	100	100	100.1	100	98.4	97.6	100.1	100.1	100	97.9	100	99.4

3.5. Pure Nickel Foils and Hydrogen Gas

In the most recent experiments nickel foil[1] was used with H_2. This was originally intended as a preliminary test for nickel foil with a pure palladium coating. Using 4.47 g of pure nickel foil and a DC input of 109.3 W a temperature of 667 °C was produced. Figure 9 shows a set of step test curves (T, P_{DC} input) in the inactive state at different H_2 pressures for untreated nickel foil. The bottom grey line shows the temperature curve of the reactor system when it

---

[1] H+S Präzisionsfolien GmbH; Fe = 0.02%; Mg = 0.01%; Co = 0.01%.

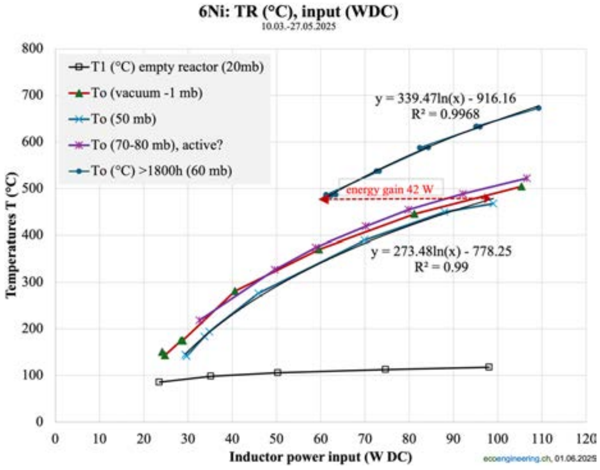

Figure 9. T, input at inactive and active state.

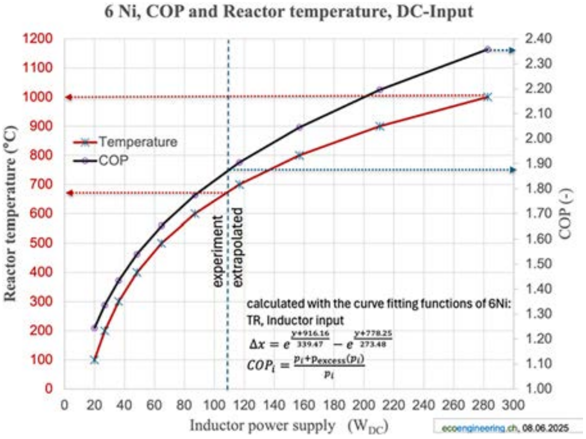

Figure 10. COP with plain Ni and extrapolated.

contains no reacting material, i.e. only the thermocouples. The middle set of curves shows the test of the influence of hydrogen pressure on nickel foil in the inactive state. The top curve shows the temperature behaviour in the active state at 60 mbar.

An input of 109.3 W was found to give a coefficient of performance (COP) of 1.87 ± 0.1. Curve fitting and extrapolation suggest that an input of approximately 280 W would be required to reach a temperature of around 1000 °C, giving a COP of 2.36 (see Fig. 10).

While temperature measurements are accurate to 1 K and flow measurements have a margin error of 10%, calorimetric measurements only provide rough indications. Considering the somewhat unstable efficiency of the inductor (0.37–0.43) and the fact that the device is still far from optimised, the thermal balance data are consistent with these values.

4. Discussion

The inductively heated and activated reactor consistently produced temperature rises and measurable excess heat under well-defined conditions. Comparable calorimetric signatures have been reported for gas-phase Ni–H systems and metal-hydride composites under dynamic loading conditions [8], [9]. Inductive excitation in the 100 kHz range, as applied here, represents a rarely explored method of activating such systems, enabling both thermal and electromagnetic stimulation without electrical contact to the active core.

4.1. Mechanism of Activation and Deactivation

Activation was reproducibly triggered by a gradual reduction in hydrogen pressure, while deactivation was induced with short H_2 pulses. This behaviour implies a controllable mechanism governed by hydrogen concentration dynamics within the lattice. Cyclic loading may rearrange hydride areas, producing metastable configurations of high local hydrogen density. Kitamura et al. [9] demonstrated that Pd/Ni ratios strongly affect excess power generation, suggesting that the 80:20 w/w Pd–Ni coatings used here may favour optimal hydrogen absorption and lattice strain. The repeatable sharp transition from a steady rise to constant temperature values at different power and temperature levels, observed with different materials, cannot be explained by a transition from ferromagnetic to paramagnetic behaviour, as the Curie temperature is a material constant (360 °C for Ni). This equilibrium phase is possibly linked to hydrogen redistribution or local field-induced electronic changes. As Widom and Larsen postulated, certain transitions could be interpreted as threshold phenomena related to hydrogen loading and local electronic shielding [10]. However, no directly comparable observations or theoretical explanation have been reported to date.

Plasma phenomena could be observed in a recent experiment using a micro camera. But it remains speculative whether this temperature kink could be due to the saturation of a plasma effect.

4.2. Excess Heat and Reproducibility

Step tests demonstrated that identical reactor temperatures required substantially less input power in the activated state, indicating an internal energy contribution. The 28 % reduction in electrical power at 380 °C corresponds to a coefficient of performance (COP) of 1.4 and 2.4 at 1000 °C. These values exceed chemical reaction limits by one to two orders of magnitude: typical metal hydride formation enthalpies are < 0.1 eV per atom [11], whereas the observed heat release corresponds up to 10 eV per reacting atom, consistent with proposed LENR mechanisms. Repetition under various conditions confirmed that the effect is stable and reversible, implying that it is not an artefact of instrumentation or external disturbance. The accuracy and reproducibility of the measurements were verified through multiple repetitions and checks.

4.3. Surface Morphology and Compositional Evidence

Surface analyses provide further evidence of reaction-related processes. Scanning electron microscopy (SEM) revealed localised melting zones and pore formation at bulk temperatures well below the melting point of palladium. This pattern differs slightly from the formation of small craters observed previously, on which carbon was analysed [12]. Ruer provides insights into the formation of such surface effects by means of simulations on cathodes [13]. Such effects suggest highly localised energy release, possibly associated with microscopic reaction centres, so-called nuclear active environments [14].

Energy-dispersive X-ray analysis (EDX) revealed a pronounced depletion of palladium in the reacted layer and the appearance of light elements (C, O, Al, Si) that were not detected in the initial state. These compositional changes are unlikely to arise from incidental contamination: other runs (e.g., with pure nickel foil) performed under comparable vacuum, temperature, and hydrogen-loading conditions did not show any corresponding elemental shifts. The relative magnitudes are similar to those reported by Iwamura et al. [15], who studied hydrogen-loaded, nanostructured, nickel-based, multilayer composites exposed to hydrogen. Such consistent observations across independent laboratories reinforce the interpretation of in-situ element formation.

The observed depletion of palladium, as detected by EDX, is thought to be primarily due to the rearrangement of the Pd layer next to the pores through local melting and resolidification rather than consumption in a reaction.

4.4. Possible Nuclear and Electronic Processes

The magnitude of the heat and the formation of new elements both exceed the scope of chemical reactions. Several nuclear-scale mechanisms could account for the results. Widom and Larsen [10] proposed ultra-low-momentum neutron formation via electron screening on hydride surfaces, which could enable subsequent nuclear transmutation without high-energy emission. NASAs lattice-confinement fusion (LCF) model [16] assumes that hydrogen nuclei, confined in metallic lattices, undergo fusion or fission assisted by local electron density. Both frameworks involve strong coupling between lattice electrons and absorbed hydrogen.

The inductive 100 kHz field used here may further enhance these interactions by generating oscillating currents and transient micro-plasmas that concentrate energy in confined lattice regions. Such field-induced effects are consistent with observations of threshold-like temperature transitions and may represent a distinctive excitation pathway. The Structured Atomic Model (SAM) of Kaal et al. [17] offers a geometric description of atomic rearrangements that could explain local element formation through sub-nuclear reconfiguration within a dense-packed atomic core.

Overall, the convergence of calorimetric, morphological, and compositional evidence supports the hypothesis that hydrogen-metal interactions in dynamically excited lattices may lead to nuclear-scale processes occurring under condensed-matter conditions. The observed reproducibility and controllability distinguish this system from earlier open-cell LENR experiments and point toward an electronically mediated nuclear mechanism driven by combined lattice confinement and inductive excitation.

5. Conclusion

The high-frequency induction reactor developed in this work provides a compact and reproducible platform for studying hydrogen-metal interactions under controllable electromagnetic excitation. Furthermore, the concept is ideal for scaling up. It has a wide range of potential technical applications. Experiments with Ni and Pd–Ni foils demonstrated repeatable activation by gradual hydrogen pressure reduction and deactivation by short pressure pulses. In the active state, identical temperatures required significantly less input power, corresponding to a power gain. The COP of 1.4–2.4 that has been achieved so far is a good starting point for further optimisation.

Surface analyses revealed localised melting and the formation of new elements (C, O, Al, Si) that cannot be attributed to chemical contamination. Together, the thermal, morphological, and compositional results indicate that the observed excess energy originates from hydrogen-induced processes involving nuclear interactions at the lattice level.

Future work should include (i) optimisation of induction frequency and coupling efficiency, (ii) comprehensive isotopic and gas analyses to identify possible reaction products such as helium or neon, and (iii) independent replication under calibrated calorimetry. With continued refinement, inductively activated hydrogen-metal systems could contribute not only to clean, radiation-free energy generation but may also open routes toward controlled low-energy transmutation of materials.

Acknowledgements

Working together as a small team was crucial to our success. During my laboratory experiments, electronics and electrical engineers Lucas Egloff and Enrico Lareida provided invaluable support in developing the electronics and data acquisition system, adapting sensors, and installing safety measures. Without their expertise, this research would not have been possible. The project was originally initiated by mechanical engineer Jack R. Metz, who continues to contribute to it. Thanks also go to the Institute for Materials and Process Engineering at the Zurich University of Applied Sciences (ZHAW), which provided laboratory and process engineering equipment, including high-vacuum pumps and a precision scale. We would also like to thank the Nano Imaging Lab at the Swiss Nanoscience Institute (SNI) at the University of Basel for their invaluable thorough analysis. Finally, I am deeply grateful to my wife Monika, who has endured my experiments at home and my nightly evaluations with tireless patience and attentive feedback.

References

[1] Clean Energy from Hydrogen-Metal Systems | CleanHME | Project | Fact Sheet | H2020, CORDIS | European Commission *https://cordis.europa.eu/project/id/951974*

[2] Breakthrough zero-emissions heat generation with hydrogen-metal systems, Hermes EU Grant ID: 952184 Finland. *https://cordis.europa.eu/project/id/952184*

[3] U.S. Department of Energy Announces $10 Million in Funding to Projects Studying Low-Energy Nuclear Reactions | ARPA-E: *https://arpa-e.energy.gov/news-and-events/news-and-insights/us-department-energy-announces-10-million-funding-projects-studying-low-energy-nuclear-reactions.*

[4] S. Focardi, V. Gabbani, V. Montalbano, Piantelli Francesco, and S. Veronesi, Large excess heat production in Ni-H systems, *Il Nuovo Cimento A*, vol. 111, Nov. 1998.

[5] S. Focardi, V. Gabbani, V. Montalbano, F. Piantelli and S. Veronesi, Evidence of Electromagnetic Radiation from Ni-H Systems, in *Condensed Matter Nuclear Science*, World Scientific NJ, London, 2006, pp. 70–80. doi: 10.1142/9789812774354_0005.

[6] H. B. Winzeler, Vorrichtung und Verfahren Zur Gewinnung Thermischer Energie mit Niedrig Energetischer Kernreaktion, WO2023093990A2, June 01, 2023

[7] H. B. Winzeler, Device and Process for Generating Heat Energy using Low-Energy Nuclear Reaction, *US 2025/0022619 A1*, Dec. 16, 2025

[8] E. Storms, The Science of Low Energy Nuclear Reaction, A Comprehensive Compilation of Evidence and Explanations about Cold Fusion. *World Scientific* NJ, London, Singapore, 2007.

[9] A. Kitamura *et al.*, Excess heat evolution from nanocomposite samples under exposure to hydrogen isotope gases, *International Journal of Hydrogen Energy*, vol. 43, no. 33, pp. 16187–16200, Aug. 2018, doi: 10.1016/j.ijhydene.2018.06.187.

[10] A. Widom and L. Larsen, Ultra low momentum neutron catalyzed nuclear reactions on metallic hydride surfaces, *European Physical Journal C*, vol. 46, pp. 107–111, Apr. 2006, doi: 10.1140/epjc/s2006-02479-8.

[11] A. Züttel, Materials for hydrogen storage, *Materials Today*, vol. 6, no. 9, pp. 24–33, Sept. 2003, doi: 10.1016/S1369-7021(03)00922-2.

[12] H. B. Winzeler et al., Inductively activated LENR reactor: *Internatinal Conference on Condensed Matter Nuclear Science,* ICCF25, Szczecin, Poland, Aug. 2023.

[13] J. Ruer, Simulation of Crater Formation on LENR Cathodes Surfaces, *Journal of Condensed Matter Nuclear Science*, vol. 12, no. 1, Dec. 2013, doi: 10.70923/001c.72226.

[14] Storms, Edmund, An Explanation of Low-energy Nuclear Reactions (Cold Fusion), *J. Condensed Matter Nucl. Sci.*, vol. 9, pp. 1–22, 2012.

[15] Y. Iwamura, T. Itoh, S. Yamauchi, and T. Takahashi, Anomalous heat generation that cannot be explained by known chemical reactions produced by nano-structured multilayer metal composites and hydrogen gas, *Japanese Journal of Applied Physics*, vol. 63, Feb. 2024, doi: 10.35848/1347-4065/ad2622.

[16] T. L. Benyo, Lattice Confinement Fusion (LCF) Overview, Mar. 2023. *https://ntrs.nasa.gov/citations/20230003100*

[17] J. E. Kaal, J. G. Emming, A. Otte, and J. A. Sorensen, *The Nature of the Atom: An Introduction to the Structured Atom Model*. Curtis Press, 2021.

J. Condensed Matter Nucl. Sci. 41 (2026) 164–169

Research Article

Discussion on Causal Network of LENR Process

Wu-yun Xiao, Da-hai Liu, Xin-hua Ma,
Yan-xia Liang, Ling-hui Hou, Kang Zhou, Jun-li Hou
State Key Laboratory of Chemistry for NBC Hazards Protection, China

Wu-Shou Zhang
Institute of Chemistry, Chinese Academy of Sciences, China

Abstract

The detailed mechanism of low energy nuclear reactions (LENRs) remains poorly understood at present. Because causal networks are valuable tools for analysing complex processes, they can be applied to LENR. Drawing on the insights of Edmund Storms and other experts, the entire process of a typical gas-loading LENR is divided into four cascaded stages. To clarify this, we have created a schematic diagram of the causal network. This diagram shows several influencing factors, allowing quantitative cause-effect relationships between input variables and the final output of excess power to be derived. It is important to note that this causal network and the relationships are still at an early stage and will require further updates and refinement.

Keywords: Causal Network, Complex System, Gas-loading LENR Process, Nuclear Physicochemistry, Cause-Effect Relationship

---

1. Introduction

It has been thirty-six years since Martin Fleischmann and Stanley Pons first announced their findings [1]. Over these years, a large body of experimental evidence has been reported, which forcefully confirms the existence of the anomalous nuclear phenomena now known as low energy nuclear reactions (LENR) [2]. Nevertheless, the detailed mechanism underlying LENR has not yet been clearly elucidated. Edmund Storms proposed a phenomenological model to explain this process [3]. His framework divides the entire LENR process into four cascaded stages. The first stage is the formation of a nuclear active environment (NAE); the second is the generation of nuclear active structures (NAS); the third involves the occurrence of primary nuclear reactions with non-radiation emission; and the fourth consists of secondary normal nuclear reactions triggered by the energetic products of the primary nuclear reactions. Stages 1 and 2 are related to physicochemical interactions, while stages 3 and 4 are associated with nuclear interactions. This theory provided valuable insights for discussing the occurrence and development of LENR, as well as analysing and controlling the key influencing factors.

Based on existing research results, the LENR process is a typical complex system that is closely linked to various factors, including the metallic materials, hydrogen isotopes, applied stimuli, nuclear reactions, multiple output

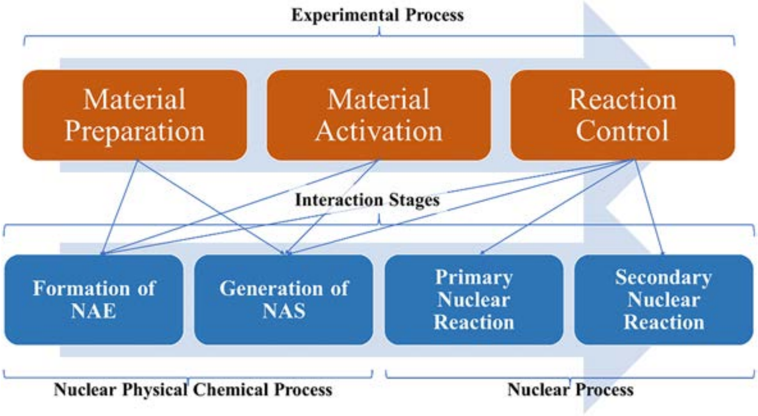

Figure 1. The experimental process and interaction stages of LENR.

effects, and so on. Common external stimuli used in LENR studies involve heating, the application of electric current, electromagnetic fields, plasma discharge, laser irradiation, ion bombardment, etc. Due to the unique nature of the physicochemical environment and conditions which can initiate and regulate subsequent nuclear reactions, we collectively refer to this field as nuclear physicochemistry. In addition, it is important to note that nuclear reactions in the LENR process can take various forms, such as nuclear fusion, nuclear fission, nuclear transmutation, and even nuclear decay [4]. Causal networks can serve as effective tools for analysing the complex LENR process, enabling us to examine the key influencing factors and their interconnections. For the sake of simplicity, this paper focuses specially on gas-loading LENR experiments.

2. Decomposition of the Gas-loading LENR Process

Gas-loading LENR experiments are typically performed in three main steps. The first step is the preparation of metal materials, where source materials such as metals, alloys, metal oxides, and/or hydrogen isotopes are processed into special forms, including micro-nano particles, multi-layer films, bulk materials, wire meshes, etc. The second step is activation or pre-processing, which aims to create or increase the activity of the samples. The third step is reaction control, which involves vacuum pumping, gas-loading, and the application of one or more appropriate stimuli. Output effects are usually measured either simultaneously with, or after, the third step.

Figure 1 illustrates the aforementioned experimental steps along with Storms' four-stage theory about the LENR mechanism [2]–[4]. Each experimental step may have an impact on one or more stages of the LENR mechanism. However, it is difficult to determine the precise correspondence between the three experimental steps and the four stages of the mechanism. Therefore, the arrowed lines in this figure only indicate a potential relation.

3. Causal Network of the Gas-loading LENR Process

Judea Pearl proposed the use of causal networks to visualize cause-effect relations, eliminate misunderstanding and realize causal inference [5]. Causal networks use directed acyclic graphs (DAGs), where each node represents a parameter, action or result, and each arrowed connection defines an influential link from a cause to an effect. Given the complexity of the LENR process, which involves multiple stages and numerous influencing factors, a causal network can be highly useful for describing it.

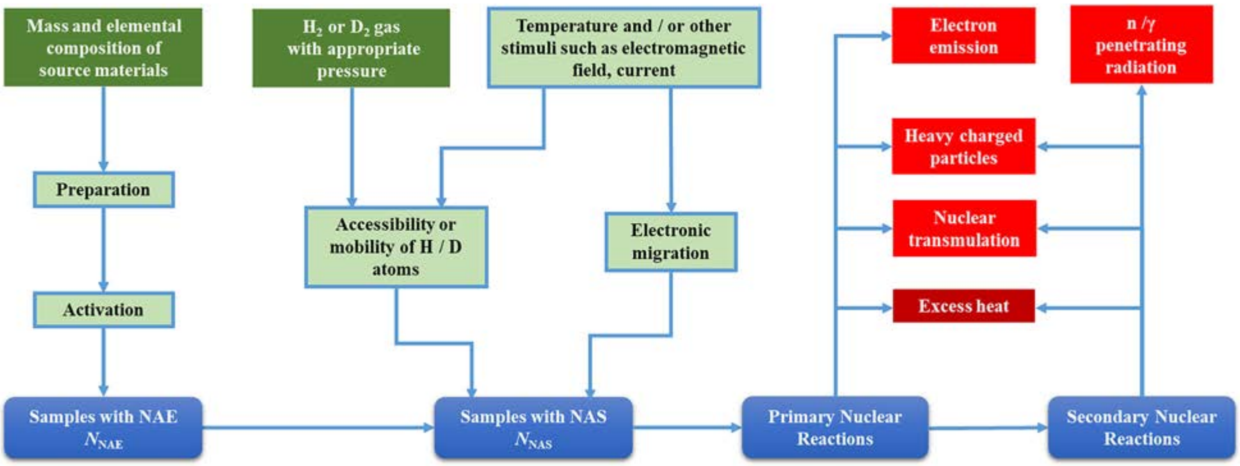

Figure 2. A schematic diagram of the causal network for the gas-loading LENR process.

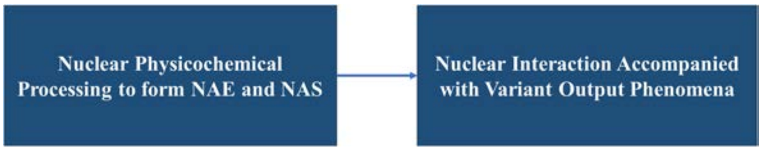

Figure 3. Top layer of LENR causal network.

Building on Storms' four-stage theory, we constructed a preliminary causal network for the gas-loading LENR process, as shown in Figure 2. This network focuses on nuclear physicochemistry, particularly the main influencing factors of LENR. It also depicts the main output effects of nuclear reactions. Because secondary nuclear reactions are less frequent than primary ones, most of the excess heat is believed to be produced by primary nuclear reactions. Due to the lack of understanding of the detailed nuclear interaction mechanism, the processes of primary and secondary nuclear reactions are temporarily omitted from the network.

Figure 3 illustrates the top layer of the LENR causal network. This figure suggests that the nuclear physicochemical processing involved in forming samples with NAE and NAS is the key cause, and the nuclear interactions accompanied by various output phenomena are the fundamental effects. This implies that as long as the nuclear physicochemical environment and conditions are met, the output effects will inevitably and immediately occur. Therefore, close attention should be paid to exploring the nuclear physicochemical process.

The nature of NAE in condensed matter remains unclear. Based on Storms' hypothesis, NAE may exist in the form of cracks or gaps of critical size within the material [2]. NAE does not naturally occur in ordinary materials. Special preparation and activation processes are essential for its formation. The generation of NAS is considered to be the process of assembling nuclear fuel and electrons within NAE. Consequently, providing an adequate supply of H or D atoms and free electrons while ensuring their sufficient mobility is crucial for the generation of NAS. Temperature and other stimuli do not directly trigger nuclear reactions. These factors accelerate the preceding stages of nuclear physicochemical process. Excess heat is the most significant output effect, often accompanied by nuclear transmutation and the emission of heavy charged particles and electrons. Very low-level penetrating radiation, such as gamma rays and neutrons, may originate from secondary nuclear reactions.

4. Discussion on the Relation Between Influencing Variables and Output Effect

Figure 2 shows several output effects of nuclear reactions, among which the excess heat is the most prominent. For this reason, excess power (*P*) is often used as a quantitative measure of the output effect, representing the rate of nuclear reactions. However, there is currently no consensus regarding the influencing variables, and different scholars hold varying views on this matter.

Michael McKubre put forward an empirical formula to predict the excess power (*P*) in electrolysis experiments conducted in heavy water [6], [7]:

$$P = M\left(x - x^{\circ}\right)^{2}\left(i - i^{\circ}\right)|i_{\mathrm{D}}|, \tag{1}$$

where *M* is a proportionality constant, *x* is the D/Pd ratio, x° is a threshold value typically around 0.875, *i* is the electrochemical current density at the cathode, i° is a threshold value of current density, and i_{D} is the absorption deuterium interfacial flux expressed as a current density. This function indicates that the excess power depends on the D/Pd ratio, current density and deuterium flux. In contrast, Wu-Shou Zhang proposed that, instead of the D/Pd ratio, an elevated temperature is a key factor in the production of excess heat, as well as pre-electrolysis at high temperature, the current density, etc [8], [9].

Storms summarized the variables that affect the LENR process and proposed the following equation [4]:

$$P = K(XACe^{-\frac{B}{RT}}), \tag{2}$$

where *K* is a proportionality constant, *X* is a value determined by the type of hydrogen isotope, *A* is the number of NAE in the material (also denoted as N_{NAE}), *C* is the concentration of hydrogen isotopes in the material surrounding the NAE, *B* is the activation energy required for the movement of hydrogen atoms within the material, *R* is the gas constant, and *T* is the absolute temperature of the material surrounding the NAE. Storms also pointed out that a high D/Pd ratio is not always necessary for the production of excess heat; temperature is an important factor because it affects the physicochemical process that limits the rate of nuclear reaction. The semi-logarithmic relationship between excess power and temperature has been verified by many reports [10], [11], both for electrolysis and gas-loading experiments. Additionally, this equation shows that the number of NAE in a material determines the maximum amount of nuclear power that can be produced, and the greater number of NAE within the material, the more excess power is produced.

According to Eq. (2), a higher hydrogen concentration should result in more excess power. However, Tadahiko Mizuno disagreed with this view. From his gas-loading experiments, he concluded that the permeability of H or D atoms, rather than high loading, is essential. On the contrary, high loading apparently reduces the amount of excess heat [12].

If the causal network shown in Figure 2 is valid, the excess power should be proportional to the generation rate of NAS (n_{NAS}), which is defined as the ratio of the increased number of NAS (ΔN_{NAS}) to the corresponding time interval (Δt):

$$n_{\mathrm{NAS}} = \frac{\Delta N_{\mathrm{NAS}}}{\Delta t}. \tag{3}$$

Thus, the excess power is proportional to n_{NAS}:

$$P = f n_{\mathrm{NAS}}, \tag{4}$$

where *f* is a proportional coefficient. Referring to Figure 2, we can infer that the generation of NAS is the result of the interaction between mobile reactants and static NAE. Therefore, it's natural to assume that the n_{NAS} is determined by the product of two causal factors: the number of NAE in the material (A) and the diffusion flux of reactants (*J*), just like the interaction between incident particles and target nuclides:

$$n_{\mathrm{NAS}} = \sigma A J. \tag{5}$$

Here, σ is a constant conversion coefficient, called interaction cross section, denoting the capturing probability of mobile reactants by NAE. The diffusion flux (*J*) is defined as the number of mobile reactants passing through a unit area per unit time, representing the accessibility or mobility of reactants moving towards NAE. The mobile reactants here mainly refer to hydrogen isotopes, and may also include free electrons. According to Fick's first law:

$$\begin{gathered} J = -D\nabla C, \\ \text{or}: \ J_x = -D\frac{\partial C}{\partial x}\ , \end{gathered} \tag{6}$$

where J_x is the diffusion flux in the *x* direction, *D* is the diffusion coefficient, *C* is the concentration of moving reactants, ∇C is the gradient of reactant concentration, and *x* is the distance in the diffusion direction [13]. The diffusion coefficient (*D*) is a function of temperature (*T* in K), and follows the Arrhenius law:

$$D = D_0 \mathrm{e}^{-\frac{B}{RT}}, \tag{7}$$

where D_0 is a constant, *B* is the activation energy for the diffusion of reactants within the material.

Combining Eqs. (4) to (7), we obtain the following result:

$$P = -f\sigma D_0 A \nabla C \mathrm{e}^{-\frac{B}{RT}}. \tag{8}$$

Taking into account the different output effects of H and D isotopes, we can rewrite the above equation as:

$$P = K(XA\nabla C\mathrm{e}^{-\frac{B}{RT}}), \tag{9}$$

in which *K* is a proportion coefficient, and *X* is a weighted factor whose value depends on the type of hydrogen isotope.

Comparing Eq. (2) and Eq. (9), the only difference lies in the replacement of the hydrogen concentration (*C*) with its gradient (∇C). This modification shows that it is the spatial variation of the H or D concentration rather than the static concentration itself that determines the final output effect. All measures aimed at increasing the concentration gradient are beneficial for stimulating and enhancing LENR, which typically occurs in non-equilibrium environments. This conclusion is roughly consistent with Mizuno's view on the importance of high permeability and the multiplicative term of the absorption deuterium interfacial flux ($|i_{\mathrm{D}}|$) in Eq. (1).

5. Summary

The LENR process is of high complexity, and its driving mechanism remains a mystery to this day. However, after decades of intensive research, our understanding of this phenomenon has gradually improved, and this black box has turned grey little by little. By leveraging Judea Pearl's idea and methodology on causal inference, Storms' four-stage theory can be expanded as a cause-effect network. Although this network is still preliminary and relatively simple, it provides a useful framework for analysing the complex interaction processes and key influencing factors of LENR. Based on this network, a new cause-effect equation was derived, which integrates multiple existing research findings.

Through the aforementioned cause-effect analysis and theoretical derivation, the following conclusions can be drawn: (1) The nuclear physicochemical processing involved in forming NAE and NAS is the crucial cause of LENR, and the nuclear interactions accompanied by various output phenomena are the natural effects. (2) The generation rate of NAS (n_{NAS}) serves as a characteristic quantity representing the cause, similar to the output excess power (*P*) for the final effect. These two quantities are directly proportional to each other. (3) The key influencing factors include the number of NAE in the material, the gradient of reactant concentration, and the temperature. In contrast, the reactant concentration or the D/Pd ratio is not an essential condition.

Although the causal network and cause-effect equation presented in this paper are still relatively simple and may contain some defects, they provide a preliminary framework for understanding the LENR process, clarifying which factors may be important and which may not be. Further experimental research, empirical analysis and theoretical analysis are required to continuously revise, refine and validate these models. Special attention should be paid to the analysis of material preparation and activation processes, which are also complex subsystems. It is believed that the final, improved causal network and equation will be more valuable for advancing our understanding of LENR.

Acknowledgments

The authors greatly appreciate the careful review and corrections from Jed Rothwell (LENR-CANR.org), which have significantly improved the linguistic presentation of this paper.

References

[1] M. Fleischmann, S. Pons, Electrochemically Induced Nuclear Fusion of Deuterium. *Journal of Electroanalytical Chemistry* **261** (1989) 301–308.

[2] E. Storms, The Science of Low Energy Nuclear Reaction. World Scientific Pub., 2007.

[3] E. Storms, Cold Fusion Explained. Journal of Condensed Matter Nuclear Science, **39** (2025) 249–285.

[4] E. Storms, The Explanation of Low Energy Nuclear Reaction. Infinite Energy Press, 2014.

[5] Judea Pearl, Dana Mackenzie, The Book of Why. Basic Books, New York, USA, May 2018.

[6] M.C.H. McKubre, S. Crouch-Baker, A.K. Hauser, et al., Concerning Reproducibility of Excess Power Production. Proceedings of 5th International Conference on Cold Fusion. 1995. Monte Carlo, Monaco, pp. 17–33.

[7] M.C.H. McKubre, Excess Power Observations in Electrochemical Studies of the D/Pd System; the Operating Parameter Space. Proceedings of 15th International Conference on Condensed Matter Nuclear Science. 2009. Rome, Italy: ENEA, pp. 5–10.

[8] W.-S. Zhang, J. Dash, Q.-S. Wang, Seebeck Envelope Calorimetry with a Pd|D_2O+H_2SO_4 Electrolytic Cells. Proceedings of 12th International Conference on Cold Fusion, 2005, Yokohama, Japan, pp. 86–96.

[9] W.-S. Zhang, J. Dash, Excess Heat reproducibility and Evidence of Anomalous Elements after Electrolysis in Pd/D_2O+H_2SO_4 Electrolytic Cells. Proceedings of 13th International Conference on Condensed Matter Nuclear Science. 2007. Sochi, Russia, pp. 202–216.

[10] Z.M. Dong, C.L. Liang, X.Z. Li, S.X. Zheng, Tempearture Dependence of Excess Power in Both Electrolysis and Gas-Loading Experiments. *Journal of Condensed Matter Nuclear Science* **29** (2019) 85–94.

[11] T. Mizuno, Observation of Excess Heat by Activated Metal and Deuterium gas. *Journal of Condensed Matter Nuclear Science* **25** (2017) 1–25.

[12] T. Mizuno, J. Rothwell, Excess Heat from Palladium Deposited on Nickel. *Journal of Condensed Matter Nuclear Science* **29** (2019) 21–33

[13] H. Mehrer, Diffusion in Solids: Fundamentals, Methods, Materials, Diffusion-Controlled Processes. Springer, 2007: 28.

J. Condensed Matter Nucl. Sci. 41 (2026) 170–181

Research Article

Excess Heat and Influences of Temperature and Atmosphere on the Microstructure of Pd-Ni-Zr Alloy Nanopowders

Yanxia Liang, Hui Zhao, Linghui Hou, Dahai Liu, Xinhua Ma,
Junli Hou, Wuyun Xiao*
State Key Laboratory of Chemistry for NBC Hazards Protection, Beijing 102205, China

Wu-Shou Zhang*
Institute of Chemistry, CAS, Beijing 100190, China

Abstract

The Pd-Ni-Zr alloy has been identified as one of the most promising materials for low-energy nuclear reactions (LENR). The simple and efficient fabrication of the Pd-Ni-Zr alloy, in conjunction with systematic investigations into its control factors, significantly advances the progress of LENR. In this study, Pd-Ni-Zr alloy nanopowders with different compositions were prepared by high-energy ball milling and subjected to heat treatment including high-temperature vacuum annealing, high-temperature oxidation and deuterium reduction. The grain refinement process of Pd-Ni-Zr alloy nanopowder was explored based on different ball milling times. The deuterium reduction of Pd-Ni-Zr samples prepared under different ball-milling conditions reached a minimum of 27 nm, accompanied by a high density of defects including dislocations, interfaces, and amorphous structure. From the results of scanning electron microscopy (SEM), transmission electron microscopy (TEM) and X-ray diffraction (XRD), the influence of temperature and atmosphere on the morphology, phase structure, and crystallinity of Pd-Ni-Zr alloy was revealed. Excess heat of Pd-Ni-Zr alloy nanopowder in D_2 was assessed with a high-precision Seebeck calorimeter. Results demonstrate that both the activation treatment (involving high-temperature oxidation and deuterium reduction) and the stepwise variation of reaction temperature are critical factors for enhancing the excess heat of Pd-Ni-Zr alloy. Excess power of 0.6 W (or 120 W/kg of the sample) was obtained with the optimized Pd-Ni-Zr alloy samples.

Keywords: High-energy ball milling, Pd-Ni-Zr, Heat treatment, Microstructure, Seebeck calorimetry

---

1. Introduction

Pd-based alloys have proven to be an effective material for promoting low-energy nuclear reactions (LENR) since Pd-Ni alloys were first reported in the field [1]–[4]. On the other hand, Pd-Ni alloys are widely used in hydrogen

---

*Corresponding authors: W.-S. Zhang and W. Xiao energy applications due to their excellent catalytic ability and cost-effectiveness [5]–[8]. Previous studies revealed that the properties of metallic nanocrystals are significantly influenced by their composition, shape and structure [9]–[11]. It has been demonstrated that a nanograin structure enhances the adsorption performance of materials in interactions with hydrogen [5], [12]–[14]. Given the noble metal attributes and scarcity of Pd, enhancing per-atom efficiency remains a critical goal in current research.

In addition, incorporating non-noble metal elements into Pd-based materials can effectively enhance the activity through the synergistic structural and electronic effects, while also reducing the amount of Pd usage. Significant discoveries have been made in the field of LENR through the use of Pd-Ni-Zr ternary alloys, which are formed by incorporating ZrO_2 into nickel-palladium alloys. A. Kitamura *et al.* fabricated Pd-Ni-Zr ternary alloys by alloy smelting, mechanically pulverized them to micrometer-scale dimensions, and then performed hydrogen/deuterium charging experiments, which produced anomalous excess heat [15]. They further observed that repeated calcination and oxidation processes enhanced the magnitude of the excess heat [3], [16]. Therefore, temperature and atmospheric conditions are crucial for activating materials to produce larger excess heat. However, the influence of heat treatment parameters on the microstructure of materials remains unclear.

Chemical synthesis methods are predominantly employed to produce Pd-based nanomaterials [17]. However, constrained by the limited single-batch synthesis quantity and strict selectivity for chemical elements, chemical synthesis methods are not suitable for LENR. High-energy ball milling (HEBM) is recognized as a versatile mechanical synthesis technique in nanomaterials, widely used in the ultrafine processing of metals, ceramics, and biomaterials [18]–[20]. HEBM enables efficient reduction of raw material particles to the nanoscale under simple and impurity-free conditions, achieved by mechanical collision and friction forces between grinding balls and raw powders [21]. Notably, it also generates nanoscale defects that contribute to enhanced material performance. The nanocrystalline/amorphous structure of Al-Fe-Nb powders is controlled with HEBM, which renders the powders more suitable for applications demanding high thermal stability and customized magnetic response [22], [23]. By regulating milling parameters, precise control over the microstructure of alloy powders can be achieved.

In this paper, Pd-Ni-Zr alloy nanopowder with the average particle size of 27 nm was prepared by HEBM, and subjected to heat treatment including high-temperature vacuum annealing, high-temperature oxidation and deuterium reduction. By characterizing samples at different ball milling stages and those subjected to heat treatment under various conditions, using scanning electron microscopy (SEM), transmission electron microscopy (TEM) and X-ray diffraction (XRD), this study identified the Pd-Ni-Zr grain control factors and the influence of heat treatment parameters on the microstructure. Calorimetry was carried out on the treated samples under deuterium gas charging and discharging conditions, and the results showed that the pretreated samples exhibited clear-cut excess heat of 0.6 W.

2. Experiments

To prepare Pd-Ni-Zr alloy nanopowder, pure Pd, Ni and ZrO_2 powders (all from Alfa Aesar) were used as initial materials. The HEBM was performed using a Fritsch P-7 reinforced planetary ball mill (Fritsch GmbH, Germany). The ball milling process was conducted at room temperature with a rotation speed of 500 rpm. The ratio of the grinding jar rotation to its revolution speed was maintained at 1:2. The ball-to-powder ratio (BPR) of 15:1 was adopted in the experiment using grinding balls of 1 mm diameter. Wet ball milling was utilized to improve ball milling efficiency and reduce material adhesion to the grinding jar wall, where chromatographic grade ethanol (purity > 99.997%, Aladdin Scientific Corp.) was used as the process control agent. SEM equipped with energy dispersive spectroscopy (EDS), TEM and XRD were employed to characterize the microstructure and phase structure of the samples. Nano Measurer software was utilized for particle size statistics, and the Martin diameter (the length of the area bisector of polygonal particles measured horizontally) was used to define the particle diameter.

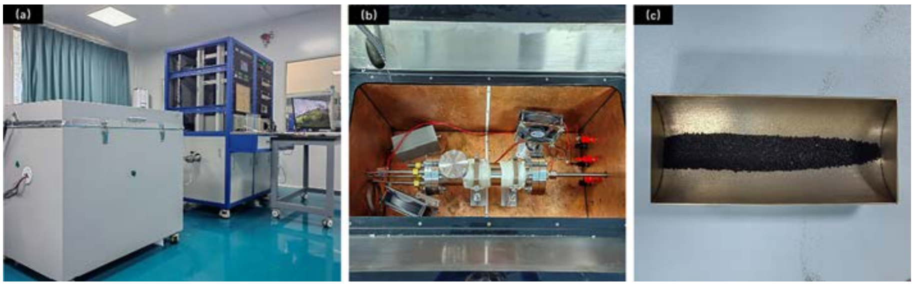

Figure 1. The calorimetric system. (a) Seebeck calorimeter and the control systems, (b) reactor in the calorimeter chamber, and (c) sample boat with Pd-Ni-Zr samples.

The Pd-Ni-Zr alloy nanopowder obtained by HEBM was subjected to vacuum drying. Subsequently, the samples were placed into the atmospheric treatment system (NMS, RCL) for heat treatment in three phases:

- High-temperature vacuum annealing: the vacuum pump was used to evacuate the sample tube until the vacuum level reached better than 10^{-4} Pa. The annealing temperature was 500°C with a heating rate of 7°C/min and a holding time of 600 min.
- High-temperature oxidation: the heating process and temperature holding conditions were the same as those for the high-temperature vacuum annealing. Throughout the heating process, the sample was maintained in a flowing air atmosphere.
- Deuterium reduction: the oxidized samples were placed in the atmospheric treatment system for deuteration. After the vacuum level reached better than 10^{-4} Pa, deuterium gas was filled into the tube until a stable pressure (approximately 20 kPa) was achieved. The heating process and temperature were the same as those for the high-temperature vacuum annealing. After deuterium reduction, the deuterated samples were allowed to cool naturally to room temperature.

The measurement of excess heat for the heat-treated samples was conducted using a high-precision calorimetric system, as shown in Figure 1. The calorimetric system includes a Seebeck calorimeter, temperature and gas circuit control system (Figure 1(a)), as well as a reactor serving as the reaction chamber (Figure 1(b)). Pd-Ni-Zr alloy nanopowder was placed in a sample boat made of pure nickel (Figure 1(c)), which was then placed in the reaction chamber. Tests of excess heat for LENR were performed under controlled conditions of temperature and hydrogen/deuterium gas pressure.

To guarantee the accuracy of the heat measurement, the calorimetric experiments consist of the following steps: sample loading, vacuum pumping, gas flushing, helium-based calibration, blank experiment, and deuterium charging experiment. Prior to the final charging of hydrogen or deuterium gas, it is necessary to ensure the purity of the atmosphere through gas displacement and cyclic purification, which is crucial to avoid the influence of redox heat. During calorimeter calibration, helium gas was introduced into the reactor. Calibration was performed at five power steps, with input power from 0 to 200 W. Each power level step lasted for 480 minutes and only the most stable output signals of 30 minutes were used. In blank experiments, nitrogen gas was introduced into the reactor, followed by the heating program and calorimetric programs described above. In deuterium-charging calorimetry experiments, the reactor must be cyclically refilled with deuterium gas to determine how deuterium cycles affect performance. Calibrations were repeated after deuterium-charging calorimetry to ensure data accuracy and reproducibility, and to reduce drift caused by environmental changes or system program instability.

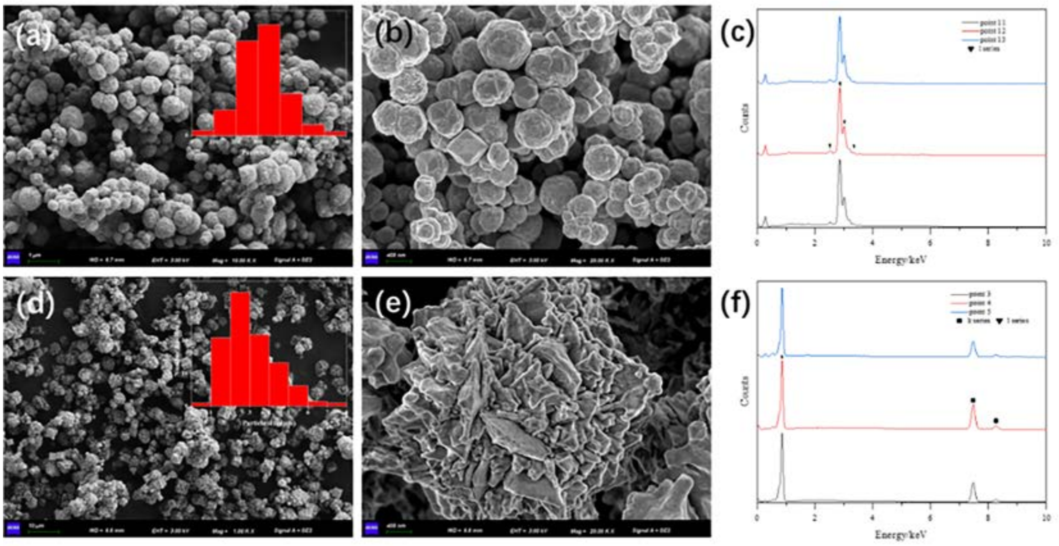

Figure 2. (a) SEM, (b) enlarged image and (c) EDS of initial Pd powder. (d) SEM, (e) enlarged image and (f) EDS of initial Ni powder. Insets are the corresponding statistical histograms.

3. Results and Discussion

3.1. The Microstructure of Pd-Ni-Zr Alloy Nanopowder Obtained With HEBM

Before synthesizing the Pd-Ni-Zr alloy nanopowder with ball milling, the microstructural and composition of the original materials were characterized. Figure 2 shows SEM images of the original Pd and Ni powder at different magnifications, as well as the size distribution and element spectra. The original Pd powder shown in Figures 2(a) and 2(b) has a nearly spherical structure, and the surface has a rough and undulating texture. While a number of small particles exhibit aggregation, individual particles remain distinguishable, with all particles in the aggregates included in the histogram analysis. The average Pd particle size is about 320 nm from the histogram in the inset in Figure 2(a). Figure 2(c) presents the EDS at three points in different regions of Pd powder, with all peak positions corresponding to the element Pd. The original Ni powder shown in Figure 2(d) has an approximately polygonal shape, and the magnified SEM image presented in Figure 2(e) shows that its surface structure exhibits a sawtooth structure. The statistical histogram in the inset of Figure 2(d) reveals an average particle diameter of 3.1 μm for the Ni powder. The EDS result shown in Figure 2(f) confirms that the composition of this powder is pure Ni. The sample information of the initial $\mathrm{ZrO_2}$ is consistent with that in the previous work [24], and thus no further elaboration is given herein.

Samples with atomic ratios of Pd:Ni:Zr = 1:7:1 (labeled as $\mathrm{PNZ_1}$) and Pd:Ni:Zr = 1:7:7 (labeled as $\mathrm{PNZ_7}$) were prepared with HEBM. Figure 3 presents the SEM images of $\mathrm{PNZ_1}$ at various ball milling stages, along with the diagram of particle size variation with ball milling time. During the early stage of ball milling (Figure 3(a)), the particles exhibit an irregular morphology. The particle size is relatively large, while the distribution of particles is highly inhomogeneous. The surfaces of larger particles are coated with tiny particles. This can be attributed to the fact that Pd and Ni experience plastic deformation under the action of impact forces along the axial direction, leading to a reduction in the axial size while stretched in the radial direction. Meanwhile, $\mathrm{ZrO_2}$ is rapidly crushed into nano-sized particles under the action of forces, which then coat the surfaces of large particles. With the increase of ball milling time, the relatively thin regions on the particle edges break off due to impact forces and friction, leading to an

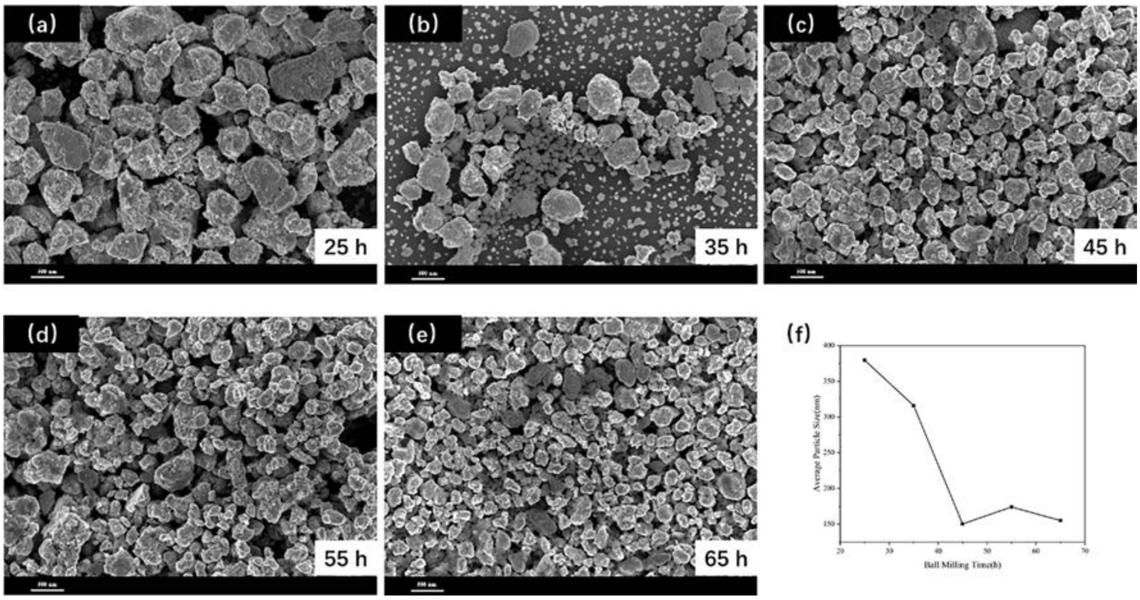

Figure 3. SEM images of PNZ_1 (i.e. $PdNi_7(ZrO_2)$) powder ball milled for (a) 25 h, (b) 35 h, (c) 45 h, (d) 55 h, and (e) 65 h and (f) the relationship between the average size of PNZ_1 particle and ball milling time.

increase in the density of small-diameter particles (Figure 3(b)). Pd, Ni and ZrO_2 powders further integrate with the continuous progress of ball milling. Due to the pinning effect exerted by ZrO_2, the average particle diameter of the entire alloy nanopowder decreases rapidly. As ball milling time further increases to 45 h, the particle size of PNZ_1 powder decreases to less than 200 nm (Figure 3(c)). The ball milling process ultimately reaches a state of dynamic balance as particle fragmentation and agglomeration rates become nearly equal. In this stage, the particle size of the sample varies with time without obvious reduction (Figure 3(d) and 3(e)), and its average particle diameter is about 149 nm. Figure 3(f) shows the relationship between the average size of PNZ_1 particle and ball milling time, presenting the time of the powder particles in different ball milling stages as well as the particle size corresponding to each stage.

The particle fragmentation process of PNZ_7 sample is similar to that of PNZ_1. In terms of the final equilibrium particle size, the average particle size of PNZ_7 sample is about 27 nm with the maximum particle diameter of 119 nm, and the minimum diameter of 11 nm, which is smaller than that of PNZ_1. The PNZ_7 sample exhibits a significantly enhanced refinement effect on the alloy powder due to the increased atomic ratio of ZrO_2 powder.

To clarify the crystalline microstructure and defects of the alloy nanopowder, TEM characterization was performed on the PNZ_7 sample, as shown in Figure 4. TEM bright-field image (Figure 4(a)) of typical PNZ_7 particles indicates that this material consists entirely of nanocrystals with rough boundaries. The polycrystalline ring illustrated in the selected area electron diffraction (SAED) pattern (top-right inset in Figure 4(a)) indicates that the polycrystalline with small grain size has more complex crystal orientations. The statistical result of grain size in this region (bottom-right inset in Figure 4(a)) indicates that the largest grain size is 42 nm and the smallest is 5 nm, and the average grain size is 16 nm. Figure 4(b) is a high-resolution TEM image of one PNZ_7 grain with a size of about 25 nm, and the fast Fourier transform (FFT) patterns (bottom-right inset in Figure 4(b)) show the diffraction points clearly.

Figures 4(c) and 4(d) represent the interfacial and internal microstructure of PNZ_7 nanoparticles. The rough grain boundary (marked by yellow dotted curve) shown in Figure 4(d) indicates that abundant interfacial atoms exist

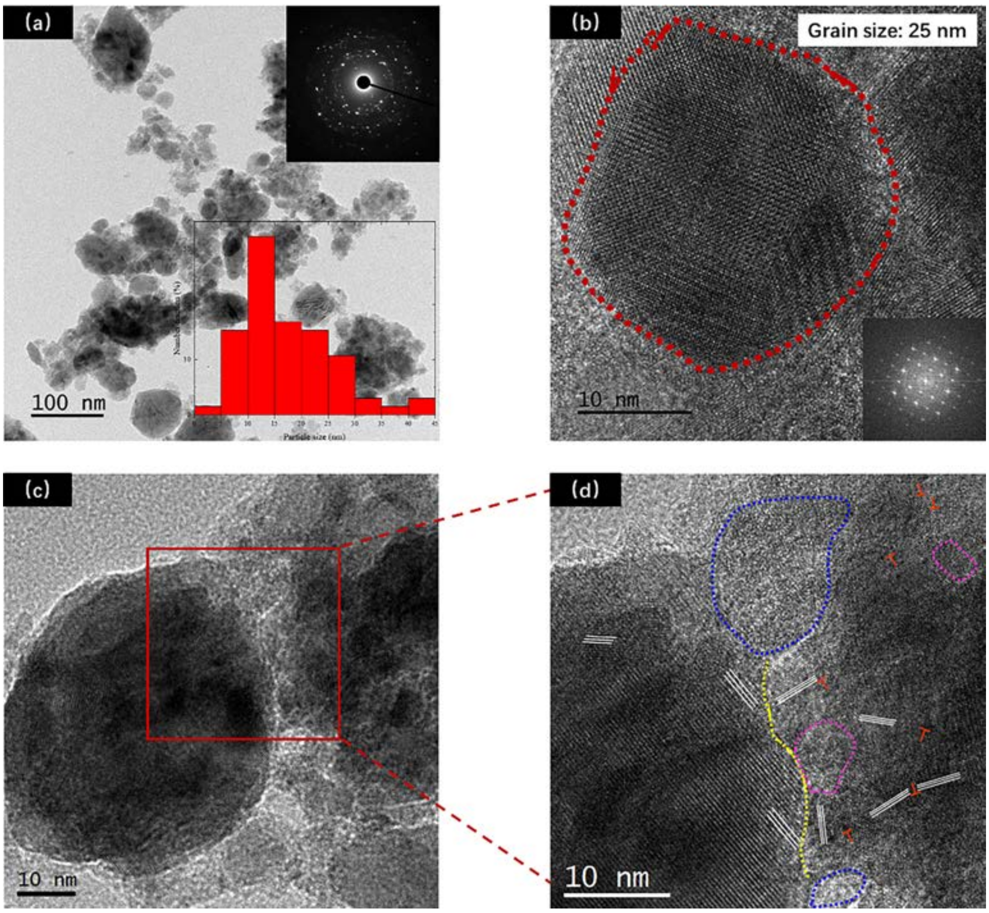

Figure 4. TEM of PNZ_7 (i.e. $\mathrm{PdNi_7(ZrO_2)_7}$) sample. (a) TEM bright-field image. The top-right inset is SAED pattern and bottom-right inset is a grain size statistical histogram. (b) High-resolution TEM of the grain with FFT pattern. (c) Low-magnification image and (d) high-magnification image of interfacial and internal microstructure. The grain boundary is marked by yellow dotted lines, the amorphous regions between grains are marked by blue dotted curves and the intragranular amorphous regions are marked by pink dotted curves. White parallel lines represent different crystal orientations and the red T-shaped marks represent dislocation defects.

in the ball-milled powders. In addition, the sample also contains amorphous regions, which can be divided into interfacial amorphous regions (marked by blue dotted curves) and intragranular amorphous regions (marked by pink dotted curves). By comparing the two kinds of amorphous structures, it is found that the area of amorphous regions at the crystal edges is larger than that of amorphous regions inside the crystals. This finding is related to the amorphous formation energy. Due to the higher atomic surface energy at the crystal boundaries, amorphous phases form more easily in these areas. In contrast, atoms inside the crystals have a stronger tendency to arrange into an ordered structure, which not only makes amorphous formation more difficult but also hinders the expansion of existing amorphous regions. Numerous crystal orientations (marked by white parallel lines) and dislocations (marked by red “T” marks) also exist inside the PNZ_7 nanocrystals. Atoms at the interfaces and dislocations are in an asymmetric high-energy

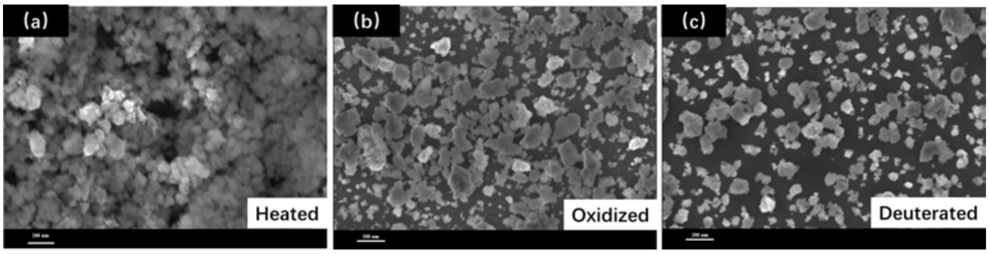

Figure 5. SEM images of PNZ_7 powder samples after (a) high-temperature vacuum annealing, (b) high-temperature oxidation, and (c) high-temperature deuterium reduction.

state, which in turn exerts an effect on the interaction between hydrogen and deuterium. This is considered one of the key factors influencing the LENR performance of PNZ alloys.

3.2. Effects of Temperature and Atmosphere on Microstructure of Pd-Ni-Zr Alloy Nanopowder

Previous studies have shown that repeated calcination of Pd-Ni-Zr alloy in air can enhance the anomalous exothermic performance under hydrogen/deuterium atmosphere [15], [16]. To clarify the influence of heat treatment conditions on the microstructure of Pd-Ni-Zr alloy nanopowder, material activation methods including high-temperature vacuum annealing, high-temperature oxidation and deuterium reduction were applied to PNZ_7. Figure 5 presents SEM of the PNZ_7 samples after different heat treatment conditions. The particle morphology (see Figure 5(a)) of the sample treated by high-temperature vacuum annealing shows almost no change compared with the original powder. However, the agglomeration phenomenon becomes more severe with the particle size increasing to 45 nm. Small particles dissolve and are absorbed by larger particles at high temperatures, thereby promoting continuous growth. Figure 5(b) shows the SEM of PNZ_7 powder treated by high-temperature oxidation, which reveals oxidative sintering between particles and a consequent increase in the size of some particles. Additionally, the particle sizes exhibit partial non-uniformity, with unsintered small particles adhering to the surfaces of large particles. Compared with the sample after ball milling, the average particle size of the oxidation-treated sample rises significantly to 147 nm. Figure 5(c) presents the SEM image of the PNZ_7 powder sample after high-temperature deuterium reduction treatment. After deuterium reduction, the density of small-sized particles in the sample is higher than that in the oxidized sample. This is probably the result of hydrogen embrittlement. Meanwhile, small-sized particles generally exhibit a morphology where they agglomerate tightly to form a single large particle. Compared to the large-particle powder formed after oxidative sintering, the deuterated sample exhibits a higher specific surface area.

The particle size affects adsorption performance primarily because it directly modifies the effective interaction conditions between metal and hydrogen/deuterium. Specifically, smaller particles typically increase the specific surface area to provide more adsorption sites, reduce diffusion resistance by accelerating the transport of hydrogen/deuterium to the active sites of the material, and enhance mass transfer efficiency. However, particle agglomeration can block the adsorption pores and impair the adsorption process.

Particle size affects the hydrogen/deuterium adsorption performance of alloy powders significantly, and the phase composition of alloy powder is also a factor influencing the interaction between the material and hydrogen/deuterium. Herein, XRD tests were performed to reveal the effect of heat treatment on the phase composition of Pd-Ni-Zr alloy nanopowder, as shown in Figure 6. The gray pattern in Figure 6 corresponds to the constituent phases of the ball-milled PNZ_7 powder sample, indicating that the as-prepared sample mainly consists of the PdNiZr, NiZr and PdZr compound phases. In addition, a portion of the ZrO_2 phase was retained after the ball milling due to the relatively high addition amount of ZrO_2 in the PNZ_7 sample. The broadening of peaks indicates small crystallite size according

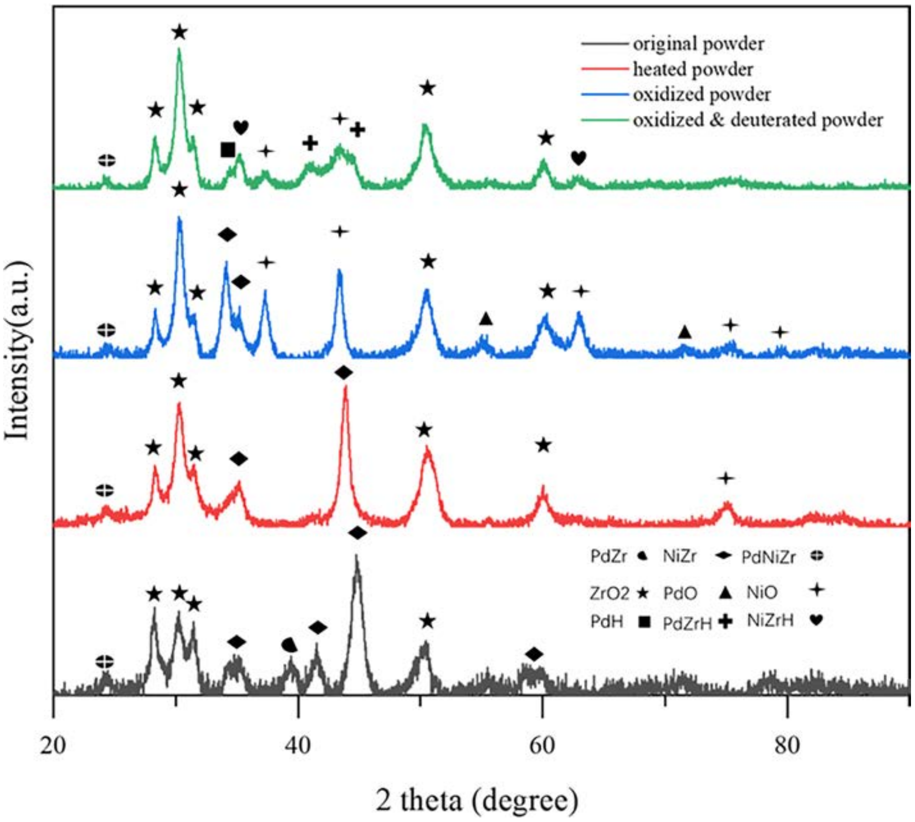

Figure 6. XRD patterns of original PNZ_7 powder sample (the gray spectrum), the sample after high-temperature vacuum annealing (the red spectrum), the sample after high-temperature oxidation (the blue spectrum), and the sample after high-temperature deuterium reduction (the green spectrum).

to the Scherrer equation. After the prepared PNZ_7 sample was subjected to high-temperature vacuum annealing, the full width at half maximum (FWHM) of diffraction peaks narrowed, which corresponds to the increase of grain size. Meanwhile, new phase constituents including a small amount of NiO were generated as shown in the red spectrum in Figure 6. The blue and green patterns in Figure 6 correspond to the phases of the PNZ_7 sample after high-temperature oxidation and deuterium reduction respectively. The FWHM of diffraction peaks become narrower for the samples subjected to oxidation and deuterium reduction. It suggests that the grain size increases further, which is consistent with the SEM results in Figure 5. Besides, more oxide components (such as PdO and NiO) appear in the oxidized sample, and hydride components (such as PdH, PdZrH and NiZrH) are present in the deuterated sample.

High-temperature treatment applied to the sample enhances the kinetic energy of the particles, which promotes their combination and the formation of particles with a larger size. Although the standard Gibbs free energy of formation indicates that Zr has a stronger binding capacity to oxygen than Ni, a small amount of free oxygen in ball-milled PNZ_7 is captured by Ni in the process of element enrichment at high temperature. Consequently, a minor amount of NiO phase forms in the sample after the high-temperature vacuum treatment. Under oxygen-sufficient conditions, elements such as Pd and Zr will combine with oxygen to form oxides. Consequently, the NiZr alloy phase disappears while the

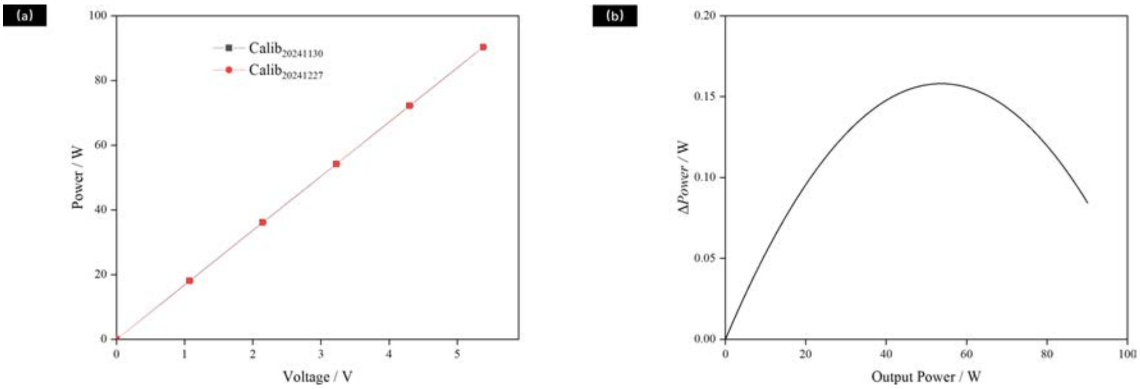

Figure 7. (a) The relationship between the output signal of Seebeck calorimeter and input thermal power. (b) Comparison of the difference between two calibrations before and after the test.

phases of PdO, NiO, and ZrO_2 increase. In contrast, some oxide phase components are reduced by deuterium to form hydrides under high-temperature deuterium conditions.

3.3. Excess Heat of Pd-Ni-Zr Alloy Nanopowders

The LENR experiment, which involves charging hydrogen/deuterium into metal samples and performing calorimetry after heating, is characterized by a long experimental cycle and stringent requirements for control of the experimental conditions. To improve accuracy, the Seebeck calorimeter was calibrated just before and after the test. Figure 7(a) shows the relationship, which can be fitted with a quadratic form, between the output signal of Seebeck calorimeter and the corresponding input power during the two calibrations (marked by $\mathrm{Calib}_{20241130}$ and $\mathrm{Calib}_{20241227}$). Figure 7(b) presents the difference between $\mathrm{Calib}_{20241130}$ and $\mathrm{Calib}_{20241227}$ under the same input power. The discrepancy reaches the maximum of 158 mW with the input power of 53 W, and 82 mW with the thermal power of 90 W. This means the calorimetric error was less than 0.16 W up to 90 W during the period from Nov. 30 to Dec. 27, 2024.

The excess heat from activated samples is more pronounced than from untreated PNZ_7 samples. Figure 8(a) shows the changes in heating current, input power, excess power, temperature and pressure over time in a deuterium-charging 5 g sample of PNZ_7 alloy nanopowders. It is evident that the temperature increases four times caused by a gradual increase of power, and each increase in power was accompanied by a change in both current and voltage (black curve in Figure 8(a)). To simplify interpreting the data, the excess power after each current adjustment must be monitored for more than 6 hours (the relaxation time of the calorimeter). The calorimeter maintains a constant external temperature of $25 \pm 0.01°\mathrm{C}$ in a water bath to ensure the accuracy of calorimetry (green curve in Figure 8(a)). The topmost graph in Figure 8(a) demonstrates that an increase in input power leads to a rise in the sample temperature and an increase in the pressure inside the reactor.

A blank experiment began with the charging of N_2 into the reactor. No excess power was detected during this process. In contrast, when D_2 was introduced during the target experiments, excess power was generated to varying extents. Figures 8(b) and 8(c) respectively show the variations of excess power (indicated by the blue curves), input power (indicated by the black curves), and temperature (indicated by the red curves) over time during the two deuterium experiments. Overall, the initial input power in Figure 8(b) is 85 W, the same as the final input power in Figure 8(c), while the initial power in Figure 8(c) is 65 W, the same as the final power in Figure 8(b). By comparing the excess power results of the two experiments, it is found that regardless of whether the initial input power is 65 W or 85 W, neither test produces excess power at the very beginning. However, the temperature change caused by the variation of

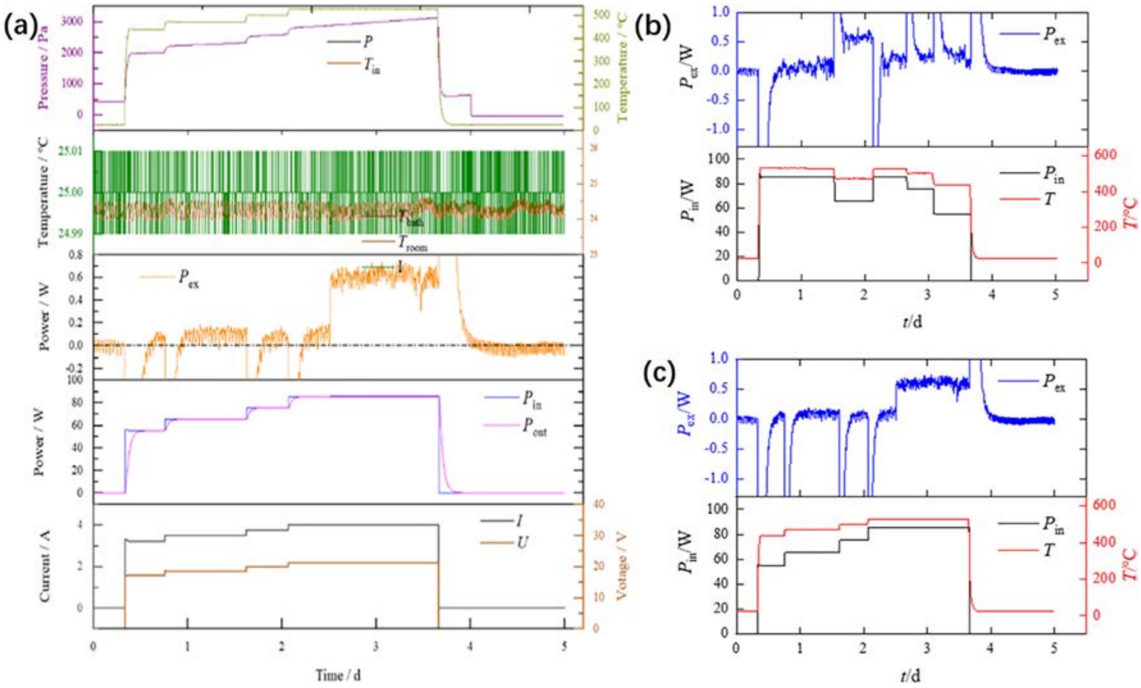

Figure 8. (a) The changes in heating current, input power, excess power, temperature, and pressure in the calorimetric system over time. During the (b) temperature-rise and (c) temperature-fall process, the changes in excess power (blue curves), input power (black curves), and temperature (red curves) over time.

input power disrupts the adsorption equilibrium of the materials within the reactor, resulting in continuous changes in the adsorption and desorption of deuterium within the materials, and leading to the emergence of excess power. When the input power decreases from 85 W to 65 W, the temperature drops from 530°C to 473°C, and the excess power increases from 51 ± 93 mW to 564 ± 82 mW, showing excess power significantly higher than the standard deviation. When input power is restored to the higher level, the temperature rises to 527°C. The excess power decreases but still exists, with a value of 232 ± 94 mW, which is greater than twice the standard deviation. In the experiment shown in Figure 8(c), the initial input power is 65 W, the temperature is 470°C, and the excess power is 105 ± 82 mW, which indicates no statistically significant excess power. As the power increases to 85 W and the temperature rises to 526°C, the excess power also increases to 613 ± 94 mW.

4. Conclusions

Pd-Ni-Zr alloy nanopowder with different atomic ratios was successfully prepared by high-energy ball milling. The microstructure of the samples was analyzed in detail to clarify the particle refinement process and the microstructural features of the Pd-Ni-Zr alloy nanopowder. The powders with atomic ratios of Pd:Ni:Zr = 1:7:1 and Pd:Ni:Zr = 1:7:7 achieved average particle sizes of 149 nm and 27 nm, respectively. A large number of interface structures, amorphous regions, and defects are present inside the Pd-Ni-Zr alloy nanopowder, which are believed to promote the interaction between metal atoms and hydrogen/deuterium. Moreover, the high-temperature and atmosphere treatment of the samples leads to an increase in the particle size of the Pd-Ni-Zr powders as well as changes in their morphology and phase composition, thereby influencing the hydrogen/deuterium adsorption-desorption processes. A more scientific and reliable calorimetric experimental method was proposed in this paper. Through deuterium charging calorimetry tests conducted on the alloy nanopowder, the significance of temperature changes in the production of excess power was identified, and excess power of 613 ± 94 mW was obtained with 5 g of treated Pd-Ni-Zr powder.

Acknowledgements

Y. X. Liang and H. Zhao contributed equally. This work was supported by NSFC (12205371, 21153003 and 22373106) and State Key Laboratory of Chemistry for NBC Hazards Protection.

References

[1] P. Mosier-Boss, S. Szpak, F. Gordon, L. Forsley, Use of CR-39 in Pd/D co-deposition experiments. *Eur. Phys. J. Appl. Phys.* **40** (2007) 293–303.

[2] Y. Miyoshi, H. Sakoh, A. Taniike, A. Kitamura, A. Takahashi, R. Seto, Y. Fujita, Effect of forced oxidation on hydrogen isotope absorption/adsorption characteristics of Pd-Ni-Zr oxide compounds. *J. Condensed Matter Nucl. Sci.* **10** (2013) 46–62.

[3] Y. Iwamura, T. Itoh, J. Kasagi, A. Kitamura, A. Takahashi, et al., Anomalous heat effects induced by metal nano-composites and hydrogen gas. *J. Condensed Matter Nucl. Sci.* **29** (2019) 119–128.

[4] A. Takahashi, T. Yokose, Y. Mori, A. Taniike, Y. Furuyama, H. Ido, A. Hattori, R. Seto, A. Kamei, J. Hachisuka, Latest progress in research on AHE and circumstantial nuclear evidence by interaction of nano-metal and H(D)-gas. *J. Condensed Matter Nucl. Sci.* **33** (2020) 14–32.

[5] M. Thi, T. Tran, P. Anh, H. Nhac, Q. Bui, An innovative catalyst of nickel-palladium alloy nanocrystals embedded nitrogen-doped graphene for efficient oxygen reduction reaction. *J. Alloy. Comp.* **79** (2019) 314–324.

[6] L. Kravchuk and N. Ivashchenko, Palladium nickel zirconium oxide catalyst for low-temperature oxidation of carbon monoxide. *Russ. J. Appl. Chem.* **71** (1998) 645–647.

[7] S. Van Wyk, M. Onani, E. Nordlander, Bimetallic nickel and palladium complexes for catalytic applications. *Chem. Pap.* **70** (2016) 1003–1023.

[8] U. Kamarulzaman, M. Rahman, M. Su, Improvement of the performance of dye-sensitized solar cells employing Nickel-Palladium alloy-reduced graphene oxide counter electrode: influence of palladium content. *Optik.* **276** (2023) 170658.

[9] V. Tuong, S. Dong, D. Thanh, O. Geun, S. Gi-Seung, Y. Yeon-Tae, Alloy core composition effect of Pd-Au-alloy @ZnO core-shell nanoparticles on hydrogen gas sensing performance. *Chem. Eng. J.* **483** (2024) 149050.

[10] P. Filomena, A. Rui, F. Carlos, C. Carlos, G. Ibrahim, Effect of syngas composition on hydrogen permeation through a Pd-Ag membrane. *Fuel.* **103** (2013) 444–453.

[11] P. Mariya, S. Shcherbakova, A. Saraev, A. Knyazev, I. Kurzina, Pd-Bi-based catalysts for selective oxidation of glucose into gluconic acid: the role of local environment of nanoparticles in dependence of their composition. *Catalysts* **14** (2024) 66.

[12] S. Lu, Y. Hu, M. Hao, L. Xiong, D. Ma, Q. Yue, Interlayer-confined synthesis of sub-nanometer high-entropy alloys for high-efficiency oxygen reduction. *Nano Research.* **18** (2025) 94907908.

[13] C. Mei, J. Liu, P. Chuang, T. Song, F. Tang, H. Su, J. Huang, Y. Wu, High-temperature ferromagnetism of Ni-doped $\mathrm{PbPdO_2}$ nanograin films synthesized by sol-gel spin-coating method. *Ceram. Int.* **43** (2017) 1997–2003.

[14] J. Huang, T. Odoom, X. Jing et al., Plant-mediated synthesis of zinc oxide supported nickel-palladium alloy catalyst for the selective hydrogenation of 1,3-butadiene. *ChemCatChem.* **9** (2017) 870–881.

[15] A. Kitamura, A. Takahashi, K. Takahashi, R. Seto, T. Hatano, et al., Excess heat evolution from nanocomposite samples under exposure to hydrogen isotope gases. *Int. J. Hydrogen Energy* **43** (2018) 16187–16200.

[16] T. Kobayashi, J. Shigemura, K. Naitoh, Temperature and pressure dependence of anomalous heat generation occurring in hydrogen gas absorption by metal powder. *J. Condensed Matter Nucl. Sci.* **36** (2022) 318–326.

[17] D. Han, Z. Zhang, Z. Bao, H. Xing, Q. Ren, Pd-Ni nanoparticles supported on titanium oxide as effective catalysts for Suzuki-Miyaura coupling reactions. *Front. Chem. Sci. Eng.* **12** (2018) 24–31.

[18] X. Yu, S. Wu, Z. Zhang, C. Wang, Application of ball milling technology in removal of PFAS and ball milling modified materials: A review. *J. Hazard. Mater. Adv.* **18** (2025) 100709.

[19] T. El-Sayed, A. Aboelnaga, M. El-Atawy, M. Hagar, Ball milling promoted N-heterocycles synthesis. *Molecules* **23** (2018) 1348.

[20] A. Hafs, T. Hafs, D. Berdjane, L. Yandjah, N. Hasnaoui, Investigating on structural, microstructural and magnetic properties of nanocrystalline $Fe_{60}Al_{35}Mg_5$ alloy synthesised by high-energy ball milling. *Trans. Indian. Inst. Met.* **76** (2023) 3447–3454.

[21] Y. Liang, Z. Wu, E. Fu, J. Du, P. Wang, Y. Zhao, Y. Qiu, Z. Hu, Refinement process and mechanisms of tungsten powder by high energy ball milling. *Int. J. Refract. Met. Hard Mater.* **67** (2017) 1–8.

[22] N. Oanh, D. An, N. Viet, Nanocrystalline/amorphous tuning of Al-Fe-Nb (Mn) alloy powders produced via high-energy ball milling. *Materials* **17** (2024) 5627.

[23] M. Akmal, A. Malik, W. Jeong, H. Ryu, Incorporating microstructural and mechanical heterogeneity to Ti-Zr-Nb alloy by partial high-energy ball milling. *Mater. Chem. Phys.* **315** (2024) 129037.

[24] H. Zhao, Y. Liang, W. Xiao, W.-S. Zhang, D. Liu, X. Ma, Refinement process and mechanism of nano Cu-Ni-Zr alloy by high-energy ball milling. *J. Condensed Matter Nucl. Sci.* **39** (2024) 130–139.

J. Condensed Matter Nucl. Sci. 41 (2026) 182–188

Research Article

Experiment on Detecting Neutrons Produced by Low-Energy Nuclear Reactions Using CR-39

Hang Zhang
Qiuran Laboratory

Kang Zhou
State Key Laboratory of Chemistry for NBC Hazards Protection, Beijing

---

Abstract

We designed an experimental setup to qualitatively reveal the existence of low-energy nuclear reactions or other possible nuclear processes during laser irradiation, by detecting fast neutrons. Inspired by the experimental scheme first proposed by MIT, laser emitters projecting red light with a wavelength of 445 nm were utilized to target titanium and palladium metal sheets inside chambers filled with helium, hydrogen, deuterium, or argon gas. After 30 days of laser irradiation, a large number of fast neutron tracks were found on both sides of the detectors. Counts were estimated to be one order of magnitude higher than the background, warranting the argument that titanium and palladium sheets, when loaded with certain gases and exposed to prolonged laser irradiation, can produce neutrons. Elements not originally present were detected, consistent with possible transmutation. The new elements due were discovered in most of the samples, and were largely consistent with the neutron production.

Keywords: LENR, Laser, Neutron, CR-39.

---

1. Introduction

From 2016 to 2022, scientists from all over the world, such as Mastromatteo, Biberian, Barrowes, and Uchikoshi, carried out laser low-energy nuclear reaction experiments and measured transmutation elements and neutrons.

In 2023, Florian Metzler and colleagues at MIT put forward an experimental scheme, which is the first attempt to test the hypothesis of low-energy fission reaction. The experimental scheme of MIT is to irradiate palladium or titanium metal targets with lasers in an atmosphere of hydrogen or deuterium, and detect neutrons and nuclear fragments to prove the existence of nuclear processes.

Inspired by MIT's experiment, we designed and fabricated a simple reaction device, based on MIT's drawings. Accordingly, laser experiments were carried out on four gases and two metals, and the nuclear products, including neutrons were detected primarily with CR-39, a solid-state nuclear track detector. Here is a brief introduction to some of the preliminary results of our experiment.

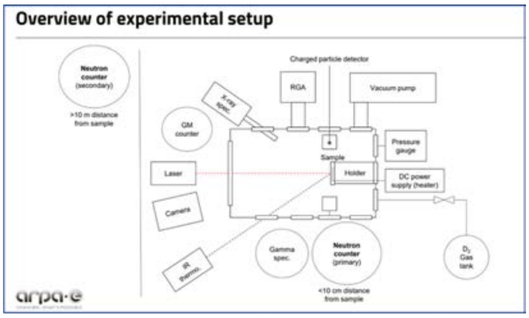

Figure 1. Schematic posted by MIT for the verification of laser-stimulated LENR by detecting neutrons.

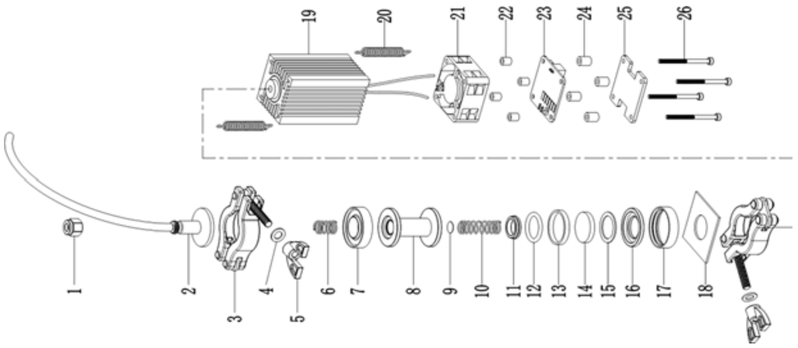

Figure 2. Exploded view of mechanical parts showing the structure of the container. The outer diameter of the container is 14 mm, the diameter of the laser point is 1 mm, the laser output power is 3-5 W with a wavelength of 445 nm, the diameter of the metal sheet is 9 mm, and the thickness for each of metal sheet is 0.1 mm.

2. Methods

Before the experiment started, calibration was conducted with CR-39 detectors covered by film. Only the neutrons passing through the detectors will leave certain tracks. Alpha particles will leave nuclear tracks on the naked CR-39, but they are blocked by the film cover.

The CR-39 detection efficiency was calibrated with a standard americium-beryllium (Am-Be) neutron source at the National Institute of Metrology, China, using a BARYOTRAK detector (Fukuvi Chemical Industry, Co.). The Am-Be neutron source had an activity of 10^7 Bq, and it produced dozens of tracks. The pits were counted using a microscope. The counting results gave a detection efficiency, which was about 4440 neutrons to produce one pit. The CR-39 used in the calibration was also covered with a protective film to block incident alpha particles, so only pits left by neutrons are counted.

After being etched with sodium hydroxide solution, pits left by neutrons on both sides of CR-39 can be seen using a microscope. The field of view of the microscope was estimated. The total pits on a CR-39 sample were estimated by multiplying the number of pits in the area of the microscope image by the total area of the chip. The ambient temperature constantly cooled the CR-39, ensuring clear images and accurate counting. The neutron distribution on the chip was uneven. The neutron count is measured at a spot where the laser illuminated the sample, which probably has the highest density of pits. Thus, the estimated neutron count should be higher than the actual one.

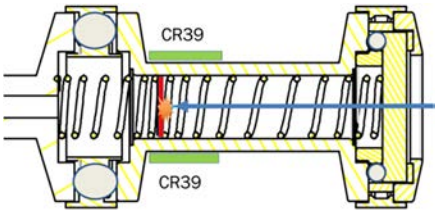

Figure 3. Section view of the container sealed by two pairs of flanges. The blue arrow represents the laser targeting the metal sheet.

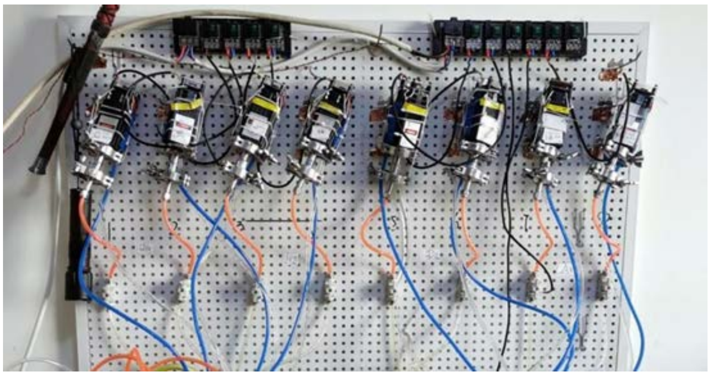

Figure 4. Top view for 8 laser emitters cooled by tap water. The containers next to them are evacuated then filled with specific gases.

The experimental system consisted of eight containers holding the metallic samples. Either a palladium or titanium sheet was placed inside the chamber perpendicular to axial direction, facing the directed laser at a right angle, ready for irradiation. Noble gases including helium and argon gases and isotopes of hydrogen gas, i.e., deuterium and hydrogen, were employed to carry out the experiment. The power of the laser emitter is between 3.5 to 4 watts, thereby producing a strong heating effect inside the containers. Hence two CR-39 samples were attached to the exterior surface of the container, about 13 mm away from the laser focal point upon the sheets. Another CR-39 sample 7 mm away from the focal point was placed inside the chamber for reference.

After the installation was completed, each chamber of the container was evacuated and then filled with a pure gas. When the gas charging is complete, all the gas pressures were kept at around 1 atm. The container was sealed and the laser was turned on to start the experiment. The number of pits on CR-39 left by neutrons was counted after 5 days and again after 30 days of continuous laser irradiation. The titanium and palladium sheets were retrieved after irradiation and sent to the Tan Kah Kee Innovation Laboratory in Xiamen, Fujian Province, for EDS analysis to see if there was change in elements.

3. Results

The titanium sheet was apparently scorched after laser irradiation. The scorch mark can be seen with the naked eye. New elements were detected at the dark spot at the exact location targeted by the laser beam. In contrast, no scorched spots from laser irradiation were found on the palladium sheet after the exposure, thus making it difficult to map the exact location where the laser targeted the palladium surface. Indeed, no new elements were found on the palladium sheet in container 2, while new elements were detected in other containers.

Table 1. New elements found on 11 or 10 spots selected from the scorched location on Ti. The fraction represents the ratio of specimens with a specific new element over the total specimens selected from the surface of the sheet.

New Elements Found on Ti							
Gases	**Label**	**Si**	**Fe**	**Al**	**Ca**	**Ni**	**S**
He	1	4/11	2/11	0	0	0	0
H_2	3	10/10	2/10	1/10	1/10	2/10	1/10
D_2	5	10/10	1/10	0	0	0	0
Ar	7	1/10	0	0	0	0	0

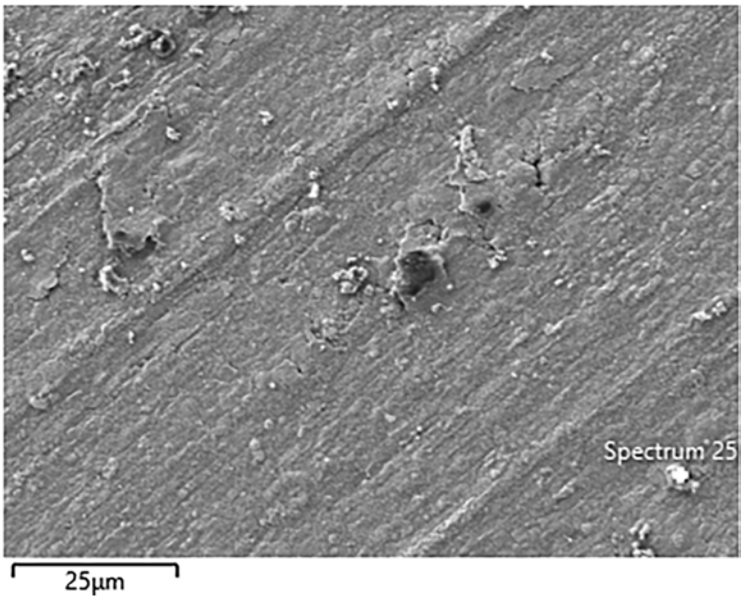

Figure 5. "Spot NO. 25" within the scorched position on the Ti sheet after 30 days of exposure in H_2 where six new elements, i.e., Si, Fe, Al, Ca, Ni, S were detected using EDS.

After five days of laser irradiation, nuclear tracks due to the neutrons were compared with the neutron tracks gathered from National Institute of Metrology, and then were counted and recorded. Neutron tracks were detected on CR-39 for all eight containers. As for the most "active" sample, i.e., the helium loaded Titanium sheet exposed to laser, it was estimated that about 200 neutrons were emitted per second per container on average, which is higher than the background by a factor of three. For each container, calculation was conducted based on average number of pits per cm^2 denoted as $n_i (i = 1,\ 2,\ 3, ..., 9)$. The value of n_i times 4440, as was mentioned earlier, gives the entire number of neutron emitted during the 5 or 30 days. The time duration for the experiment is denoted as t_j(in seconds, $j = 1,\ 2$). The total area of the imagined sphere having the radius represented by the average distance between the CR-39 and the targeted spot, which is 13 mm in this case, is 21.24 cm^2. The number of neutron emitted per container was estimated to be:

$$\frac{n_i \times 4440}{t_j} \times 21.24\,\mathrm{cm}^2$$

Table 2. New elements found on 10 spots selected from the exposed surface on Pd.

New Elements Found on Pd										
Gases	**Label**	**Au**	**Fe**	**Mg**	**Na**	**Ni**	**Pt**	**Ag**	**S**	**Si**
He	2	0	0	0	0	0	0	0	0	0
H_2	4	1/10	0	0	0	0	1/10	0	0	0
D_2	6	0	2/10	2/10	1/10	0	0	0	0	2/10
Ar	8	0	0	1/10	5/10	1/10	0	1/10	1/10	1/10

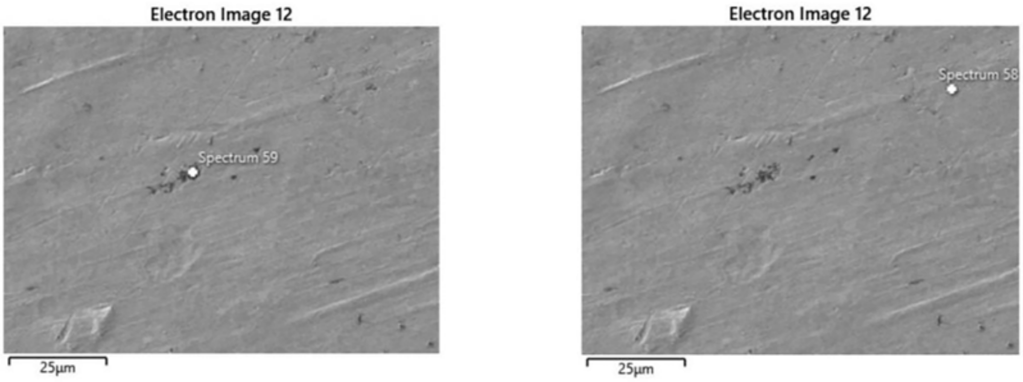

Figure 6. An example of spots selected from Pd exposed to D_2 gas and laser for 30 days where new elements Fe, Mg, Na, Si were found via EDS analysis.

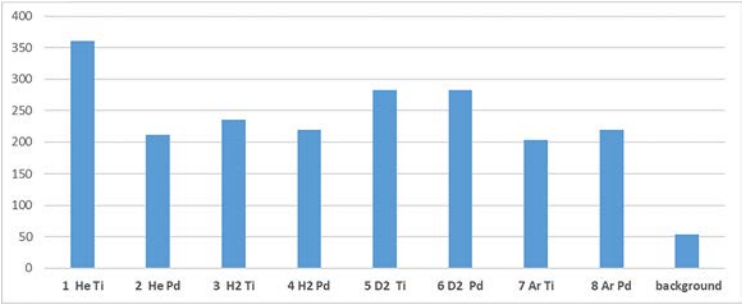

Figure 7. Counts per second (CPS) estimated for the eight chips after 5 days' laser exposure. Whenever there was a difference in the counts from the pair of chips around the same container, the larger number would be used.

The control group employed CR-39 with the same gases but without laser stimulation. The quantity of pits left on the chip inside the chamber was found to be influenced by partial melting caused by the high temperature within the chamber, making it difficult to cunt the number under a microscope.

After 30 days of laser irradiation, nuclear tracks were again counted and recorded. Neutron tracks were detected on CR-39 for all 8 containers. It was estimated that during this period, about 100 neutrons were emitted per second on average, about one order of magnitude higher than the background.

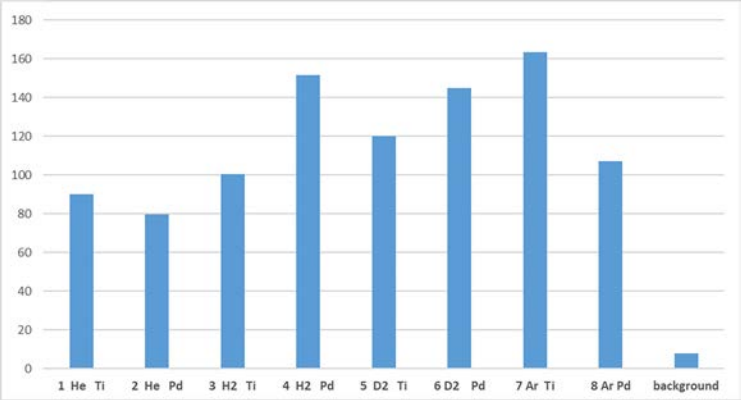

Figure 8. Counts per second (CPS) estimated for the eight chips after 30 days of laser exposure.

In summary, three implications may be deduced from the above experimental results:

1. Neutron tracks were detected using CR-39 after laser irradiation of titanium and palladium in different gases. The average neutron generation was about 100-200 counts per second (cps), and the distribution density of neutron tracks was uneven. Neutron flux turns out to be different for the first 5 days and the remaining 25 days of the experiments. Furthermore, there seems to be a large variation in the number of background neutrons.
2. Possible transmutation elements were detected in most samples of titanium and palladium after laser irradiation in different gases. Among them, Fe, Al, Ca, Ni, Na, Mg, seem to be from fission reactions, rather than fusion reactions. However, the discovery of Ag, Au and Pt indicates fusion reactions also took place. Unlike titanium, palladium after exposure showed no evident scorched spot. Thus the elemental analysis from container No. 2 may still be valid since the specimens might be simply selected from the wrong place.
3. For titanium, loading with hydrogen produces the most abundant new elements, while for palladium, loading with argon produces most abundant new elements. Silicon was occasionally found on the sample without laser irradiation, and its presence in irradiated sample might be owing to a physical dominated process of phase change and diffusion, rather than transmutation. The same hypothesis applies to oxygen and carbon (which were not listed in the table), which are difficult to distinguish from the background at present.

4. Discussion

The accuracy of the experiment is limited by many factors during the gas loading and irradiation. There was a potential slow leakage of the chambers so extra gas was needed to intermittently refill the chamber. Only the cumulative number of neutrons can be counted. There is no way to know the exact time of the neutron bursts.

The reported neutron flux is higher than other papers reporting neutrons captured from LENR. But when the same experiment was repeated with scintillator or He-3 neutron detector, no signals were detected. The low detection efficiency might be the reason for the mismatched results. The energy of the neutrons needs to be studied in depth using real-time detectors or even neutron activation analysis (NAA).

Neutrons have been detected in Ti and Pd in the four types of gases, among which two are inert gases. This counter-intuitive result may assist in gas loading and laser stimulation experiments in future, and broaden the scope of LENR.

This experiment is a preliminary attempt to replicate MIT's experimental scheme. It qualitatively supports the existence of nuclear processes during laser irradiation upon certain metals. However, the evidence is as yet insufficient to analyze the properties of the tracks left in the CR-39.

The distribution of new elements is dominated by fission reaction products, rather than fusion reaction products. Currently, no clear correlation can be drawn between the neutron flux and the abundance of possible transmutation elements. The experiments need to be repeated to understand the rule governing the distribution of elements.

In the next step, we plan to use real time detectors with better sensitivity. Because of the low neutron quantity, it is necessary to design a special moderator and a combined measurement scheme to increase the detection efficiency, and capture more information regarding the tracks left on CR-39. This work is in progress. We also realize that the counting and the spherical approximation for calculating the emitted neutron is only a rough approximation. More repetitions are needed to address the problem of random error that may appear in a single experimental run and invalidate the result.

Acknowledgements

Many thanks to the support given by Dr. Peter Hagelstein, Florian Metzler, Lynn Bowen, Jean-Paul Biberian, Ubaldo Mastromatteo, David Nagel, Jacques Ruer, Alan Smith, Akito Takahashi. And special thanks to Prof. Xingzhong Li, Tieshan Wang, Wushou Zhang, and student Qianqian Zhou, and many others who have offered their generous support to this work.

References

[1] Probing neutrons and purported fission daughter products from gas-loaded, laser-irradiated metal-hydrogen targets. Principal Investigator: Yet-Ming Chiang, Professor, MIT Presentation by Florian Metzler, Research Scientist, MIT

[2] Laser induced transmutation in palladium thin films in hydrogen atmosphere. Jean-Paul Biberian, Pamela Mosier-Boss, Larry Forsley. Aix-Marseille University, France Global Energy Corporation, U.S.A.

[3] LENR Anomalies in Pd–H2 Systems Submitted to Laser Stimulation Ubaldo Mastromatteo, A.R.G.A.L. Via S. Stefano, 27 – 20010 Bareggio (MI), Italy

J. Condensed Matter Nucl. Sci. 41 (2026) 189–202

Research Article

An XAFS Study on the Surface Structure After an Anomalous Heat Generation Experiment Using a Material System of Ni/Cu Multilayer on Ni Substrate

Tatsumi Hioki

Institutes of Innovation for Future Society, Nagoya University, Nagoya, Japan

Yasuhiro Iwamura, Takehiko Itoh

School of Science, Yokohama City University, Yokohama, Japan

Takehiko Itoh, Jirohta Kasagi

Research Center for Accelerator and Radioisotope Science (RARIS), Tohoku University, Sendai, Japan

Tatsumi Hioki, Shinobu Yamauchi

Previously with CLEAN PLANET Inc., Tokyo, Japan

Tomonori Takahashi

CLEAN PLANET Inc., Tokyo, Japan

Abstract

The anomalously large heat generation phenomenon using hydrogen gas and nanoscale Ni/Cu multilayer films on Ni sheets was investigated by SEM-EDX and XAFS analyses for a sample that showed significant excess heat generation during a long-term heat generation experiment. SEM observations of the sample in back scattered electron mode revealed randomly distributed dark regions of anomalously high oxygen concentration, surrounded by grey regions with only trace oxygen concentration. The dark regions corresponded to the regions of high oxygen concentration (RHOC) reported in previous studies. XAFS analyses of the sample suggested that approximately 5% of the Ni or Cu atoms in the surface layer were in a chemical state similar to oxygen-deficient NiO$_{1-\delta}$ or CuO$_{1-\delta}$, and were localized in the RHOC. It was also suggested that the RHOC extended to a depth of $\sim$0.8 μm or more which was much deeper than the initial multilayer thickness of $\sim$150 nm. If the RHOC were formed as a result of cumulative events of anomalous heat generation, then a local atomic configuration, in which a significant number of both oxygen atoms and their vacancies occupy octahedral interstitial sites adjacent to Ni atoms with a face-centered cubic structure, may be an efficient nuclear active environment for anomalous heat generation.

© 2026 ICCF. All rights reserved. ISSN 2227-3123

Keywords: Anomalous heat generation, Ni/Cu multilayer, Region of high oxygen concentration, XAFS, Oxygen deficient nickel oxide, Oxygen, Vacancy.

---

1. Introduction

An anomalously large heat generation phenomenon using nanoscale Ni/Cu multilayer films and hydrogen gas has been reported by Iwamura et al [1]–[6]. They prepared a material system consisting of $\sim$100 nm-Ni/Cu multilayers on a 100 μm-Ni substrate. When the system was preloaded with hydrogen followed by rapid evacuation of the hydrogen and simultaneous heating to several hundred °C, excess heat was triggered. Once triggered, the excess heat occurred continuously over a long period (e.g., 6 $\sim$ 80 h [7], [8]), sometimes accompanied by sudden bursts of heat [2]–[5], [9], [10]. This anomalously large heat generation phenomenon was also confirmed by the photon radiation calorimetry method established by Kasagi et al. [7]–[10]. The total amount of excess heat was so large that it could not be explained by known chemical reactions. This anomalously large heat generation is hypothesized to originate from nuclear-related reactions [5], [8], although direct evidence such as gamma-rays or neutrons has not been clearly observed [5]. Furthermore, no significant increase in helium-4 (^{4}He) was observed in mass spectroscopy measurements during anomalous heat generation experiments [5]. However, scanning electron microscopy (SEM) observations revealed that there were characteristic regions on the surface of the sample after the anomalous heat generation experiments, namely regions of high oxygen concentration (RHOC) [5], [6]. The RHOC were randomly distributed on the surface, and their size was $\sim$5 μm. The oxygen concentration within the RHOC was 10 $\sim$ 40 at % which was anomalously high compared to less than $\sim$1 at % in the normal regions around the RHOC [5]. RHOC were more pronounced in samples with larger excess heat, RHOC were therefore expected to be hot spots for anomalous heat generation. Various analytical methods have been used to clarify the origin of RHOC [5], [6], but the material aspects of RHOC, such as the chemical state of oxygen in RHOC and the extent of RHOC in the depth direction have not been fully elucidated. In this study, to further characterize the RHOC, X-ray absorption fine structure (XAFS) and SEM-EDX (energy dispersive X-ray) measurements were carried out for a sample that showed a large excess heat in an anomalous heat generation experiment.

2. Experimental

2.1. Sample Preparation for SEM-EDX and XAFS Measurements

The sample used in the present study was prepared in the same way as previously reported by Iwamura et al [1]–[6]. First, using magnetron sputter deposition, 6 layers of Ni (20 nm)/Cu (3.8 nm) bilayer were deposited on a Ni sheet with a size of 0.1 mm× 25 mm× 25 mm. The Ni sheet of purity 99.9% was obtained commercially from the Furuuchi Chemical Co. It was washed with acetone and annealed in vacuum (<10^{-4} Pa) at 900 °C for 72 h, and then washed with HNO_3/H_2O to remove impurities from the surface. After these pre-treatments, 3.8 nm-Cu and 20 nm-Ni films were repeatedly deposited on the Ni sheet by magnetron sputtering. The base pressure of the deposition chamber was 7.4×10^{-5} Pa. High purity Ar gas was supplied as the sputtering gas at a rate of 0.12 mL/s and the pressure of the chamber was 0.14 Pa during deposition. The sputtering conditions were 50 W for 82 s for Cu and 100 W for 368 s for Ni. To ensure uniform deposition, the substrate was rotated at 20 rpm. Figure 1 shows schematic cross-section of the multilayer sample to be fabricated by the magnetron sputtering deposition. The atomic ratio of Cu to Ni in the multilayer film 143 nm thick was $Cu_{0.16}$ $Ni_{0.84}$.

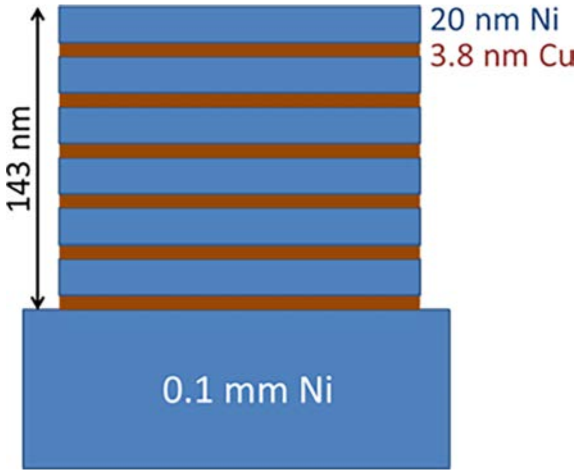

Figure 1. Schematic cross-section of the fabricated multilayer sample.

After sputtering, the multilayer sample was mounted on a sample holder in the experimental chamber for anomalous heat generation. A ceramic heater and a thermocouple were embedded in the sample holder to control the sample temperature. The experimental procedures for anomalous heat generation were as follows. First, the multilayer sample was baked for 2 days at a heater temperature of 900 °C under a vacuum of 10^{-4} Pa or less. After this baking process, the sample was cooled to 250 °C, and H_2 gas insertion into the chamber was begun. Insertion stopped when the pressure rose to 230 Pa. The pressure in the chamber then gradually decreased over time. This hydrogen absorption process took 16 h at 250 °C. After this, H_2 gas was evacuated with a turbo molecular pump, and at the same time, the sample was rapidly heated by the ceramic heater to 900 °C. These processes triggered an anomalous heat generation reaction, followed by almost constant excess heat generation for about 10 h in a vacuum of 10^{-4} Pa or less. The excess heat power was $\sim$5 W against a fixed heater power of 23 W. After this anomalous heat generation experiment, the sample was removed from the chamber and analyzed with SEM-EDX and XAFS. Hereafter, this sample is referred to as the AHG sample. To analyze XAFS data of the AHG sample, XAFS spectra of reference samples such as Ni-foil, NiO, $Ni(OH)_2$, NiOOH pellets, Cu-foil, CuO, Cu_2O, and $Cu(OH)_2$ pellets were measured by the transmission method. The reference samples were provided by the Aichi Synchrotron Radiation Center.

2.2. SEM-EDX Measurements

The surface morphology of the AHG sample was observed by scanning electron microscopy (SEM) and the concentration of elements in the surface layer was measured by energy dispersive X-ray (EDX) spectroscopy, using SEM-EDX apparatus JSM-6500F (JEOL) at the Electron Microscope Center, Tohoku University. Surface morphology observations were performed by secondary electron (SE) mode and backscattered electron (BE) or COMPO mode. The former mode gives information on surface irregularities, and the latter mode gives elemental composition distribution in the surface layer, i.e., regions of heavier elements appear brighter and those of lighter elements darker. The acceleration voltage for the incident electron beam was either 5 or 15 keV. Elemental concentrations were obtained at 15 keV, where the analysis depth, i.e., the effective range of the incident electron beam, was estimated to be approximately 0.6 μm for the AHG sample assuming the sample was close to pure Ni [11].

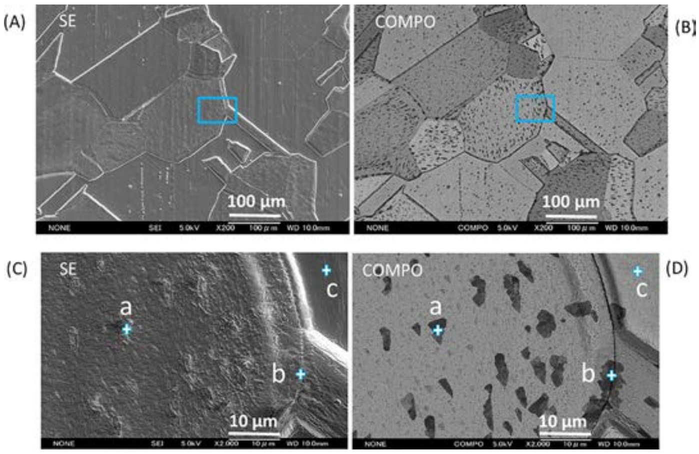

Figure 2. SEM images of the AHG sample: (A); SE image (× 200), (B); COMPO image of the same area with (A), (C); SE image (× 2000) of the blue square area in (A), (D); COMPO image of the same area with (C). These images were obtained with an acceleration voltage of 5 keV.

2.3. XAFS Measurements

To obtain information about the chemical state of the oxygen in RHOC, Ni K-edge and Cu K-edge XAFS measurements were carried out using BL5S1 at the Aichi Synchrotron Radiation Center, Aichi, Japan. The incident angle of the X-ray was fixed at 2 degrees to the sample surface to obtain information on the surface layer less than $\sim 1\ \mu$m thick. The size of the sample was 10 mm $\times$ 20 mm $\times$ 0.1 mm and the footprint of the incident X-ray at the center of the sample surface was 0.5 mm wide and 14 mm long. Ni K-edge XAFS was measured by the conversion electron yield (CEY) method. For this case, the analysis depth was estimated to be about 40 nm from the experimentally determined value of 41 nm for the case of Cu K-edge XAFS using Cu films with different thicknesses [12]. It should be mentioned that we could not apply the fluorescence yield (FY) method to measure Ni K-edge XAFS due to the thickness effect or the self-absorption effect [13]. Cu K-edge XAFS for the AHG sample was measured by the FY method, because Cu atoms in the AHG sample were dilute. In this case, the analysis depth was estimated to be about 0.8 μm as the depth at which incident X-ray intensity decreased to 1/e. For the reference samples, the transmission yield method was used to obtain Ni K-edge and Cu K-edge XAFS spectra. These XAFS data were analyzed using the Athena and Artemis programs [14]. X-ray absorption near edge structure (XANES) spectra were analyzed using the linear combination fitting (LCF) of the Athena program. Extended X-ray absorption fine structure (EXAFS) spectra were analyzed using the Artemis program.

3. Results

3.1. SEM-EDX Analyses

Surface morphology observation of the AHG sample was performed by SEM in both SE and COMPO modes. As shown in Figures 2(B) and 2(D), the surface had randomly distributed dark areas when viewed in the COMPO mode. This is the feature of the sample that showed an excess heat, as reported by Iwamura et al. [5], [6]. Figure 2(A) is an SE image which shows that the sample consists of grains with a size in a range from about 10 μm to a few hundred micrometers. Figure 2(B) is a COMPO image for the same area as Figure 2(A). Figure 2(B) shows that there are many dark spots randomly distributed within each grain. Figures 2(C) and 2(D) are enlarged images of the blue square area

Table 1. Concentration of elements at points a, b, and c in Figure 2(D) by SEM-EDX.

Element	**Atomic concentration (at %)**		
	point a (RHOC)	point b (RHOC)	point c (Normal)
O	40	32	0.90
Ni	56	62	90
Cu	∼0	0.55	0.99
C	2.7	3.5	7.8
Al	∼0	0.42	∼0
Si	0.11	0.40	∼0
Mn	0.65	0.96	∼0

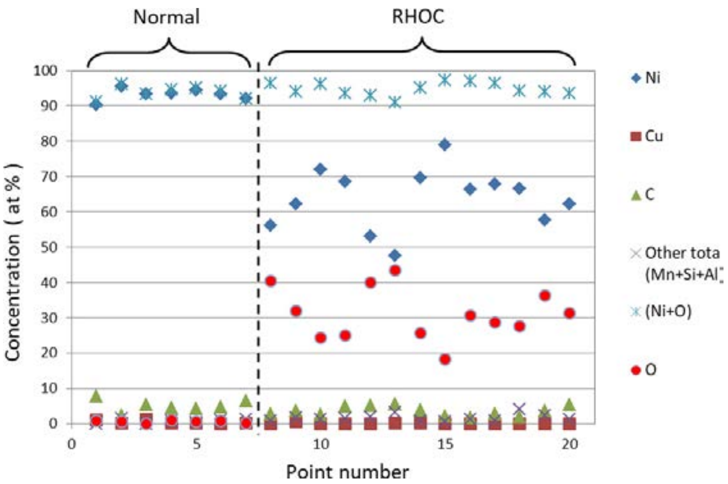

Figure 3. Elemental concentrations measured by SEM-EDX at 20 points randomly selected throughout the sample. The points a, b, and c in Figure 2 are plotted as point number 8, 9, and 1, respectively.

shown in Figure 2(A) and 2(B), respectively, and these show the same area observed in different modes. It is noted that in the COMPO images, there were many dark regions randomly distributed on the surface. The average size of the dark regions was ∼5 μm from Figure 2(D). These features of the dark regions corresponded closely to the regions of high oxygen concentration (RHOC) reported by Iwamura et al. [5], [6]. As shown in Table 1, at measurement points a and b within the dark regions in Figure 2(D), O concentrations were 40 at % and 32 at%, respectively. In contrast, at point c in a grey or normal region, O concentration was only 0.90 at%. As observed in Figure 2(C), the normal regions appear flat, whereas the RHOC resemble particles or indentations. From Figure 2(D), the total area of the dark regions (RHOC) was estimated to be roughly 10% of the total area.

As shown in Figure 2(B), dark spots were observed throughout the sample. Similar to the points a ∼ c, elemental compositions were measured at 20 randomly selected points throughout the sample; 7 points in the normal regions and 13 points in the dark regions or the RHOC. The results are shown in Figure 3, where the atomic concentrations of the detected elements O, Ni, Cu, C, Mn, Si and Al are plotted for the 20 measurement points. The concentrations of Mn, Si, and Al impurity elements are plotted as the sum of the others (Mn + Si + Al). The sum of the O and Ni concentrations (Ni + O) at each point is also plotted.

As shown in Figure 3, in the dark regions (RHOC), the O concentration varied from 20 to 45 at % depending on the measurement point. On the other hand, in the normal regions, O concentration was less than 1 at % at all points.

Table 2. Average atomic concentration for 7 normal points and 13 RHOC points (at%).

Elements	**O**	**Ni**	**Cu**	**C**	**Other total (Mn+Si+Al)**	**Ni+O**
Average of 7 points in normal regions	0.61	93	0.39	5.1	0.70	94
Average of 13 points in RHOC	31	64	0.07	3.5	1.6	95

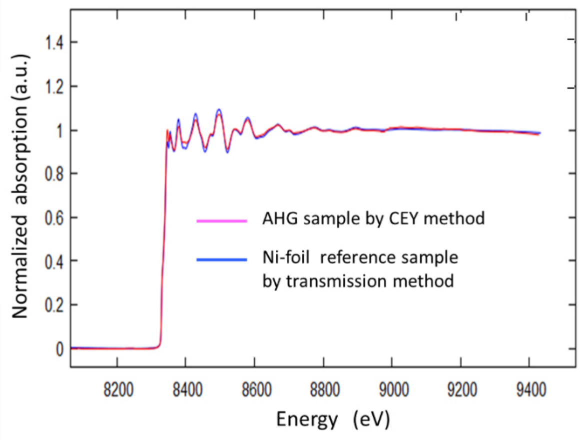

Figure 4. Ni K-edge XAFS spectra for the AHG and Ni-foil reference samples.

However, the (Ni + O) concentration at all measurement points was almost the same, at approximately 95 at%. It should be noted that several atomic percent of carbon was always detected regardless of whether it was in a normal or dark region, which was probably due to the hydrocarbons contaminated after removal of the sample from the heat generation experimental chamber to the ambient atmosphere. In addition to C, impurity elements Mn, Si, and Al were detected at low concentrations. As shown in Table 2, the average O concentration in the dark (RHOC) regions was 31 at % while that in the normal regions was 0.61 at %.

It is noteworthy that the average Cu concentration in the RHOC is much lower than that in the normal region, although the Cu concentrations in both regions are low, at less than 1 at %, which is much lower than the Cu concentration of 16 at % in the initial multilayer film. These facts suggest that Cu atoms diffused to a depth of more than 2 $\sim$ 3 μm into the Ni substrate, and that the Cu atoms in the RHOC, in particular, diffused deeper than in the normal regions. The latter fact suggests that the local temperature in the RHOC during the anomalous heat generation experiment was higher than in the normal regions.

3.2. XAFS Analyses

3.2.1. *Ni K-edge XAFS*

Figure 4 shows a comparison of the Ni K-edge XAFS spectrum for the AHG sample measured by the CEY method with the spectrum of a Ni-foil reference sample measured by the transmission method. The two spectra nearly overlap in the near-edge and extended structure regions, indicating that the AHG sample is close to metallic Ni. However, as shown in Figure 5, the Ni K-edge XANES spectra are slightly different between the two curves, with slight differences in the peak top energy and intensity. According to the report by Iwamura et al. [5], NiO and $Ni(OH)_2$ were

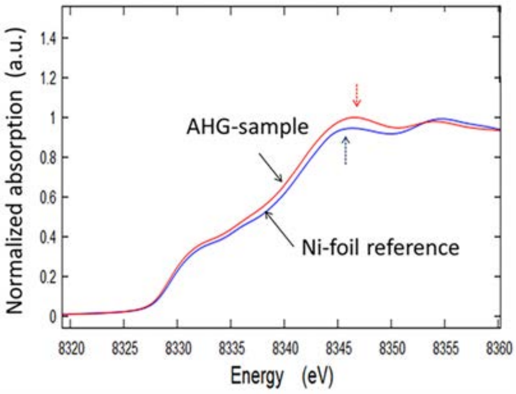

Figure 5. Ni K-edge XANES spectra for the AHG and Ni-foil reference samples.

Table 3. Results of linear combination fitting in descending order of R-factor.

Combination	**R-factor**	**A: Ni**	**B: NiO**	**C: Ni(OH)$_2$**	**D: NiOOH**
		weight: α	weight: β	weight: γ	weight: δ
A, B	0.002419	0.948187	0.051813	–	–
A, B, D	0.002505	0.931780	0.068220	–	1.445E-09
A, B, C	0.002516	0.930691	0.069309	4.724E-09	–
A, C	0.002768	0.961767	–	0.038233	–
A, C, D	0.002787	0.954165	–	0.045835	3.516E-09
A, D	0.002954	0.973061	–	–	0.026939
B	0.283693	–	1	–	–

detected on the surface of the samples after anomalous heat generation experiments using X-ray photoelectron spectroscopy (XPS), although the analysis depth of XPS was less than ~10 nm. The NiO detected by XPS was thought to be mainly due to a native oxide layer less than a few nanometers thick [15], which was likely formed during the removal of the sample from the heat generation experimental chamber into the atmosphere required for subsequent XPS measurements. During this process, the sample was exposed to atmospheric moisture, which may have resulted in the formation of Ni(OH)2 on the surface. Therefore, we assumed that the surface layer of the AHG sample was composed of Ni, NiO, Ni(OH)2, and NiOOH and attempted to reconstruct the experimental XANES spectrum as a linear combination of these reference materials, i.e.,

$$\mathrm{X\_AHG} = \alpha(\mathrm{X\_ref.A}) + \beta(\mathrm{X\_ref.B}) + \gamma(\mathrm{X\_ref.C}) + \delta(\mathrm{X\_ref.D}) \tag{1}$$

where $\alpha + \beta + \gamma + \delta = 1$, X_AHG is the XANES spectrum of the AHG sample, X_ref.A, X_ref.B, X_ref.C and X_ref.D are the XANES spectra of the reference samples of Ni, NiO, Ni(OH)$_2$, and NiOOH, respectively. In Figure 6, the XANES spectra of the AHG and the four reference samples are compared. A linear combination fitting of the spectra in the range from 8309 eV to 8359 eV was performed by using the Athena program. As shown in Table 3, among all combinations of the four reference materials, the combination of Ni and NiO showed the best fit (lowest R-factor).

Figure 7 compares the XANES spectrum of the AHG sample with the LCF fitted spectrum as the sum of 95% Ni_ref. and 5% NiO_ref. reference spectra. The analysis depth of the Ni K-edge XAFS by the CEY method was estimated to be approximately 40 nm, which is approximately 10 times the thickness of the native oxide film. There-

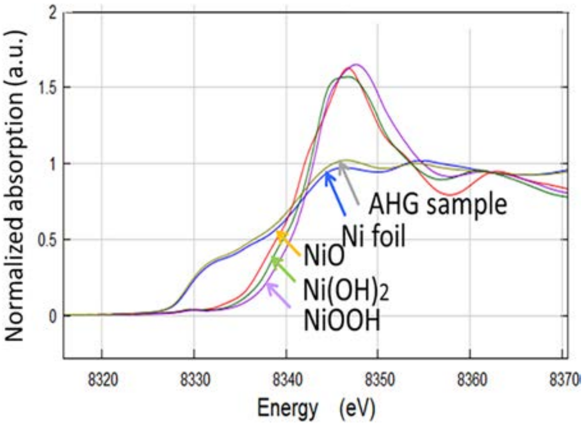

Figure 6. Ni K-edge XANES spectra for the AHG and four reference samples.

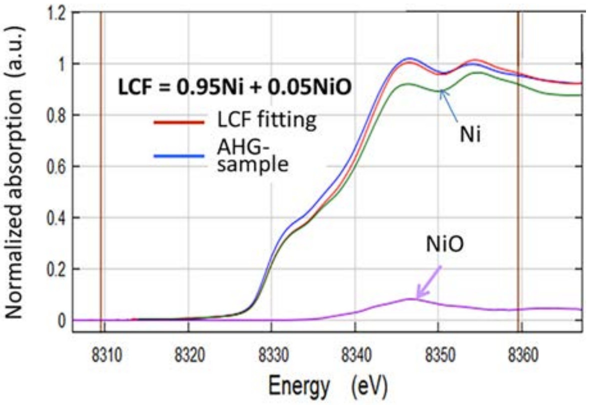

Figure 7. Ni K-edge XANES spectra of the AHG sample (blue) and the LCF fitting (red) as a sum of 95% Ni reference (green) and 5% NiO reference (purple).

fore, it was suggested that the surface layer of the AHG sample was composed of approximately 95% Ni and 5% NiO, and that the NiO extended to a depth of more than 40 nm, much deeper than the thickness of the native oxide film. Here we assume that 95% Ni and 5% NiO correspond to the normal and dark (RHOC) regions, respectively, in the COMPO-mode SEM image, as shown in Figure 8.

However, when the RHOC are stoichiometric NiO with a cubic NaCl-type crystal structure, the O concentration is always 50 at % in any RHOC. This contradicts the SEM-EDX results, which showed that the O concentration in the RHOC varied from 20 to 45 at%. Therefore, the 5% NiO component is considered to be oxygen-deficient, i.e., $NiO_{1-\delta}$. Therefore, the crystal structure of the RHOC is basically cubic NaCl-type, and the crystal structure of the normal regions is a face-centered cubic (FCC) Ni structure. It should be noted that if a $NiO_{1-\delta}$ reference sample, with $\delta = 0.57$ for example, were available, the proportion of the $NiO_{0.43}$ component would increase to more than 5%, because as δ increases, the XANES of $NiO_{1-\delta}$ approaches that of the Ni-foil reference sample.

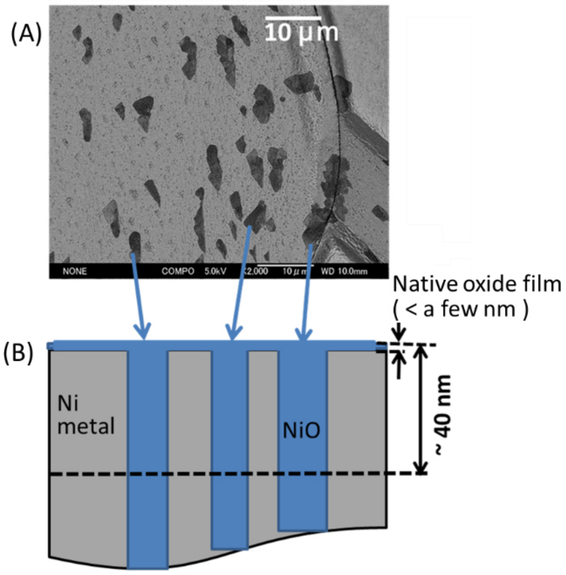

Figure 8. Possible surface layer structure of the AHG sample: (A); COMPO mode SEM image of the surface (same as Figure 2(D)), (B); schematic cross section of the dark (RHOC) regions suggested from Ni K-edge XANES analysis. Only the major elements of Ni and O are taken into account.

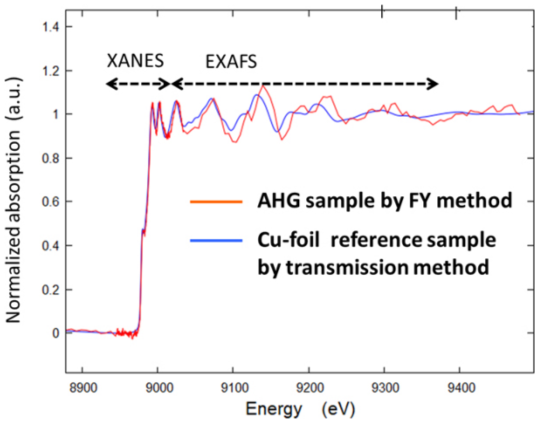

Figure 9. Comparison of Cu K-edge XAFS spectra between the AHG and Cu-foil reference samples.

3.2.2. *Cu K-edge XAFS*

As mentioned in Section 3.1, the Cu concentration in the AHG sample was less than 1 at%. Therefore, the fluorescence yield (FY) method was used for the Cu K-edge XAFS measurements. Figure 9 compares the Cu K-edge XAFS spectra of the AHG sample measured by the FY method and the Cu-foil reference sample measured by the transmission method.

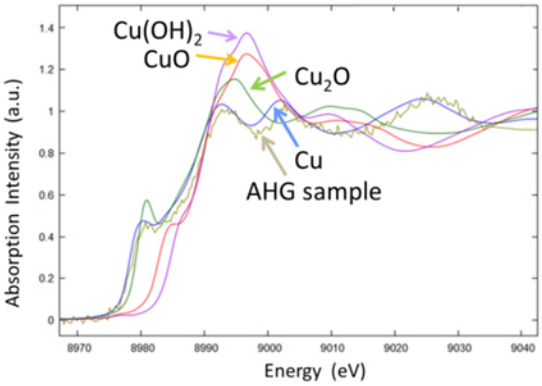

Figure 10. Cu K-edge XANES spectra for the AHG and four reference samples.

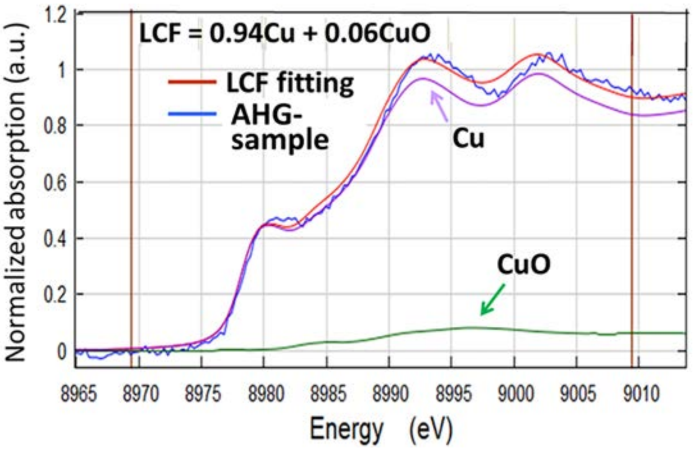

Figure 11. Cu K-edge XANES of the AHG sample (blue) and LCF fitting (red) as a sum of 94% Cu reference (purple) and 6% CuO reference (green) materials.

The two spectra are similar in the XANES region but different in the EXAFS region. The XANES region spectrum suggests that the chemical state of the Cu atoms in the AHG sample is similar to that in metallic Cu, while the EXAFS region results suggests that the environment of the Cu atom in the AHG sample is different from that in metallic Cu. The Cu K-edge XANES spectrum of the AHG sample was slightly different from that of the Cu-foil, as shown in Figure 10, which also shows the XANES spectra of the Cu-foil, CuO, Cu_2O and $Cu(OH)_2$ reference samples.

As in the case of Ni K-edge XANES, LCF fitting by the Athena program was also applied to Cu K-edge XANES using the four reference materials. Among the combinations of the reference materials, the best fit was obtained when the AHG sample was assumed to consist of 94% Cu metal and 6% CuO, as shown in Figure 11. This means that 94% and 6% of the Cu atoms in the surface layer of the AHG sample are in chemical states similar to metallic Cu and non-metallic CuO, respectively. Therefore, 94% of the Cu atoms are in the normal region and 6% of the Cu atoms are in the RHOC. Notably, 6% CuO is in close agreement with 5% NiO obtained from Ni K-edge XANES. This is natural if we consider that Cu atoms in the AHG sample would occupy the substitutional sites of Ni. The analysis

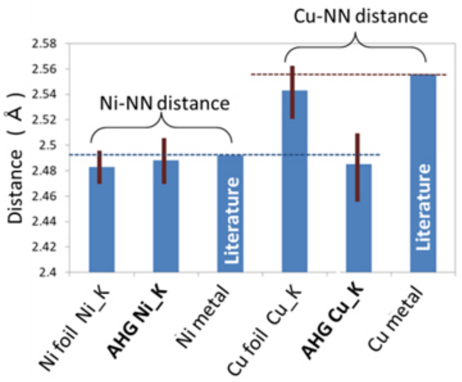

Figure 12. Comparison of experimental values of Ni-NN and Cu-NN in the AHG sample to those in the reference samples and to literature values.

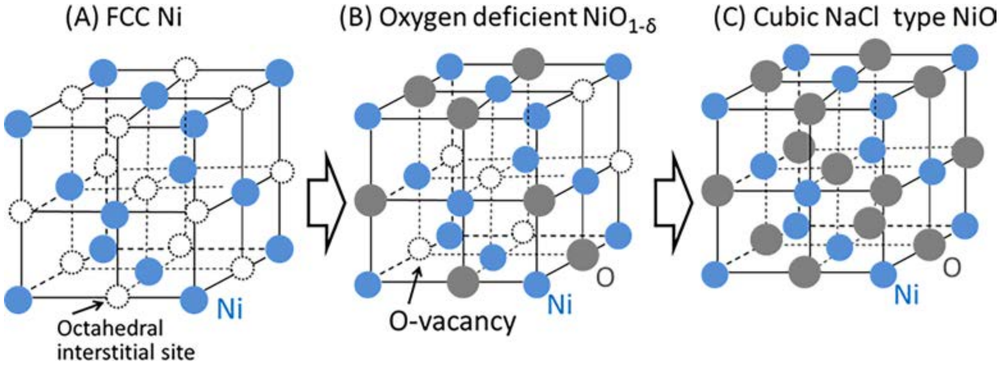

Figure 13. Comparison of crystal structures: (A) FCC Ni; (B) oxygen deficient $NiO_{1\text{-}\delta}$; (C) stoichiometric NiO. $NiO_{1-\delta}$ and NiO are formed if the octahedral interstitial sites of FCC Ni are occupied by oxygen partially and fully, respectively. In the case of (B), δ is 0.57 and O concentration (O/(Ni+O)) is 30 at %.

depth of Cu K-edge XANES by the FY method was estimated to be approximately 0.8 μm. Therefore, it is suggested that the Cu atoms in a chemical state similar to CuO extended to a depth of $\sim$0.8 μm or more. This also means that the RHOC extended to a depth of $\sim 0.8\mu$m or more, which was much deeper than the initial Ni/Cu multilayer thickness of $\sim$150 nm.

From the Cu K-edge EXAFS spectrum of the AHG sample shown in Figure 9, the distance between a Cu atom and its nearest neighboring atom (NN), i.e., the Cu-NN distance, was determined using the Artemis program. In the analysis, it was assumed that the AHG sample had an FCC structure and the coordination number of the Cu atom was 12. The result for Cu-NN distance is shown as AHG Cu_K in Figure 12. Similarly, the distance between a Ni atom and its nearest neighboring atom, Ni-NN distance, in the AHG sample was determined from the Ni K-edge EXAFS spectrum and is shown as AHG Ni_K. In the figure, experimental values determined from EXAFS spectra of the Ni-foil and Cu-foil reference samples are also shown with literature values. In the AHG sample, the Cu-NN distance was shown to be equal to the Ni-NN distance, indicating that a small number of Cu atoms randomly occupy substitutional sites of Ni atoms, the main element that forms the FCC structure of the AHG sample.

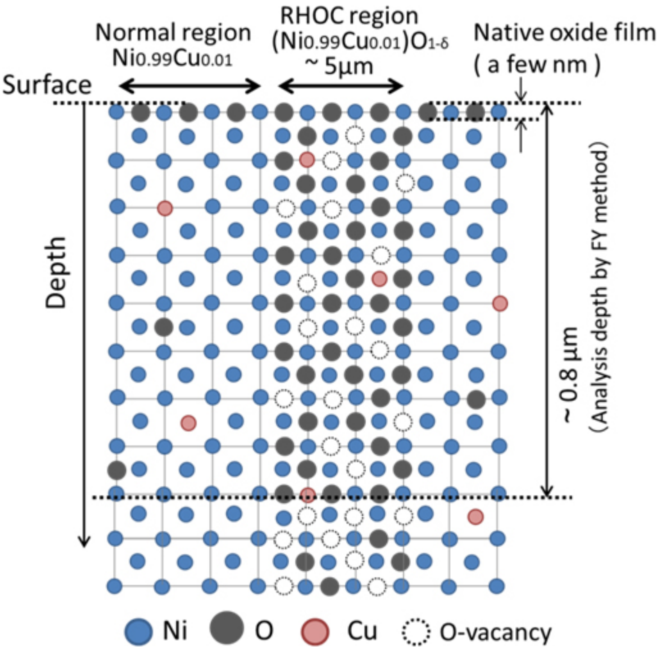

Figure 14. Schematic cross-section for the surface layer of the AHG sample. Ni atoms form FCC structure. Cu atoms of less than ∼1 at % randomly occupy the substitutional sites of Ni. O atoms in normal area are less than 1 at % and are assumed to randomly occupy octahedral interstitial sites of FCC Ni. In the RHOC region, O atoms partially occupy the octahedral interstitial sites at a high concentration in a range of 20 ∼ 45 at % and the sites unoccupied by oxygen are denoted as O-vacancy. RHOC extends to a depth of 0.8 μm or more.

4. Discussion

4.1. Surface Layer Structure of the AHG Sample

The LCF analysis for Ni K-edge XANES suggests that ∼95% of Ni atoms in the AHG sample are in a chemical state similar to metallic Ni, and the remaining ∼5% of Ni atoms are in a chemical state similar to insulating NiO. Combined with the SEM-EDX results, we assumed that 95% of the Ni atoms originate from the normal regions with an oxygen concentration of less than 1 at % and 5% of the Ni atoms originate from the RHOC with an oxygen concentration of 20 ∼ 45 at%. Stoichiometric NiO has a cubic NaCl-type structure and if the RHOC consists of NiO, O concentration in the RHOC always becomes 50 at%. This is inconsistent with the fact that O concentration in the RHOC varied, ranging from ∼20 to ∼45 at%. Therefore, the RHOC were assumed to be oxygen deficient $NiO_{1\text{-}\delta}$. It is noted that if the octahedral interstitial sites of FCC Ni are fully occupied by oxygen, the NaCl-type cubic structure of NiO is formed as shown in Figure 13. Therefore, $NiO_{1-\delta}$ is an intermediate material between metallic Ni and insulating NiO. If δ is small such as 0.2, O concentration (O/(Ni + O)) is 44 at % and the crystal structure of the RHOC is close to cubic NaCl-type structure. If δ is large, such as 0.75, O/(Ni + O) is 20 at % and the crystal structure of the RHOC is close to FCC Ni. As shown in Figure 3 and Table 2, in both regions of normal and RHOC, Cu concentrations were detected at low values of less than 1 at%, and it is suggested that the Cu atoms occupy substitutional sites of FCC Ni from the analysis of Cu K-edge EXAFS with the Artemis program. The LCF analysis for Cu K-edge XANES suggested that approximately 6% of Cu atoms within the analysis depth of ∼0.8 μm were in a chemical state similar to CuO. The value of ∼6% was approximately consistent with the value of ∼5% obtained in the LCF analysis for Ni K-edge

XANES. This fact suggests that $\sim$5% of Cu atoms exist in the RHOC which extends to a depth larger than $\sim$0.8 μm. Since the basic crystal structure is considered to be FCC Ni, the structure of the surface layer of the AHG sample is thought to be similar to the schematic picture shown in Figure 14, where impurity elements of C, Mn, Si, and Al are neglected and the area of the RHOC is tentatively assumed to be uniform in the depth direction. Actually, in the RHOC, δ-value would vary in the depth direction as well as in the horizontal direction and the boundary between the RHOC and the surrounding normal regions would be distorted.

4.2. Anomalous Heat Generation and Oxygen

The presence of the RHOC is a prominent feature of the sample that showed excess heat in the anomalous heat generation experiments using hydrogen gas and Ni/Cu multilayer films on Ni substrates. Oxygen concentration in the RHOC was anomalously high compared to that in the normal regions surrounding the RHOC. Increased concentration of O into localized regions of the RHOC is considered difficult to explain by mechanisms based on ordinary chemical reactions; small amounts of oxygen atoms in the normal region should migrate to condensate into the RHOC, and this behavior seems to violate Fick's law of diffusion at a fixed temperature. Thus, the appearance of the RHOC is considered to be related to the generation of anomalous heat that is believed to be caused by nuclear-related reactions [4], [7]. The atomic composition of the RHOC was suggested to be $(\mathrm{Ni}_{1\text{-}x}\mathrm{Cu}_x)\mathrm{O}_{1\text{-}\delta}$ with $\delta = 0.2 \sim 0.8$ and $x < 0.01$. The crystal structure of the RHOC is apparently an intermediate structure between NaCl-type cubic NiO and FCC Ni. This crystal structure is formed if the octahedral interstitial sites of FCC Ni are partially occupied by oxygen. Then, the unoccupied octahedral interstitial sites can be regarded as vacancy sites of oxygen. In the case of $\delta = 0.57$ (O concentration = $\sim$30 at%), the atomic composition of the RHOC can be denoted as $\mathrm{NiO}_{0.43}[\mathrm{V(O)}]_{0.57}$, where V(O) denotes an oxygen vacancy. Ni atoms occupy the lattice sites of FCC structure and O and V(O) occupy octahedral interstitial sites of the FCC structure. V(O) may act as a hydrogen trapping site similar to the tetrahedral interstitial sites. Therefore, it is noted that in the RHOC, a significant number of both O and V(O) are adjacent to the Ni atoms, whereas in the normal regions, only V(O)'s are adjacent to the Ni atoms. Assuming that the hot spots for the anomalous heat generation are located within the RHOC, the atomic configuration consisting of adjacent Ni-O-V(O) may work as a more effective nuclear active environment than the atomic configuration consisting of only Ni-V(O).

5. Conclusions

SEM-EDX and XAFS analyses were performed with a sample after a long-term anomalous heat generation experiment using hydrogen gas and a material system of a Ni/Cu multilayer film on a Ni substrate. The sample surface exhibited randomly-distributed regions of high oxygen concentration (RHOC) surrounded by normal regions of trace oxygen concentration. The RHOC apparently extended to a depth of 0.8 μm or more, which was much deeper than the initial multilayer thickness of $\sim$150 nm. It also appeared that the atomic composition of the RHOC was expressed as $(\mathrm{Ni}_{1\text{-}x}\mathrm{Cu}_x)\mathrm{O}_{1\text{-}\delta}$ ($x < 0.01$, $\delta = 0.2 \sim 0.8$), and the crystal structure of the RHOC was in between face-centered cubic and NaCl-type cubic structures, depending on δ-values. The δ-values varied depending on the RHOC. Even in a region of high oxygen concentration, the δ-value may vary with a horizontal position as well as with depth. The mechanism of the anomalous heat generation is not clear, but a local atomic configuration of Ni-O-V(O), where a significant number of both oxygen atoms and their vacancies occupy the octahedral interstitial sites of FCC Ni, may provide an efficient nuclear active environment for the anomalous heat generation.

Acknowledgements

The authors would like to thank Dr. S. Towata of Aichi Synchrotron Radiation Center and Prof. M. Kawasumi of Nagoya University for valuable discussions.

References

[1] Y. Iwamura, T. Itoh, M. Saito, S. Murakami, J. Kasagi, "Evidence for surface heat release reaction over nano-sized multilayer metal composite with hydrogen gas", *Proceedings of the 21st Meeting of Japan CF Research Society,* JCF21, 1–14, 2020.

[2] Y. Iwamura, T. Itoh, J. Kasagi, S. Murakami, M.Saito, "Excess energy generation using a nano-sized multilayer metal composite and hydrogen gas", *J. Condensed Matter Nucl. Sci.,* vol. 33, 1–13, 2020.

[3] Y. Iwamura, T. Itoh, T. Takahashi, S. Yamauchi, M. Saito, S. Murakami, J. Kasagi, "Energy generation using nano-sized multilayer metal composites with hydrogen gas; intentional induction of heat burst phenomenon", *Proceedings of the 22nd Meeting of Japan CF Research Society,* JCF22, 27–39, 2022.

[4] Y. Iwamura, J. Kasagi, T. Itoh, T. Takahashi, M. Saito, Y. Shibasaki, S. Murakami, "Progress in energy generation research using nano-metal with hydrogen/ deuterium gas", *J. Condensed Matter Nucl. Sci.,* vol. 36, 285–301, 2022.

[5] Y. Iwamura, T. Itoh, S. Yamauchi, T. Takahashi, "Anomalous heat generation that cannot be explained by known chemical reactions produced by nano-structured multilayer metal composites and hydrogen gas", *Jpn. J. Appl. Phys.*, vol. 63, 037001, 2024.

[6] Y. Iwamura, T. Itoh, J. Kasagi, T. Takahashi, S. Yamauchi, M. Saito, S. Murakami, T. Hioki, "Anomalous heat burst triggered by input power perturbations observed in Ni-based nanostructured thin films with hydrogen", *J. Condensed Matter Nucl. Sci.,* vol. 38, 269–286, 2024.

[7] J. Kasagi, T. Itoh, Y. Shibasaki, T. Takahashi, S. Yamauchi, Y. Iwamura, "Photon radiation calorimetry for anomalous heat generation in Ni-Cu multilayer thin film during hydrogen gas desorption", *arXiv*:2311.18347 [physics.ins-det], 2024.

[8] J. Kasagi, T. Itoh, Y. Iwamura, Y. Shibasaki, T. Takahashi, S. Yamauchi, "Photon radiation calorimetry for anomalous heat generation in NiCu multilayer thin film during hydrogen gas desorption", *J. Condensed Matter Nucl. Sci.*, vol. 39, 210–219, 2025.

[9] T. Itoh, Y. Shibasaki, T. Takahashi, M. Saito, J. Kasagi, Y. Iwamura, "Optical observation of spontaneous heat burst phenomena during hydrogen desorption from nano-sized metal composite", *J. Condensed Matter Nucl. Sci.*, vol. 36, 274–284, 2022.

[10] T. Itoh, Y. Shibasaki, J. Kasagi, S. Murakami, M. Saito, Y. Iwamura, "Optical observation on anomalous heat generation from nano-sized metal composite", *Proceedings of the 21st Meeting of Japan CF Research Society,* JCF21, 15–25, 2021.

[11] H. Soejima, "Depth resolution of electron spectroscopy analysis", *Journal of The Surface Science Society of Japan*, vol. 5, no. 3, 351–363, 1984.

[12] T. Nonaka, K. Kawase, S. Ozaki, K. Doumae, M. Takemura, A. Mikami, A. Yonetama, S. Kamimura, "Comparison of conversion electron yield and fluorescence yield methods in thin film and trace element XAFS measurements", presented at *16th Joint Symposium on Synchrotron Radiation Science at the Annual Meeting of the Japanese Society for Synchrotron Radiation Research*, 9–11 Jan 2003, Himeji, Japan, 10P11. https://sunbeam.spring8.or.jp/top/seika/ohp/JSSR2002/10P11

[13] L. Troger, D. Arvanitis, K. Baberschke, H. Michaelis, U. Grimm, E. Zscheck, "Full correction of the self-absorption in soft-fluorescence extended x-ray absorption fine structure", *Phys. Rev. B*, vol. 46, 3283–3289, 1992.

[14] B. Ravel and M. Newville, "Athena, Artemis, Hephaestus: data analysis for x–ray absorption spectroscopy using IFEFFIT", *J. Synchrotron Rad.,* vol.12, 537–541, 2005.

[15] S. Suzuki, Y. Ishikawa, M. Isshiki, Y. Waseda, "Native oxide layers formed on the surface of ultra-high-purity iron and copper investigated by angle resolved XPS", *Material Transactions, JIM,* vol. 38, 1004–1009, 1997.